



**HAL**  
open science

**Transferts d'énergie ultrarapides à l'échelle  
nanométrique : dynamiques de refroidissement et  
vibrationnelle de nano-objets métalliques individuels  
supportés**

Clément Panais

► **To cite this version:**

Clément Panais. Transferts d'énergie ultrarapides à l'échelle nanométrique : dynamiques de refroidissement et vibrationnelle de nano-objets métalliques individuels supportés. Physique [physics]. Université Claude Bernard - Lyon I, 2024. Français. NNT : 2024LYO10251 . tel-04848443

**HAL Id: tel-04848443**

**<https://theses.hal.science/tel-04848443v1>**

Submitted on 19 Dec 2024

**HAL** is a multi-disciplinary open access archive for the deposit and dissemination of scientific research documents, whether they are published or not. The documents may come from teaching and research institutions in France or abroad, or from public or private research centers.

L'archive ouverte pluridisciplinaire **HAL**, est destinée au dépôt et à la diffusion de documents scientifiques de niveau recherche, publiés ou non, émanant des établissements d'enseignement et de recherche français ou étrangers, des laboratoires publics ou privés.

THÈSE de DOCTORAT DE L'UNIVERSITÉ DE LYON

Opérée au sein de :

l'Université Claude Bernard Lyon 1

Ecole Doctorale ED52  
Physique et Astrophysique

Spécialité de doctorat : Physique

Soutenue publiquement le 29/11/2024, par :

**Clément Panais**

---

**Ultrafast energy transfers at the nanoscale :  
cooling and vibrational dynamics of single  
supported metal nano-objects**

---

Devant le jury composé de :

**Nathalie Destouches**

Professeure des Universités, Université Jean Monnet, Saint-Etienne

**Stefan Dilhaire**

Professeur des Universités, Université de Bordeaux

**Pascal Ruello**

Professeur des Universités, Le Mans Université

**Gianpietro Cagnoli**

Professeur des Universités, UCBL

**Aurélien Crut**

Maître de Conférences, UCBL

**Natalia Del Fatti**

Professeure des Universités, UCBL

**Noëlle Lascoux**

Chargée de recherches CNRS, UCBL

**Présidente**

**Rapporteur**

**Rapporteur**

**Examineur**

**Directeur de thèse**

**Co-Directrice de thèse**

**Invitée**





# Remerciements

Cette section fait un pas de côté par rapport au reste du manuscrit, aussi bien du point de vue de la forme que du fond, pour remercier l'assemblage hétéroclite de personnes et d'entités ayant participé d'une manière ou d'une autre à l'accomplissement de cette thèse de physique.

Tout d'abord, je ne peux que remercier mes deux directeur.rice.s de thèse, Aurélien Crut et Natalia Del Fatti, pour leur encadrement et soutien tout au long de ma thèse. Natalia, tu as été une source inépuisable d'idées aussi bien théoriques qu'expérimentales. Lors des quelques manips et TP que j'ai pu faire en ta compagnie j'ai toujours senti ta très grande maîtrise des setups et ta passion pour l'étude expérimentale. Merci pour ta gentillesse, ta grande bienveillance et de m'avoir accordé ta confiance pour cette thèse. Au cours de ces 3 années, j'ai vraiment apprécié pouvoir discuter avec toi et notamment pouvoir le faire d'égal à égal à partir du moment où je maîtrisais bien le setup. Aurélien, tu es passionné par ce que tu fais et perfectionniste. Tu aimes que les choses soient carrées et bien faites (et évidemment respecter les deadlines, ce que je comprends tout à fait !). J'ai particulièrement apprécié ta grande rigueur scientifique, qui m'a notamment permis de grandir scientifiquement. Tes attentes étaient élevées et même si j'ai parfois eu du mal à suivre ton rythme cela m'a été bénéfique d'être, d'une part, confronté à des deadlines et, d'autre part, devoir rendre compte de mon avancement régulièrement. Tes simulations étaient de grande qualité et ont été cruciales pour ma thèse et je t'en remercie. Merci pour ta gentillesse et ta compréhension ! Je remercie également l'ANR pour le financement accordé au projet Ultrasingle, porté par Aurélien Crut, et qui a permis de financer ma thèse.

Je remercie chaleureusement toute l'équipe FemtoNanoOptics pour leur accueil : Fabien Vialla, Paolo Maioli, Francesco Banfi, Noëlle Lascoux, Romain Rouxel, Michele Diego, Margherita Vitucci, Arthur Allen, Nathan Berrit, Alessia Colosimo et Alessandro Casto. Fabien tu m'as accueilli en premier au sein de l'équipe via mon stage de M2 et m'as fait découvrir les manips, sans toi je ne serai pas allé jusque là. Paolo, tu as toujours été un puits de savoir d'une très grande gentillesse et bienveillance (ne change jamais ça), c'était génial de discuter avec toi ! Francesco, j'ai admiré ton enthousiasme et ton énergie (et je suis content que le set fanfare à mon pot t'ait plu !). Merci Romain de m'avoir passé le flambeau des manips, c'est à moi de le passer désormais. Michele, je t'ai peu côtoyé mais j'ai été très impressionné par ta grandeur tant intérieure que scientifique, je suis sûr que le Japon se passe à merveille pour toi. Alessia, c'est un plaisir d'avoir pu travailler avec toi sur les nanofils, ça m'a fait me poser plein de questions et élargir mon horizon scientifique au delà des nanoparticules. Margherita, Arthur et Nathan, je ne vous souhaite que du bien pour la suite et j'ai entièrement confiance en vous pour mener à bien vos thèses (je sais pertinemment que vous aurez des galères expérimentales, comme moi, mais bon c'est le jeu !). Alessandro, comme on a fait nos thèses en même temps j'ai une affection

toute particulière pour toi. C'était pas toujours évident de rester motivés mais j'ai beaucoup apprécié nos discussions dans le SAS des salles de manips ou à la frontière de nos deux salles de manips. Tu es quelqu'un de très sympa et ça a été un plaisir de te côtoyer. Je termine enfin par toi Noëlle : c'est avec toi que j'ai travaillé au quotidien, passé des journées entières dans la pénombre (ou avec une pile !) dans les salles de manips à aligner des faisceaux lasers, réoptimiser le signal SMS et pompe-sonde, installer des échantillons (t'inquiètes pas pour la manipulation des grilles TEM, Nathan sera certainement aussi compétent que moi), etc. Mais aussi, et c'est au moins aussi important, discuter de tout et de rien pendant les scans, de l'actualité, de politique, de féminisme, de cinéma, de fanfare, de musique, etc. On se rejoint sur notre approche de la science, assez pragmatique et relativement détachée, mais toujours avec le souci de bien faire et de réussir à étudier ce qu'on veut (le côté ingénieur peut-être ?). Merci pour ta bienveillance, nos discussions, les manips réalisées ensemble et tout le reste bien sûr, ça a été un plaisir immense et partagé de travailler avec toi.

Je remercie également nos collaborateurs à l'Institut Lumière Matière, l'ICMCB et au NIMBE (CEA Saclay) pour leur travail au sujet de la synthèse des nanoparticules, les dépôts de celles-ci et l'imagerie via TEM/SEM. Nicholas Blanchard, merci de m'avoir formé à la TEM, j'espère ne pas t'avoir trop fait perdre de temps avec mes cubes d'argent et mes framboises, en tout cas ça a été un plaisir de travailler et discuter avec toi. Mona Tréguer-Delapierre et Clément Vecco-Garda, je vous remercie pour votre travail au sujet de la synthèse des framboises, l'amélioration de celle-ci et de la procédure de dépôt. Je laisse le setup en de bonnes mains, Nathan devrait pouvoir poursuivre l'étude des framboises et, j'en suis sûr, obtenir de très beaux résultats au sujet des transferts énergétiques à l'intérieur d'un nanohybride. Sylvie Marguet, un grand merci à toi pour l'excellente qualité de tes synthèses et dépôts de nanodisques d'or, sans toi ma thèse aurait été totalement différente ! Je te souhaite que tes collaborations futures avec Aurélien et Natalia soient tout aussi fructueuses.

Je remercie par ailleurs les services administratifs et techniques pour l'aide apportée au sujet des missions et de la fabrication de pièces adaptées à mon setup expérimental.

Pour conclure, des remerciements tout particuliers s'imposent. Quinté+, Jo ou encore Joséphine Pelenc, merci pour toute l'aide et le soutien que tu m'as apportée, d'être à mes côtés et d'être qui tu es tout simplement. J'ai confiance en toi pour ta thèse et puis je suis là pour t'aider à mon tour. Je t'aime et ce n'est pas près de changer, tout comme ma bêtise et les pastèques numériques. Je remercie mes parents, Yves et Valérie, mon petit frère, Loris, et mon grand-père, Jean-Pierre alias Poupy, d'avoir été là pour moi et de m'avoir soutenu tout au long de ma thèse. Vous êtes ma famille et je vous aime fort. Mentions spéciales pour les entités vivantes où je vis/dort/mange/geeke/lis depuis un certain temps maintenant, la Jachère et la Langouste, ainsi que leurs habitant.e.s évidemment. Je remercie chaleureusement les deux fanfares lyonnaises dont je fais partie et qui m'accompagnent depuis plusieurs années : la Fanfare Piston (de l'Ecole Centrale de Lyon) et les Fat Ducks (un groupe de ieuv qui voulaient continuer à faire de la fanfare). Enfin je vais remercier la liste longue comme le bras des fanfaron.ne.s présent.e.s à ma soutenance ou m'ayant aidé d'une façon ou d'une autre : Quinté+, L'Exploratrix, Bolognalette, Alrabin, C3pelo, Traknard, Hamza, Gomette, Standard, Tulépliratous, Simulation, Plutard, Pissenlit, P-troll, Albertcanus, Qulbukake, Bitetrain, France Gale, Moskonard, Advitam, Cu-

bidon, Radiocanus, Ravi, Gay Tapant, Cristalyn, Carte Kiwi, Didjénifer, Origami, Vantoline, Etétoi, R2D2, etc.

PS : les dernières mentions spéciales des remerciements sont attribuées à mon laser le MaiTai, le lock-in, les climats de ma salle de manip (RIP), tous les nanodisques d'or et framboises étudiés et parfois complètement flingués (oups!), mon ordi portable et les charnières de l'écran pour avoir su rester en vie malgré la fin de thèse, la Suze car j'aime beaucoup ce breuvage, mon trombone parce qu'il fait partie de moi et qu'il m'a tellement fait voyager et grandir, ma housse de trombone pour ses bons et loyaux services malgré un côté Frankenstein (promis je vais te laisser tranquille, la nouvelle housse arrive) et enfin mon casque audio pour les longues heures passées à écouter des fanfares, des TinyDesk (je recommande) ou des albums obscurs sur Youtube (Terminal Passage).

Clément Panais / Tunordure

PPS : Si vous croisez des fanfares telles que la Fanfare Piston, les Fat Ducks ou les Fantômes un jour, n'hésitez pas à demander Tunordure (c'est mon surnom fanfare, qui découle d'un bonnet de Père Noël opportuniste) et l'information arrivera certainement jusqu'à moi, que ce soit pour discuter de ma thèse, de fanfare ou boire un coup ensemble !



# Contents

<b>Introduction</b>	<b>1</b>
<b>1 Electronic, optical and thermal properties of metallic nanoparticles</b>	<b>3</b>
1.1 Physical properties of bulk noble metals . . . . .	3
1.1.1 Electronic and thermal properties of bulk noble metals . . . . .	3
1.1.1.1 Electrons in the conduction band . . . . .	5
1.1.1.2 Volumetric lattice heat capacity . . . . .	6
1.1.2 Optical behavior of bulk noble metals . . . . .	8
1.1.2.1 Electromagnetism in a noble metal . . . . .	8
1.1.2.2 Intraband transitions . . . . .	10
1.1.2.3 Interband transitions . . . . .	10
1.2 Optical properties of metallic nanoparticles . . . . .	11
1.2.1 Energetic considerations . . . . .	11
1.2.2 Optical response of a nanoellipsoid: quasi-static approximation . . . . .	13
1.2.3 Transient optical response of a single metallic nanoparticle after excitation by a laser pulse . . . . .	17
1.3 Thermal dynamics of a supported metal nanodisk . . . . .	19
1.3.1 Heat transfers through the nanodisk surface . . . . .	20
1.3.1.1 Kapitza resistance at nanodisk-substrate interface . . . . .	20
1.3.1.2 Heat transfer in air: convection . . . . .	21
1.3.1.3 Radiative heat transfer . . . . .	22
1.3.2 Heat conduction in solids . . . . .	22
1.3.2.1 Fourier diffusion . . . . .	23
1.3.2.2 Other conduction regimes . . . . .	23
1.3.3 Quasi-uniformity of nanodisk temperature . . . . .	25
<b>2 Experimental and modeling methods</b>	<b>27</b>
2.1 Gold nanodisks: synthesis and deposition . . . . .	28
2.2 Linear and ultrafast single-particle optical spectroscopy techniques . . . . .	30
2.2.1 Laser sources . . . . .	30
2.2.2 Spatial Modulation Spectroscopy (SMS) . . . . .	31
2.2.2.1 Principle . . . . .	31
2.2.2.2 Experimental setup and calibration . . . . .	39
2.2.3 Single particle ultrafast time-resolved pump-probe spectroscopy . . . . .	42
2.2.3.1 Principle . . . . .	42
2.2.3.2 Experimental configuration . . . . .	43

2.2.3.3	Procedure for signal acquisition . . . . .	44
2.2.3.4	Signal processing . . . . .	45
2.2.3.5	Characterization of pump and probe beams . . . . .	47
2.3	Optical and thermal modeling . . . . .	49
2.3.1	FEM optical modeling . . . . .	49
2.3.2	FEM thermal modeling . . . . .	52
2.3.2.1	Time domain modeling (single nanodisk excitation) . . . . .	54
2.3.2.2	Frequency domain modeling (multiple nanodisk excitations) . . . . .	54
2.3.3	FEM thermo-optical modeling . . . . .	56
<b>3</b>	<b>Cooling dynamics of deposited gold nanodisks</b>	<b>59</b>
3.1	General context . . . . .	59
3.2	Investigated samples . . . . .	63
3.3	Optical experiments and data treatments . . . . .	64
3.3.1	Nanodisk optical characterization by linear optical spectroscopy and numerical modeling . . . . .	64
3.3.2	Experimental strategy . . . . .	65
3.3.3	Raw time-resolved measurements . . . . .	66
3.3.4	Data treatment . . . . .	67
3.4	Thermal dynamics of single gold nanodisks deposited on a thick sapphire substrate . . . . .	68
3.4.1	Experimental results . . . . .	68
3.4.2	Comparison with numerical simulations . . . . .	70
3.5	Thermal behavior of single gold nanodisks deposited on thin amorphous membranes . . . . .	71
3.5.1	Experimental results . . . . .	71
3.5.2	Modeling the accumulation effects . . . . .	73
3.5.3	Comparison between experiments and frequency-domain thermal model . . . . .	78
3.6	Thermal behavior of single gold nanodisks deposited on an ultrathin amorphous membrane . . . . .	80
3.7	Conclusion . . . . .	84
<b>4</b>	<b>Optical detection of the cooling dynamics of single plasmonic nanoparticles</b>	<b>85</b>
4.1	General context . . . . .	85
4.1.1	Link between optical measurements and heating of the nanoparticle and its environment . . . . .	85
4.1.2	Previous study: ensembles of Au nanospheres in ethanol . . . . .	87
4.1.3	Previous study: single gold nanodisk lithographed on a thick sapphire substrate . . . . .	89
4.2	Optical investigations on single Au nanodisks deposited on a thin silicon nitride membrane . . . . .	90
4.2.1	Relevance of the studied system . . . . .	90
4.2.2	Optical measurements and time-resolved signals . . . . .	91
4.2.3	Experimental determination of the optical sensitivity to nanodisk heating . . . . .	93
4.2.4	Modelization of the optical sensitivity to nanodisk heating and membrane heating . . . . .	94
4.2.5	Comparison between measured and modeled sensitivities . . . . .	96

---

4.2.6	Analyzing the temporal profiles of the time-resolved measurements . . .	98
4.2.7	Thermo-optical modeling of the transient optical response of a single supported gold nanodisk . . . . .	99
4.2.8	Normalized temporal profiles: comparison between experiments and simulations . . . . .	100
4.2.9	Signals measured in the spectral range of weak sensitivity to nanodisk heating . . . . .	101
4.3	Conclusion . . . . .	102
<b>5</b>	<b>Vibrations of single gold nanodisks deposited on thin membranes</b>	<b>105</b>
5.1	Vibrational properties of nano-objects: Navier equation, eigenmodes and quality factors . . . . .	106
5.1.1	Navier equation . . . . .	106
5.1.2	Eigenmodes and quality factors . . . . .	107
5.2	Vibrational dynamics of single colloidal gold nanodisks deposited on membranes	108
5.2.1	Experimental strategy . . . . .	109
5.2.2	Experimental signals . . . . .	112
5.2.3	Experimental frequencies and quality factors . . . . .	112
5.2.4	Numerical modeling via FEM . . . . .	113
5.2.5	Comparison between experimental results and FEM modelization . . . .	114
5.3	Optical detection of the acoustic vibrations of single gold nanodisks . . . . .	116
5.3.1	Experimental strategy and acoustic signals . . . . .	117
5.3.2	Experimental results . . . . .	118
5.4	Conclusion . . . . .	119
	<b>Conclusion and Perspectives</b>	<b>121</b>
	<b>Bibliography</b>	<b>123</b>



# Introduction

Nanoparticles have been extensively studied during the last decades, with fundamental work being performed as well as research oriented towards applications. Indeed, the physical properties of nano-objects, such as their optical, electronic, magnetic, mechanical and thermal ones, present many remarkable features, in contrast with those of bulk materials. Metal nanoparticles exhibit for instance optical extinction spectra largely affected by Surface Plasmon Resonances (SPR) [1], which originate from the collective oscillation of the electrons of the metal induced by an incident electromagnetic field. Importantly, Surface Plasmon Resonance features highly depend on the nanoparticle size, shape, composition, and environment.

The optical properties of nano-objects can be used to study ultrafast phenomena associated to non-optical properties (e.g. mechanical or thermal ones) through dedicated optical techniques. Ultrafast phenomena impacting the optical response of a nanoparticle can for example be studied at timescales ranging from a few femtoseconds to nanoseconds using an optical technique called time-resolved pump-probe spectroscopy. Such technique allows to investigate topics linked to energy transfers at the nanoscale, such as the decay of the thermal or acoustic energy injected in a nano-object. In this context, resonances in the optical response of nanoparticles (e.g., Surface Plasmon Resonances for metal ones) constitute an advantage, as they allow to more sensitively probe the ultrafast dynamics. The fundamental work performed in order to investigate the modalities of nanoscale energy transfer may be helpful for applications in the fields of sensing, thermoelectric devices or photothermal therapy [2–6].

This thesis, conducted in the FemtoNanoOptics group at the Institut Lumière Matière (ILM) and funded by the ULTRASINGLE ANR project, aimed at understanding the cooling dynamics and the acoustic vibrations of metal nanoparticles, as well as the optical detection of those phenomena. To do so, single gold nanodisks deposited on various transparent substrates were studied using the combination of two optical techniques, namely the spatial modulation spectroscopy (SMS) [7, 8] and single-particle time-resolved optical spectroscopy [9, 10].

This manuscript is composed of five chapters. The first chapter is dedicated to the description of the electronic, optical and thermal properties of metallic nano-objects, which are relevant for the understanding of the work presented in the following chapters. First, the physical origins of the heat capacity of bulk noble metals are presented, as well as their optical response. The impact of dielectric confinement on this optical response and the Surface Plasmon Resonances of metal nanoparticles are then discussed, focusing on the simple case of nanoellipsoids. The physical phenomena contributing to the experimental signals obtained via pump-probe spectroscopy are subsequently described. Finally, the different types of thermal transfers by which a suddenly heated supported nanodisk cools down are presented.

Chapter 2 describes the experimental and modeling tools used in this work. The first section focuses on the chemical synthesis and deposition of gold nanodisks, a work performed by S.

Marguet from CEA in the context of the ANR-funded ULTRASINGLE project. Then the optical techniques used in experiments are presented: the spatial modulation spectroscopy, which allows to detect a single supported nano-object and to measure its extinction spectrum, and the time-resolved pump-probe spectroscopy, which gives access to the temporal variations of the extinction cross-section of a single nanoparticle following its excitation by a femtosecond laser pulse. Finally, we introduce the optical and thermal modeling, which were used in this work to complement and interpret optical measurements.

The third chapter focuses on the experimental and theoretical study of the cooling dynamics of single gold nanodisks deposited on substrates with different compositions and thicknesses. This work aimed at providing a better understanding of the link between the cooling dynamics of a single gold nanodisk and the characteristics of its substrate. In particular, a large effect of the supporting substrate thickness and composition on the cooling dynamics was demonstrated. The reduction of substrate thickness to the nanometric range was seen to considerably slow down the nanodisk cooling dynamics and to induce accumulation effects associated to the repeated character of the optical excitation in experiments.

The fourth chapter presents experimental and theoretical results obtained about the quantitative optical detection of the cooling dynamics of single gold nanodisks supported on a thin membrane. The sensitivity of time-resolved signals to nanodisk heating was measured and successfully modeled. Additionally, a contribution of membrane heating to these signals could be demonstrated.

Chapter 5 presents experimental findings about the acoustic vibrations of single gold nanodisks supported on thin membranes. The goal of this study was to extend previous work performed within the FemtoNanoOptics group on supported single gold nanodisks synthesized by physical methods, which showed that the measured quality factors were strongly influenced by the diameter/thickness ratio range. In the present work, frequencies and quality factors obtained experimentally are shown and compared with numerical modeling and previous results. The measured frequencies and quality factors presented a marked dependence on the diameter/thickness ratio of the nanodisks. Finally, experimental measurements of the transient optical response induced by acoustic vibrations are presented.

# Chapter 1

## Electronic, optical and thermal properties of metallic nanoparticles

The work of this PhD thesis, whose results are presented in Chapters 3, 4, and 5 of this manuscript, was focused on the study of the thermal and vibrational properties of single nanoparticles, specifically nanodisks made of gold. This chapter aims at providing a general background regarding the physical properties of bulk metals and metal nanoparticles.

In this chapter, the electronic, thermal, and optical properties of bulk noble metals will first be presented. The second section will focus on the linear optical response of noble metal nanoparticles and their specificities compared to bulk metal, as well as on the physical processes involved after the excitation of a single nano-object by a femtosecond laser pulse. The last section will present the relevant thermal mechanisms involved in the cooling dynamics of a single nanodisk supported by a substrate.

### 1.1 Physical properties of bulk noble metals

#### 1.1.1 Electronic and thermal properties of bulk noble metals

Noble metals, like copper (Cu), silver (Ag) or gold (Au), are characterized by electronic structures with completely filled  $(n - 1)d$  orbitals as well as one  $n(s - p)$  hybridized external orbital containing a single electron, thus making them monovalent (Figure 1.1). In bulk materials, these atoms are organized in a face-centered cubic (fcc) crystalline structure (Figure 1.2a), its main parameters being summarized in Table 1.1.

Metal	Electronic structure	$a$ (Å)	$n_e$ ( $10^{22}$ cm $^{-3}$ )
Cu	[Ar] $3d^{10}4s^1$	3.61	8.47
Ag	[Kr] $4d^{10}5s^1$	4.09	5.86
Au	[Xe] $4f^{14}5d^{10}6s^1$	4.08	5.90

Table 1.1 – Table of the electronic structure, lattice parameter  $a$ , and electron density  $n_e$  of noble metals Cu, Ag and Au [12, 13].

Electrons of a single atom have discrete energy levels, each one corresponding to an atomic

Group	1	2	3	4	5	6	7	8	9	10	11	12	13	14	15	16	17	18
1	1 H																	2 He
2	3 Li	4 Be											5 B	6 C	7 N	8 O	9 F	10 Ne
3	11 Na	12 Mg											13 Al	14 Si	15 P	16 S	17 Cl	18 Ar
4	19 K	20 Ca	21 Sc	22 Ti	23 V	24 Cr	25 Mn	26 Fe	27 Co	28 Ni	29 Cu	30 Zn	31 Ga	32 Ge	33 As	34 Se	35 Br	36 Kr
5	37 Rb	38 Sr	39 Y	40 Zr	41 Nb	42 Mo	43 Tc	44 Ru	45 Rh	46 Pd	47 Ag	48 Cd	49 In	50 Sn	51 Sb	52 Te	53 I	54 Xe
6	55 Cs	56 Ba	* 71 Lu	72 Hf	73 Ta	74 W	75 Re	76 Os	77 Ir	78 Pt	79 Au	80 Hg	81 Tl	82 Pb	83 Bi	84 Po	85 At	86 Rn
7	87 Fr	88 Ra	* 103 Lr	104 Rf	105 Db	106 Sg	107 Bh	108 Hs	109 Mt	110 Ds	111 Rg	112 Cn	113 Nh	114 Fl	115 Mc	116 Lv	117 Ts	118 Og
			* 57 La	58 Ce	59 Pr	60 Nd	61 Pm	62 Sm	63 Eu	64 Gd	65 Tb	66 Dy	67 Ho	68 Er	69 Tm	70 Yb		
			* 89 Ac	90 Th	91 Pa	92 U	93 Np	94 Pu	95 Am	96 Cm	97 Bk	98 Cf	99 Es	100 Fm	101 Md	102 No		

Figure 1.1 – Position (red rectangle) of Cu, Ag, and Au in the periodic table of elements [11].

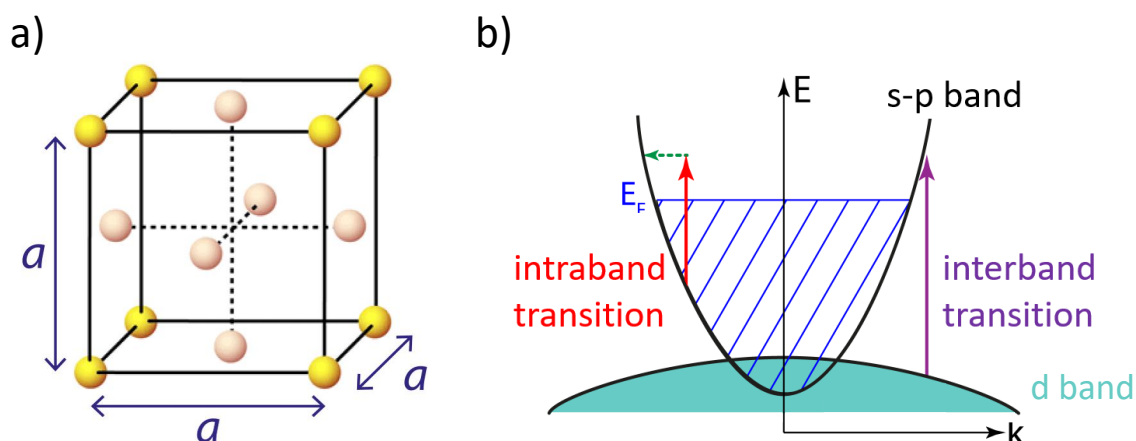


Figure 1.2 – a) Schematic of a face-centered cubic (fcc) crystalline structure with lattice parameter  $a$  and b) Schematic of the band structure of a metal with a low-dispersed valence band (d band) and a conduction band (s-p band). In b), an interband transition between the d and s-p bands can be caused by the absorption of a photon with high enough energy by an electron of the d band. The transition of a conduction electron to a higher state of the same band, an intraband transition, can happen via the absorption of a photon and the involvement of additional particle (phonon or electron) so as to conserve both energy and momentum.

orbital. In a solid, the strong interaction between atomic orbitals leads to a broadening of the quantized energy levels and to a continuum of electronic states, named *electronic bands*. The understanding of these bands is crucial as its characteristics determine many physical properties of the material. Notably, it is useful to define two major bands:

- The *valence band*, the highest energy band completely filled with electrons at zero temperature.
- The *conduction band*, the lowest energy band partially filled. In particular, the highest occupied energy level in this band at zero temperature is called the Fermi level, with energy  $E_F$ .

Electrons in the conduction band are delocalized and are responsible of most of the electronic and thermal properties of metals, while electrons in the valence band weakly contribute to these properties. A schematic of the electronic bands structure is presented in Figure 1.2b. As each atom contributes to the conduction band with a single electron in noble metals ( $ns^1$ ), the density of conduction electrons  $n_e$  (see Table 1.1) is defined as

$$n_e = N_A \frac{\rho}{M} \quad (1.1)$$

with  $N_A$  the Avogadro number,  $\rho$  the density, and  $M$  the molar mass of the material.

### 1.1.1.1 Electrons in the conduction band

The quasi-parabolic dispersion of the conduction band allows to describe conduction electrons, as in the Sommerfeld model, as free electrons with effective mass  $m^*$  (which takes into account the effects of the interactions between the electrons and the ionic lattice), with a dispersion relation linking the energy  $E$  and wavevector  $\vec{k}$  written as:

$$E(\vec{k}) = \frac{\hbar^2 k^2}{2m^*}. \quad (1.2)$$

with  $\hbar = h/2\pi$ ,  $h = 6.62 \cdot 10^{-34}$  J s being the Plank constant. The density of states  $g_e(E)$  of these electrons for a tridimensional system with volume  $V$  is then given by:

$$g_e(E) = \frac{V}{2\pi^2} \left( \frac{2m^*}{\hbar^2} \right)^{\frac{3}{2}} \sqrt{E}. \quad (1.3)$$

The Fermi energy  $E_F$  is the one corresponding to the Fermi level and is expressed as

$$E_F = \frac{\hbar^2}{2m^*} (3\pi n_e)^{\frac{2}{3}}, \quad (1.4)$$

from which can also be defined the Fermi wave vector  $k_F = \sqrt{2m^*E_F}/\hbar$  and the Fermi temperature  $T_F = E_F/k_B$ , with  $k_B$  the Boltzmann constant. The values of the main parameters describing the free electrons in the conduction band is presented are summarized in Table 1.2 for copper, silver, and gold.

At electronic temperature  $T_e$  the probability of an electronic state with energy  $E$  to be occupied follows the Fermi-Dirac distribution:

$$f(E) = \frac{1}{\exp\left(\frac{E-E_F}{k_B T_e}\right) + 1}, \quad (1.5)$$

where  $k_B$  is the Boltzmann constant and the chemical potential  $\mu(T_e)$  has been replaced by the Fermi energy  $E_F$ . This assumption can be done when  $T_e \ll T_F$ , which is the case at

Metal	$m^*/m_e$	$E_F$ (eV)	$k_F$ ( $10^8 \text{ cm}^{-1}$ )	$T_F$ ( $10^4 \text{ K}$ )
Cu	1.3	4.67	1.36	5.44
Ag	1.1	5.49	1.20	6.38
Cu	1.1	5.53	1.21	6.42

**Table 1.2** – Table of the effective electron mass  $m^*$  normalized by the electron rest mass  $m_e$ , Fermi energy  $E_F$ , Fermi wave vector  $k_F$ , and Fermi temperature  $T_F$  for Cu, Ag, and Au [13].

room temperature for noble metals (see Table 1.2). In particular, it means that the electronic distributions at room temperature and at 0 K are very similar except around the Fermi energy.

One can then calculate the volumetric specific heat of free electrons  $c_e(T_e)$  through the temperature derivative of the electron volumetric internal energy  $u_e$ :

$$c_e(T_e) = \frac{\partial u_e}{\partial T_e} = \frac{1}{V} \int_0^\infty E g_e(E) \frac{\partial f(E)}{\partial T_e} dE = \frac{\pi^2 n_e k_B}{2T_F} T_e = a_e T_e, \quad (1.6)$$

with  $g_e(E)$  given by Equation 1.3 and a proportionality constant  $a_e = \frac{\pi^2 n_e k_B}{2T_F} \approx 65 \text{ J K}^{-2} \text{ m}^{-3}$  in gold [13].

### 1.1.1.2 Volumetric lattice heat capacity

In noble metals the primitive cell of the cristalline structure contains a single atom, which only allows acoustic vibrational modes of the ionic lattice (of which energy vanishes for a zero wave vector  $\vec{q}$ ). The corresponding phonon band structure is composed of acoustic branches (associated to transverse or longitudinal vibrations), each containing  $N_i$  modes, with  $N_i$  the number of ions in the lattice.

The Debye model (introduced in 1912 to estimate the lattice heat capacity of crystals [14]) considers a simplified phononic band structure by assuming that all the acoustic modes are described by a linear dispersion relation (whereas this might not be the case for the real dispersion relation), linking the pulsation  $\omega$  to the wave vector  $\vec{q}$  through [15]:

$$\omega(\vec{q}) = c_s |\vec{q}|, \quad (1.7)$$

with  $c_s$  the average sound velocity, defined as:

$$\frac{3}{c_s^3} = \frac{1}{c_l^3} + \frac{2}{c_t^3}, \quad (1.8)$$

$c_l$  and  $c_t$  being the longitudinal and transverse sound velocities of the acoustic modes, respectively.

In the context of the Debye model, the phonon density of states can be written, as a function of energy  $E$ , as:

$$g_{ph}(E) = \frac{12\pi V}{c_s^2 h^3} E^2 \quad (1.9)$$

with  $V$  the volume of the system.

The Debye energy  $E_D$ , which corresponds to the maximal energy of phonons in the crystal, and the associated Debye temperature  $T_D = E_D/k_B$  are defined so that the total number of modes is  $3N_i$ :

$$\frac{12\pi V}{c_s^3 h^3} \int_0^{E_D} E^2 dE = 3N_i, \quad (1.10)$$

leading to:

$$T_D = \left( \frac{3N_i}{4\pi V} \right)^{1/3} \frac{c_s h}{k_B}. \quad (1.11)$$

At lattice temperature  $T_L$  the average number of phonons with energy  $\hbar\omega_s(\vec{q})$  is given by the Bose-Einstein distribution:

$$n_{BE}(\vec{q}, T_L) = \frac{1}{\exp\left(\frac{\hbar\omega_s(\vec{q})}{k_B T_L}\right) - 1}. \quad (1.12)$$

Similarly to Equation 1.6, the volumetric lattice heat capacity can be computed using the equilibrium phonon occupation number in Equation 1.12 via:

$$c_L = -k_B \beta^2 \frac{\partial u_L}{\partial \beta} = \frac{12k_B \beta^2 \pi}{c_s^3 h^3} \int_0^{E_D} \frac{E^4 e^{\beta E}}{(e^{\beta E} - 1)^2} dE, \quad (1.13)$$

with  $\beta = 1/k_B T_L$  and  $u_L$  the volumetric lattice energy. Using the dimensionless variable  $x = \beta E$ , this expression becomes:

$$c_L = 9n_i k_B \frac{T_L^3}{T_D^3} \int_0^{T_D/T_L} \frac{x^4 e^x}{(e^x - 1)^2} dx, \quad (1.14)$$

with  $n_i = \frac{N_i}{V}$  the volumetric density of modes.

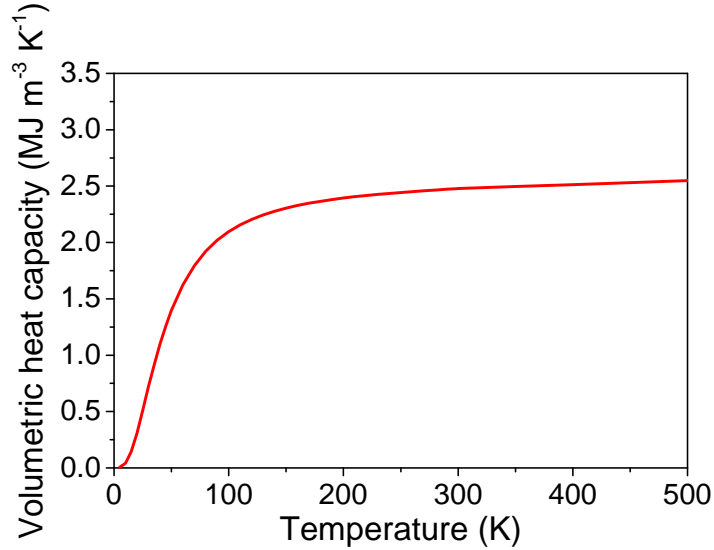


**Figure 1.3** – Experimental measurement of the volumetric heat capacity of solid gold  $c_{Au}$  as a function of temperature  $T$  from ref. [16].

In the case of gold  $T_D \approx 170$  K [13], which is largely inferior to the temperature at which our experiments are performed (room temperature at  $\approx 300$  K). In such conditions,  $T_D \ll T_L$ , a first-order development of Equation 1.14 allows to retrieve the classical Dulong-Petit law:

$$c_L \approx 3n_i k_B. \quad (1.15)$$

In the case of gold the volumetric lattice heat capacity has a  $c_L \approx 2.5 \cdot 10^6 \text{ J m}^{-3} \text{ K}^{-1}$  value. The comparison with  $c_e$  (see Equation 1.6) leads to a  $c_L/c_e$  ratio of the order of 100 at 300 K: as a result, the heat capacity of metals is mostly given by the volumetric heat capacity of the lattice  $c_L$  at temperatures of the order of 300 K and weakly depends on temperature in this range. This theoretical prediction is in good agreement with experimental measurements of the volumetric heat capacity of gold, shown in Figure 1.3, where a monotonic increase is observed at low temperatures and a weak dependence of the specific heat on temperature for  $T > 200 \text{ K}$ , with values close to that predicted by the Dulong-Petit law.

## 1.1.2 Optical behavior of bulk noble metals

### 1.1.2.1 Electromagnetism in a noble metal

Let us consider a monochromatic electromagnetic field, whose associated electric field writes:

$$\vec{E}(\vec{r}, t) = \text{Re}[\vec{E}_0 e^{i(\vec{k} \cdot \vec{r} - \omega t)}], \quad (1.16)$$

with wave vector  $\vec{k}$  and angular frequency  $\omega$ . When such field interacts with a material, its bound positive charges move in the same direction while negative charges are displaced in an opposite direction, thus creating a polarization density  $\vec{P}$ . For a homogeneous, linear and isotropic material, the polarization  $\vec{P}$  can be related to the incident field, using the electric susceptibility  $\chi(\omega)$  and vacuum permittivity  $\epsilon_0$ , as:

$$\vec{P} = \epsilon_0 \chi \vec{E}. \quad (1.17)$$

The electric displacement field  $\vec{D}$  can be written as:

$$\vec{D} = \epsilon_0 \vec{E} + \vec{P} = \epsilon_0 \epsilon \vec{E}, \quad (1.18)$$

where  $\epsilon = 1 + \chi$  corresponds to the dielectric function (relative permittivity, equivalently) of the material. The dielectric function is typically decomposed into its real and imaginary parts via

$$\epsilon = \epsilon_1(\omega) + i\epsilon_2(\omega), \quad (1.19)$$

with  $\epsilon_1$  and  $\epsilon_2$  real.

Another way to describe the optical properties of the material is to use the complex optical index

$$\tilde{n} = n + i\kappa, \quad (1.20)$$

which is linked to the dielectric function  $\epsilon$  via

$$\tilde{n}^2 = \epsilon. \quad (1.21)$$

The real part  $n$  is the refraction index, a quantity which intervenes in the definition of the phase velocity of light in the material  $v$  via  $v = c/n$ . The imaginary part  $\kappa$  is the extinction coefficient and describes to what extent the solid can absorb electromagnetic energy. This can be illustrated by the intensity  $I_t$  of an electromagnetic wave after a propagation over a distance  $L$  in the material, which is written as:

$$I_t = I_0 e^{-\alpha L} \quad \text{with} \quad \alpha(\omega) = \frac{2\omega}{c} \kappa(\omega) \quad (1.22)$$

One can link the  $(\epsilon_1, \epsilon_2)$  and  $(n, \kappa)$  quantities via the following explicit relations:

$$\begin{cases} \epsilon_1 = n^2 - \kappa^2 \\ \epsilon_2 = 2n\kappa \end{cases} \quad (1.23)$$

In the case of transparent material,  $\kappa = 0$  (i.e. it doesn't absorb light), which thus corresponds to  $\epsilon_2 = 0$  and  $\epsilon_1 = n^2$ .

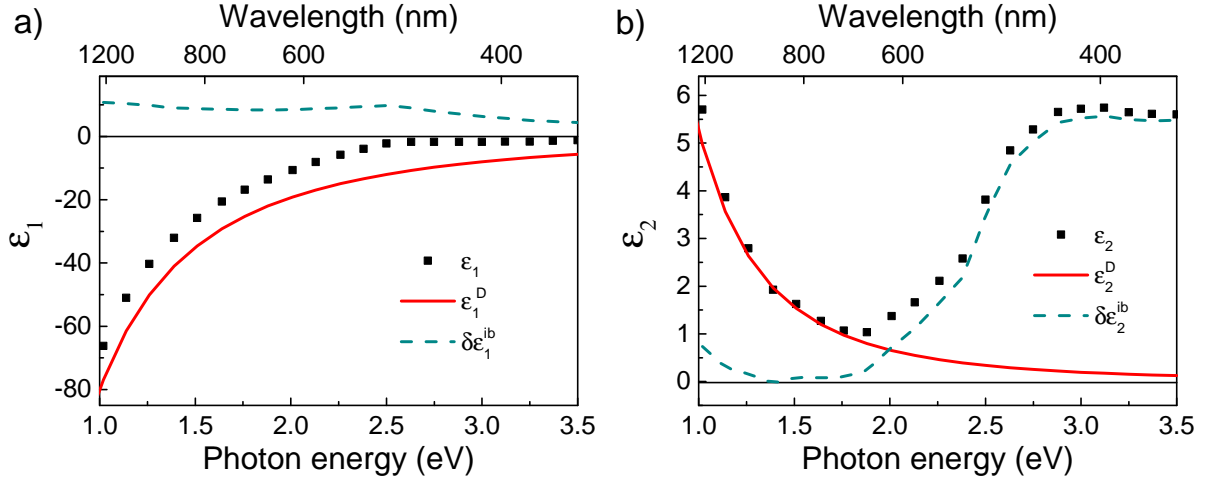


**Figure 1.4 – Dependence of a) the real part  $\epsilon_1$  and b) imaginary part  $\epsilon_2$  of the dielectric function of gold on the photon energy.** Black squares correspond to experimental data from ref. [17]. Red full lines represent the contributions from intraband electronic transitions  $\epsilon_{1,2}^D$  computed via the Drude model. The dashed green lines was obtained from  $\delta\epsilon^{ib} = \epsilon - \epsilon^D$  and are thus estimations of the contributions of interband transitions. The  $\epsilon^{ib}$  quantity can then derived from  $\epsilon^{ib} = \delta\epsilon^{ib} + 1$ .

The dielectric function  $\epsilon$  results from the sum of the contributions from two different light absorption mechanisms (a simplified description is presented in Figure 1.2b):

- *Intraband* transitions : these occur between electronic states within the conduction band. Well-described by the classical Drude model of free electrons, they involve the absorption of a photon as well as interaction with another object, such as a second electron, a phonon, or a lattice defect, in order to respect the conservation of momentum (Figure 1.2b).
- *Interband* transitions : the absorption of a photon with an energy exceeding the interband energy threshold (2.4 eV in gold, corresponding to a 520 nm wavelength) induces an electronic transition between the valence band and the conduction band. In contrast with intraband transitions, a quantum theory is necessary to describe this mechanism.

The total electric susceptibility  $\chi$  is the sum of both effects and can written as  $\chi = \chi^D + \chi^{ib}$ . Similarly, the contributions to the dielectric function  $\epsilon$  are defined as  $\epsilon^{D,ib} = 1 + \chi^{D,ib}$ . These quantities also verify the following relation:

$$\epsilon = 1 + \chi = 1 + \chi^D + \chi^{ib} = \epsilon^D + \epsilon^{ib} - 1. \quad (1.24)$$

The dependence of the dielectric functions of gold,  $\epsilon_1$  and  $\epsilon_2$ , as well the associated intraband and interband contributions, are presented in Figure 1.4.

### 1.1.2.2 Intraband transitions

The contribution of the intraband transitions (Figure 1.2b) can be calculated using the Drude model, in which the electron motion is described classically, driven by the electromagnetic force  $-e\vec{E}$  and in the presence of electron collisions (with the ionic lattice and other electrons) described by a single scattering rate  $\gamma_0 = 1/\tau_0$  ( $\tau_0$  being the characteristic collision time, i.e. the average time between one collision and the next). After each collision electrons move in random directions with random velocities that follow Maxwell-Boltzmann's distribution. Equivalently, such collisions can be modeled via a friction force  $\vec{F} = -m^*\gamma_0\vec{v}$  applied to each electron with  $\vec{v}$  the velocity of the electron and  $m^*$  its effective mass (see discussion in Section 1.1.1.1).

The dynamics of an electron submitted to an external electric field  $\vec{E}(t) = \vec{E}_0 e^{-i\omega t} + c.c.$  are described by:

$$m^* \frac{d^2 \vec{r}}{dt^2} = -m^* \gamma_0 \frac{d\vec{r}}{dt} - e\vec{E}, \quad (1.25)$$

with  $\vec{r}$  the position of the electron and  $e$  the elementary charge. The polarization  $\vec{P}$  resulting from the movement of the electrons is then obtained from the solution  $\vec{r}$  of the previous equation in the stationary regime and is given by  $\vec{P} = -n_e e \vec{r}$ . Equation 1.17,  $\vec{P} = \epsilon_0 \chi^D \vec{E}$  then allows to calculate the Drude contribution to the dielectric function:

$$\epsilon^D = 1 + \chi^D = 1 - \frac{\omega_p^2}{\omega(\omega + i\gamma_0)} \quad (1.26)$$

with  $\omega_p = \sqrt{\frac{n_e e^2}{m^* \epsilon_0}}$  the plasma frequency. The corresponding real and imaginary parts of  $\epsilon^D$  are:

$$\begin{cases} \epsilon_1^D = 1 - \frac{\omega_p^2}{\omega^2 + \gamma_0^2} \approx 1 - \frac{\omega_p^2}{\omega^2} \text{ for } \gamma_0 \ll \omega \\ \epsilon_2^D = \frac{\gamma_0 \omega_p^2}{\omega(\omega^2 + \gamma_0^2)} \approx \gamma_0 \frac{\omega_p^2}{\omega^3} \text{ for } \gamma_0 \ll \omega \end{cases} \quad (1.27)$$

The plasma frequency  $\omega_p$  and optical scattering rate  $\gamma_0$  can be estimated thanks to fits of experimental measurements of the gold dielectric functions  $\epsilon_1$  and  $\epsilon_2$  using the previous formulas. Such fits lead to  $\hbar\omega_p \approx 9.01$  eV and  $\hbar\gamma_0 \approx 70$  eV (see Figure 1.4 [17]). In the visible and near-infrared ranges (corresponding to a photon energy  $\hbar\omega$  in the 1-3 eV range), the  $\gamma_0 \ll \omega$  condition is thus valid for gold and approximations in Equation 1.27 can be used.

The case  $\omega = 0$  corresponds to two-bodies interaction processes.  $\gamma(\omega = 0)$  is the static damping rate and is linked to scattering occurring between electrons and lattice (electron-phonon scattering) or other electrons (electron-electron scattering). In contrast, for  $\omega \neq 0$ ,  $\gamma(\omega \neq 0)$  is the optical scattering rate and takes into account the absorption of a photon with energy  $\hbar\omega$  by a conduction electron. The momentum of the photon being negligible, the intraband transition requires an additional body (electron or phonon) to fully respect the energy and momentum conservation.

### 1.1.2.3 Interband transitions

The contribution of intraband transitions to the dielectric function is not sufficient to correctly describe the spectral dependence of  $\epsilon_2$  (at high energy mostly), as shown in Figure 1.4. As a consequence the contribution of interband transitions, from the valence band to the conduction band, above the Fermi level, must be taken into account. Such transitions can only be

described by a quantum approach : the corresponding dielectric function contribution  $\epsilon^{ib}$  is usually calculated using Lindhard's theory [18].

Moreover, the interband energy threshold, which corresponds to the energy difference between the top of the valence band and the Fermi energy  $E_F$ , is around 2.4 eV (i.e. 520 nm wavelength) in gold, providing an explanation for the yellow color of gold. Similarly, the interband energy threshold occurs around 4 eV for silver (i.e. ultraviolet domain), which leads to a weak absorption in the visible range and explains the fact that bulk silver is colorless.

## 1.2 Optical properties of metallic nanoparticles

Noble metal nano-objects have optical responses which differ from bulk metals. Indeed, the dielectric confinement of electrons within nanometric boundaries induces resonances in their absorption and scattering spectra, called Surface Plasmon Resonances (SPR). The characteristics of these resonances (i.e. amplitude, central position, and width) strongly depend on the nanoparticles size, geometry, composition as well as on their local environment.

### 1.2.1 Energetic considerations

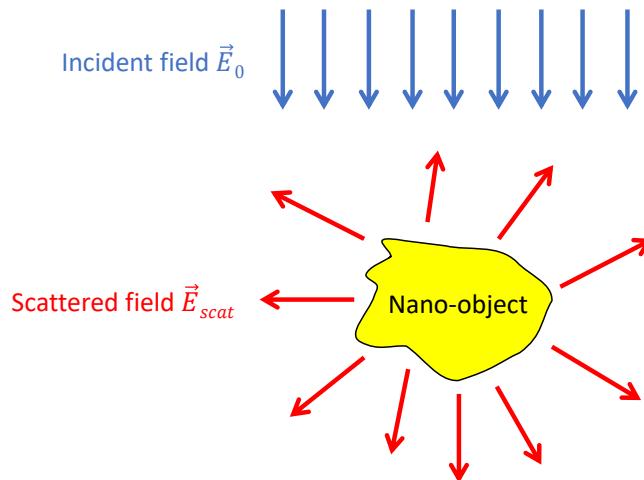


**Figure 1.5** – Schematic of a nano-object shined by an incident electromagnetic field  $\vec{E}_0$ , generating via their interaction a scattered electromagnetic field  $\vec{E}_{scat}$ .

We consider a single metallic nanoparticle surrounded by a transparent environment and shined by an incident oscillating electromagnetic wave  $(\vec{E}_0, \vec{H}_0)$ , as illustrated in Figure 1.5. In this context the nanoparticle electrons oscillate at the frequency of  $\vec{E}_0$ , which induces a scattered electromagnetic field at the same frequency  $(\vec{E}_{scat}, \vec{H}_{scat})$  propagating from the nano-object to the surrounding medium. The total external electromagnetic field corresponds to:

$$\begin{cases} \vec{E}_{tot} = \vec{E}_0 + \vec{E}_{scat} \\ \vec{H}_{tot} = \vec{H}_0 + \vec{H}_{scat} \end{cases} \quad (1.28)$$

The associated time-averaged Poynting vector can be decomposed into three terms [7]:

$$\vec{\Pi}_{tot} = \frac{1}{2} \text{Re}(\vec{E}_{tot} \times \vec{H}_{tot}^*) = \vec{\Pi}_0 + \vec{\Pi}_{scat} + \vec{\Pi}_{ext} \quad (1.29)$$

with

$$\begin{cases} \vec{\Pi}_0 = \frac{1}{2} \text{Re}(\vec{E}_0 \times \vec{H}_0^*) \\ \vec{\Pi}_{scat} = \frac{1}{2} \text{Re}(\vec{E}_{scat} \times \vec{H}_{scat}^*) \\ \vec{\Pi}_{ext} = \frac{1}{2} \text{Re}(\vec{E}_0 \times \vec{H}_{scat}^* + \vec{E}_{scat} \times \vec{H}_0^*) \end{cases} \quad (1.30)$$

In the case of a homogeneous environment one can write the power absorbed by the nano-object,  $P_{abs}$ , as:

$$P_{abs} = - \oiint_S \vec{\Pi}_{tot} \cdot \vec{n} \, dS, \quad (1.31)$$

i.e. the flux of the total Poynting vector  $\vec{\Pi}_{tot}$  through the surface  $S$  of the nanoparticle (here  $\vec{n}$  is a unitary vector directed from the inside to the outside of the nano-object and normal to its surface). Similarly, the scattering and extinction powers,  $P_{scat}$  and  $P_{ext}$ , can be defined as:

$$\begin{cases} P_{scat} = \oiint_S \vec{\Pi}_{scat} \cdot \vec{n} \, dS \\ P_{ext} = - \oiint_S \vec{\Pi}_{ext} \cdot \vec{n} \, dS \end{cases} \quad (1.32)$$

As the environment is transparent, a simple relation links  $P_{ext}$ , the power attenuation of the incident field due to absorption and scattering of the nanoparticle, to  $P_{abs}$  and  $P_{scat}$ :

$$P_{ext} = P_{abs} + P_{scat}. \quad (1.33)$$

Useful quantities can then be defined from these powers: the extinction, absorption and scattering cross-sections,  $\sigma_{ext}$ ,  $\sigma_{abs}$  and  $\sigma_{scat}$ . These are the ratios between the different powers and the intensity of the incident field at the position of the nanoparticle,  $I_0$ :

$$\begin{cases} \sigma_{ext} = \frac{P_{ext}}{I_0} \\ \sigma_{abs} = \frac{P_{abs}}{I_0} \\ \sigma_{scat} = \frac{P_{scat}}{I_0}, \end{cases} \quad (1.34)$$

As a consequence of Equation 1.33, they are linked via:

$$\sigma_{ext} = \sigma_{abs} + \sigma_{scat}. \quad (1.35)$$

However, experimental techniques used to measure the extinction of a single nanoparticle (e.g. Spatial Modulation Spectroscopy and single-particle time-resolved spectroscopy, both presented in Chapter 2) include a photodetector placed in the incident light beam path. For a photodetector of surface  $S_D$ , the power measured by it,  $P_{S_D} = \oiint_{S_D} \vec{\Pi}_{tot} \cdot \vec{n} \, dS$ , can be written as:

$$P_{S_D} = P_{0,S_D} - P_{ext,S_D} + P_{scat,S_D} \quad (1.36)$$

with

$$\begin{cases} P_{0,S_D} = \iint_{S_D} \vec{\Pi}_0 \cdot \vec{n} \, dS \\ P_{scat,S_D} = \iint_{S_D} \vec{\Pi}_{scat} \cdot \vec{n} \, dS \\ P_{ext,S_D} = - \iint_{S_D} \vec{\Pi}_{ext} \cdot \vec{n} \, dS \end{cases} \quad (1.37)$$

For a photodetector with a surface  $S_D$  sufficiently large to fully collect the incident light (which is the case in practice)  $P_{0,S_D} = P_0$  and  $P_{ext,S_D} = P_{ext}$ . Thanks to Equation 1.36, the attenuation of power caused by the presence of the nanoparticle,  $\Delta P = P_0 - P_{S_D}$ , can thus be written as:

$$\Delta P = P_{ext} - P_{scat,S_D} = \sigma_{ext} I_0 - P_{scat,S_D}. \quad (1.38)$$

This equation means that collection of scattered light by the photodetector disturbs the measurement of the extinction power and thus of the extinction cross-section. In practice, the surface of the detector  $S_D$  is chosen larger than the surface of the incident laser beam while being small enough to limit the effect of scattered light recollection. Moreover, in the context of optical measurements on small nanoparticles the associated scattered power becomes negligible compared to the extinction one (see discussion in next section).

Under these conditions, the power attenuation can be expressed as:

$$\Delta P = P_0 - P_{S_D} \approx P_{ext} = \sigma_{ext} I_0, \quad (1.39)$$

an assumption which was made in this work.

## 1.2.2 Optical response of a nanoellipsoid: quasi-static approximation

In this section a metallic nanoparticle with dielectric function  $\epsilon = \epsilon_1 + i\epsilon_2$ , immersed in a homogeneous transparent medium of real weakly dispersed dielectric function  $\epsilon_m$ , and shined by an oscillating electric field  $\vec{E}_0$  of wavelength  $\lambda$  is considered (see Figure 1.6a). A simple case is the one where the size of the nanoparticle is small compared to the wavelength  $\lambda$  of the electric field: in this context, a quasi-static approximation can be done, i.e. the spatial variations of  $\vec{E}_0$  are neglected at the length scale of the nanoparticle and  $\vec{E}_0$  is thus considered homogeneous (left side of Figure 1.6a). The oscillating electric field induces a collective motion of the electrons of the nano-object, which can be described thanks to the dipolar approximation, with an induced dipole  $\vec{p}(\omega)$  with the same orientation as the external electric field  $\vec{E}_0$ , as [19]:

$$\vec{p}(\omega) = \epsilon_0 \epsilon_m \tilde{\alpha}(\omega) \vec{E}_0(\omega), \quad (1.40)$$

with  $\tilde{\alpha}$  the linear polarizability of the nanoparticle.

This quantity can be expressed analytically only for a few simple nanoparticle shapes: in particular, it can be done for a sphere or an ellipsoid characterized by semi-axes  $a$ ,  $b$ ,  $c$  (see Figure 1.6b), which is the configuration that will be considered here due to its proximity with the geometry of the nanoparticles investigated in this work, i.e. nanodisks. For such ellipsoid the polarizability can be expressed as [20]:

$$\tilde{\alpha}(\omega) = \frac{V}{L_i} \frac{\epsilon(\omega) - \epsilon_m}{\epsilon(\omega) + \frac{1-L_i}{L_i} \epsilon_m}, \quad (1.41)$$

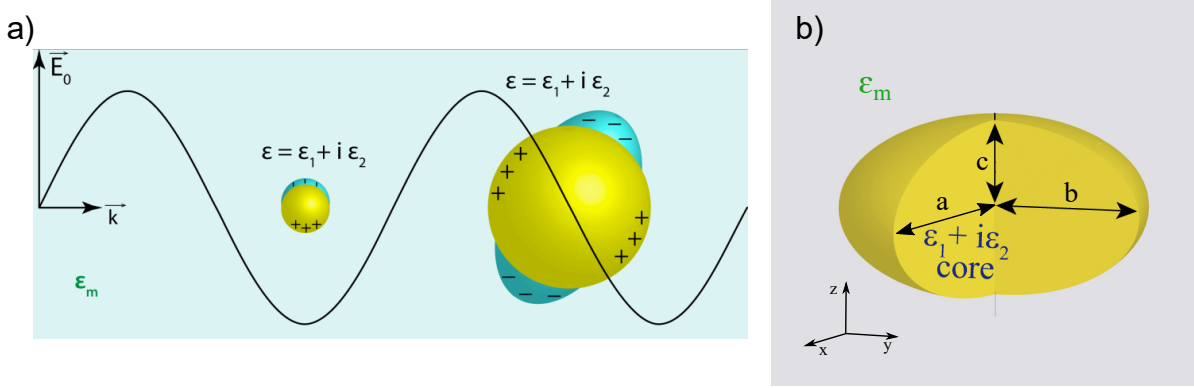


**Figure 1.6** – a) Schematic of nanospheres of dielectric function  $\epsilon = \epsilon_1 + i\epsilon_2$  in a transparent matrix submitted to an electric field  $\vec{E}_0$  and b) schematic of an oblate spheroid of semi-axes  $a$ ,  $b$ , and  $c$ . The environment is characterized by a real dielectric function  $\epsilon_m$ . The electric field  $\vec{E}_0$  leads to the creation of a polarization  $\vec{P}$  associated to the collective motion of the electrons of the nanosphere. For a nanosphere of diameter  $D$  smaller than wavelength  $\lambda$  of the electric field, the resulting charge distribution corresponds to that of a dipole. For a nanosphere with  $D \sim \lambda$ , taking into account higher-order multipolar electromagnetic mode is necessary.

with  $V = \frac{4}{3}\pi abc$  the volume of the ellipsoid and  $L_i$  a factor depending on both the geometry of the nano-object (i.e on the  $a$ ,  $b$ , and  $c$  parameters of the ellipsoid) and the linear polarization of the incident light (along the  $i = x, y$  or  $z$  axis). The simple case of a nanosphere (i.e.  $a = b = c$ ) leads to a  $L_i = \frac{1}{3}$  value and a polarizability  $\tilde{\alpha}$  independent on the light polarization. In the case of an oblate nanospheroid (i.e.  $a = b > c$ ) and a polarization along the  $x$  or  $y$  axis (see Figure 1.6b), the geometrical factors  $L_x$ ,  $L_y$ , and  $L_z$  are written as [20]:

$$L_x = L_y = \frac{1}{2}(1 - L_z) = \frac{g(e)}{2e^2} \left[ \frac{\pi}{2} - \arctan g(e) \right] - \frac{g^2(e)}{2}, \quad (1.42)$$

with

$$g(e) = \left( \frac{1 - e^2}{e^2} \right)^{\frac{1}{2}} \quad (1.43)$$

and

$$e = \left( 1 - \frac{c^2}{a^2} \right)^{\frac{1}{2}} \quad (1.44)$$

the ellipsoid eccentricity. Note that this configuration and the one studied in the experiments presented in this work are quite close: indeed, measurements were performed on single gold nanodisks with diameters always larger than thicknesses and an incident light beam polarized in the plane of their diameter.

Having an analytical expression for the polarizability  $\tilde{\alpha}$  allows to deduce the absorption and scattering cross-sections (Section 1.2.1) of the nanoellipsoid:

$$\begin{cases} \sigma_{abs} = k \text{Im}(\tilde{\alpha}) = \frac{\omega V}{cL_i^2} \frac{\epsilon_m^2 \epsilon_2(\omega)}{|\epsilon(\omega) + H_i \epsilon_m|} \\ \sigma_{scat} = \frac{k^4}{6\pi} |\tilde{\alpha}|^2 = \frac{\omega^4 V^2}{6\pi c^4 L_i^2} \frac{\epsilon_m^2}{|\epsilon(\omega) + H_i \epsilon_m|^2} \end{cases} \quad (1.45)$$

with  $k = \omega \frac{\epsilon_m^{1/2}}{c}$  the modulus of the wave vector of the incident electric field and  $H_i = (1 - L_i)/L_i$ . Equation 1.45 shows that the extinction cross-section  $\sigma_{ext} = \sigma_{abs} + \sigma_{scat}$ , as well as the absorption and scattering ones, depend on the dielectric function of the material of the nanoparticle, via  $\epsilon_1$  and  $\epsilon_2$ , on its shape, via  $H_i$ , and on the dielectric function of the material  $\epsilon_m$ . These expressions also show that the absorption cross-section is proportional to  $V$ , the volume of the nanoellipsoid, whereas the scattering one is proportional to  $V^2$ , which implies that for a sufficiently small nanoellipsoid scattering becomes negligible compared to absorption. For such small nanoparticle one can do the following approximation:

$$\sigma_{ext} \approx \sigma_{abs} = \frac{\omega V}{cL_i^2} \frac{\epsilon_m^{3/2} \epsilon_2(\omega)}{(\epsilon_1(\omega) + H_i \epsilon_m)^2 + \epsilon_2^2(\omega)}. \quad (1.46)$$

The Surface Plasmon Resonance (SPR) corresponds to a strong enhancement of the extinction cross-section  $\sigma_{ext}$ . Assuming a weak or quasi-constant imaginary part  $\epsilon_2$  of the dielectric function  $\epsilon$ , this resonance occurs when:

$$\epsilon_1(\omega) + H_i \epsilon_m = 0. \quad (1.47)$$

This condition leads to the following expression for the resonance frequency  $\omega_{SPR}$ , using  $\epsilon_1 = \epsilon_1^D + \epsilon_1^{ib} - 1 = -\frac{\omega_p^2}{\omega^2} + \epsilon_1^{ib}$  for  $\gamma_0 \ll \omega$  (see Equation 1.27):

$$\omega_{SPR} = \frac{\omega_p}{\sqrt{\epsilon_1^{ib}(\omega_R) + H_i \epsilon_m}} \quad (1.48)$$

Equation 1.48 shows that, in the dipolar approximation, the central frequency of the Surface Plasmon Resonance,  $\omega_{SPR}$ , depends on the composition of the nanoellipsoid (via  $\omega_p$  and  $\epsilon_1^{ib}$ ) and of its environment ( $\epsilon_m$ ) as well as on the geometry of the nanoparticle and on the polarization of light ( $H_i$ ). One can also remark that its expression, valid in the small size regime, is fully independent of the volume  $V$  of the nanoellipsoid.

Moreover, in the case of a small or weakly-dispersed  $\epsilon^{ib}$  near the resonance frequency  $\omega_{SPR}$  (which is the case if  $\omega_{SPR}$  is below the interband transition threshold in noble metals, a valid assumption for silver nanospheres or elongated gold nanoparticles), it is possible to show that the extinction cross-section of the nano-object is a quasi-Lorentzian function of the photon frequency  $\hbar\omega$ , whose central position is  $\omega_{SPR}$ , and with a Full Width at Half-Maximum (FWHM) written as [21]:

$$\Gamma \approx \gamma_0(\omega_{SPR}) + \frac{\omega_{SPR}^2}{\omega_p^2} \epsilon_2^{ib}(\omega_{SPR}). \quad (1.49)$$

It is composed of two distinct contributions: one linked to electron scattering processes in intra-band transitions,  $\gamma_0(\omega_{SPR})$  (see Section 1.1.2.2), and another damping contribution originating from interband transitions,  $\frac{\omega_{SPR}^2}{\omega_p^2} \epsilon_2^{ib}(\omega_{SPR})$  (Section 1.1.2.3).

Figure 1.7 presents the extinction, absorption, and scattering spectra of two gold oblate nanoellipsoids with  $2c = 20$  nm and  $2a = 50$  or  $100$  nm computed using the dipolar approximation. In the case of the smaller ellipsoid, in Figure 1.7a, the extinction of the nano-object mainly originates from its absorption while the scattering contribution is almost negligible. In contrast, in the case of the larger ellipsoid, in Figure 1.7b, the absorption and scattering cross-sections are of the same order and both are required to fully determine the extinction spectra of the nano-object.

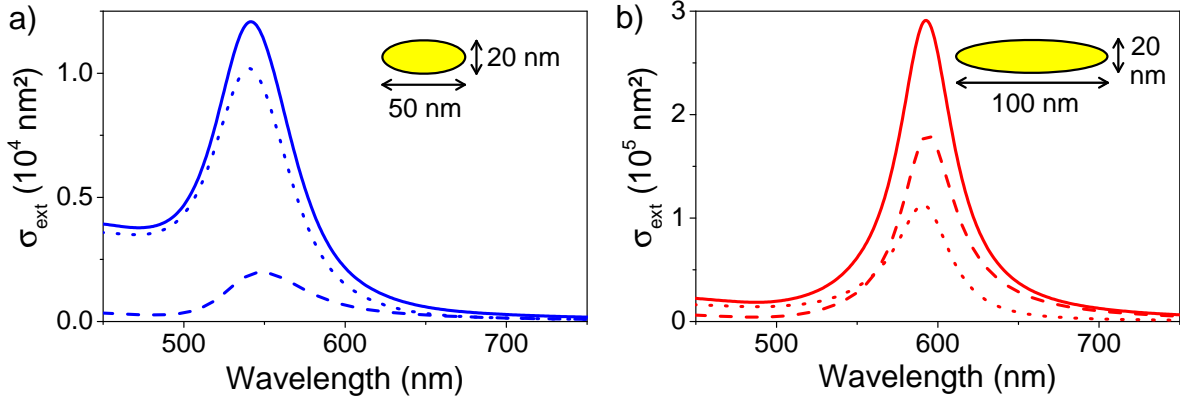


**Figure 1.7 – Extinction (full line), absorption (dotted line), and scattering (dashed line) spectra of two gold oblate nanoellipsoids with  $2c = 20$  nm and a)  $2a = 50$  and b)  $100$  nm, respectively.** The incident light is polarized along one of the major axes ( $a$  or  $b$ ), the refractive index of the environment is  $n_m = 1.5$  and gold dielectric function  $\epsilon_{1,2}$  is taken from ref. [17]. Schematic 2D representations of the ellipsoids with their dimensions are included.

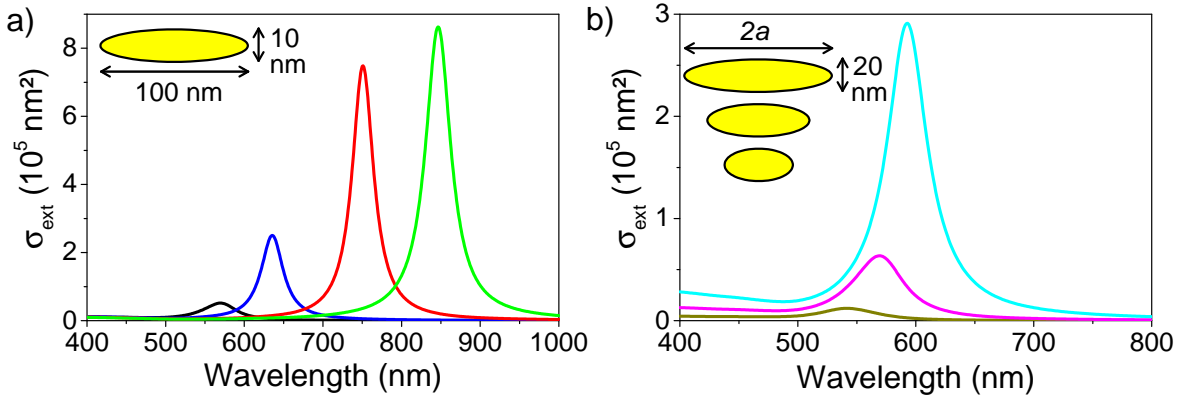


**Figure 1.8 – a) Effect of the refractive index of an homogeneous environment and b) effect of the aspect ratio  $\eta = a/c$  on the extinction spectra of gold oblate nanoellipsoids.** For both figures, the incident light is polarized along one of the major axes ( $a$  or  $b$ ) and gold dielectric function  $\epsilon_{1,2}$  is taken from ref. [17]. a) Extinction spectra are calculated using the dipolar approximation for a gold oblate spheroid with  $2a = 100$  nm and  $2c = 10$  nm for an environment of refractive index  $n_m = 1.0$  (black),  $1.3$  (blue),  $1.7$  (red), and  $2.0$  (green). b) Extinction spectra for gold oblate nanoellipsoids with  $2c = 20$  nm and aspect ratios  $\eta = a/c = 2.5$  (brown),  $3.75$  (purple), and  $5$  (light blue). The environment refractive index is  $n_m = 1.5$ . Schematic 2D representations of the ellipsoids with their dimensions are included.

As shown in Equation 1.48, the position of the Surface Plasmon Resonance of the nanoparticle depends on the refractive index of the environment  $n_m = \sqrt{\epsilon_m}$ . This effect is illustrated in Figure 1.8a, with significantly different central positions of the resonance of a single gold oblate nanoellipsoid, from 570 nm to 850 nm, computed using the dipolar approximation for different

values of the refraction index of the surrounding homogeneous environment ( $n$  being chosen between 1 and 2, values close to the ones of the supporting substrates described in the next chapters). This figure also shows that the amplitudes of the resonances also greatly depend on the environment properties.

Moreover, the morphology of the nanoparticle impacts its optical properties. As shown in Figure 1.8b, the extinction spectra of gold oblate nanoellipsoids with  $2c = 20$  nm but varied aspect ratios ( $\eta = a/c$ , ranging from 2.5 to 5), computed using the dipolar approximation, exhibit significantly different central positions. This morphology effect can be explained, in the dipolar approximation, by the fact that the  $H_i$  geometrical factor depends on the aspect ratio  $\eta$  of the nanoellipsoid (see Equations 1.42, 1.43, and 1.44).

### 1.2.3 Transient optical response of a single metallic nanoparticle after excitation by a laser pulse

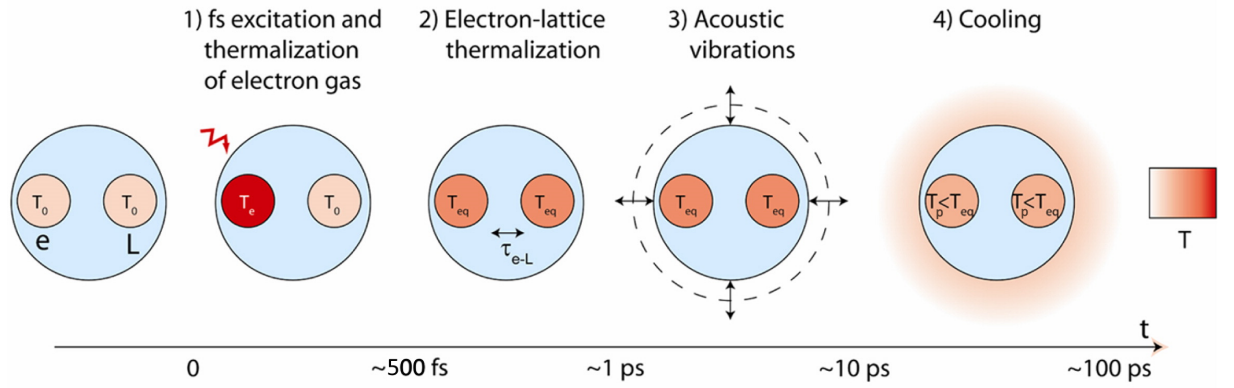


**Figure 1.9 – Ultrafast phenomena occurring after the excitation by a femtosecond laser pulse of a metallic nanoparticle.** The little circles with indices  $e$  and  $L$  correspond to the electron gas and the ionic lattice, respectively, of the nanoparticle, which is represented via the bigger circle. Color indicates the temperature, ranging from low (white) to high temperatures (red). Figure from ref. [7].

A technique described in Chapter 2 Section 2.2.3, the time-resolved spectroscopy, was used in this work to study the transient properties of single gold nanoparticles. In such experiments, a femtosecond light pulse (denoted as the *pump* pulse) excites a single nano-object and induces several ultrafast phenomena before a return to equilibrium. A second light pulse (the *probe* pulse) allows to monitor the temporal variations of the extinction cross-section of the nano-object thanks to a controllable time delay between the pump and the probe. Figure 1.9 presents the associated processes as well as the typical timescales over which they occur. Before the arrival of the pump pulse the nanoparticle, as well as its electron gas and ionic lattice, are thermalized at temperature  $T_0$ . The femtosecond pump pulse then excites the electron gas while leaving intact the ionic lattice, which leads, after an internal thermalization of the electron gas via electron-electron scattering processes (happening in a time  $\tau_{e-e}^{th}$  of a few hundreds of fs in gold [22]), to an electronic temperature  $T_e$ . This is followed by electron-phonon scattering processes (in a time

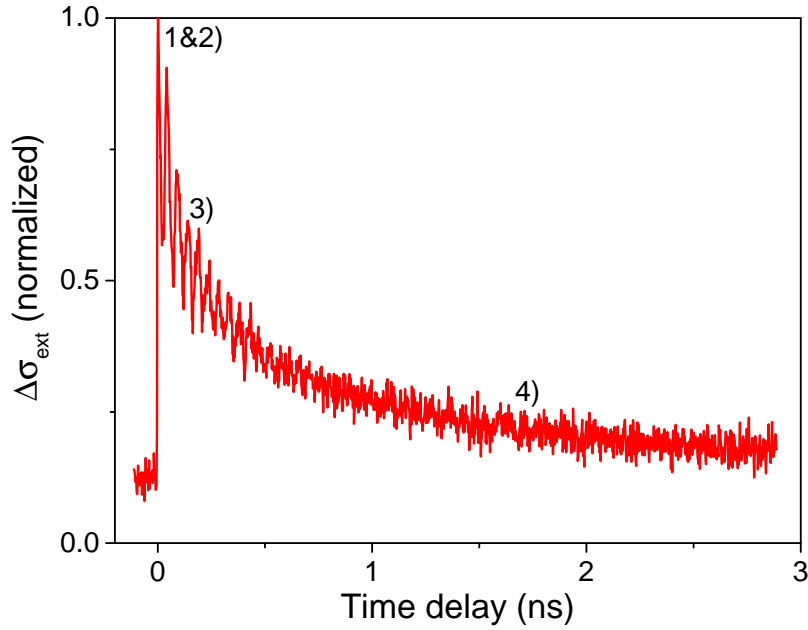


**Figure 1.10 – Typical pump-probe signal for a single gold nanodisk obtained using pump-probe spectroscopy.** The experimental signal, represented as a function of the time delay between the pump and the probe (a zero delay corresponding to temporally superimposed beams), corresponds to the transient variations of the extinction cross-section of the gold nanodisk  $\Delta\sigma_{ext}$  and is normalized here but more details can be found in Chapter 2 Section 2.2.3. The numbers alongside the data correspond to the ones in Figure 1.9 and indicate the sections of the curve corresponding to each phenomena following the excitation of the single nano-object by a pump pulse.

$\tau_{e-L}$  around 1 ps in gold [22]) which allow the temperatures of both the electron gas and the ionic lattice,  $T_e$  and  $T_L$ , respectively, to equilibrate. This allows the nanoparticle to thermalize at a temperature  $T_{eq} > T_0$  a few ps after the excitation by the pump light pulse. Another phenomenon can then occur due to this fast heating : acoustic vibrations resulting from the dilation of the nanoparticle. The associated vibrational modes exhibit periods that depend on the size of the nano-object and are in the 1-100 ps range range, while their quality factors are of the order of 10. In parallel to this phenomenon, the nanoparticle begins to cool down (with a temperature  $T_{NP}(t)$ ) as heat is being transferred to its environment over time. This process allows the nanoparticle to return to equilibrium at temperature  $T_0$  after a time depending on its dimension and its environment, typically ranging from several hundred ps to several ns.

All these phenomena can be observed in measurements performed using pump-probe spectroscopy, as shown in Figure 1.10, which represents the typical signal obtained experimentally for a single gold nanoparticle. Indeed, time-resolved spectroscopy allows to measure the transient variations of the extinction cross-section  $\Delta\sigma_{ext}(\lambda, t)$  (see Chapter 2 Section 2.2.3), which, for an ultrafast process only affecting the nanoparticle dielectric function, can be linked to the transient changes of the real and imaginary part of the dielectric function of the nanoparticle  $\Delta\epsilon_1(\lambda, t)$  and  $\Delta\epsilon_2(\lambda, t)$ , respectively. The equation linking these quantities can be written, at

first order, as:

$$\Delta\sigma_{ext}(\lambda, t) = \frac{\partial\sigma_{ext}}{\partial\epsilon_1}(\lambda)\Delta\epsilon_1(\lambda, t) + \frac{\partial\sigma_{ext}}{\partial\epsilon_2}(\lambda)\Delta\epsilon_2(\lambda, t). \quad (1.50)$$

As the different physical phenomena shown in Figure 1.9 affect differently the transient changes of the dielectric function  $\Delta\epsilon_{1,2}(\lambda, t)$ , Equation 1.50 shows that the analysis of the temporal variations of the extinction cross-section of the nano-object  $\Delta\sigma_{ext}(\lambda, t)$  allows to study the ultrafast phenomena induced by the excitation of a single nano-object by a pump pulse. Equation 1.50 presents a simplified vision of the reality by neglecting the contribution of transient modifications of the dielectric function  $\epsilon_m$  of the environment, which will be further explored in Chapter 4. As a side note, the non-vanishing value of the signal at negative delays in Figure 1.10 reflects the occurrence of accumulation effects related to the periodical excitation of the nano-object by multiple pump pulses (see Chapter 3).

Two of the physical processes, the cooling of the nanoparticle as well as its acoustic vibrations, will be more thoroughly described and studied in Chapters 3 and 4 for the former, and Chapter 5 for the latter.

### 1.3 Thermal dynamics of a supported metal nanodisk

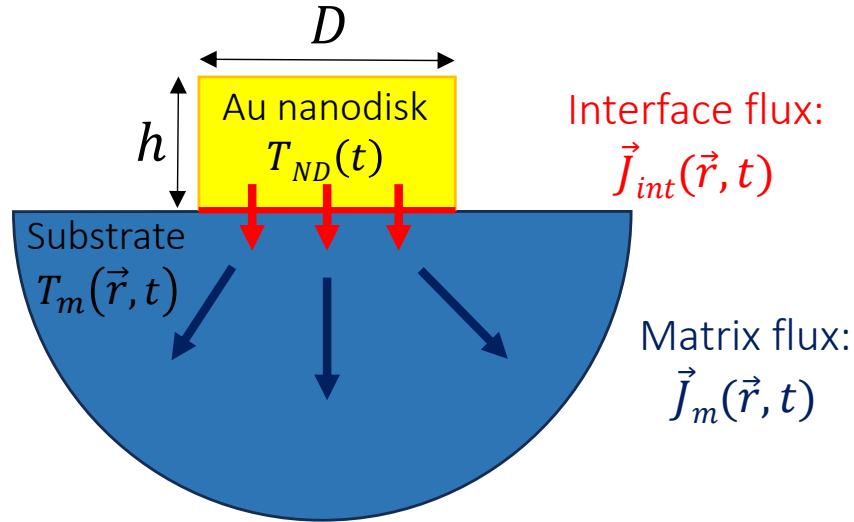


**Figure 1.11 – Schematic of the heat transfer processes considered in the experimental geometry.** The geometry consists of a gold nanodisk (diameter  $D$ , thickness  $h$ ) of temperature  $T_{ND}(t)$  supported on a transparent substrate of temperature  $T_m(\vec{r}, t)$ . Heat transfers at the nanodisk-substrate interface and in the substrate are represented via red and blue arrows (corresponding to heat current densities  $\vec{J}_{int}(\vec{r}, t)$  and  $\vec{J}_m(\vec{r}, t)$ , respectively).

We consider in this section the nanosystem described in Figure 1.11, i.e. a single gold nanodisk supported on a solid and transparent substrate, as it will be the configuration studied in Chapters 3, 4 and 5. The initial configuration assumed here corresponds to the selective excitation of the nanodisk by a femtosecond laser pulse, which leads, after its internal thermalization

(see Section 1.2.3) to  $T_{ND} > T_{ref}$ , with  $T_{ND}$  the nanodisk temperature and  $T_{ref}$  the room temperature, assumed at equilibrium. This temperature difference initiates thermal dynamics involving two processes:

- Interfacial heat transfer (see Section 1.3.1.1).
- Heat conduction, via thermal diffusion in the supporting medium (see Section 1.3.2.1).

In practice, other thermal processes, such as convection or radiation, occur but can be neglected, as discussed below.

### 1.3.1 Heat transfers through the nanodisk surface

#### 1.3.1.1 Kapitza resistance at nanodisk-substrate interface

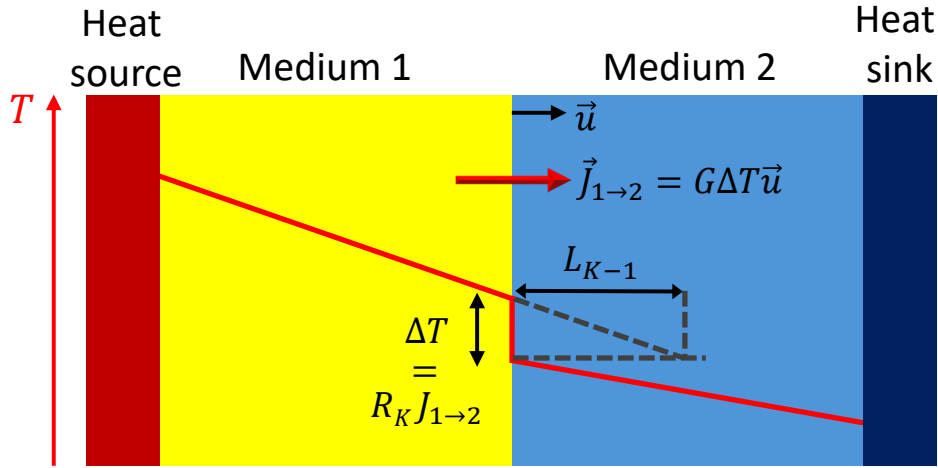


**Figure 1.12 – Schematic of the interfacial heat transfer between media 1 and 2, in contact with a heat source on the left and a heat sink on the right.** Interface between media 1 and 2 is an infinite plane and  $\vec{J}_{1 \rightarrow 2}$  the heat flow at the interface,  $\vec{u}$  being a unit vector perpendicular to the interface and oriented from 1 to 2.  $R_K$  and  $G$  are the Kapitza resistance and conductance, respectively, while  $L_{K-1}$  is the Kapitza length associated to the first medium. The evolution of temperature in the two media is indicated via the red lines in arbitrary unit.

P. Kapitza proposed in 1941 to define the thermal boundary resistance  $R_K$  (also called Kapitza resistance), or alternatively the thermal boundary conductance  $G = 1/R_K$  (in  $\text{W m}^{-2} \text{K}^{-1}$ ), to describe the heat flux originating from the partial transmission of phonons between a copper heater and liquid helium, for which a linear relation to the temperature difference between the two media was observed at their interface [23, 24]. In the configuration represented in Figure 1.12, i.e. an infinite plane interface between two media with a heat source on the left and a heat sink on the right, the thermal boundary conductance  $G$  links linearly the heat flux at the interface  $\vec{J}_{1 \rightarrow 2}$  and the temperature difference between the two media at the interface  $\Delta T$ , as:

$$\vec{J}_{1 \rightarrow 2} = G \Delta T \vec{u}. \quad (1.51)$$

with  $\vec{u}$  a unit vector defined in Figure 1.12.

Additionally, another useful quantity, called the Kapitza length  $L_K$ , can be introduced. This parameter, which can be defined for both media, is defined through:

$$L_{K-1,2} = R_K \Lambda_{1,2}, \quad (1.52)$$

where  $\Lambda_{1,2}$  is the thermal conductivity of one of the two media (see next section). It can be interpreted as the thickness of medium 1 or 2 that would be thermally equivalent to the interface (see Figure 1.12). The interest of the Kapitza length lies in the fact that if the characteristic dimension of a system is of the order of or smaller than the Kapitza length then the interfaces play a significant role in the heat processes occurring in the system. As an example, the Kapitza length for a gold-sapphire interface associated to the sapphire medium  $L_{K-\text{Al}_2\text{O}_3}$  is around 400 nm, using the interface conductance  $G = 60 \text{ MW m}^{-2} \text{ K}^{-1}$  obtained in previous work of the FemtoNanoOptics group [25].

Materials	$G$ (MW m <sup>-2</sup> K <sup>-1</sup> )
AuPd alloy-Toluene	5
Bi-Si	10-20
Au-SiO <sub>2</sub>	40-140
Au-Ethanol	110
Pt-Water	130
TiN-MgO	700

**Table 1.3 – Table of the typical interfacial conductances  $G$  for interfaces between different materials.** Values of the interfacial conductances are from refs. [26–33] and were all measured around 300 K.

$G$  values largely differ from an interface to another, as shown in Table 1.3, which presents the typical experimental values of the interfacial conductance  $G$  for a few systems. The conductance  $G$  of Au-SiO<sub>2</sub> interfaces (which will be present in the nanosystems that will be studied in the next chapters) ranges from 40 to 140 MW m<sup>-2</sup> K<sup>-1</sup>, according to previous measurements [30–32].

### 1.3.1.2 Heat transfer in air: convection

Convective heat transfers occur between a solid and a fluid, the movements of the latter allowing the energy to be transferred from the solid to the fluid. This phenomenon is described using Newton’s law:

$$J_{conv} = h_{conv}(T_S - T_F) \quad (1.53)$$

with  $J_{conv}$  the convective heat flux density,  $h_{conv}$  the convective heat transfer coefficient, and  $T_S$  and  $T_F$  the temperatures of the solid and the surrounding fluid at the interface, respectively. In the case of natural convection (as opposed to forced convection, which will not be the case of the experiments presented in the next chapters), the convective heat transfer coefficient  $h_{conv}$  in air is of the order of 10 W m<sup>-2</sup> K<sup>-1</sup> for bulk solids.

In the case of the nanosystem studied in this work, a single gold nanodisk supported on a solid substrate (Figure 1.11), the typical value of the interfacial heat conductance  $G$  is several

orders of magnitude larger than the value of  $h_{conv}$  (see  $G$  value for Au-SiO<sub>2</sub> in Table 1.3). Convective heat processes were thus neglected in this work.

### 1.3.1.3 Radiative heat transfer

Radiative heat transfer originates from the fact that all materials emit electromagnetic radiation if their temperature is greater than absolute zero. Thermal radiation is induced by thermal agitation and occurs both in matter and vacuum. A black body (i.e. an object absorbing all incident light, an ideal emitter) follows the Stefan-Boltzmann law which writes:

$$J_{rad} = \sigma T_S^4 \quad (1.54)$$

with  $J_{rad}$  the radiative heat flux density,  $\sigma = 5.67 \cdot 10^{-8} \text{ W m}^{-2} \text{ K}^{-1}$  the Stefan constant, and  $T_S$  the temperature of the black body. In practice, real materials are characterized by an emissivity  $\epsilon$  (between 0 and 1) that depends on the composition and shape of the object, and which describes their radiative behavior on a scale ranging from the one of a black body ( $\epsilon = 1$ ) and a white body ( $\epsilon = 0$ , an object that neither absorbs or emits light). The Stefan-Boltzmann's law, corrected by this emissivity, becomes:

$$J_{rad} = \sigma \epsilon_{rad} T_S^4. \quad (1.55)$$

A simple way to compare the efficiency of radiative heat transfers with the ones of other thermal processes is to use the radiative heat flux density between two planar surfaces  $S_1$  and  $S_2$  at temperatures  $T_1$  and  $T_2$  with emissivities  $\epsilon_{rad-1}$  and  $\epsilon_{rad-2}$ , respectively, which is written as [34]:

$$J_{rad,S_1 \rightarrow S_2} = \frac{\sigma(T_1^4 - T_2^4)}{\frac{1}{\epsilon_{rad-1}} + \frac{1}{\epsilon_{rad-2}} - 1}. \quad (1.56)$$

For small temperature differences this expression can be linearized in order to make it resemble Equation 1.53 and introduce a radiative heat transfer coefficient  $h_{rad}$ :

$$J_{rad,S_1 \rightarrow S_2} = h_{rad}(T_1 - T_2) \quad (1.57)$$

with

$$h_{rad} = \frac{\sigma(T_1^2 + T_2^2)(T_1 + T_2)}{\frac{1}{\epsilon_{rad-1}} + \frac{1}{\epsilon_{rad-2}} - 1}. \quad (1.58)$$

The radiative heat transfer coefficient  $h_{rad}$  is of course not a constant and largely depends on the temperatures of the two surfaces  $T_1$  and  $T_2$ . Nevertheless, it allows us to compare the efficiency of the convective and radiative heat transfers around 300 K (e.g.  $T_1 = T_2 \approx 300 \text{ K}$ ). In this context, the value of  $h_{rad}$ , assuming optical radiative transfer (i.e.  $\epsilon_{rad-1} = \epsilon_{rad-2} = 1$ ), is estimated to be of the order of  $1 \text{ W m}^{-2} \text{ K}^{-1}$ , several orders of magnitude lower than the interfacial conductances values for Au-SiO<sub>2</sub> interface (see Section 1.3.1.1). As a result, radiative heat transfers can be also be neglected for our system.

## 1.3.2 Heat conduction in solids

Different modes of heat conduction can intervene inside solids, depending on the considered temperature and length scale. As such, the next sections present the Fourier diffusion, which will be the heat conduction regime considered in the substrate supporting the single gold nanodisk, as well as the hydrodynamic and ballistic heat conduction regimes.

### 1.3.2.1 Fourier diffusion

Heat conduction is a heat transport regime occurring in a material originating from a temperature gradient and without any bulk matter movement. In this context heat propagates thanks to the vibrations of atoms and molecules of the material (phonons) and, for metals, via conduction electrons (see Section 1.1.1). Heat conduction occurs from regions with high temperatures to ones with low temperatures and can usually be described using the Fourier law [35]:

$$\vec{J}_{diff} = -\Lambda_m \vec{\nabla} T, \quad (1.59)$$

with  $\vec{J}_{diff}$  the diffusive heat flux density,  $\Lambda_m$  the thermal conductivity of the material, and  $T$  the temperature of the material ( $\vec{\nabla} T$  being the temperature gradient).

For a homogeneous material, calculating the energy balance in a small volume in the absence of heat source within the solid allows to write:

$$c_m \frac{\partial T}{\partial t} = -\vec{\nabla} \cdot \vec{J}_{diff} \quad (1.60)$$

where  $c_m$  is the volumetric heat capacity of the material. Assuming a temperature-independent thermal conductivity  $\Lambda_m$  (valid for small temperature gradients), one can write the Fourier heat equation

$$\frac{\partial T}{\partial t} = \alpha_m \nabla^2 T \quad (1.61)$$

with

$$\alpha_m = \frac{\Lambda_m}{c_m} \quad (1.62)$$

the thermal diffusivity.

A fundamental solution of the Fourier heat equation is the one for a infinite 3D medium heated by a point source at position  $(0, 0, 0)$  (the solution for a semi-infinite medium being almost identical). The corresponding temporal temperature evolution  $\Delta T$  at position  $(x, y, z)$  is given by:

$$\Delta T(t, x, y, z) = \frac{e^{-(x^2+y^2+z^2)/4\alpha_m t}}{c_m(4\pi\alpha_m t)^{3/2}}. \quad (1.63)$$

This solution can also be expressed in the frequency domain as:

$$\Delta \tilde{T}(\omega, x, y, z) = \frac{e^{-i\sqrt{-i\omega(x^2+y^2+z^2)/\alpha_m}}}{2\Lambda_m \sqrt{x^2 + y^2 + z^2}} \quad (1.64)$$

with  $\Lambda_m$  the thermal conductivity of the material and  $\omega$  the frequency.

Figure 1.13 illustrates the temporal evolution of temperature at different positions as well as the temperature profiles along the  $x$  axis at several instants in the case of infinite medium composed of gold heated by a point source located at  $(0, 0, 0)$ .

### 1.3.2.2 Other conduction regimes

Heat conduction originates, at the microscopic scale, from the random collisions of heat carriers (e.g. phonons), which are characterized by a mean free path (describing the average distance over which they propagate before any collision). At macroscopic scales the Fourier heat law, previously described, correctly describes heat diffusion in a material. However, at scales of the

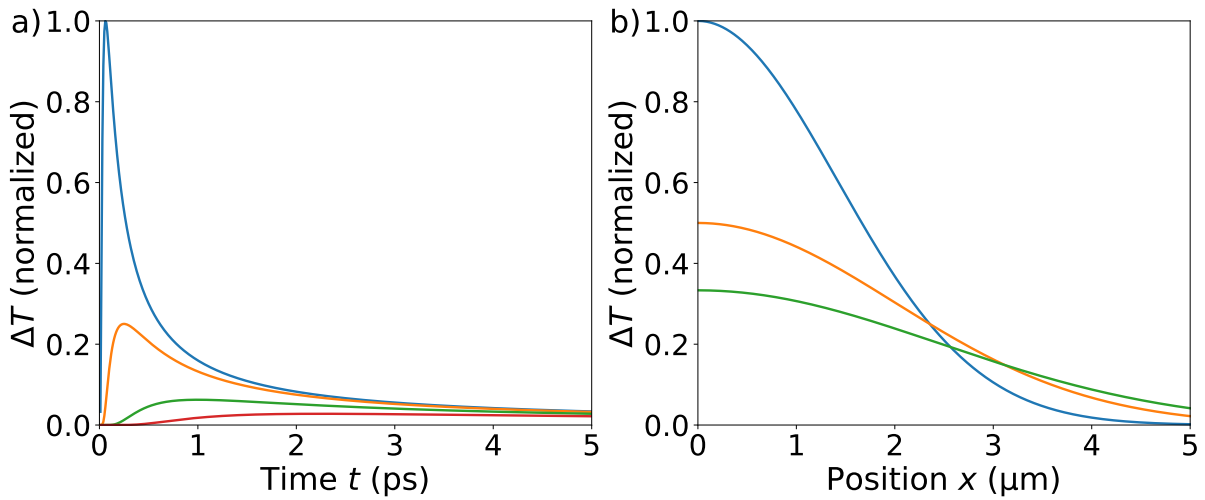


**Figure 1.13** – a) Evolution of temperature at different positions and b) temperature profiles at different instants for a infinite medium heated by a point source at position  $(0, 0, 0)$ . a) Temperature evolutions at positions  $x = 0.5$  (blue line), 1 (orange), 2 (green), and 3  $\mu\text{m}$  (red), normalized by maximum temperature at position  $x = 1 \mu\text{m}$ . b) Temperature profiles along the  $x$  axis in the 0-5  $\mu\text{m}$  range at instants  $t = 1$  (blue line), 2 (orange), and 3 ps (green) normalized by maximum temperature of the first profile. The diffusivity of gold  $\alpha_{Au}$  was used (see Table 3.1).

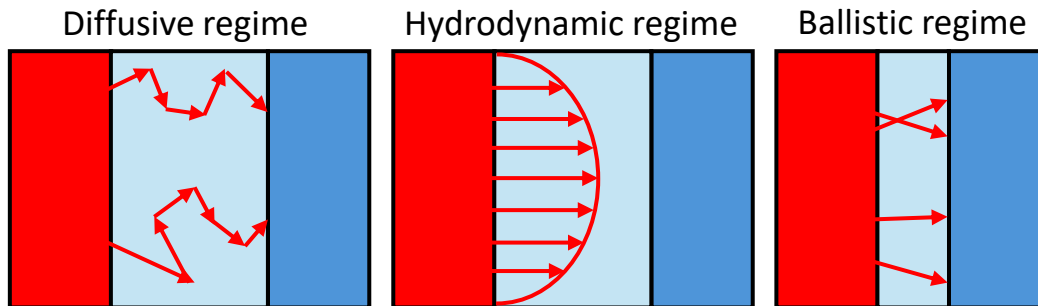


**Figure 1.14** – Schematic representation of the three main heat conduction regimes : diffusive, hydrodynamic, and ballistic. Red arrows represent the motion of heat carriers.

order of or smaller than the mean free path of the heat carriers of the material, the motion of heat carriers can become more complex than in diffusive case, requiring other heat conduction regimes (see Figure 1.14) to accurately describe experimental results [36].

The hydrodynamic regime corresponds to a case where the behavior of the phonons of the material is best described using a fluid-like approach [37]. Phonon hydrodynamics use a macroscopic heat transport equation to describe phonons, the Guyer–Krumhansl equation, in a similar way to the Navier-Stokes equation for fluids. Different phenomena, such as wavelike propagation of thermal energy (or second sound) or Poiseuille’s phonon flow can occur within

this heat conduction regime.

The ballistic regime is a heat conduction regime where heat carriers are able to move freely inside the material without being scattered by impurities or defects. Such regime can be observed if the mean free path of heat carriers exceeds the characteristic length of the object that is studied.

Non diffusive effects, such as those linked to the ballistic and hydrodynamic regimes, have been initially observed in low temperature systems [38]. Their role in the context of nanoscale heat transfer has been more recently demonstrated [39,40] and is currently the object of a large interest in this scientific community. However, invoking such effects was not required in this work (see discussion in Chapter 3).

### 1.3.3 Quasi-uniformity of nanodisk temperature

The heat transfer within a single gold nanodisk and at the nanodisk-substrate interface (see Figure 1.11) can be compared by introducing the Biot number  $Bi$ , a dimensionless number which allows, in this configuration, to compare the interfacial heat transfer at the nanodisk-substrate interface and the heat conduction inside the nanodisk. In this system, the Biot number can be defined as the ratio between the maximal temperature variation inside the gold nanodisk,  $\Delta T_{ND}$ , and the temperature difference at the nanodisk-substrate interface,  $\Delta T_{ND \rightarrow sub}$ . Using the conservation of heat flux at the nanodisk-substrate interface, one can write:

$$J_{ND \rightarrow sub} = J_{ND|int}, \quad (1.65)$$

$J_{ND \rightarrow sub}$  being the heat flux density at the nanodisk-substrate interface, linked to an interfacial Kapitza conductance  $G$  (Equation 1.51), and  $J_{ND|int}$  the heat flux density in the nanodisk taken at the interface, obeying to the Fourier diffusion law (Equation 1.59). These two terms can be written as:

$$J_{ND \rightarrow sub} = G \Delta T_{ND \rightarrow sub} \quad (1.66)$$

and

$$J_{ND|int} = \Lambda_{Au} |(\vec{\nabla} T_{ND})|_{int} \approx \Lambda_{Au} \frac{|\Delta T_{ND}|}{h}, \quad (1.67)$$

respectively, with  $T_{ND}$  the temperature in the nanodisk,  $\Lambda_{Au}$  the thermal conductivity of gold, and  $h$  the thickness of the nanodisk. The Biot number can thus be expressed as:

$$Bi = \frac{\Delta T_{ND}}{\Delta T_{ND \rightarrow sub}} = \frac{hG}{\Lambda_{Au}}. \quad (1.68)$$

The value of the Biot number in our experimental conditions can be estimated in the case of a single gold nanodisk with a thickness  $h = 10$  nm and thermal conductivity  $\Lambda_{Au} = 317$  W m<sup>-1</sup> K<sup>-1</sup> supported on a thick sapphire substrate. For this estimation we use a  $G = 50$  MW m<sup>-2</sup> K<sup>-1</sup>, consistent with previous measurements for gold-sapphire interfaces [41–45] (and close to the  $G$  values of the other interfaces studied experimentally in the next chapters), and obtain a  $Bi = 2 \cdot 10^{-3} \ll 1$  value. This implies that the temperature variations in the gold nanodisk are much smaller than the ones at the nanodisk-sapphire interface, and thus that the nanodisk remains nearly isothermal during its thermal cooling.



# Chapter 2

## Experimental and modeling methods

The study of the physical properties of nanoparticles generally requires three main tools :

- The synthesis of the investigated nanoparticles, which can be achieved using a variety of different methods (physical or chemical, bottom-up or top-down), including laser ablation, lithography and colloidal synthesis.
- Experimental techniques allowing to study the physical properties of the nanoparticles (e.g. optical, mechanical, thermal or magnetic properties), of their local environment (e.g. substrate or surrounding medium, molecules), and of the nanoparticles-environment interface. There are many techniques available for this. They are based on different principles, including the interaction of the nanoparticles with light beams (measuring for instance the absorption, scattering, photoluminescence or Raman scattering resulting from nanoparticle illumination [46–50]), with electron beams (e.g. detecting the diffraction or energy loss of electrons [51, 52]), electric currents (as in the  $3\omega$  technique [53]) or with local probes (as in AFM or STM [54, 55]).
- Numerical methods allowing to simulate the investigated system and its properties. These modeling tools are in particular helpful for extracting physical information from indirect measurements (e.g. to determine quantities such as temperature or pressure from optical measurements).

Regarding the activities of our FemtoNanoOptics group, nanoparticle synthesis is performed by external partners, while nano-objects are investigated using a combination of optical studies and finite-element multiphysics modeling. The optical properties of nanoparticles thus stand at the core of the group’s activities. These optical properties have been studied for a long time, as far as the middle of the 19th century, with the study of colloidal gold by Faraday in 1857 [56]. However, techniques were first limited to the study of ensembles of nanoparticles: in this context, experimental measurements could only give access to quantities averaged over all the individual responses of the nano-objects, which always exhibit some dispersion of their internal characteristics (e.g. size, morphology, composition), and external environment (substrate, molecules). A schematic illustration of the effect of this dispersion on an extinction spectrum is represented in Figure 2.1. This effect constitutes a strong limitation for quantitative investigations of the physical properties of nanosystems.

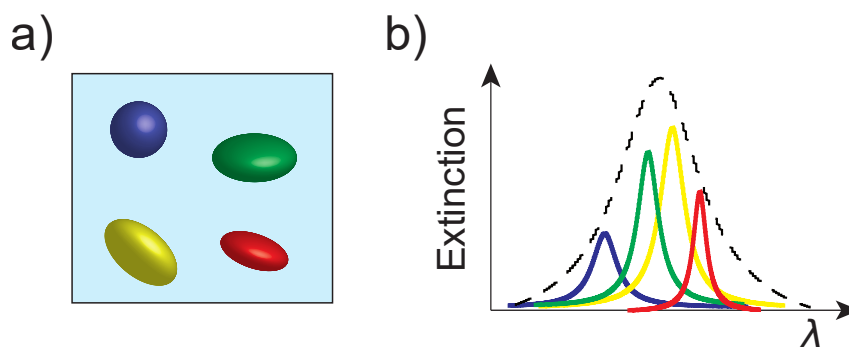


**Figure 2.1 – Schematic illustrating the influence of the dispersion of the characteristics of the nano-objects on the extinction (or other optical properties) associated to the ensemble of nanoparticles.** a) An ensemble of nanometric ellipsoids with different sizes. b) Extinction spectrum (see Chapter 1 Section 1.2) of the ensemble of nanoellipsoids (dashed line) and extinction spectra associated to each nano-object (same color code as in a).

Thus, single-particle spectroscopy techniques were developed and helped to further understand the properties of nanosystems. The first successful detection of a single molecule was based on the detection of its absorption, using modulation of the wavelength of the incident laser around one of the absorption lines of the studied molecule [57]. Further developments allowed to perform near-field [58] or far-field [59] detection and spectroscopy of single nano-objects, based on their luminescence, scattering or absorption. Different approaches involved the modulation of the polarization of the incident light [60] or of the position of the nanoparticle [8, 61] (see Spatial Modulation Spectroscopy in Section 2.2.2), and single-particle ultrafast time-resolved spectroscopy [9, 10] (see Section 2.2.3).

In the first section of this chapter, the process used to synthesize the investigated nanoparticles (gold nanodisks), performed by our collaborators (Sylvie Marguet, CEA Saclay), will be briefly presented. The second section will detail the two optical techniques used in this work :

- Spatial modulation spectroscopy (SMS), a microscopy/spectroscopy technique allowing to detect single nano-objects and measure quantitatively their extinction spectra
- Single-particle ultrafast time-resolved spectroscopy, also referred to as pump-probe spectroscopy in the following, which gives access to the temporal variations of the extinction cross-section of a nano-object following its initial excitation by a laser pulse.

The last section will present the finite element modeling (FEM) simulations, performed in our group (Dr Aurélien Crut), of the optical response of a single gold nanodisk supported by a solid substrate as well as its cooling dynamics. These two types of simulations were also combined to study the optical detection of nanodisk thermal dynamics in the context of single-particle time-resolved experiments (as described in Chapter 4).

## 2.1 Gold nanodisks: synthesis and deposition

Gold nanodisks were chosen for this work as model nano-objects because they present a rather simple geometry characterized by only two parameters (diameter  $D$  and thickness  $h$ , see Figure

2.2a). Lithographed gold nanodisks had been used in the context of several previous studies in the FemtoNanoOptics group [25, 62–64]. The nanodisks used in this work were prepared using colloidal chemistry by Sylvie Marguet (CEA Saclay, our partner in the context of the ULTRA-SINGLE project), following an already published protocol [65]. Syntheses were performed in aqueous solution in the presence of the cetyltrimethylammonium bromide (CTAB) surfactant. In a first step, gold nanoplates were obtained using a method initially proposed by Mirkin’s group to produce triangular nanoplates [66]. A high percentage of hexagonal nanoplates ( $\approx 90\%$ ) was obtained to the detriment of triangular shapes ( $\approx 10\%$ ) by optimizing the concentrations of the reactants in the growth solution, i.e. CTAB 0.1 M,  $\text{HAuCl}_4$  0.7 mM, and ascorbic acid 1.6 mM. Au nanodisks were obtained in a second step, by mild oxidation of these hexagonal and triangular nanoplates smoothing their vertices and edges, using the Au(III)/CTAB oxidant complex [67, 68].

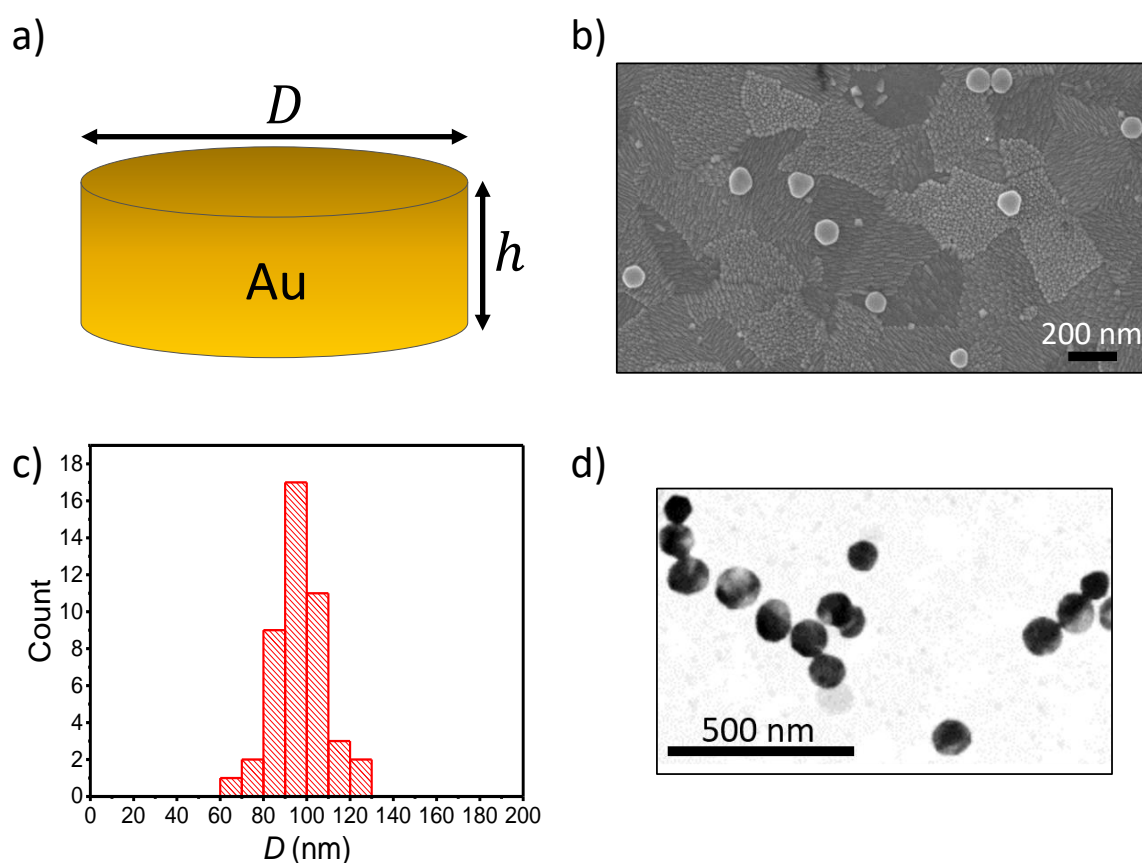


**Figure 2.2 – Geometry, electron microscopy images, and histogram of the average diameters of the synthesized gold nanodisks.** a) Ideal cylindrical geometry of a nanodisk, characterized by its diameter  $D$  and thickness  $h$ . b) SEM images of the synthesized gold nanodisks deposited on an ITO substrate. c) Histogram of the average diameters of 45 gold nanodisks, measured via SEM images. d) TEM images of the gold nanodisks supported on a 15 nm thick  $\text{Si}_3\text{N}_4$  membrane.

The morphological distribution of the Au nanodisks synthesized by this 2-step procedure was investigated using SEM imaging (Figure 2.2b), following nanodisk deposition on an ITO

substrate. Close to circular sections were observed for a majority of the produced nano-objects, a fraction of them however still presenting quasi-hexagonal or triangular sections. Statistics on the obtained SEM images yielded an average nanodisk diameter of  $D = (97 \pm 12)$  nm (see histogram of average diameters in Figure 2.2c). The occasional observation of a few nanodisks contacting the substrate via their lateral surface rather than via one of their parallel bases also showed that their thickness  $h$  was of the order of 10 nm. A precise estimation of the average value of  $h$  could however not be performed using SEM, due to the weak number of nanodisks in this configuration and to uncertainties about their precise orientation. These nanodisks were used in thermal and thermo-optical studies, which are presented in Chapter 3 and 4, and vibrational studies, presented in Chapter 5, and were also observed via TEM imaging (Figure 2.2d). Moreover, others gold nanodisks, with different aspect ratio  $\eta = D/h$  were also synthesized to study its impact on the vibrational response of single gold nanodisks, presented in Chapter 5.

## 2.2 Linear and ultrafast single-particle optical spectroscopy techniques

### 2.2.1 Laser sources

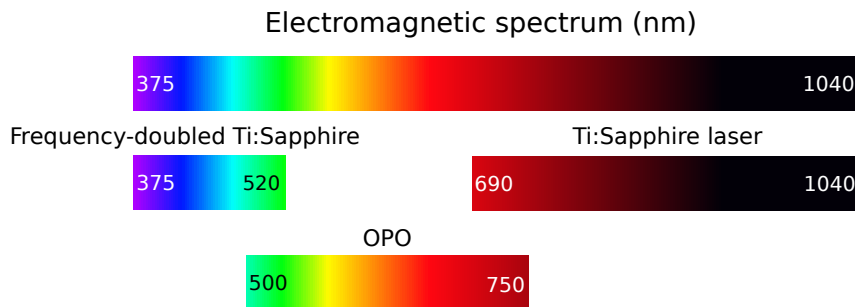


**Figure 2.3** – Spectral ranges covered by the three light sources used in experiments.

The measurement of the extinction linear spectra of single nanoparticles as well as their study through time-resolved experiments necessitated light sources with a broad spectral range, from the near ultraviolet to the near infrared. Several light sources were used in our experiments, allowing to cover the whole 375-1040 nm range (Figure 2.3):

- a Ti:Sapphire laser (emission in the 690-1040 nm range)
- a non-linear crystal allowing frequency doubling of the Ti:Sapphire beam (generation of light in the 375-520 nm range)
- an Optical Parametric Oscillator (OPO, 500-750 nm range)

The Ti:Sapphire laser is a tunable commercial mode-locked oscillator with an average output power of 2 W and giving access to the 690-1040 nm range. It uses a sapphire ( $\text{Al}_2\text{O}_3$ ) crystal doped with trivalent titanium ions  $\text{Ti}^{3+}$  for its amplifying medium. A continuous wave

Nd : YVO<sub>4</sub> laser, which generates a 1064 nm wavelength, is used to produce the population inversion within the titanium ions. This is frequency-doubled by a non-linear lithium triborate crystal (LBO) to create a 532 nm wavelength close to the absorption peak of the Ti:Sapphire crystal. The longitudinal modes of the cavity allow the generation of short pulses of the order of 150 fs with a repetition frequency  $f_{rep}$  of 80 MHz (corresponding to a pulse repetition period  $T_{rep} = 12.5$  ns).

The UV-blue part of the spectral range (375-520 nm) is produced through the frequency-doubling of the Ti:Sapphire laser beam using the Second-Harmonic Generation (SHG) of a 100  $\mu\text{m}$  thick barium beta-borate ( $\beta - \text{BaB}_2\text{O}_4$ ) crystal (BBO). This light source can technically reach wavelengths as low as the 345-375 nm range but using them in our experiments is prevented by the low reflectivity of the mirrors as well as the poor transmission of the objectives at such wavelength range.

The last light source is an automated optical parametric oscillator (OPO) covering the 500-750 nm wavelength range. Inside, the incident pump beam, provided by the Ti:Sapphire laser at 820 nm, is first frequency-doubled through a SHG crystal. This 410 nm beam is combined with a birefringent crystal to perform a non-linear optical process called parametric amplification. In the birefringent medium a photon of frequency and wavevector  $(\omega_p, \vec{k}_p)$  (pump wave) is converted into two photons with  $(\omega_s, \vec{k}_s)$  and  $(\omega_i, \vec{k}_i)$  (denoted as signal and idler waves). These quantities respect the energy and momentum conservation with  $(\omega_p = \omega_s + \omega_i, \vec{k}_p = \vec{k}_s + \vec{k}_i)$ . The frequency  $\omega_s$  of the signal wave can be tuned through the rotation of the birefringent crystal and covers the 500-750 nm range. This is finally amplified in a resonant cavity to generate coherent ultrashort light pulses with durations similar to the ones of the Ti:Sapphire pulses.

## 2.2.2 Spatial Modulation Spectroscopy (SMS)

### 2.2.2.1 Principle

Spatial Modulation Spectroscopy is a far-field optical spectroscopy technique that permits a quantitative measurement of the extinction cross-section  $\sigma_{ext}$  (see Chapter 1 Section 1.2) in the case of nano-objects with sizes larger than  $\sim 5$  nm (Au) or  $\sim 2$  nm (Ag) [8] deposited on transparent or thin absorbing substrates. In our work, it was used to localize single nanodisks randomly deposited on a solid transparent substrate and measure their extinction cross-sections as a function of wavelength and polarization of the incident light.

This technique exploits the attenuation (by both absorption and scattering phenomena, see Chapter 1) of a light beam induced by the presence of a nanoparticle. As presented in Chapter 1 Section 1.2.1, the power attenuation measured by a photodetector of surface  $S_D$  placed in the direction of propagation of light is written, for a small nanoparticle shined by a beam with intensity profile  $I(x, y)$  (see Equation 1.39 in Chapter 1), as:

$$\Delta P = P_0 - P_{S_D} \approx P_{ext} = \sigma_{ext} I(x_0, y_0), \quad (2.1)$$

with  $P_0$ ,  $P_{S_D}$ , and  $P_{ext}$  the incident, detected and extinction powers, respectively, and  $I(x_0, y_0)$  the intensity of the incident light beam at the position of the nanoparticle (here assumed punctiform).

The direct measurement of  $\Delta P$  for nanoparticles with sizes much smaller than that of the light beam can be quite challenging as the  $\frac{\Delta P}{P_0}$  ratio is small. Indeed, this ratio is for instance of

the order of  $10^{-3}$  for a 20 nm diameter gold nanosphere shined by a diffraction-limited Gaussian beam, making the sought signal dominated by the power fluctuations of the laser source.

Increasing the signal-to-noise ratio was thus critical to be able to detect small nanoparticles based on their extinction. In this context a powerful general method consists in forcing  $\Delta P$  to oscillate in time. This has been done by modulating the polarization of the light beam [60], the light wavelength [57], or the position of the nano-object relatively to the light beam [10,69]. Then the synchronous detection of  $\Delta P(t)$  at the modulation frequency  $f$  (or one of its harmonics like  $2f$  or  $3f$ , typically done via a lock-in amplifier (LIA)), allows one to considerably enhance the sensitivity of the measurement of the attenuation of the light beam caused by the nanoparticle, by removing all the noise components at frequencies different from the modulating one.

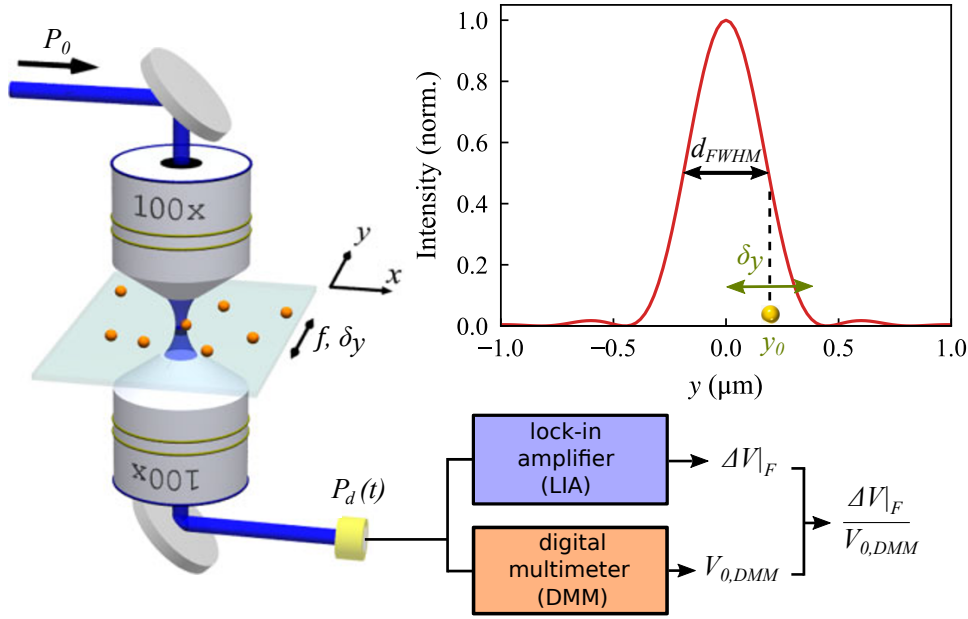


**Figure 2.4 – Principle of Spatial Modulation Spectroscopy.** A laser beam is strongly focused via an objective on a single nano-object supported on a transparent substrate. The sample position is modulated along the  $y$  direction via a periodic vibration of spatial amplitude  $\delta_y$  thanks to a piezoelectric actuator. The periodic displacement leads to a modulation of the transmitted power  $P_d = P_0 - \Delta P$ , with  $P_0$  the incident power of the light beam. The transmitted light is recollimated by a second objective and then detected thanks to a photodiode. Two quantities are extracted from the measured output voltage of the photodiode: a lock-in amplifier demodulates the signal and gives access to its oscillating component at frequency  $F$  induced by the piezoelectric actuation  $\Delta V|_F$  while the average voltage signal  $V_{0,DMM}$  is measured by a digital multimeter (DMM) and is linked to  $\langle P_d \rangle$  ( $\approx P_0$  in the case of a small nanoparticle).

The third approach has been developed in the FemtoNanoOptics group and is denoted as Spatial Modulation Spectroscopy (SMS). In the SMS technique, whose principle is schematized in Figure 2.4, the position of a single nanoparticle is periodically modulated in the focal plane of a strongly focused light beam, of Full Width at Half-Maximum (FWHM)  $d_{FWHM}$ , through a vibration generated by a piezoelectric actuator. A XY piezoelectric stage also allows to position

the nanoparticle under the light beam. In the case of a vibration along the  $y$  direction with spatial amplitude  $\delta_y$  and frequency  $f$ , the position of the nano-object, relatively to the beam, is  $(x_0, y(t))$  with

$$y(t) = y_0 + \delta_y \sin(2\pi ft). \quad (2.2)$$

The power attenuation from Equation 2.1 then becomes:

$$\Delta P(t, x_0, y_0) = \sigma_{ext} I(x_0, y_0 + \delta_y \sin(2\pi ft)). \quad (2.3)$$

Some insight about the process used to measure  $\sigma_{ext}$  in practice can be gained by assuming that the vibration amplitude is much smaller than the FWHM ( $\delta_y \ll d_{FWHM}$ ). In that case Equation 2.3 can be expressed, via a second-order development, as:

$$\Delta P(t, x_0, y_0) \approx \Delta P_0(x_0, y_0) + \Delta P|_f(x_0, y_0) \sin(2\pi ft) + \Delta P|_{2f}(x_0, y_0) \cos(4\pi ft) + o(\delta_y^2) \quad (2.4)$$

with

$$\left\{ \begin{array}{l} \Delta P_0(x_0, y_0) = \sigma_{ext} \left[ I(x_0, y_0) + \frac{\delta_y^2}{4} \frac{\partial^2 I}{\partial y^2}(x_0, y_0) \right] \\ \Delta P|_f(x_0, y_0) = \sigma_{ext} \delta_y \frac{\partial I}{\partial y}(x_0, y_0) \\ \Delta P|_{2f}(x_0, y_0) = -\frac{1}{4} \sigma_{ext} \delta_y^2 \frac{\partial^2 I}{\partial y^2}(x_0, y_0). \end{array} \right. \quad (2.5)$$

As a consequence, the modulated power  $\Delta P(t)$  is a combination of constant and sinusoidal terms that are all proportional to the extinction cross-section of the nanoparticle  $\sigma_{ext}$ . The first harmonic and second harmonic components,  $\Delta P|_f(x_0, y_0)$  and  $\Delta P|_{2f}(x_0, y_0)$ , respectively, are proportional to the first and second derivatives of the intensity profile of the light beam with respect to the  $y$  coordinate (vibrational axis) and evaluated in  $(x_0, y_0)$ .

In the general case, even without the previous  $\delta_y \ll d_{FWHM}$  condition, the Fourier components of the modulated power  $\Delta P(t)$  (from Equation 2.3) detected by the lock-in amplifier in our experiments at frequencies  $nf$  ( $n$  an integer) can be expressed as:

$$\left\{ \begin{array}{l} \Delta P|_{nf}(x_0, y_0) = \frac{2}{T} \sigma_{ext} \int_{-\frac{T}{2}}^{\frac{T}{2}} I(x_0, y_0 + \delta_y \sin(2\pi ft)) \sin(2\pi nft) dt \quad n \text{ odd} \\ \Delta P|_{nf}(x_0, y_0) = \frac{2}{T} \sigma_{ext} \int_{-\frac{T}{2}}^{\frac{T}{2}} I(x_0, y_0 + \delta_y \sin(2\pi ft)) \cos(2\pi nft) dt \quad n \text{ even} \end{array} \right. \quad (2.6)$$

with  $T = 1/f$ .

Similarly to Equation 2.5, all Fourier components are proportional to the extinction cross-section  $\sigma_{ext}$  of the nano-object. In practice, however, only the  $F = f$  ( $n = 1$ ) or  $2f$  ( $n = 2$ ) components are exploited as the  $n \geq 3$  harmonics present significantly lower amplitudes. The associated Fourier components, deduced from Equation 2.6, write:

$$\left\{ \begin{array}{l} \Delta P|_f(x_0, y_0) = \frac{2}{T} \sigma_{ext} \int_{-\frac{T}{2}}^{\frac{T}{2}} I(x_0, y_0 + \delta_y \sin(2\pi ft)) \sin(2\pi(f)t) dt \\ \Delta P|_{2f}(x_0, y_0) = \frac{2}{T} \sigma_{ext} \int_{-\frac{T}{2}}^{\frac{T}{2}} I(x_0, y_0 + \delta_y \sin(2\pi ft)) \cos(2\pi(2f)t) dt. \end{array} \right. \quad (2.7)$$

In SMS experiments performed in this work only the second harmonic was used (a theoretical SMS image corresponding to the  $f$  component can however be found in Figure 2.6).

Experimentally, the Gaussian laser beam entering the focusing objective (top one in Figure 2.4) is diaphragmed by the entrance pupil of this objective. This quasi plane wave leads to an intensity profile  $I(x, y)$  in the sample plane closer to an Airy distribution than to a Gaussian one [70]. The associated intensity profile centered at  $(0,0)$  appearing in Equation 2.7 can thus be written as:

$$I(r) = I_0 \left[ \frac{2J_1 \left( 1.62 \cdot \frac{2r}{d_{FWHM}} \right)}{1.62 \cdot \frac{2r}{d_{FWHM}}} \right]^2, \quad (2.8)$$

with  $J_1$  the Bessel function of the first kind of order one,  $r = \sqrt{x^2 + y^2}$  the distance to the center, and  $d_{FWHM}$  the FWHM of the Airy profile. The power  $P_0$  of a light beam (incident power) with such intensity profile can then be expressed as:

$$P_0 = \iint I(x, y) dx dy, \quad (2.9)$$

from which one can deduce the relation:

$$I_0 \approx 0.8316 \frac{P_0}{d_{FWHM}^2}. \quad (2.10)$$

In practice (see Figure 2.4), an avalanche photodiode (APD) is used to detect the power transmitted through the sample  $P_d = P_0 - \Delta P$ . A lock-in amplifier, connected to it, is used to demodulate the signal and retrieve the  $\Delta P|_F$  component. For small nanoparticles, for which  $\max(|\Delta P(t)|) \ll P_0$ , the assumption about the average power detected by the photodiode  $\langle P_d \rangle = \langle P_0 - \Delta P \rangle \approx P_0$  can therefore be done. Practically, a digital multimeter (DMM) is also connected to the photodiode and allows to directly measure  $P_0$  in the presence of the nanoparticle, for a small one, and in the absence of the nanoparticle for a larger one, as the previous assumption is no longer valid.

Moreover, the photodiode used in practice is not perfect and is characterized by a frequency-dependent gain  $G(F)$  in its linear regime (which is the case in our experiments), typically corresponding to the response of a low-frequency filter. More precisely, the  $F$ -component  $V|_F$  of a voltage output  $V$  of the photodiode can be linked to  $P|_F$ , the  $F$ -component of the detected power  $P$ , through:

$$V|_F = G(F)P|_F \quad (2.11)$$

with  $G(F)$  the gain of the photodiode at frequency  $F$  in its linear regime. We also define the normalized gain of the photodiode as:

$$g(F) = \frac{G(F)}{G(0)}. \quad (2.12)$$

The voltage  $\Delta V|_F$  measured by the photodiode (Figure 2.4) depends not only on the optical properties of the investigated nanoparticle, but also on the laser intensity and on the detector characteristics. An experimental quantity (referred to as "SMS signal" in the following) independent of the two latter characteristics can be defined as:

$$\text{SMS signal} = \frac{\Delta V|_F}{V_0|_F} \quad (2.13)$$

- $\Delta V|_F$  the Fourier component extracted by a lock-in amplifier at operating frequency  $F$  ( $= 2f$  in the experiments reported here) originating from the demodulation of the voltage signal of the photodiode linked to the detected power  $P_d$  (the modulation being generated by the piezoelectric actuator with a sinusoidal oscillation of the position of the nanoparticle). This quantity is proportional to  $\sigma_{ext}$ , the sought optical property of the studied nanoparticle.
- $V_0|_F$  the  $F$ -component of the voltage signal obtained using the same acquisition chain when modulating the incident power  $P_0$  with a mechanical chopper at operating frequency  $F$  (yielding square power oscillations).

This choice of convention:

- Guarantees a quantity that is independent from the intensity of the incident light beam (provided the photodiode is used in its linear range).
- Allows to get rid of the spectral response of the photodiode at operating frequency  $F$  (see  $G(F)$  frequency-dependent gain in Equation 2.11).

The normalized quantity in Equation 2.13 can be written as:

$$\frac{\Delta V|_F}{V_0|_F} = \frac{\Delta P|_F}{P_0|_F} = \frac{\pi}{2} \frac{\Delta P|_F}{P_0} \quad (2.14)$$

where the  $\pi/2$  factor takes into account the temporal square shape of the modulated power  $P_0(t)$  from which is extracted  $P_0|_F$  (of which definition is similar to the one of  $V_0|_F$ ).

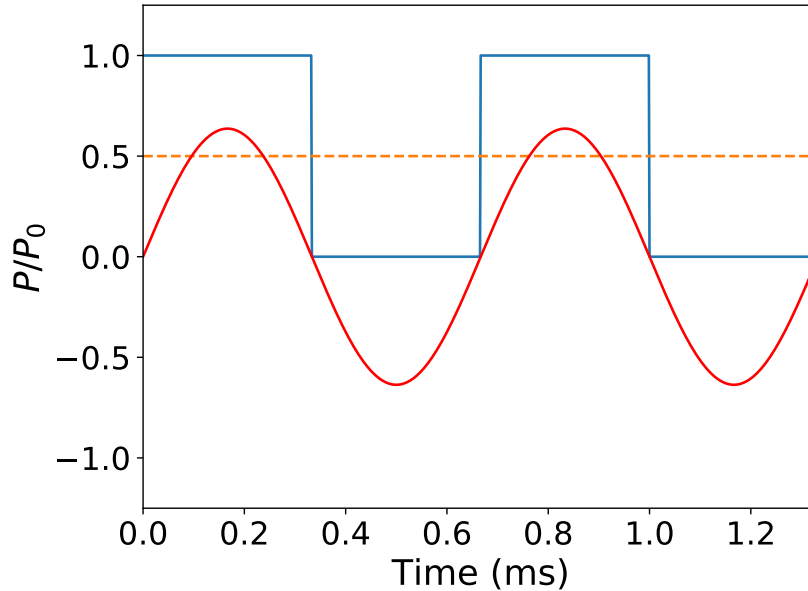


**Figure 2.5 – Continuous and fundamental sinusoidal Fourier components of a square signal.** A square signal oscillating between 0 and 1 with an arbitrary frequency is plotted (blue line). Its mean value is represented (dashed orange line) as well as its first Fourier component, a pure sinusoid with a  $\frac{4}{\pi}$  amplitude (red line).

Indeed, as shown in Figure 2.5 (with normalized amplitude), the modulation of  $P_0$  via a square signal using a mechanical chopper produces a  $P_0(t)$  signal (blue signal) composed of a constant part of amplitude  $\frac{P_0}{2}$  (dashed orange line) and of a zero-mean square wave component that oscillates between  $-\frac{P_0}{2}$  and  $\frac{P_0}{2}$  (red line). The fundamental Fourier component of a square signal oscillating between 0 and  $P_0$  has a  $\frac{2}{\pi}P_0$  amplitude (Figure 2.5). As a consequence,  $P_0$  and  $P_0|_F$  can be linked via:

$$P_0|_F = \frac{2}{\pi} \cdot P_0, \quad (2.15)$$

justifying the corresponding factor in Equation 2.14.

Using Equations 2.7, 2.10, and 2.14, one can express the SMS signals at  $F = f$  and  $F = 2f$ :

$$\left\{ \begin{array}{l} \frac{\Delta V|_f}{V_0|_f} = \sigma_{ext} \frac{0.8316\pi}{d_{FWHM}^2} \frac{1}{T} \int_{-\frac{T}{2}}^{\frac{T}{2}} \frac{I(x_0, y_0 + \delta_y \sin(2\pi ft))}{I_0} \sin(2\pi(f)t) dt \\ \frac{\Delta V|_{2f}}{V_0|_{2f}} = \sigma_{ext} \frac{0.8316\pi}{d_{FWHM}^2} \frac{1}{T} \int_{-\frac{T}{2}}^{\frac{T}{2}} \frac{I(x_0, y_0 + \delta_y \sin(2\pi ft))}{I_0} \cos(2\pi(2f)t) dt \end{array} \right. \quad (2.16)$$

A practical drawback of the  $\frac{\Delta V|_F}{V_0|_F}$  ratio appearing in Equations 2.13, 2.14 and 2.16 is that its measurement requires frequent mounting/unmounting of a chopper on the path of the incident light. To avoid this, the denominator  $V_0|_F$  can be deduced from a measurement via a DMM of the continuous voltage signal  $V_{0,DMM}$  associated to the unmodulated power  $P_0$  (Figure 2.4). This however requires to take into account the frequency-dependent gain of the photodiode (Equation 2.11) and the effect of different measurement devices (DMM vs LIA).

To do this a calibration protocol is effectuated. A photodiode shined in direct transmission with a light beam is considered. In this context,  $P_0$ , the average power of the incident light beam, corresponds to a continuous voltage signal read on the DMM,  $V_{0,DMM}$ . Then a mechanical chopper at the operating frequency  $F$  is placed in the light beam, producing a modulated voltage signal  $V_0(t)$ , which is a square wave oscillating between 0 and  $V_{0,DMM}$ . After that the lock-in amplifier is used to extract the first harmonic of the modulated signal  $V_0(t)$  at frequency  $F$ ,  $V_0|_F$ .

First, the demodulation process leads to a  $\frac{2}{\pi}$  factor, identically to what was explained in Equation 2.14. Secondly, the lock-in amplifier gives Root Mean Square (RMS) values leading to an additional  $\frac{1}{\sqrt{2}}$  factor. Finally, as the photodiode is submitted to a modulated signal, its normalized gain at frequency  $F$ ,  $g(F)$ , must be taken into account. Thanks to these steps one can define the  $\alpha_{SMS}$  coefficient:

$$\alpha_{SMS} = \frac{V_{0,DMM}}{V_0|_F} = \frac{\pi}{\sqrt{2}} \frac{1}{g(F)} \quad (2.17)$$

The SMS signal  $\frac{\Delta V|_F}{V_0|_F}$  (Equations 2.13 and 2.16) can thus be linked to the experimentally measured quantity  $\frac{\Delta V|_F}{V_{0,DMM}}$  through:

$$\frac{\Delta V|_F}{V_0|_F} = \alpha_{SMS} \frac{\Delta V|_F}{V_{0,DMM}} \quad (2.18)$$

In the case of an ideal photodiode (with  $g(F) = 1$ ) as well as a perfect chopper with a 50% duty cycle and a small incident beam, the theoretical value of the  $\alpha$  coefficient would be:

$$\alpha_{SMS-th} = \frac{\pi}{\sqrt{2}} \approx 2.22. \quad (2.19)$$

In practice, the modulation of the incident beam by the mechanical chopper does not lead to a perfect square temporal profile and the spectral response of the photodiode is not perfectly flat either, leading to  $\alpha_{SMS}$  values differing from that of Equation 2.19. The experimental value of the  $\alpha_{SMS}$  coefficient is obtained via the measurement of the two quantities involved in its definition (see Equation 2.17). A laser beam of power  $P_0$  is shined on the photodiode, leading to the evaluation of  $V_{0,DMM}$  via the DMM. Then a chopper at frequency  $F$  is placed on the beam path and the lock-in amplifier is used to extract the first Fourier component of the modulated signal at frequency  $F$ ,  $V_{0|F}$ . The ratio of these two quantities gives access to the experimental value of  $\alpha_{SMS}$ .

In the experimental conditions of most of my experiments (including the use of an avalanche fast photodiode), an  $\alpha_{SMS}$  value very close to the theoretical one was achieved:  $\alpha_{SMS-exp} = 2.24$ . In contrast, previous measurements performed in the group using standard photodiodes with less performant spectral responses involved much higher  $\alpha_{SMS}$  values (of the order of 5).

Thus, an initial calibration of the  $\alpha_{SMS}$  coefficient allows to convert the experimentally measured quantity  $\frac{\Delta V|_F}{V_{0,DMM}}$  into the SMS signal  $\frac{\Delta V|_F}{V_{0|F}}$ , which will be the only quantity used in the following.

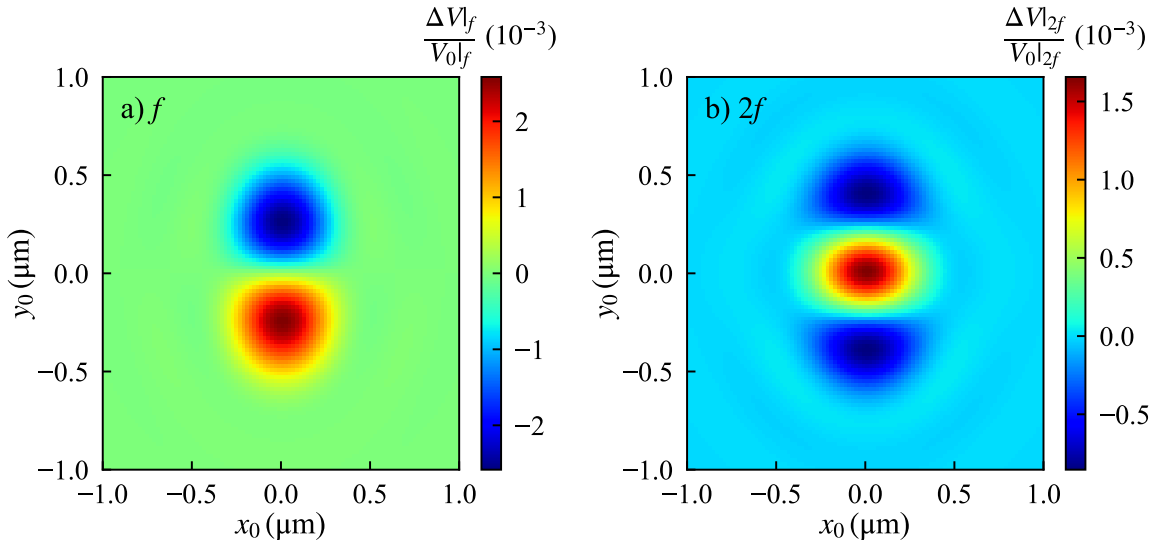


**Figure 2.6 – Theoretical SMS signal of a small nano-object for a demodulation at a)  $F = f$  or b)  $2f$  as a function of the position of the nanoparticle  $(x_0, y_0)$ .**

2D maps of the  $\frac{\Delta V|_{2f}(x_0, y_0)}{V_{0|2f}}$  and  $\frac{\Delta V|_f(x_0, y_0)}{V_{0|f}}$  quantities can be computed using the expressions in Equation 2.16. They are plotted in Figures 2.6a and 2.6b using the previously defined Airy profile, centered at  $(0, 0)$ , as a function of the average position of the nanoparticle  $(x_0, y_0)$ . These images correspond to the theoretical SMS signal for a single punctual nanoparticle obtained through the spatial scanning of the surface of the sample. For this computation the values used for the spatial modulation and FWHM of the light beam were similar to the experimental values ( $\delta_y = 300$  nm and  $d_{FWHM} = 430$  nm). In Figure 2.6a, the SMS signal at frequency  $f$  presents two identical lobes along the  $y$  axis (direction of modulation) with opposite signs. In contrast, the signal at  $2f$  is characterized by a central peak with maximum amplitude and two

lower negative lobes on each side of it. The position of the nanoparticle coincides with a signal maximum in this case, in contrast with a vanishing at  $f$ , making the demodulation at  $2f$  the most practical one and thus the chosen configuration in our experiments.

In order to link the SMS signal  $\frac{\Delta V|_F}{V_0|_F}$  to the extinction cross-section of the nano-object  $\sigma_{ext}$ , a response function  $R(F, \delta_y, d_{FWHM}, x_0, y_0)$  is defined as:

$$\frac{\Delta V|_F}{V_0|_F} = \sigma_{ext} * R(F, \delta_y, d_{FWHM}). \quad (2.20)$$

Its expression depends on the operating frequency  $F$ , the amplitude of the spatial modulation  $\delta_y$ , the FWHM of the light beam  $d_{FWHM}$ , and the position of the nanoparticle relatively to the beam  $(x_0, y_0)$ .

For spectroscopy purposes, the proportionality coefficient  $R(F, \delta_y, d_{FWHM})$  between the SMS signal  $\frac{\Delta V|_F}{V_0|_F}$  measured for a laser beam centered on the investigated nanoparticle  $((x_0, y_0) = (0, 0))$  and the extinction cross-section  $\sigma_{ext}$  of this nanoparticle must be known. According to Equation 2.16, this coefficient writes, for  $F = 2f$  (the only configuration used in our spectroscopy measurements):

$$R(2f, \delta_y, d_{FWHM}) = \frac{0.8316\pi}{d_{FWHM}^2} \frac{1}{T} \int_{-\frac{T}{2}}^{\frac{T}{2}} \frac{I(0, \delta_y \sin(2\pi ft))}{I_0} \cos(2\pi(2f)t) dt \quad (2.21)$$

The integral can also be written, using the Mathematica software, as:

$$\begin{aligned} & \frac{1}{T} \int_{-\frac{T}{2}}^{\frac{T}{2}} \frac{I(0, \delta_y \sin(2\pi ft))}{I_0} \cos(2\pi(2f)t) dt = \\ & \left[ {}_2F_3 \left( 0.5, 1.5; 1, 2, 3; -10.45 \frac{\delta_y^2}{d_{FWHM}^2} \right) - {}_2F_3 \left( 1.5, 1.5; 2, 2, 3; -10.45 \frac{\delta_y^2}{d_{FWHM}^2} \right) \right], \end{aligned} \quad (2.22)$$

where  ${}_pF_q(a_1, \dots, a_p; b_1, \dots, b_q; z)$  are the generalized hypergeometric functions [71], leading to an analytical expression of the response function:

$$\begin{aligned} R(2f, \delta_y, d_{FWHM}) = & \\ & \frac{0.8316\pi}{d_{FWHM}^2} \left[ {}_2F_3 \left( 0.5, 1.5; 1, 2, 3; -10.45 \frac{\delta_y^2}{d_{FWHM}^2} \right) - {}_2F_3 \left( 1.5, 1.5; 2, 2, 3; -10.45 \frac{\delta_y^2}{d_{FWHM}^2} \right) \right]. \end{aligned} \quad (2.23)$$

As a side note, in the case of a Gaussian profile, whose intensity profile can be written as:

$$I_{Gaussian}(r) = I_0 \exp\left(-\frac{2r^2}{w^2}\right), \quad (2.24)$$

with  $I_0 = \frac{2P_0}{\pi w^2}$  and  $w$  the Gaussian width, linked to its Full Width at Half-Maximum  $d_{FWHM}$  through  $w = d_{FWHM}/\sqrt{2 \ln 2}$ , the corresponding response function can be analytically computed and is expressed as:

$$R_{Gaussian}(2f, \delta_y, d_{FWHM}) = \frac{4 \ln 2}{d_{FWHM}^2} J_1 \left( 2 \ln 2 \frac{\delta_y^2}{d_{FWHM}^2} \right) \exp\left(-2 \ln 2 \frac{\delta_y^2}{d_{FWHM}^2}\right). \quad (2.25)$$

The next section will illustrate, via Figure 2.9, the minor differences in the response functions resulting from the precise light beam profile.

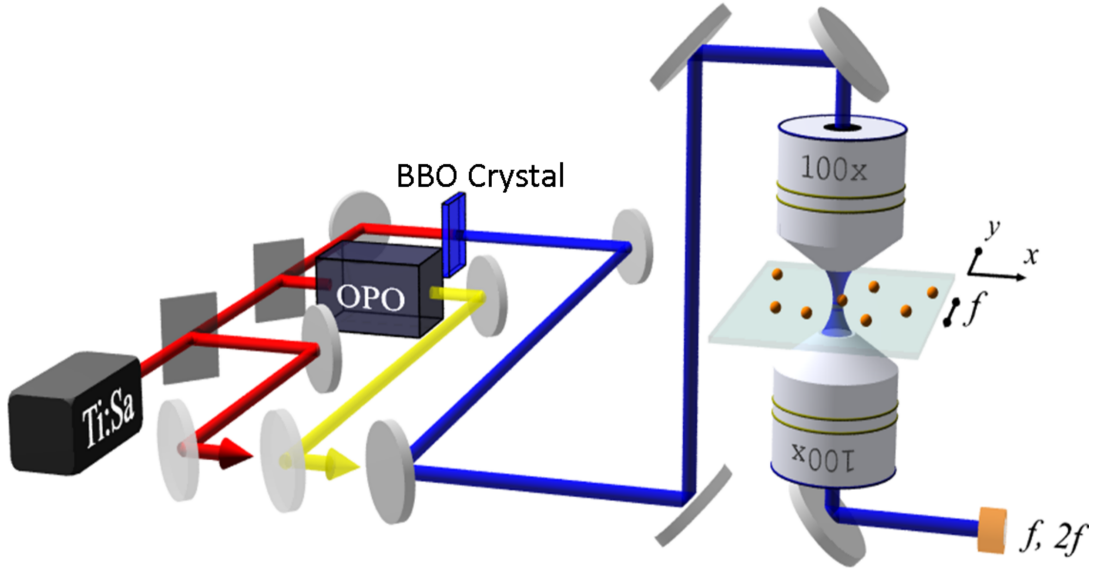


**Figure 2.7 – Schematic of the experimental configuration of the light sources used for SMS measurements.** In SMS configuration, movable mirrors allow to select one of the three available light sources.

### 2.2.2.2 Experimental setup and calibration

The SMS experimental setup used in this work consists of a manual XY stage allowing to position the sample, a solid substrate on which the nano-objects are present, in the horizontal  $(x, y)$  plane. This coarse motion is complemented by a XY piezoelectric stage with a  $100 \times 100 \mu\text{m}^2$  window range and 0.3 nm spatial resolution. A piezoelectric actuator is used to produce the spatial modulation of the sample in the  $y$  direction with tunable amplitude and frequency (typically  $f = 1.5$  kHz and  $\delta_y \approx 300$  nm in our experiments). In order to guarantee a selective illumination of a single nanoparticle by a strongly focused laser beam a  $\geq 2 \mu\text{m}$  minimal distance from other nano-objects is necessary. A laser beam, with wavelength in the 375-1040 nm range and produced by one of the three aforementioned sources (see Section 2.2.1 and Figure 2.7), is focused on the surface of the sample using a 100X apochromatic infinity-corrected objective of numerical aperture  $N.A. = 0.95$ . The incident beam is also enlarged by a telescope before the objective to obtain a quasi plane wave at the entrance pupil of the objective. In this configuration the intensity profile in the focal plane is an Airy profile with a FWHM  $d_{FWHM}$  close to the theoretical diffraction limit, which corresponds to:

$$d_{FWHM} = 0.515 \frac{\lambda}{N.A.} \approx 0.55\lambda, \quad (2.26)$$

with  $\lambda$  the wavelength of the light beam. Additionally, another piezoelectric actuator mounted on the focusing objective allows to precisely set the vertical position ( $z$  axis) of the focal plane of the incident beam.

After transmission through the sample the laser beam is collected by a second objective with 100X magnification and numerical aperture  $N.A.' = 0.75$  smaller than  $N.A.$ . Finally, the collected light is sent to an avalanche photodiode and the measured signal is demodulated by a

lock-in amplifier at frequency  $F = 2f$  while its average value is measured by a digital multimeter (see Figure 2.4). These signals are then sent to a computer to give access to the instantaneous value of  $\left| \frac{\Delta V|_{2f}}{V_{0,DMM}} \right|$ , which is converted into  $\left| \frac{\Delta V|_{2f}}{V_0|_{2f}} \right|$  via the  $\alpha_{SMS}$  coefficient and Equation 2.18 before being saved in data files.

The detection of single nanoparticles is achieved through a combination of the scanning of the sample of the surface using the XY piezoelectric stage and preliminary identification via microscopy images (Scanning or Tunneling Electronic Microscopy). An example of an experimental SMS 2D map, obtained for a single gold nanodisk, can be seen in Figure 2.8a.

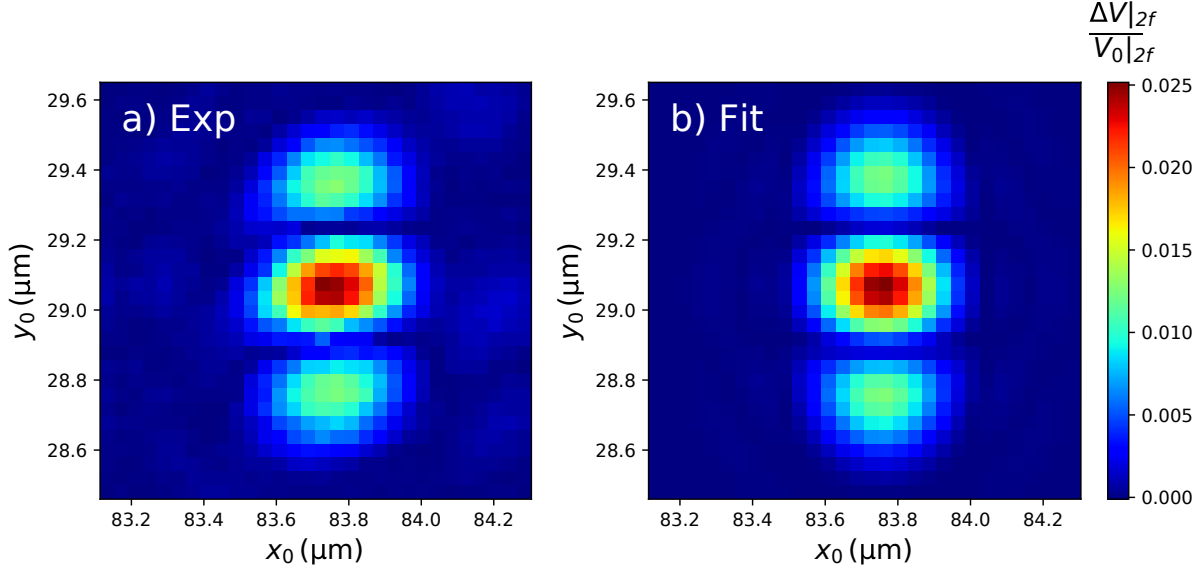


**Figure 2.8 – Fit of the 2D SMS scan of a nanoparticle.** a) Experimental SMS scan of a single gold nanodisk with a diameter  $D \approx 100$  nm and height  $h \approx 10$  nm for a laser beam with a  $\lambda = 410$  nm wavelength. b) Fit of experimental scan a) through the numerical evaluation of  $\frac{\Delta V|_{2f}}{V_0|_{2f}}(x_0, y_0)$  from Equation 2.16 with a fixed  $\delta_y = 300$  nm value and  $d_{FWHM}$  left as a free parameter (leading to a fitted value  $d_{FWHM} = 280$  nm). Both images share the same color code.

Once a single nano-object is localized its extinction cross-section for a given wavelength and polarization (controlled through the use of a wire-grid polarizer allowing to tune the direction of linear polarization of the light beam) can be obtained by measuring the value of the SMS signal with the nanoparticle at the center of the beam,  $\frac{\Delta V|_{2f}}{V_0|_{2f}}(0, 0)$ , and converting the measured signal into  $\sigma_{ext}$  using the response function  $R(2f, \delta_y, d_{FWHM})$  (the calibration of which is described below). The extinction cross-section of the nanoparticle is thus obtained via

$$\sigma_{ext} = \frac{\frac{\Delta V|_{2f}}{V_0|_{2f}}(0, 0)}{R(2f, \delta_y, d_{FWHM})}, \quad (2.27)$$

allowing to perform experimental measurements of the extinction spectra of single nanoparticles (polarization-dependent extinction spectra of single nanodisks will be presented in the next chapter).

The expression for the experimental response function in Equation 2.27 depends on two parameters : the amplitude of the spatial modulation  $\delta_y$  and the FWHM of the laser beam in the plane of the nanoparticle  $d_{FWHM}$ .

In order to determine them, SMS images of a small nano-object were acquired with different wavelengths. These 2D maps were then fitted using the theoretical expression of the SMS signal  $\frac{\Delta V|_F}{V_0|_F}$  (see Equation 2.16) with  $\delta_y$  and  $d_{FWHM}$  left as free parameters. In this context the FWHM  $d_{FWHM}$  depends linearly on the wavelength through a coefficient

$$c = \frac{d_{FWHM}}{\lambda} \quad (2.28)$$

(see Equation 2.26), while  $\delta_y$  is a constant and was thus chosen to be a shared parameter between all fits. This calibration lead to  $\delta_y = 300$  nm and  $c_{Ti:Sa} = 0.66$ . Distinct values of the last coefficient were obtained for the two other light sources used in the experiments:  $c_{OPO} = 0.70$  and  $c_{BBO} = 0.75$ . These are relatively close to the diffraction limit one,  $c_{th} = 0.55$ , except for the blue range where optical aberrations begin to have a significant impact on the light beam. Additionally, fits of SMS images of a small nanoparticle were regularly performed at different wavelengths with a fixed  $\delta_y = 300$  nm (operating with a fixed piezoelectric voltage of 0.4 V and at modulation frequency  $f = 1.5$  kHz) and  $d_{FWHM}$  left as a free parameter in order to take into account changes of the  $c$  coefficient linked to a modification of the light beam (e.g. by new lenses or different positioning of current lenses). An example of such fit is represented in Figure 2.8.

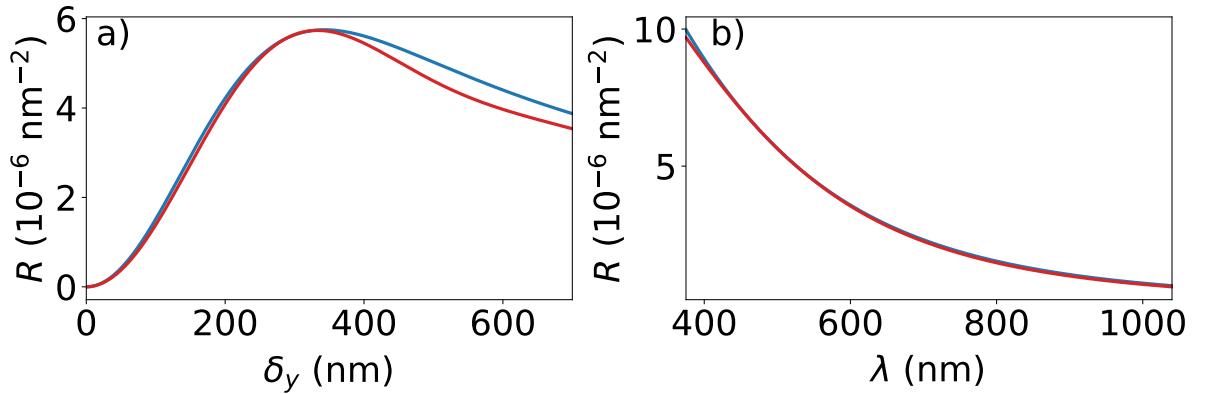


**Figure 2.9 – Response function  $R$  at operating frequency  $F = 2f$  dependence on a) the amplitude of spatial modulation  $\delta_y$  (for  $\lambda = 500$  nm and  $d_{FWHM} = 330$  nm) and b) on the wavelength of the laser beam  $\lambda$  for a Gaussian (blue line) and an Airy (red line) beam profile. The two curves were plotted using the experimental proportionality factor between FWHM and wavelength,  $c = 0.66$  (only the factor for the Ti:Sapphire light source was used for simplicity). b)  $\delta_y = 300$  nm was used for this plot.**

Figure 2.9a shows the response function  $R(2f, \delta_y, d_{FWHM})$  computed as a function of the amplitude of the spatial modulation  $\delta_y$  at  $\lambda = 500$  nm (and using  $c_{Ti:Sa} = 0.66$ ) for a Gaussian and an Airy beam profile. It presents a maximum around  $\delta_y \approx d_{FWHM}$  that consequently depends on the wavelength. The  $\delta_y = 300$  nm value used in all experiments corresponds to

an optimum of the response function for  $\lambda = 500$  nm but it provides good signal values for all the used wavelength range. Moreover, the response function  $R$  is plotted as a function of  $\lambda$  for Gaussian and Airy profiles in Figure 2.9b. It presents a decreasing behavior at increasing wavelengths : as the raw SMS signal must be divided by this function in order to obtain the extinction cross-section  $\sigma_{ext}$  (see Equation 2.27), this means that SMS is more sensitive to the extinction cross-section at shorter wavelengths, which is related to the smaller sizes of focused light beam in this range.

The uncertainty about the determination of the response function  $R$ , combined with the one coming from experimental measurements, lead to an estimated 10% uncertainty on the measured extinction cross-section  $\sigma_{ext}$  values. However, this uncertainty has a weak impact on the positions and widths of the LSPR of nanoparticles, as it similarly affects measurements at different wavelengths.

## 2.2.3 Single particle ultrafast time-resolved pump-probe spectroscopy

### 2.2.3.1 Principle

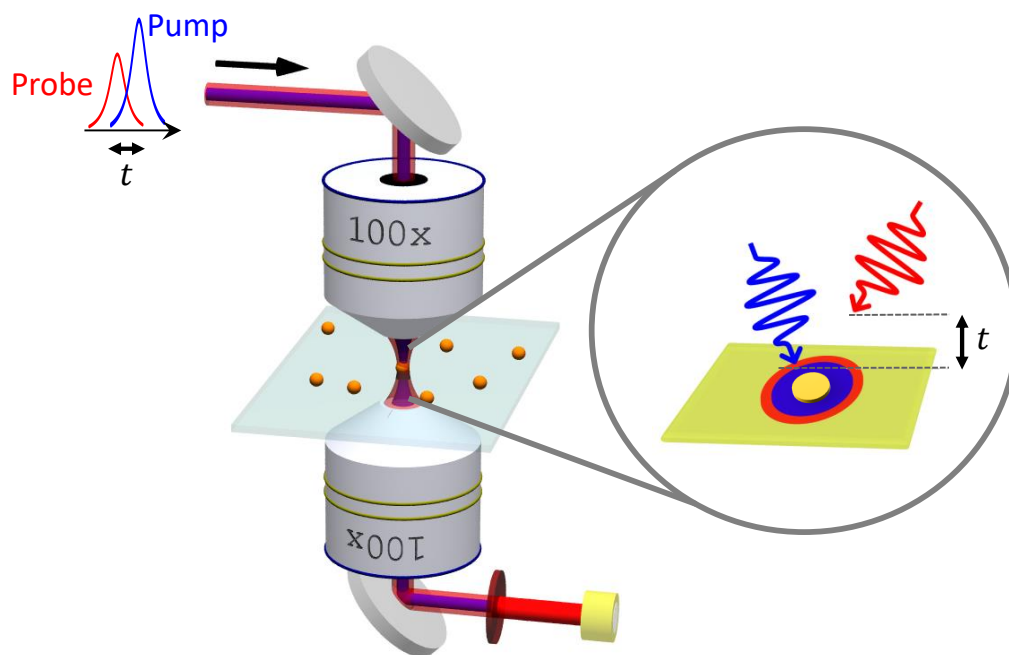


**Figure 2.10 – Principle of single-particle time-resolved spectroscopy (pump-probe technique).** Two strongly focused and spatially superimposed but temporally shifted pulsed laser beams are used. First, a pump pulse (in blue) excites the nanoparticle. Then a probe pulse (in red), whose temporal delay is controlled by a mechanical delay line, allows to monitor the relaxation processes induced by the initial excitation by the pump through the measurement of the variations of transmission of the second beam.

Figure 2.10 presents the general principle of a pump-probe experiment in a transmission

and single-particle configuration [9, 10]. In such single-particle time-resolved experiment two femtosecond laser beams are strongly focused and spatially superimposed on a single nano-object. A first light pulse, the pump pulse, excites the nanoparticle and induces different ultrafast relaxation mechanisms (see Chapter 1 Section 1.2.3) which produce temporal variations of the extinction cross-section of the nano-object. Then a second pulse, the probe pulse, reaches it after a controllable time delay  $t$  and allows to probe the state of the system at instant  $t$  after the initial excitation. The study of the pump-induced variations of probe pulse transmission, which are linked to the temporal extinction cross-section changes  $\Delta\sigma_{ext}(t)$ , can thus provide information on the electronic, vibrational and thermal relaxation dynamics occurring in the system.

### 2.2.3.2 Experimental configuration

The setup used in our pump-probe experiments corresponds to a two-color pump-probe spectroscopy configuration (see Figure 2.11). The pump and probe beams were femtosecond pulsed lasers beams with the same repetition rate and of different wavelengths,  $\lambda_{pp}$  and  $\lambda_{pr}$ , respectively, and generated via the light sources described in Section 2.2.1. In particular, the output pulse train from the Ti:Sapphire oscillator was used to generate both the pump and probe beams by splitting it in two parts. In my thesis experiments on single gold nanodisks the first one was frequency-doubled using second harmonic generation (in a BBO crystal) to produce the pump beam ( $\lambda_{pp} = 375 - 520$  nm). This spectral range is in the domain of gold interband absorption, and thus allowing nanodisk excitation. The second part of the Ti:Sapphire light beam was either left unaltered ( $\lambda_{pr} = 690 - 1040$  nm) or converted into the OPO beam ( $\lambda_{pr} = 500 - 750$  nm) to produce the probe beam (allowing to probe nanodisks at wavelengths in the spectral domain of their LSPRs). The pump and probe beams were then injected in the same objectives as in the SMS experiments, and strongly focused on a single nanoparticle. SMS was used to achieve superposition of both beams on the nano-object and position it in the center of the focal spots (see next section for the detailed procedure). An edgepass filter was used to only select the transmitted probe beam, allowing it to reach the avalanche photodiode. A motorized linear translation stage was used to modify the length of the optical path of the probe beam and allowed to control the time delay  $t$  between the pump and probe pulses.

The experimentally measured quantity is the probe relative transmission change,  $\frac{\Delta Tr}{Tr}(t)$ , as a function of the time-delay  $t$  between the excitation of the nano-object by the pump pulse and the probing by the second pulse. This allows to quantitatively determine the temporal variations of the extinction cross-section of the nanoparticle,  $\Delta\sigma_{ext}(\lambda_{pr}, t)$ , through:

$$\frac{\Delta Tr}{Tr}(t) = -\frac{\Delta\sigma_{ext}(\lambda_{pr}, t)}{S_{pr}}, \quad (2.29)$$

with

$$S_{pr} = \pi \frac{d_{FWHM,pr}^2}{4 \ln 2} \quad (2.30)$$

the equivalent area of the probe beam (defined as  $S_{pr} = P_{0,pr}/I_{0,pr}$ ) for a Gaussian beam with FWHM  $d_{FWHM}$  [9]. In order to detect these variations with a sufficient sensitivity the pump beam was modulated at  $f_{chopper} = 30$  kHz using a mechanical chopper placed in the beam path (see Figure 2.11). The temporal variations of the transmitted probe beam,  $\Delta Tr$  induced by the modulated pump beam and detected by the avalanche photodiode, were demodulated at frequency  $f_{chopper}$  by the lock-in amplifier.

Similarly to the SMS technique, the two quantities composing the left side of equation 2.29 must be acquired through the same acquisition chain to avoid a dependence on illumination and detection parameters, e.g. by demodulation through the lock-in amplifier at frequency  $f_{chopper} = 30$  kHz. The normalized transmission changes  $\frac{\Delta T_r}{T_r}$  can then be expressed as:

$$\frac{\Delta T_r}{T_r} = \frac{\Delta V|_{f_{chopper}}}{V_0|_{f_{chopper}}} = \alpha_{PP} \frac{\Delta V|_{f_{chopper}}}{V_{0,DMM}} \quad (2.31)$$

with the  $\alpha_{PP}$  coefficient being defined as

$$\alpha_{PP} = \frac{V_{0,DMM}}{V_0|_{f_{chopper}}} = \frac{\pi}{\sqrt{2}} \frac{1}{g(f_{chopper})}, \quad (2.32)$$

an expression identical to the SMS case (Equation 2.17) and resulting from the same analysis.

Its theoretical value (for ideal photodiode and chopper) is  $\alpha_{PP-th} = 2.22$  (same as in the SMS case, see Equation 2.19). To determine its experimental value, one must measure the voltage output of the DMM for a probe beam without any modulation and divide it by the Fourier component at frequency  $f_{chopper}$  extracted by the lock-in amplifier from the probe beam modulated by a chopper at  $f_{chopper}$ . In practice, an  $\alpha_{PP-exp} = 2.55$  value was obtained (the higher value, as compared to  $\alpha_{SMS-exp} = 2.22$  (Equation 2.19), can be ascribed to the higher operating frequency in time-resolved measurements,  $f_{chopper} = 30$  kHz, as compared to the one used in SMS,  $F = 2f = 3$  kHz), leading to a decreased  $g(f)$  value in Equation 2.32.

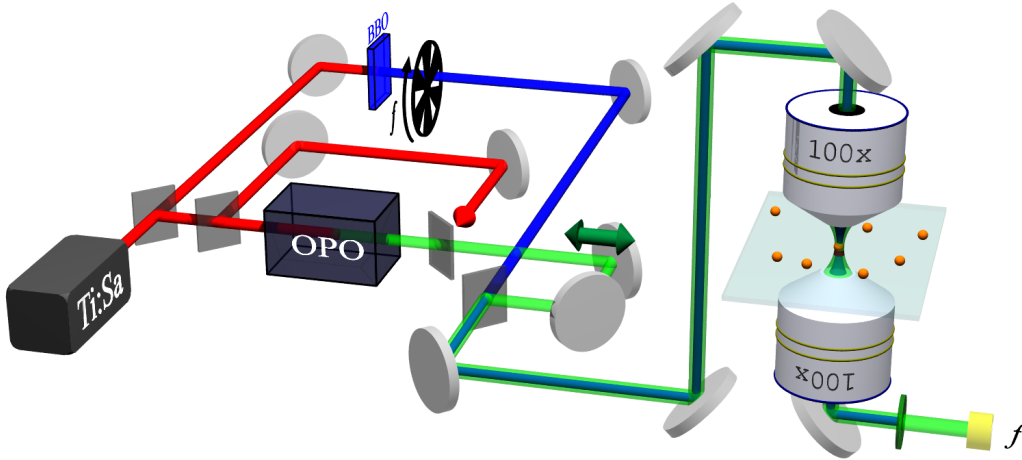


**Figure 2.11 – Schematic of the experimental configuration used in pump-probe measurements and the three light sources available.** In the measurements described in this manuscript the pump beam was the frequency-doubled output of the Ti:Sapphire oscillator (wavelength in 375-520 nm range), while the probe beam was either provided by the Ti:Sapphire laser (690-1040 nm) or generated by the OPO (500-750 nm).

### 2.2.3.3 Procedure for signal acquisition

In order to realize the sought time-resolved measurements on a single nano-object a precise procedure was followed. First, an initial alignment of the pump and probe beams was performed

in order to have them roughly aligned on the surface of the sample, close to the nanoparticle. The nanoparticle was placed at the center of the pump beam by optimizing the SMS signal with the XY piezo stage (the probe beam being blocked). Next, the transmitted light beam was switched from the pump beam to the probe beam. The final alignment of the probe beam onto the nanoparticle was achieved through the use of the micrometric adjustment screws of two injection mirrors controlling the beam angle and position. This allowed to optimize the associated SMS signal while also verifying the correct injection of the probe beam using its back-reflection on the sample, which was detected by a CCD camera. Thanks to these steps the axial superposition and centering on the nanoparticle of the two laser beams was achieved.

However, note that chromatic aberrations induced by the objective lead to focal planes that did not necessarily coincide. The  $x$  and  $y$  positions being already constrained, the vertical position  $z$  of the objective was set by maximizing the pump-probe signal, which usually corresponded to an intermediate position of the nano-object between the focal planes of the two beams. Instability of the XY piezo stage leads to a gradual shift of the position of the sample, which was corrected by frequent realignments. Fluctuations of air density along laser paths induced by the air conditioning system was also prevented by opaque tubes and plates protecting the beams.

Long-delay time-resolved signals were typically acquired with a 1 to 4 ps time step and a 100 ms lock-in time constant. The available time delay  $t$  window between the pump and probe beam was set by the length of the translation stage (15 cm) combined with multiples passes in the stage (3 round trips), leading to a 3 ns total time window. The repartition of the data points before and after temporal superposition of the pump and probe beams, corresponding to  $t = 0$ , was not symmetrical : in particular, there was a  $\sim 100$  ps window at negative time-delays for a Ti:Sapphire probe beam, and  $\sim 300$  ps window in the case of an OPO probe beam. Signals were averaged over multiple measurements in order to increase the signal-to-noise ratio (S/N). This ratio, which scales as  $\sqrt{n}$ , with  $n$  the number of individual measurements, was optimized by the acquisition of  $n = 3$  to 50 traces, depending on the signal amplitude. Finally, pump and probe beam powers have a different impact on the signal level. In particular, the relative probe beam transmission  $\frac{\Delta T_r}{T_r}(t)$  is independent from the probe power : as a consequence, the latter was tuned in a range ensuring that the measured voltages fell within the range of the linear regime of the avalanche photodiode. In contrast, the amplitude of the signal (after internal thermalization of the nanoparticle) is roughly proportional to the pump power : thus, the pump fluences used in experiments resulted from a compromise between an optimization of the signal and moderate increase of the temperature of the nano-object ( $\leq 20$  K), as higher temperature rises were previously seen to be associated with irreversible modifications of the nano-object's optical properties [25].

#### 2.2.3.4 Signal processing

As shown in Chapter 1 Section 1.2.3, the typical raw pump-probe signal exhibits an initial peak linked to the excitation and internal thermalization of the nanoparticle, oscillations associated to its acoustic vibrations and a decay at longer time scales related to the thermal cooling of the nanoparticle. An example of such signal is shown in Figure 2.12a.

The initial peak is taken as origin for the time axis as it roughly corresponds to a situation where the pump and probe pulses are synchronized and reach the nano-object at the same instant. As the initial peak won't be analyzed in this work, only the signal for long time delay

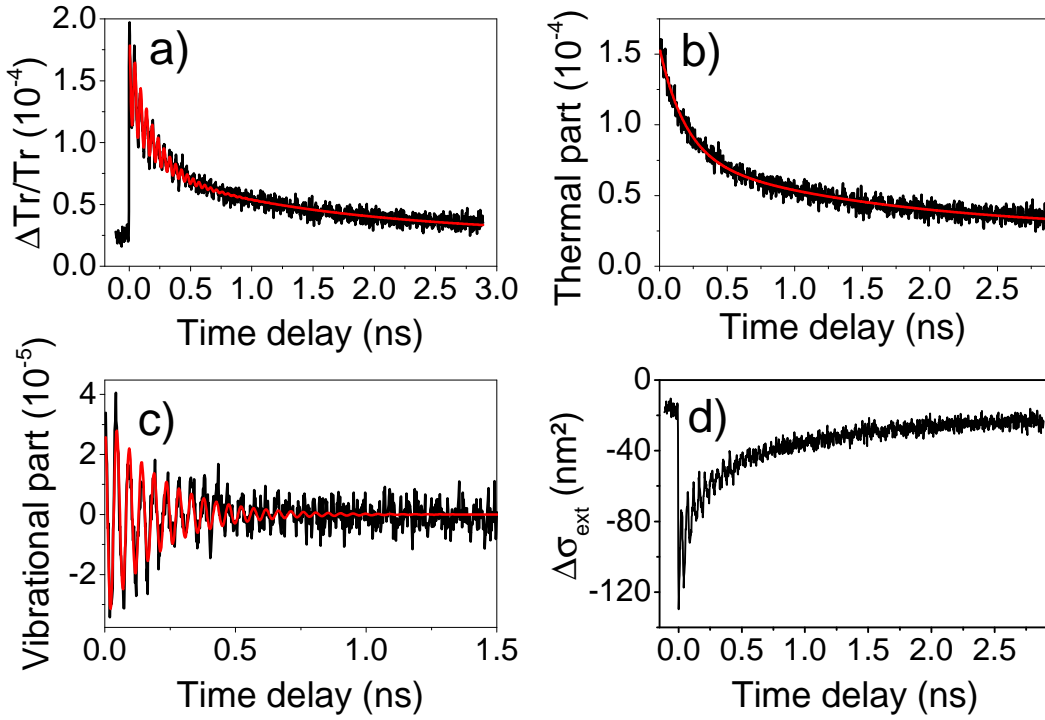


**Figure 2.12 – Fitting of experimental time-resolved signals and conversion to variations of extinction cross-section of the nano-object  $\Delta\sigma_{ext}(t)$ .** a) Raw transient variations of the transmission change  $\frac{\Delta Tr}{Tr}(t)$  for a single gold nanodisk, with diameter  $D \approx 100$  nm and  $h \approx 10$  nm, supported on a 40 nm thick  $\text{SiO}_2$  membrane, measured with  $\lambda_{pp} = 385$  nm and  $\lambda_{pr} = 770$  nm pump and probe wavelengths (black line). The red line corresponds to a fit of the raw signal after  $t = 4$  ps (e.g. after the nanodisk internal thermalization) with the function defined in Equation 2.33, with in this case  $N_{th} = 2$  and  $N_{vib} = 1$ . b) Raw signal from a) to which the oscillatory part of the total fit was subtracted, thus extracting the thermal part (black), and its biexponential fit (red) c) Raw signal from a) to which the two decaying exponentials of the total fit were subtracted, leading to the isolation of the contribution of the acoustic vibrations (black), and its fit by a damped sinusoid with period  $\approx 48$  ps and damping time  $\approx 203$  ps (red). d) Temporal variations of extinction cross-section  $\Delta\sigma_{ext}$  computed from the raw transmission changes  $\frac{\Delta Tr}{Tr}(t)$  via Equation 2.29).

$t \geq 5$ -20 ps (e.g. after complete internal thermalization of the nano-object) will be considered in the following. This signal is fitted by the sum of 2-4 exponential decays, linked to the thermal cooling of the nano-object, and 0-2 damped sinusoids, each associated to the contribution of a different vibrational mode. The total fit function is thus expressed as:

$$f_{fit}(t) = f_{fit-th}(t) + f_{fit-vib}(t) = \sum_{i=1}^{N_{th}} A_i e^{-t/\tau_i^{th}} + \sum_{j=1}^{N_{vib}} B_j e^{-t/\tau_j^{vib}} \sin\left(\frac{2\pi}{T_j} t + \phi_j\right) \quad (2.33)$$

with  $A_i$  and  $B_j$ ,  $\tau_i^{th}$  and  $\tau_j^{vib}$  the thermal and vibrational amplitudes and time constants, respectively,  $T_j$  and  $\phi_j$  the period and the phase of the vibrational modes. The multi-exponential

expression used to reproduce the thermal component is not associated to a physical model (a numerical modeling of these dynamics will be presented in Chapter 3) and was only used here as it allows a good reproduction of experimental signals (provided  $N_{th}$  is sufficiently high), thus enabling the separation of its thermal and acoustic components, which will be extensively analyzed in Chapters 3, 4 (thermal component), and 5 (vibrational component). The amplitudes ( $A_i$  and  $B_j$ ) deduced from the fitting procedures are strongly dependent on probe wavelength, as discussed in Chapters 4 and 5. In contrast, the periods ( $T_j$ , typically of the order of 40 ps in my experiments) and damping times ( $\tau_j$ , typically in the 100-500 ps range) of vibrational modes are intrinsic characteristics of these modes, and do not display a dependence on probe wavelength.

The thermal component composing the raw time-resolved signal is obtained by subtracting from it the damped sinusoids defined in the total fit function  $f_{fit}(t)$ . Similarly, the vibrational component, which may be composed of several acoustic modes, is extracted by subtracting to the raw pump-probe signal the sum of the decaying exponentials. The total fit as well as the extracted thermal and vibrational components are illustrated in Figure 2.12 in the case of a raw time-resolved signal obtained for a single gold nanodisk deposited on a 40 nm thick SiO<sub>2</sub> membrane.

The measured relative transmission changes  $\frac{\Delta T_r}{T_r}(t)$  can be converted in transient extinction changes  $\Delta\sigma_{ext}(t)$  (Equation 2.29), as shown in Figure 2.12d for the total signal.

### 2.2.3.5 Characterization of pump and probe beams

A quantity that will be relevant for the results presented in Chapter 3, 4, and 5 is the initial heating of the nanoparticle induced by a pump pulse. It depends on the pump beam characteristics, that needs to be determined, as well as the physical properties of the studied nano-object.

The first quantity needed is the average power of the pump beam  $P_{pp}$  seen by the nanoparticle: as the values used in the experiments were quite low, it was measured via a powermeter placed right before the focusing objective. Ideally, the powermeter should have been placed between the two objectives (to measure the power on the sample) but it could not be done due to, first, the size of the powermeter and of the sample-holder and, secondly, the transmission coefficient of the focusing objective  $c_{obj}$  (determined at higher powers without any sample) that greatly reduces the already low power. The transmission coefficient of the focusing objective was experimentally measured in the 390-450nm range and varied from 0.3 to 0.7. This attenuation can be explained by a size of the pump spot larger than the entrance pupil of the top objective, as needed for an optimal light focusing.

Practically, the average power of the pump was measured thanks to the powermeter in the presence of the mechanical chopper (at a frequency  $f_{chopper} = 30$  kHz) present on the pump path (to avoid frequent mounting/unmounting of the chopper required for time-resolved studies). One must be careful about the power that the studied nanoparticle is actually submitted to. The measured dynamics occur in the range of picoseconds to nanoseconds while the temporal modulation accomplished through the chopper occurs every  $1/f_{chopper} = 33$  ms : as a result the power seen by the nanoparticle corresponds to a pump beam not impacted by the chopper. The associated coefficient linking the effect of the chopper at the frequency  $f_{chopper} = 30$  kHz on the

pump power can thus be defined as:

$$c_{chopper} = \frac{P_{no-chopper}}{P_{chopper}} \quad (2.34)$$

where  $P_{no-chopper}$  and  $P_{chopper}$  are the powers measured with a powermeter right before the top objective respectively without and with the mechanical chopper. An ideal chopper should block the pump beam half of the time and lead to  $c_{chopper-th} = 2$  but in practice the chopper is not ideal and the experimental value of  $c_{chopper}$ , obtained by comparing the powers measured by the powermeter with and without the chopper in the beam path (as in Equation 2.34), is found to be around 2.55.

Thus, the pump power seen by the nanoparticle can be written as:

$$P_{pp} = P_{chopper} c_{chopper} c_{obj}. \quad (2.35)$$

Another important characteristic of the pump beam is its area  $S_{pp}$  in the XY plane: as seen in section 2.2.2 the SMS technique provides 2D maps of the studied nanoparticle that contains the characteristics of the laser beam shining the nano-object. In particular these maps give access to the Full Width at Half-Maximum (FWHM)  $d_{pp}$  of the beam : its equivalent area (defined as  $S_{pp} = P_{pp}/I_{0,pp}$ ) can then be calculated (for a Gaussian beam) through

$$S_{pp} = \frac{\pi d_{pp}^2}{4 \ln 2}. \quad (2.36)$$

SMS maps with the pump beam were acquired alongside time-resolved measurements in order to have a measurement of the pump area for each configuration. As a reminder, the probe area was also necessary to convert the raw measurements into the variations of the extinction cross-section of the nano-object, using the previous formula  $\frac{\Delta Tr}{Tr} = -\frac{\Delta \sigma_{ext}(\lambda_{pr})}{S_{pr}}$ , and was also systematically deduced from SMS maps using 2.36.

The fluence of the pump beam  $F_{pp}$ , corresponding to the optical energy delivered per unit area of a single pulse, can then be deduced from the previous quantities via

$$F_{pp} = \frac{T_{rep} P_{pp}}{S_{pp}} \quad (2.37)$$

with  $T_{rep} = 1/f_{rep} = 1/(80 \text{ MHz}) = 12.5 \text{ ns}$  the repetition period of the pulsed laser. The volumetric density of energy absorbed by the nanoparticle  $u_{abs}$  can then be estimated thanks to

$$u_{abs} = \frac{\sigma_{abs}(\lambda_{pp}) F_{pp}}{V} \quad (2.38)$$

where  $\sigma_{abs}(\lambda_{pp})$  is the absorption cross-section of the nano-object at the pump wavelength,  $F_{pp}$  the fluence previously calculated and  $V$  the volume of the nanoparticle.  $\sigma_{abs}(\lambda_{pp})$  and  $V$  are deduced from optical simulations leading to a good reproduction of SMS-measured extinction spectra. Moreover,  $u_{abs}$  can be linked to the initial heating of the nanoparticle (after internal thermalization)  $\Delta T_0$  through  $u_{abs} = c_{Au}(T_f - T_0) = c_{Au} \Delta T_0$  with  $c_{Au} = 2.5 \text{ J cm}^{-3} \text{ K}^{-1}$  the volumetric heat capacity of bulk gold and  $T_f$  the excitation temperature of the internally thermalized nanoparticle (after internal electron-lattice relaxation). Combining Equations 2.37 and 2.38, one can estimate the initial temperature increase of the nanoparticle following the excitation by a pump pulse by

$$\Delta T_0 = \frac{\sigma_{abs}(\lambda_{pp}) T_{rep} P_{pp}}{c_{Au} V S_{pp}}. \quad (2.39)$$

In the experiments, the fluence  $F_{pp}$  was of the order of a few  $\text{J m}^{-2}$  and the initial heating of the nanodisk of the order of 10-20 K.

## 2.3 Optical and thermal modeling

In this work, the experimental study of nanoparticles, specifically single gold nanodisks supported by a solid transparent substrate, was completed by the computation by Finite-Element Method (FEM) of both the optical response of a single nanodisk and the thermal dynamics induced by its pulsed excitation. This work was developed in our group by Aurélien Crut based on a commercial software (COMSOL).

FEM is based on approximating the exact solution of a problem involving partial differential equations within a finite-dimensional vector space. The approximate solution is expressed as a combination of basis functions defined over finite elements, which are small, discrete subdomains of the problem's domain. The coefficients of these basis functions are determined by solving a finite system of linear equations derived from the problem's governing equations and boundary conditions.

### 2.3.1 FEM optical modeling

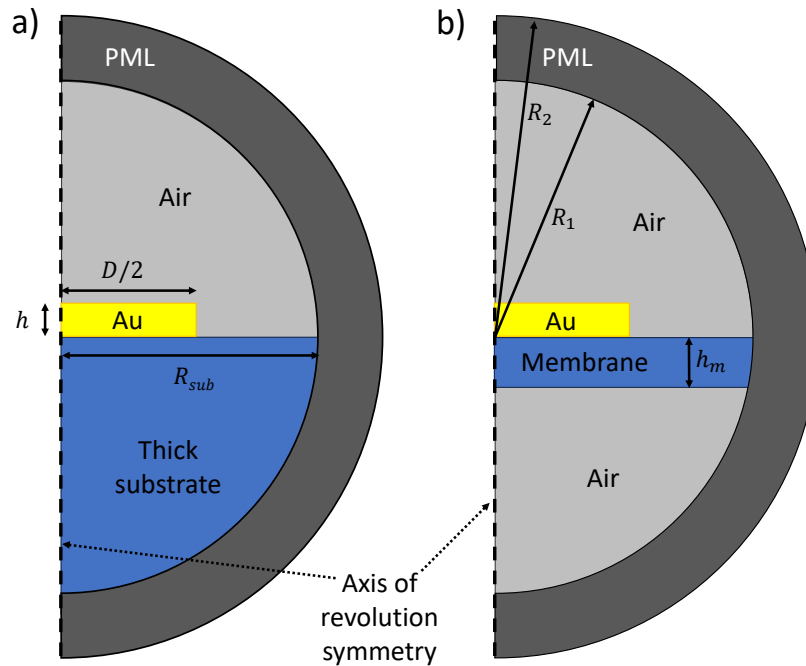


**Figure 2.13 – 2D view of the geometry used in the optical FEM calculations.** a) Single gold nanodisk with half-space substrate under it, with a radius  $R_{sub}$ , and air on top. b) Single gold nanodisk supported by a membrane of thickness  $h_m$  and surrounded by air both under and on top of it. In both cases the gold nanodisk is modeled as a cylinder characterized by a diameter  $D$  and thickness  $h$ . A perfectly-matched layer (PML), of internal radius  $R_1$  and external radius  $R_2$ , is placed at the border of the simulation domain.

In optical simulations, FEM is used to compute the electromagnetic field in and around the investigated nanoparticle. In this context the following steps are required prior to the calculation:

1. Definition of the geometry (and building of a mesh by the software).
2. Definition of the optical properties (dielectric function in particular) in all the specific geometry domains.
3. Definition of the incident electromagnetic wave.
4. Definition of the boundary conditions.

The procedure followed by the program is then to solve Maxwell's equations in space with the indicated boundary conditions. This calculation is performed successively for multiple wavelengths of the incident light. In the context of optical FEM one must be careful about the definition of the mesh, as the finite elements need to be small enough. Mesh elements must be significantly smaller than wavelength in homogeneous regions. The mesh must also allow to accurately describe the rapid changes of the electromagnetic fields occurring around the sharp features of the geometry.

The geometry used in simulations consisted in two versions corresponding to the two categories of situations encountered in the experimental measurements:

- a single gold nanodisk surrounded by air and substrate half-spaces, shown in Figure 2.13a
- a single gold nanodisk supported by a membrane of thickness  $h_m$  and air above and below it, shown in Figure 2.13b.

In both cases the gold nanodisk was modeled as a perfect cylinder with a diameter  $D$  and height  $h$  and a Perfectly Matched Layer (PML) enclosing the simulation domain (typically with an interior radius  $R_1 = 300$  nm and external radius  $R_2 = 400$  nm) was used to avoid spurious effects associated to the reflection of electromagnetic waves at the border of the simulation domain. The material composing the substrate was alternatively sapphire,  $\text{SiO}_2$  or  $\text{Si}_3\text{N}_4$  depending on the investigated sample (see next chapter). A refractive index of 1 was used for the air, while the ones used for the different substrates can be found in Table 2.1.

Material	$n_m$
$\text{SiO}_2$	1.45
$\text{Si}_3\text{N}_4$	2.02
Sapphire $\text{Al}_2\text{O}_3$	1.33

**Table 2.1 – Refractive indices at room temperature of the materials composing the substrates used in experiments.**

As discussed in Chapter 1 Section 1.1.2, the dielectric function  $\epsilon = \epsilon_1 + i\epsilon_2$  of bulk gold in the visible/near-infrared range can be written as the sum of interband (ib) and intraband (Drude-like) components as [1, 7, 72]

$$\epsilon(\omega) = \epsilon^{ib}(\omega) + \epsilon^D(\omega) - 1 = \epsilon^{ib}(\omega) - \frac{\omega_p^2}{\omega(\omega + i\gamma)}, \quad (2.40)$$

with  $\omega_p$  the plasma frequency and  $\gamma$  the optical scattering rate of the conduction electrons ( $\hbar\omega_p = 9.01$  eV and  $\hbar\gamma \approx 70$  meV for bulk gold). In this work, we used bulk  $\omega_p$  and  $\epsilon^{ib}$  values (the latter being deduced from Johnson and Christy tables [17]) and  $\hbar\gamma$  values larger (typically by  $\approx 100$  meV) than the bulk gold value, as required to reproduce the Surface Plasmon Resonance widths measured on single nano-objects. This corresponds to taking into account additional non-radiative plasmon damping mechanisms in metal nano-objects as compared to the bulk metal case [73–76].

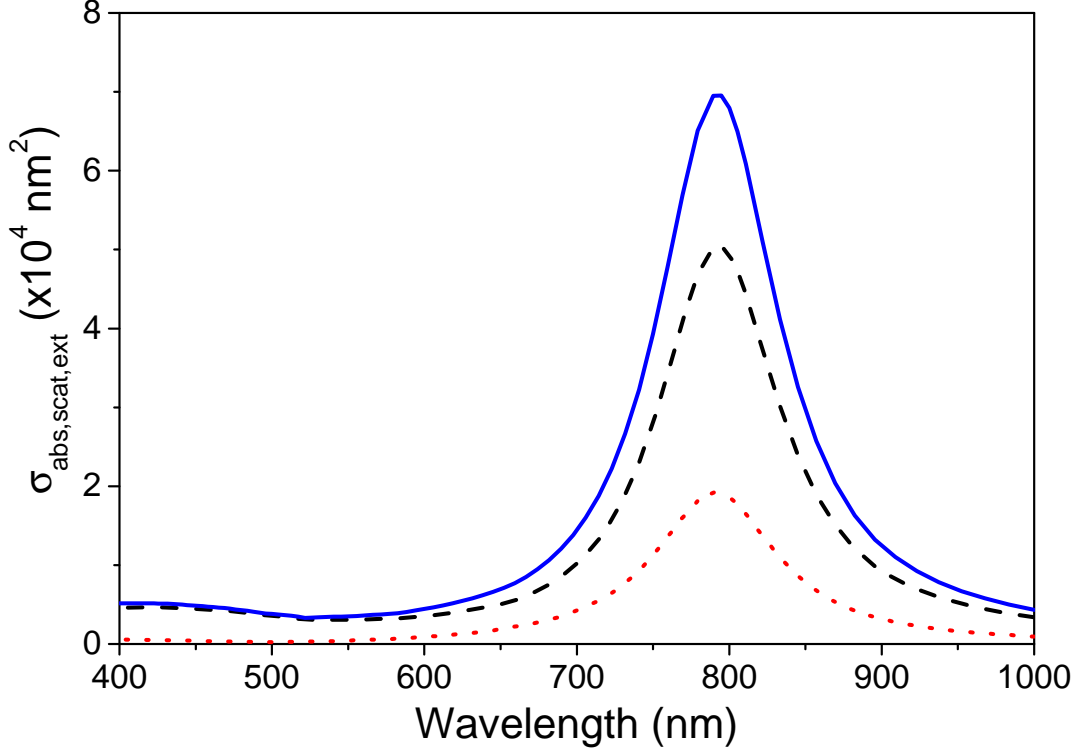


**Figure 2.14 – Absorption, scattered, and extinction cross-sections spectra computed for a single gold nanodisk supported on a 15 nm thick  $\text{Si}_3\text{N}_4$  membrane.** A gold nanodisk with a diameter  $D = 96.2$  nm and height  $h = 10.8$  nm is considered. A 87 meV broadening of  $\hbar\gamma$  as compared to its bulk value (see Equation 2.40) was used. Three quantities are represented : the absorption cross-section  $\sigma_{abs}$  (dashed black line), scattered cross-section  $\sigma_{scat}$  (dotted red line), and extinction cross-section  $\sigma_{ext}$  (full blue line). The Surface Plasmon Resonance is located around 790 nm.

Nanodisk illumination by a linearly polarized plane wave  $\vec{E}_0$  arriving with normal incidence was considered. As presented in Chapter 1 Section 1.2.1, the total electric field  $\vec{E}_{tot}$  considered in the simulation domain is the sum of the incident field  $\vec{E}_0$ , defined by the user and solution of Maxwell’s equations in the absence of the nanodisk, and of the field scattered by the nanodisk  $\vec{E}_{scat}$ . The program then calculates the internal field in the nanodisk and the scattered field  $\vec{E}_{scat}$ , from which absorption and scattering cross-sections are deduced. In particular, the integration of the Joule dissipated power density over the nanodisk volume  $V$  gives access to the absorption

cross-section  $\sigma_{abs}$  through:

$$\sigma_{abs} = \frac{1}{I_0} \iiint_V \text{Re}(\vec{j} \cdot \vec{E}_{tot}^*) dV \quad (2.41)$$

with  $I_0$  the intensity of the transmitted plane wave at the position of the particle and  $\vec{j}$  the current density in the metal (also computed by the FEM software).

Moreover, integrating the flux of the Poynting vector of the scattered field through a surface  $A$  enclosing the nanodisk gives access to the scattered extinction cross-section  $\sigma_{scat}$ :

$$\sigma_{scat} = \frac{1}{I_0} \oint_A \frac{1}{2} \text{Re}(\vec{E}_{scat} \times \vec{H}_{scat}^*) \cdot d\vec{S}. \quad (2.42)$$

In practice a closed spherical surface located between the nanodisk and the PML is chosen for  $A$ .

Finally, the extinction cross-section  $\sigma_{ext}$  is given by the sum of the previously computed absorption cross-section and the scattered cross-section (Equation 1.35 in Chapter 1 Section 1.2.1). An example of the absorption, scattering, and extinction spectra of a single gold nanodisk supported on a 15 nm thick  $\text{Si}_3\text{N}_4$  membrane (well reproducing that measured for one of the investigated nanodisks) is represented in Figure 2.14. For this system, the absorption cross-section is dominant compared to the scattered one, in contrast to the case of larger nanodisks.

Additionally, it is also possible to compute the sensitivity of the extinction cross-section of the nanodisk to the dielectric functions of gold,  $\frac{\partial \sigma_{ext}}{\partial \epsilon_{1,2}}(\lambda_{pr})$ , and of the substrate  $\frac{\partial \sigma_{ext}}{\partial \epsilon_m}(\lambda_{pr})$  from the previous calculation. The strategy is to compute the extinction cross-section  $\sigma_{ext}$  for slightly modified  $\epsilon_{1,2,m}$  values and to deduce the  $\frac{\partial \sigma_{ext}}{\partial \epsilon_{1,2}}(\lambda_{pr})$  and  $\frac{\partial \sigma_{ext}}{\partial \epsilon_m}(\lambda_{pr})$  values by performing discrete derivation (see Chapter 4).

### 2.3.2 FEM thermal modeling

The cooling dynamics of the single gold nanodisk and its supporting substrate were also computed by FEM. In this context the procedure is the same as the one for optical FEM with the exception a few differences. Indeed, the thermal properties and heat sources need to be defined in the geometry domains. As before, the single gold nanodisk was described by a perfect cylinder with a diameter  $D$  and height  $h$ .

Heat diffusion in all materials was described by Fourier's law with a diffusion coefficient in each material (heat diffusivity  $\alpha$ ) equal to the ratio of its thermal conductivity  $\Lambda_m$  and volumetric heat capacity  $c_m$  (see Chapter 1 Section 1.3.2.1). The nanodisk-substrate interface was described by a thermal interface conductance  $G$ , left as a free parameter (see Kapitza resistance in Chapter 1 Section 1.3.1.1). The case of small variations of temperature is considered, allowing to neglect the temperature-dependence of the thermal properties of the materials.

Similarly to FEM optical modeling, two geometries were considered:

- a single gold nanodisk supported on a half-sphere substrate, shown in Figure 2.15a
- a single gold nanodisk supported by a membrane of thickness  $h_m$ , shown in Figure 2.15b.

Simulations were performed in 2D, exploiting the perfect rotational symmetry of the considered problems. In the case of the half-sphere substrate, thermal insulation boundary conditions were applied on the top of the substrate and constant temperatures conditions on the border of the simulation domain (at reference temperature  $T_{ref}$ ). In the case of a membrane, thermal

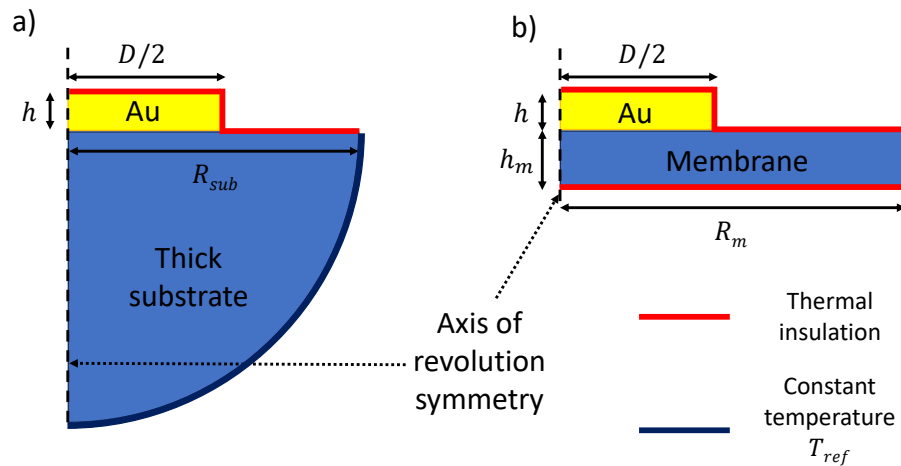


**Figure 2.15 – 2D geometry used in the thermal FEM calculations taking advantage of the revolution symmetry of the problem.** a) Single gold nanodisk with half-space substrate under it, with a radius  $R_{sub}$ . b) Single gold nanodisk supported by a membrane of thickness  $h_m$  and lateral extension  $R_m$ . In both cases the gold nanodisk is modeled as a cylinder characterized by a diameter  $D$  and thickness  $h$ . Boundary conditions for the half-sphere substrate and membrane are indicated in red and blue, corresponding to thermal insulation and to a constant temperature  $T_{ref}$ , respectively.

insulation boundary conditions were applied this time on the upper and lower circular bases of the cylindrical membranes and similar constant temperature ones (at reference temperature  $T_{ref}$ ) on their lateral surface. The boundary conditions at the lateral surfaces of the substrates allowed a thermal flux out of the simulation system, which is important for avoiding divergence of nanodisk temperature. In both cases, thermal insulation boundary conditions were applied on the upper and lateral sides of the gold nanodisk

The present model doesn't take into account several sources of heat dissipation much less efficient than conduction in the gold nanodisk and its substrate (see details in Chapter 1, Sections 1.3.1.2 and 1.3.1.3). First, it neglects heat dissipation to the surrounding air, a phenomenon whose efficiency is low for bulk systems (the convective heat transfer coefficient being of the order of  $10 \text{ W m}^{-2} \text{ K}^{-1}$  for natural convection in air, i.e., more than  $10^6$  times smaller than typical  $G$  values) but which may become more significant for micro- and nanometric systems [77] and has been previously demonstrated to influence the thermal dynamics of some suspended 2D systems [78–80]. Radiative heat transfer from gold to its environment was also not taken into account as its efficiency is even lower (radiative heat transfer coefficient of the order of  $1 \text{ W m}^{-2} \text{ K}^{-1}$ ).

Time domain and frequency domain calculations, described in the next sections, were used to modelize the thermal dynamics in the nanodisk and its supporting substrate or membrane resulting from different excitation processes. Both models used the geometries and boundary conditions previously described.

### 2.3.2.1 Time domain modeling (single nanodisk excitation)

The first type of FEM calculation is operated in the time domain to compute the spatially-dependent temperature rises in both a nanodisk and its supporting substrate from a single excitation of the nanodisk resulting from its sudden heating. The initial excitation of the gold nanodisk by a single pump pulse was transcribed as an initial temperature rise of the nanodisk  $\Delta T_{ini}$ . The extension of the substrate/membrane was chosen sufficiently large so that the temperature changes did not reach the boundaries in the simulated time-interval ( $R_{sub} = R_m = 1 \mu\text{m}$  in simulations, making the results weakly dependent on the choice of  $R_{sub}/R_m$ ).

### 2.3.2.2 Frequency domain modeling (multiple nanodisk excitations)

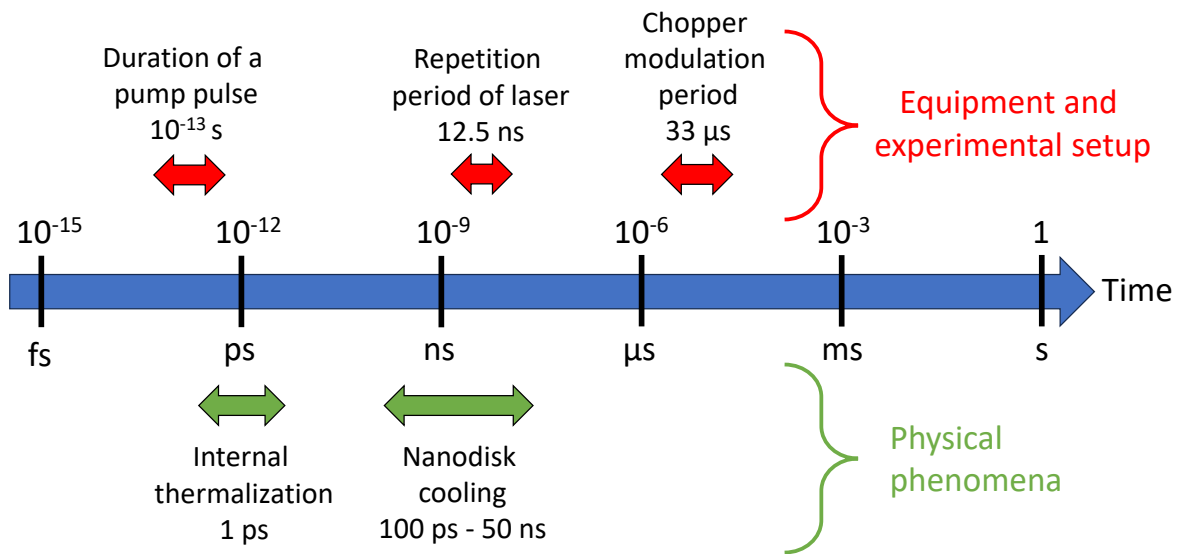


**Figure 2.16 – Schematic of the relevant timescales in time-resolved measurements.** In red, timescales linked to the equipment used and the experimental setup (characteristics of the laser and mechanical chopper) and, in green, the ones associated to the physical phenomena occurring in the gold nanodisk.

The nanodisk excitation process in our time-resolved experiments, described below by  $\tilde{q}(f)$  in Equation 2.43, involves several very different time scales, ranging from  $\approx 10^{-13}$  s (duration of pump pulses) to  $\approx 10^{-5}$  s (pump beam modulation, with a period  $T_{chopper} = \frac{1}{f_{chopper}} = 1/(30 \text{ kHz}) \approx 33 \mu\text{s}$ ) which are however not all relevant to describe the measured nanodisk temperature evolution. On the one hand, with modulation of the pump beam being performed at a low frequency (30 kHz), more than 2000 times smaller than the repetition frequency of the used laser source (80 MHz) in our experiments, its effect was neglected in the model. Time-resolved measurements were performed on a single gold nanodisk with different chopper frequencies in order to verify the absence of influence on the measured dynamics. The associated signals, measured at three different values of  $f_{chopper}$  and represented in Figure 2.17, clearly superpose and confirm that there was no significant effect on the measured dynamics, considering the level of noise present in these measurements, supporting the previous simplification.

On the other hand, with the duration of the used laser pulses ( $\approx 150$  fs) and that of internal nanodisk thermalization by energy exchanges between electrons and the ionic lattice (about 1 ps [64]) being both much smaller than the characteristic times of nanodisk cooling (of the order of a few hundreds of ps to several ns, see Chapter 1 Section 1.2.3), excitation by each pump pulse was supposed to be instantaneous.

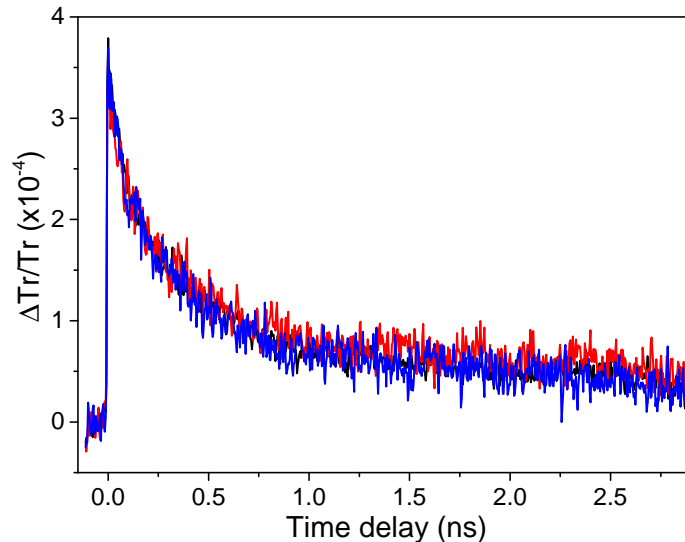


**Figure 2.17 – Raw temporal variations of transmission  $\frac{\Delta T_r}{T_r}$  for a single gold nanodisk with different values of the chopper frequency.** Blue, red, and black full lines correspond to time-resolved signals obtained with  $f_{chopper} = 15$  kHz, 20 kHz, and 30 kHz, respectively. The mean value at negative time delay of each signal was subtracted before plotting.

In most of the experiments described in this work, the time separating two successive pump pulses ( $T_{rep} = 12.5$  ns) is not sufficient for complete cooling of the nanodisks, in contrast with previous works in the FemtoNanoOptics group [25]. This gives rise to accumulation effects which can be adequately described only by considering the periodical character of the nanodisk excitation in our experiments. This was done by using a different modeling approach allowing, in the linear regime, computation of the thermal dynamics of a substrate-supported nanodisk for any time-dependent heating process. This approach was largely inspired by previous works in the field of time-domain thermoreflectance [3, 81, 82]. Its main idea consists in decomposing (by Fourier transform) the considered time-dependent excitation process as a sum of sinusoidal excitations with well-defined frequency and computing the associated thermal dynamics by summing the sinusoidal temperature evolutions induced by each of these individual sinusoidal excitations. The core of this approach is the calculation of the complex frequency-domain impulse response  $\tilde{h}(f)$  of the investigated system (here performed numerically, using FEM), whose modulus and argument respectively describe the amplitude and phase of the temperature oscillations at each point of the system with respect to a time-harmonic heating at frequency  $f$ .

The Fourier transform  $\Delta\tilde{T}(f)$  of the spatially-dependent thermal dynamics induced by any time-dependent excitation process  $q(t)$ , of Fourier transform  $\tilde{q}(f)$ , is then given by

$$\Delta\tilde{T}(f) = \tilde{h}(f)\tilde{q}(f), \quad (2.43)$$

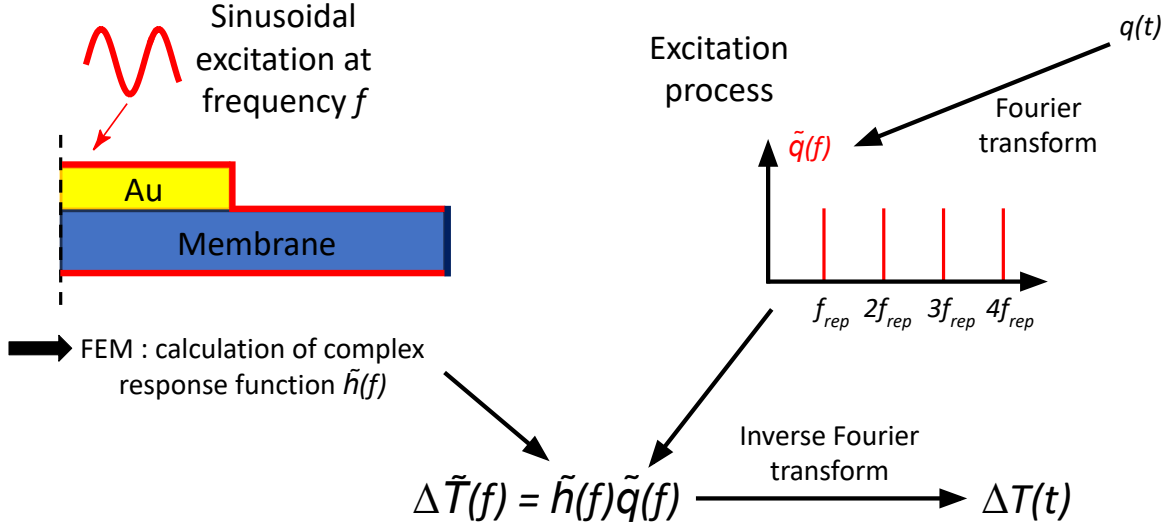


**Figure 2.18 – Modeling steps required to perform frequency domain computation of the cooling dynamics of a single gold nanodisk supported on a substrate.** The geometry and boundary conditions represented are identical to the ones in Figure 2.13. FEM calculations are used to deduce the amplitude and phase of the complex response function  $\tilde{h}(f)$  of the system for a sinusoidal thermal excitation at frequency  $f$ . The excitation process of the system in the frequency domain is  $\tilde{q}(f)$ , Fourier transform of the temporal excitation  $q(t)$ . The product of these two quantities give access to the Fourier transform of the thermal dynamics of the system  $\Delta\tilde{T}(f)$  resulting from the excitation process  $q(t)$ . Computing the inverse Fourier transform then allows to retrieve the temporal cooling dynamics of the system  $\Delta T(t)$ .

allowing deduction of the corresponding temporal dynamics  $\Delta T(t)$  by reverse Fourier transform.

In frequency-domain simulations, we considered a nanodisk excitation process described in the time domain by a periodic train of delta pulses, describing the light impulsive excitation at the repetition rate  $1/T_{rep}$  of the femtosecond laser:

$$q(t) \propto \sum_{n=-\infty}^{+\infty} \delta(t - nT_{rep}) \quad (2.44)$$

to which is associated the Fourier transform

$$\tilde{q}(f) \propto \sum_{n=-\infty}^{+\infty} \delta(f - nf_{rep}). \quad (2.45)$$

The combination of the frequency-domain impulse response  $\tilde{h}(f)$  of the nanodisk-substrate system with this excitation process  $\tilde{q}(f)$  thus allowed to compute the cooling dynamics of the nanodisk and in the substrate for a periodic excitation by pump pulses.

### 2.3.3 FEM thermo-optical modeling

It is possible to combine the previous FEM thermal and optical modeling in order to compute the transient optical response of the nanoparticle  $\Delta\sigma_{ext}(\lambda_{pr}, t)$  that depends on the cooling dynamics

of the nanodisk-substrate system. Such thermo-optical modeling is described in Chapter 4 Section 4.2.7.



# Chapter 3

## Cooling dynamics of deposited gold nanodisks

### 3.1 General context

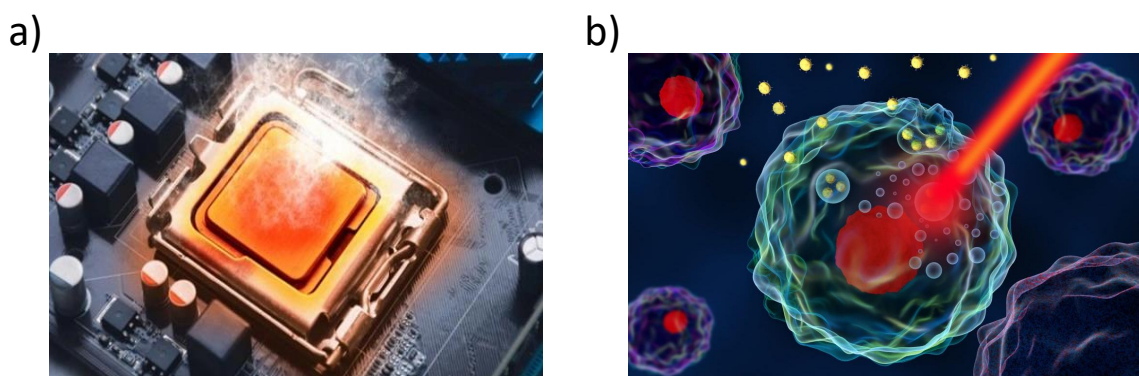


**Figure 3.1 – Examples of applications benefiting from a better understanding of the thermal dynamics of nanosystems.** Artistic representations of a) an overheating processor and b) photothermal therapy with a cancer cell being destroyed via a laser [83,84] .

Investigating the thermal dynamics of nanosystems is of great interest for many technological applications. It is for instance essential in modern electronics for meeting the challenges set by the heating of densely packed nanometric transistors : a better control of heat fluxes in processors would help reduce the power consumption used to cool them in data centers for example. Others applications are related to the design of efficient nanostructured thermoelectric devices or the development of imaging and therapeutic approaches exploiting the photothermal properties of nanoparticles to treat pathologies like cancers [2,5,6,33,85] (see Figure 3.1). Understanding the cooling dynamics of nanosystems is thus crucial to be able to further develop these applications.

Notably, the cooling dynamics of nano-systems are characterized by two main phenomena:

- The increased role played by interfaces, which induce thermal resistances often referred

to as "Kapitza resistances" [24, 41] (see Chapter 1 Section 1.3.1.1 and Figure 1.12). They can have a great influence on the cooling dynamics for systems with dimensions in the nanoscale range, as the surface over volume ratio increases with decreasing size.

- The limited validity of Fourier's law, which efficiently describes heat diffusion at macroscopic scales. Indeed, assuming a diffusive motion of heat carriers becomes questionable at length scales of the order of (or even smaller than) their characteristic mean free paths [39, 86]. In that case hydrodynamic or even ballistic regimes can be encountered for heat propagation (see Chapter 1 Section 1.3.2.2 and Figure 1.14).

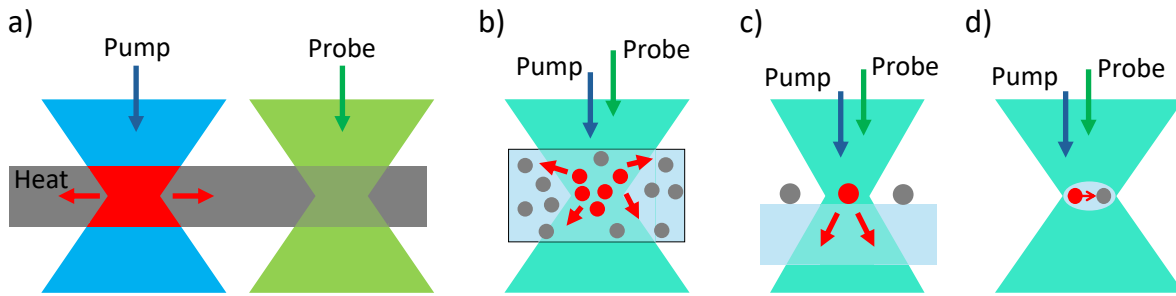


**Figure 3.2 – Schematic of some of the pump-probe configurations used in experiments.** a) Spatially shifted pump and probe beams are focused on an absorbing sample. The size of the spot of the pump beam defines the heated area, typically of the order of few hundred nm. b) Ensemble of nanoparticles immersed in a liquid or embedded in glass. The nano-objects located in the spot of the pump beam are heated while heat propagates to the surrounding transparent medium as well as the unheated nanoparticles. c) Superimposed pump and probe beams focused on a single nanoparticle supported on a transparent substrate. The volume heated by the pump pulse corresponds to the one of the nanoparticle. d) Single nanohybrid composed of two different nanoparticles, which are used as heater and thermometer, respectively, an approach not yet reported in the literature, but currently explored in the FemtoNanoOptics group in the context of the ULTRASINGLE project. All the presented configurations are in transmission.

A large part of the current understanding of nanoscale heat transfer has been obtained using far-field optical pump-probe techniques working in the time or frequency domains [87–89] (see Chapter 2 Section 2.2.3 for the description of the pump-probe technique). These noncontact approaches rely on the selective heating of the absorbing parts of a sample using a pump pulse and on the optical monitoring of the induced thermal dynamics with a probe beam, whose propagation is modified by the pump-induced heating due to the temperature-dependence of the dielectric function of materials. Different configurations, illustrated in Figure 3.2, have been developed to study, for example, heat transfers in absorbing media via overlapped or spatially separated pump and probe beams or between metallic nanoheaters and a dielectric medium. This approach has for instance been successfully applied to study the thermal dynamics of bulk systems, layered structures, and suspended nanometric membranes [3, 27, 89–91].

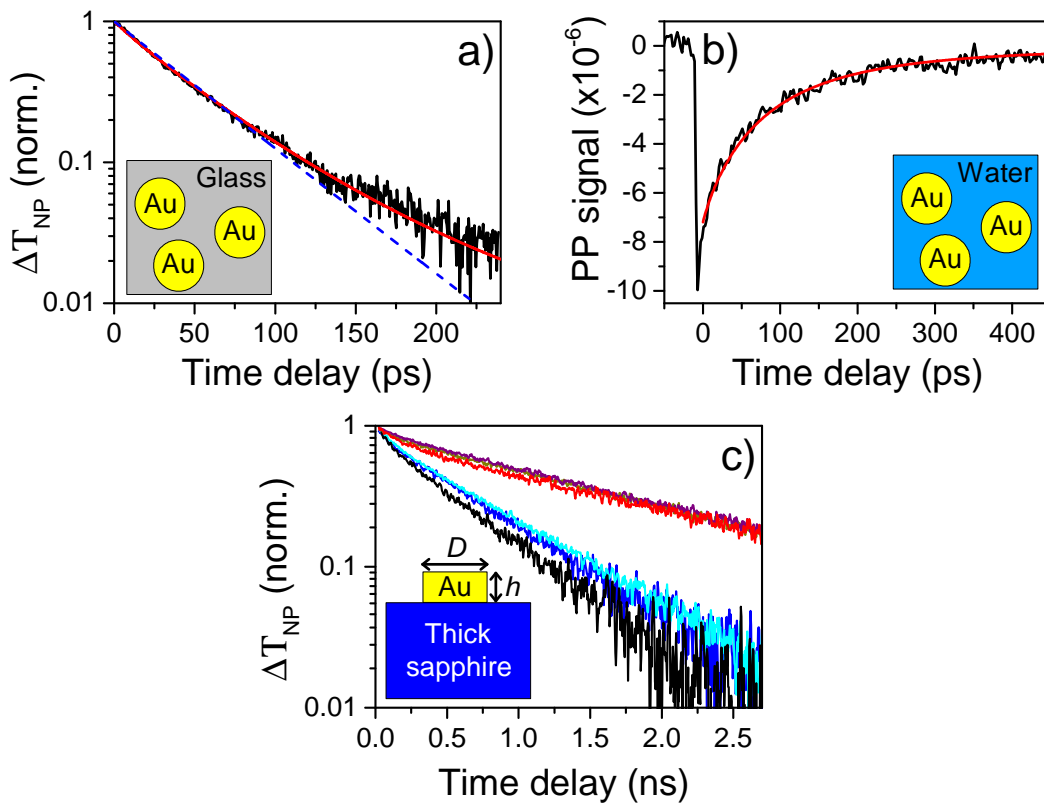


**Figure 3.3** – Examples of previous thermal investigations in FemtoNanoOptics group, performed a) by Vincent Juvé [92], b) Tatjana Stoll [29], and c) by Romain Rouxel [25]. Figures adapted from aforementioned references. a) Normalized nanoparticle temperature rise for gold nanospheres with a diameter  $D = 9$  nm embedded in glass. The experimental black line corresponds to a 890 nm probe wavelength ensuring probing of nanoparticle temperature rise. Full red line is a fit using an analytical model taking into account interface thermal resistance and heat diffusion with  $G_{Au-Glass} = 100$  MW m $^{-2}$  K $^{-1}$  and  $\Lambda_{Glass} = 0.9$  W m $^{-1}$  K $^{-1}$  while the dashed blue line corresponds to a modeling using only interface thermal resistance. b) Raw time-resolved signal for gold nanospheres with a diameter  $D = 19$  nm immersed in ethanol. The experimental black line corresponds to a 820 nm probe wavelength. Full red line is a fit with a model taking into account the thermal dynamics in both the nanoparticle and its environment, using an interface thermal resistance value of  $G_{Au-Ethanol} = 110$  MW m $^{-2}$  K $^{-1}$ . c) Normalized thermal components of experimental time-resolved signals measured on single gold nanodisks with  $h = 18$  nm thickness (estimated by AFM) and diameters of about 60 (black), 120 (blue) and 180 nm (cyan), and  $h = 40$  nm thickness and diameters of about 70 (red), 120 (purple) and 180 nm (yellow) (estimated by SEM).

Composite materials involving absorbing nanoparticles (e.g., metal ones) in a dielectric environment are highly relevant for investigating nanoscale heat transfer, as the heated and probed volumes in such experiments, set by the geometrical size of the used nanoparticles, can be much smaller than the diffraction-limited lateral size of optical beams (a few hundreds of nm).

Evacuation of the energy optically injected in a nanoparticle away from it requires two successive processes: heat transfer at the interface between the nanoparticle and its environment and heat propagation in the latter as previously described (see Chapter 1 Section 1.3. The kinetics of these two processes (and therefore their relative contributions to the cooling dynamics) depend on many characteristics of the nanoparticle and of its environment, such as their thermal properties, morphologies, and initial and transient temperatures, as well as on the nature of their interface. Depending on the investigated system, measurement of the cooling dynamics of metal nanoparticles is thus able to provide information about interface thermal conductances [26,29,93–96] (e.g., determining how their values depend on nanoparticle, environment, and interface compositions) and/or about the modalities of heat conduction in the close environment of the nanoparticles [39,97–102], where Fourier’s law can become invalid because of ballistic and hydrodynamic effects (see Chapter 1 Section 1.14).

Historically, the FemtoNanoOptics group focused its work on the optical study of ensembles of metallic nano-objects or single metallic nanoparticles (the second aspect constituting a specificity of the group on the international research scene). This has led to a number of results helping to understand the thermal behavior of metallic nanosystems and their environment. Specifically, time-resolved experiments conducted on gold nanospheres with a diameter  $D \approx 9$  nm embedded in glass have shown that the observed cooling dynamics were controlled by both the thermal resistance at the nanosphere-glass interface and Fourier heat diffusion in the glass matrix, as shown in Figure 3.3a [92]. Reproducing these experiments for different nanoparticle/glass compositions, a connection between interface conductance and interfacial acoustic mismatch could be established. Experiments were also conducted on gold nanospheres with a diameter  $D \approx 9$  nm in water. A numerical model taking into account the thermal dynamics in both the nanoparticle and its environment allowed to fit the experimental data and give access to the value of the interfacial thermal conductance between them (Figure 3.3b). Another work, performed on single gold nanodisks with thicknesses  $h = 18$  nm or  $h = 40$  nm and diameters  $D$  ranging from 60 to 190 nm that were lithographed on a thick sapphire substrate, has shown that the measured cooling dynamics were exponential and limited by the heat transfer at the gold-sapphire interface with a decay time strongly dependent on nanodisk thickness, as illustrated by Figure 3.3c.

The main motivation behind the experiments described in the following of this chapter was to clarify the dependence of the cooling dynamics of single supported nanoparticles on the properties of their underlying substrate. All investigated gold nanodisks came from the same colloidal solution (see synthesis in Chapter 2 Section 2.1) in order to focus the analysis on the potential dependence of the optical time-resolved signals on the substrates. Fundamentally different supporting substrates were used in the experiments : a thick sapphire substrate, which has a relatively high thermal conductivity, was studied, while thin and ultrathin membranes made of  $\text{Si}_3\text{N}_4$  and  $\text{SiO}_2$  with thermal conductivities much lower than the sapphire one were also investigated (see Table 3.1).

During my PhD, I performed these experiments, which are described in detail in this chapter and the subsequent ones, with the help of Noelle Lascoux, a CNRS researcher working in the FemtoNanoOptics group.

## 3.2 Investigated samples

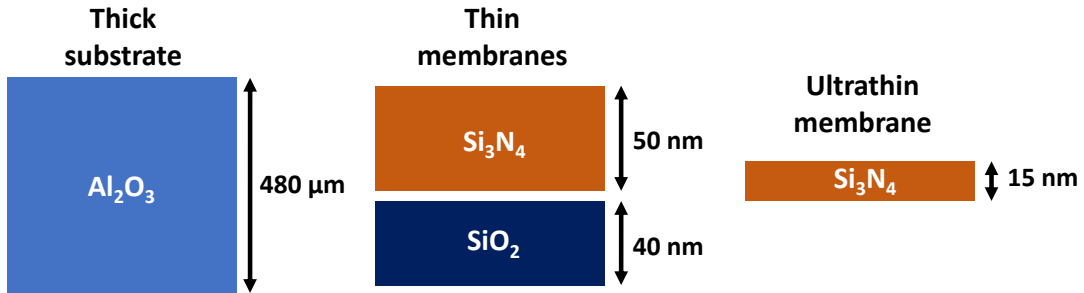


Figure 3.4 – Schematic of the investigated categories of substrates: thick, thin and ultrathin substrates.

In this chapter time-resolved experiments performed on single gold nanodisks supported on transparent substrates with different compositions and thicknesses will be presented. These substrates, presented in Figure 3.4, consist of:

- A thick crystalline substrate (a  $480 \mu\text{m}$  thick (0001)  $\alpha - \text{Al}_2\text{O}_3$  (sapphire) single-crystal substrate).
- Thin amorphous membranes (a  $40 \text{ nm}$  thick silica ( $\text{SiO}_2$ ) membrane and a  $50 \text{ nm}$  thick silicon nitride ( $\text{Si}_3\text{N}_4$ ) membrane).
- An ultrathin amorphous membrane (a  $15 \text{ nm}$  thick silicon nitride ( $\text{Si}_3\text{N}_4$ ) membrane).

These substrates were purchased from commercial suppliers selling them for electron microscopy applications. In the FemtoNanoOptics group, such thin transparent membranes are often used for the deposition of colloidal nano-objects in view of single-particle investigations, as they allow the combination of optical investigations and electronic imaging of the samples. Images taken by Scanning Electron Microscopy (SEM) illustrating the structure of the grids supporting the thin and ultrathin membranes can be seen in Figure 3.5. The values of the thermal constants ( $c_m$ ,  $\Lambda_m$ , and  $\alpha_m = \frac{\Lambda_m}{c_m}$ , see Chapter 1 Section 1.3.2.1) of gold and the materials composing the different substrates are presented in Table 3.1.

Material	Au	$\text{Al}_2\text{O}_3$	$\text{SiO}_2$	$\text{Si}_3\text{N}_4$
Volumetric heat capacity $c_m$ ( $\text{MJ m}^{-3} \text{K}^{-1}$ )	2.49	3.1	1.59	2.13
Thermal conductivity $\Lambda_m$ ( $\text{W m}^{-1} \text{K}^{-1}$ )	317	25	1.4	0.3-10
Thermal diffusivity $\alpha_m$ ( $\text{m}^2 \text{s}^{-1}$ )	$1.27 \cdot 10^{-4}$	$8.1 \cdot 10^{-6}$	$8.8 \cdot 10^{-7}$	$(0.14-4.7) \cdot 10^{-6}$

Table 3.1 – Table of thermal properties for Au, crystalline  $\text{Al}_2\text{O}_3$ , amorphous  $\text{SiO}_2$  and  $\text{Si}_3\text{N}_4$ . The values are given for bulk materials except for the conductivity of  $\text{Si}_3\text{N}_4$ , given for thin films, with a large dispersion in the literature [103–108].

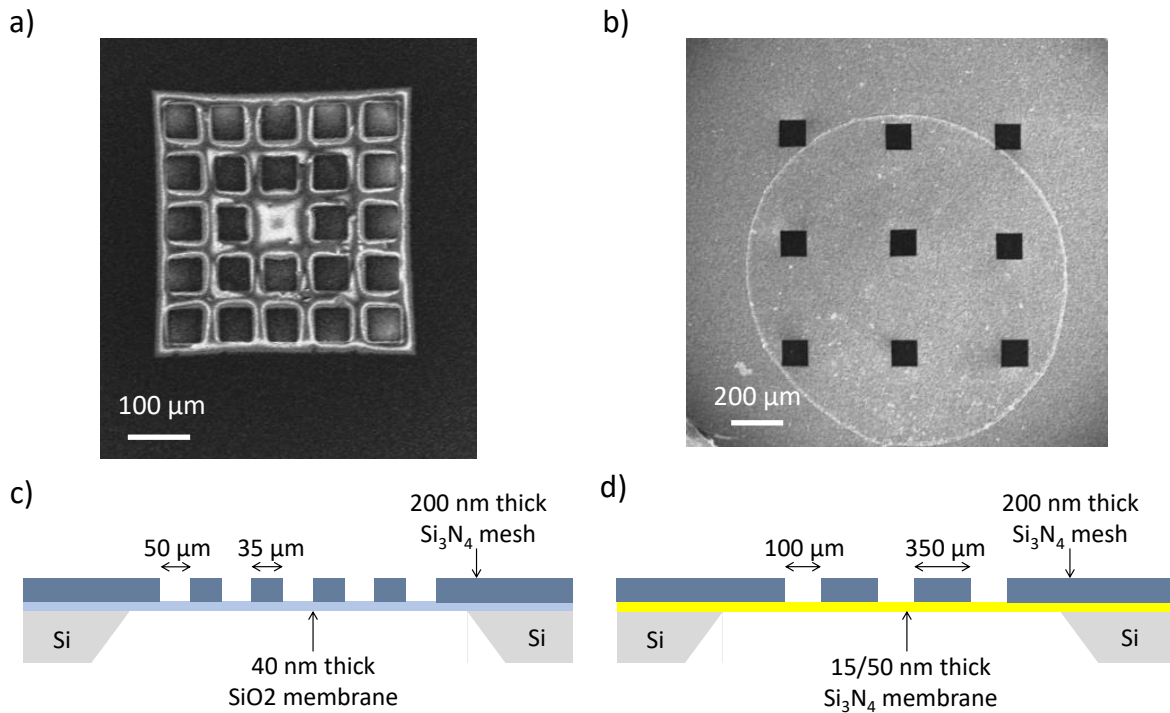


**Figure 3.5** – Scanning Electron Microscopy images of commercial grids supporting a) a 40 nm thick  $\text{SiO}_2$  membrane and b) a 15 nm thick  $\text{Si}_3\text{N}_4$  and schematics of the associated geometries in c) and d), respectively. Grids are patterned with  $50 \times 50 \mu\text{m}$  (silica) or  $100 \times 100 \mu\text{m}$  (silicon nitride) apertures etched in a 200 nm thick support mesh.

### 3.3 Optical experiments and data treatments

#### 3.3.1 Nanodisk optical characterization by linear optical spectroscopy and numerical modeling

Experiments were performed on nanodisk samples synthesized and deposited by Sylvie Marguet (CEA Saclay, our partner in the context of the ULTRASINGLE project). Following their synthesis (see Chapter 2 Section 2.1), the immobilization of nanodisks at the surface of the substrates listed above was performed by depositing a drop of a very diluted solution of gold nanodisks which was left to dry, leading to a low density of deposited nanodisks ( $< 1 \text{ nanodisk}/\mu\text{m}^2$ ) as needed for performing far-field single-particle optical studies. Several copious ethanol rinsings followed by a UV/Ozone treatment were applied to remove any organic residues, as previously detailed in Mosvesyan et al. [109]. It can be noted that these deposition steps are by no means trivial, and greatly benefited from the expertise acquired by Sylvie Marguet in this field. The surfaces of the substrates were then imaged using SEM (at CEA), allowing to estimate the dimensions of the nanodisks ( $D = 97 \pm 12 \text{ nm}$ ,  $h$  of the order of 10 nm, see Chapter 2 Section 2.1).

In this work, SMS (see Chapter 2 section 2.2.2) was first used to localize individual gold nanodisks, which are randomly distributed over the substrate surface following the deposition

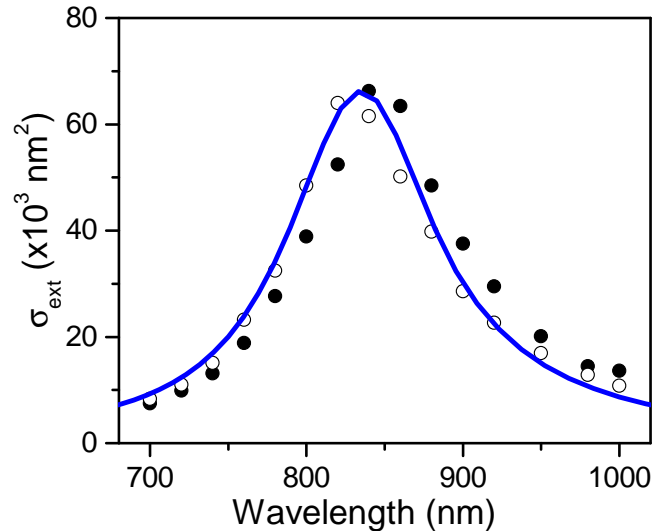


**Figure 3.6** – Measured extinction spectrum of one of the investigated single gold nanodisks. The full and empty markers in the data points correspond to the two orthogonal polarizations of incident light beam. The solid blue line is the result of a FEM simulation with  $D = 112$  nm and  $h = 7.8$  nm.

step. Their  $\sigma_{ext}$  spectra presented a resonance associated with their in-plane dipolar Surface Plasmon Resonance, with a central position  $\lambda_{SPR}$  varying from 700 to 900 nm. For some of the investigated nano-objects, a weak dependence of  $\sigma_{ext}$  on the polarization angle of the beam of light and a slight dipolar SPR degeneracy lift, signatures of a moderate in-plane morphological anisotropy [63] were observed. Individual estimations of nanodisk diameter  $D$  and thickness  $h$  were performed by comparing the integrated spectral area  $\Xi$ , the width  $\Gamma$  and the central position  $\Omega_R$  of the quasi-Lorentzian experimental  $\sigma_{ext}$  spectra (see Chapter 2) with those obtained in optical FEM simulations considering substrate-supported circular nanodisks.  $D$  and  $h$  values respectively in the 85-115 nm and 7-12 nm ranges were deduced from this analysis for the investigated nanodisks. FEM modeling of extinction spectra thus leads to  $D$  values consistent with those deduced from SEM imaging of the synthesized nanodisks, while allowing a quantitative estimation of  $h$ , whose evaluation using SEM is challenging. Moreover, only nanodisks with an extinction spectrum weakly dependent on polarization, consistent with quasi-circular geometrical section, were selected for further time-resolved investigations. As an example, Figure 3.6 represents the experimental extinction cross-section spectra of one of the investigated nanodisks as well as the associated FEM modeling.

### 3.3.2 Experimental strategy

Single-particle time-resolved measurements were conducted on 4-5 gold nanodisks on each type of substrate. In this work, a probe wavelength  $\lambda_{pr}$  close to  $\lambda_{SPR}$  was chosen for each investigated nanodisk. This choice was based on previous numerical and experimental studies of the thermo-optical dynamics of single metal nanoparticles in dielectric environments [25, 110, 111]. Indeed, these investigations have shown that the sensitivity of time-resolved signals to nanoparticle heating is maximal when  $\lambda_{pr} \approx \lambda_{SPR}$ , while the contribution of environment heating to the

measured signals simultaneously vanishes in these conditions, ensuring specific probing of the nanoparticle temperature evolution. Measurements using different probe wavelengths will be presented in the next chapter.

### 3.3.3 Raw time-resolved measurements

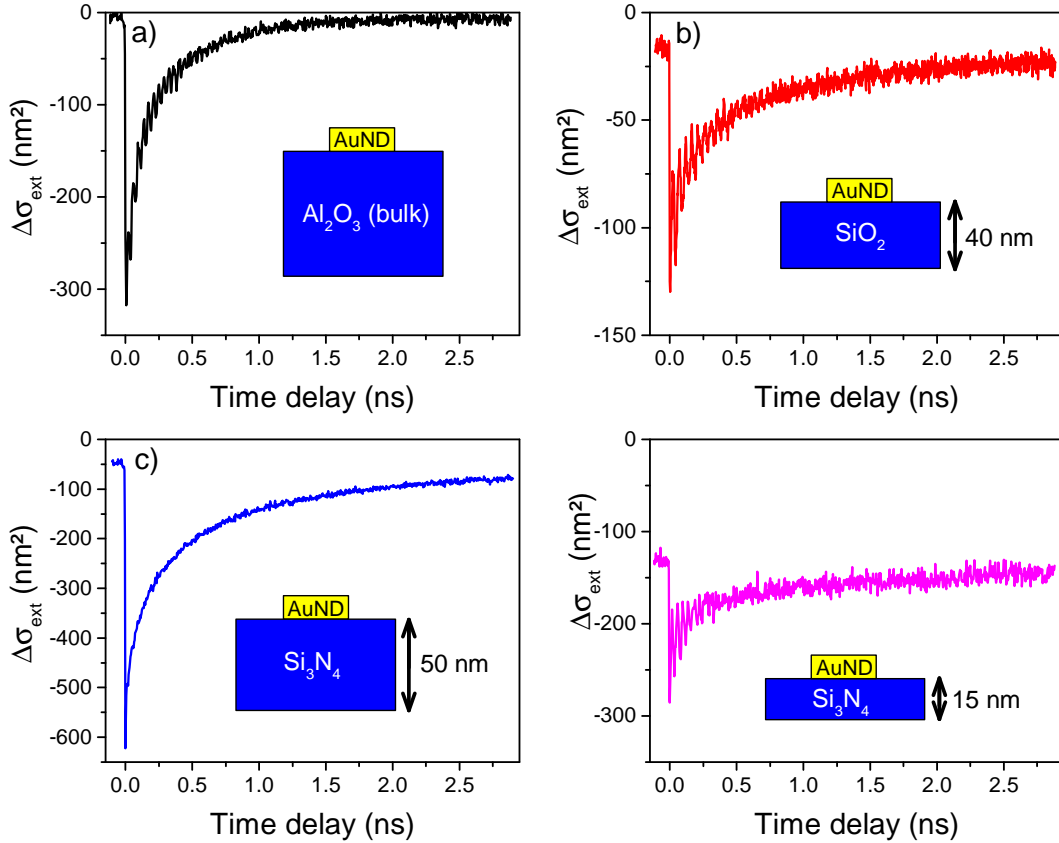


**Figure 3.7** – Raw temporal variations of the extinction cross-section  $\Delta\sigma_{ext}(t)$  for 4 single gold nanodisks supported on the 4 substrates considered in this work. The corresponding substrate is indicated on each panel.

The raw time-resolved signals measured on 4 single gold nanodisks deposited on the 4 substrates considered in this study (Figure 3.4) are presented in Figure 3.7. They illustrate the general shape of the measured signals for nanodisks in all cases: as described in Chapter 1 Section 1.2.3, the signals are composed of three components which are an initial peak associated to the excitation and the internal thermalization of the nano-objects, oscillations linked to acoustic vibrations, and, finally, relaxation of the signal corresponding to thermal cooling of the nanodisks. A quick look at the different curves already shows that there is some variability of the average value of the optical signal at negative time delay: in the sapphire case this value is close to 0 while on thin membranes it reaches a few tens of  $\text{nm}^2$  and even  $>100 \text{ nm}^2$  for the ultrathin membrane. The temporal dynamics measured at positive delays are also significantly different, as will be detailed in the next sections.

## 3.3.4 Data treatment

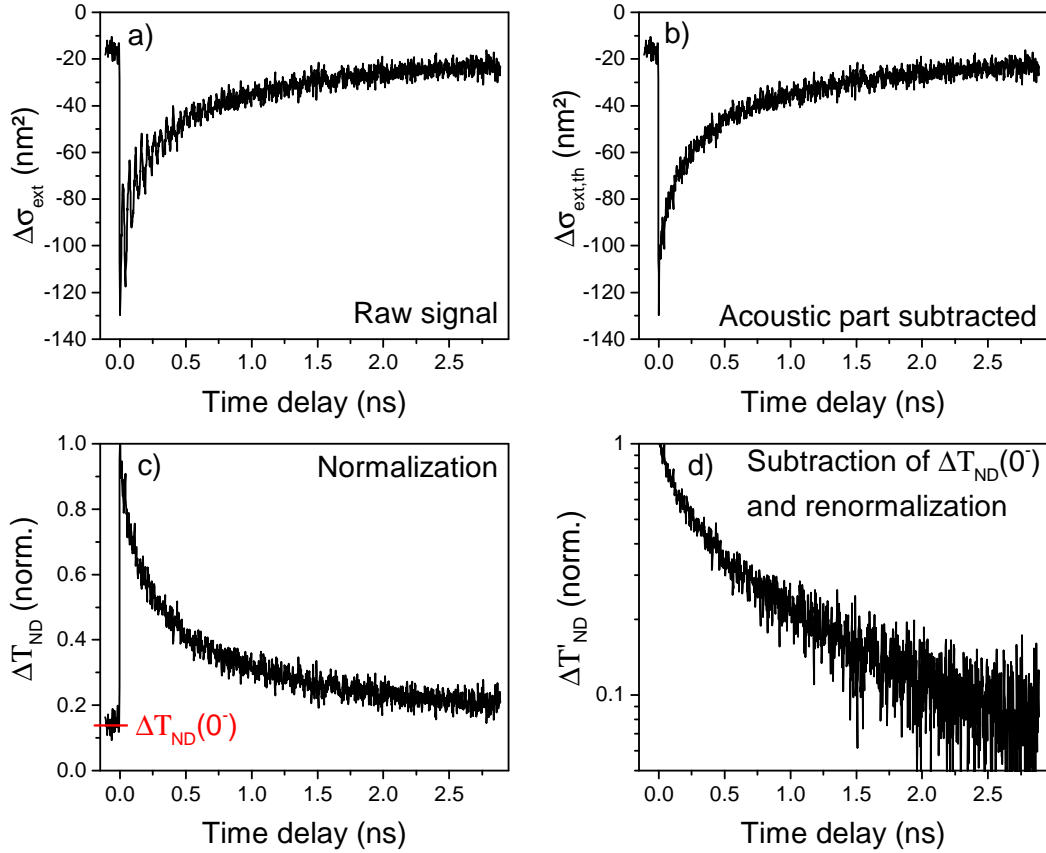


**Figure 3.8** – a)  $\Delta\sigma_{ext}(t)$ , b)  $\Delta\sigma_{ext,th}(t)$ , c)  $\Delta T_{ND}(t)$  and d)  $\Delta T'_{ND}(t)$  quantities extracted from time-resolved measurements for a single gold nanodisk supported by a 40 nm  $\text{SiO}_2$  thick membrane. c) The mean value at negative time delay  $\Delta T_{ND}(0^-)$  used to compute  $\Delta T'_{ND}$  in d) is indicated in red.

The analysis of the thermal dynamics from raw measured transient extinction changes  $\Delta\sigma_{ext}(t)$  (Figure 3.7) was performed by applying successive data treatments and lead to 3 new quantities:  $\Delta\sigma_{ext,th}(t)$ ,  $\Delta T_{ND}(t)$  and  $\Delta T'_{ND}(t)$ , of which calculation is described in the following. They are all presented in Figure 3.8 in the case of an optical signal measured on a single gold nanodisk supported by a 40 nm thick  $\text{SiO}_2$  membrane.

First, the acoustic component was fitted and subtracted from the raw optical signals  $\Delta\sigma_{ext}(t)$  (Figure 3.8a) using the method described in Chapter 2 Section 2.2.3.4. The remaining signal  $\Delta\sigma_{ext,th}(t)$ , represented in Figure 3.8b, is composed of an initial peak associated to the excitation and internal thermalization of the nanoparticle by electron-electron and electron-phonon interactions (typically 5-10 ps corresponding to 1-3 data points) as well as a thermal component linked to the cooling of the nano-object. The value of the thermal component after excitation being inaccessible due to the initial peak, a monoexponential fit of the thermal component, over 50-100 ps and after the initial peak, was performed and used to extrapolate the initial value of the thermal component. As discussed in Section 3.3.2, experiments were done in conditions ensuring that the thermal component is solely linked to the heating of the nanodisk and pro-

portional to it. This allowed to more easily compare signals measured for different nanodisks, which exhibit different absolute variations of their extinction cross-sections. As a consequence the  $\Delta\sigma_{ext,th}(t)$  quantity, once normalized by the initial value of the thermal component, was denoted as  $\Delta T_{ND}(t)$ , i.e. the temporal variations of the temperature increase in the nanodisk. It is represented in Figure 3.8c for the considered gold nanodisk (note that the 1-3 data points associated to the initial peak were not removed as they appeared outside of the 0-1 normalized window used to plot  $\Delta T_{ND}(t)$ ). Finally, the mean value at negative time delays  $\Delta T_{ND}(0^-)$  was subtracted from the previous signal leading to a new quantity  $\Delta T'_{ND}(t) = \Delta T_{ND}(t) - \Delta T_{ND}(0^-)$ , which was then renormalized and represented with a semilogarithmic scale in Figure 3.8d.

## 3.4 Thermal dynamics of single gold nanodisks deposited on a thick sapphire substrate

### 3.4.1 Experimental results

First, time-resolved experiments were conducted on 4 gold nanodisks deposited on a thick sapphire substrate. The normalized temporal dynamics of the  $\Delta T_{ND}(t)$  temperature rises (or thermal components) extracted from the measured signals are shown in Figure 3.9 as well as the  $\Delta T'_{ND}(t)$  quantity in Figure 3.10. Here each trace corresponds to a measurement done on a single gold nanodisk.

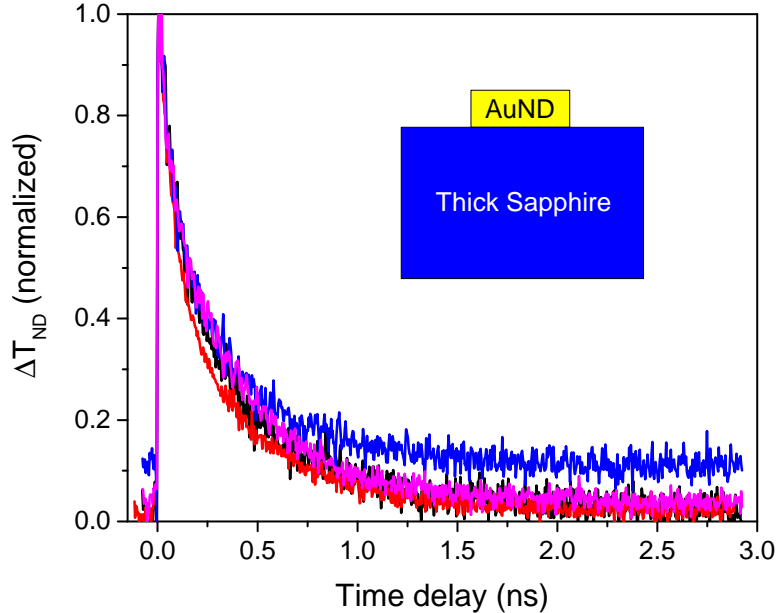
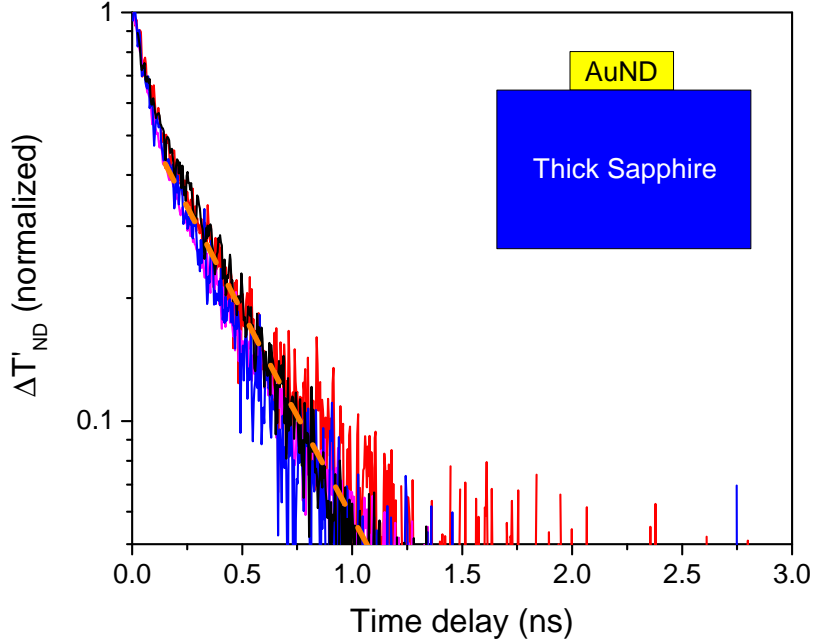


Figure 3.9 – Normalized  $\Delta T_{ND}(t)$  temperature rise for the 4 single gold nanodisks deposited on a thick sapphire substrate.

The normalized  $\Delta T_{ND}(t)$  signals present low values at negative pump-probe delays that are  $< 0.02$  except for one signal, where this value is of the order of 0.1 : this is an indication that the cooling process is almost finished after  $T_{rep} = 12.5$  ns. Indeed in our experiments nanodisks

### 3.4. Thermal dynamics of single gold nanodisks deposited on a thick sapphire substrate

are excited by a pump pulse every  $T_{rep} = 12.5$  ns: values at negative time delays thus also correspond to the values at time delays  $t \approx 12.5$  ns. If the time necessary for the nanodisk to cool down to the ambient temperature is smaller than 12.5 ns then the values measured at negative time delays will be close to 0, as it is the case here (see Section 3.5.2 for more details about accumulation effects).



**Figure 3.10** –  $\Delta T'_{ND}(t)$  quantity for the 4 gold nanodisks deposited on a thick sapphire substrate and FEM modelization with an interfacial conductance  $G = 65 \text{ MW m}^{-2} \text{ K}^{-1}$ .

The  $\Delta T'_{ND}$  curves for all investigated nanodisks are highly similar and all overlap in Figure 3.10. They exhibit biexponential dynamics characterized by time constants  $\tau_1 \approx 0.4$  ns and  $\tau_2 \approx 50 - 100$  ps. Similar dynamics were already observed within work done in the FemtoNanoOptics group in the case of gold nanodisks with thicknesses around  $h = 18$  nm and 40 nm and diameter  $D$  range from 60 to 190 nm, synthesized by electron beam lithography on a sapphire substrate, that were studied using the same single-particle time-resolved spectroscopy approach and investigated in the context of Romain Rouxel's PhD work [25, 112] (see Figure 3.3).

The second exponential, with a short time constant  $\tau_2$ , is still not fully understood, especially in terms of physical origin. The fact that these fast dynamics have been observed in the case of both colloidal and lithographed nanodisks indicates that their origin is not associated to a specific synthesis procedure. Such a fast exponential appears in numerical models when considering a nanodisk covered by a transparent impurity such as an ultrathin water layer, leading to a fast internal thermalization of the nanodisk-impurity system following selective nanodisk heating (see Romain Rouxel's PhD work [112]).

Similarly to what was done in previous work in the FemtoNanoOptics group [25], the first exponential dynamic, with a time constant  $\tau_1$ , is attributed to interface-limited cooling dynamics

of the nanodisk [26, 92].

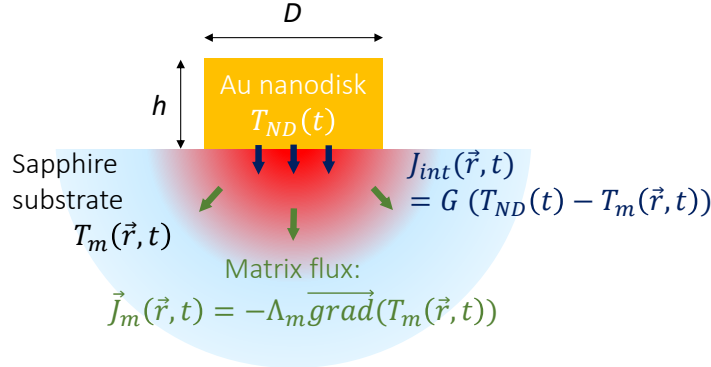


**Figure 3.11** – Schematic of the Au nanodisk-Sapphire substrate system with heat fluxes considered at the interface and in the substrate, described by the interface conductance  $G$  and thermal conductivity of Sapphire  $\Lambda_{\text{Al}_2\text{O}_3}$  respectively.

Indeed, in the case of a Biot number  $Bi = hG/\Lambda_{Au} \ll 1$  (with  $h$  the height of the nanodisk,  $G$  the interface conductance, and  $\Lambda_{Au}$  the gold nanodisk thermal conductivity, see Chapter 1 Section 1.3.3), which guarantees that the nanodisk remains isothermal throughout its thermal cooling, and of a substrate heat conductivity  $\Lambda_{\text{Al}_2\text{O}_3}$  high enough to ensure negligible modification of substrate temperature near the nanodisk being cooled (two relevant assumptions in the case of Au nanodisks on sapphire), integrating the interfacial heat current density  $J_{int} = G\Delta T_{ND}$  (see Figure 3.11) over the nanodisk surface  $S$  in contact with the substrate leads to

$$V c_{Au} \frac{d\Delta T_{ND}}{dt} = GS\Delta T_{ND} \quad (3.1)$$

with  $V$  being the volume of the nanodisk and  $c_{Au}$  the volumetric heat capacity of gold and  $G$  the Kapitza thermal conductance of the nanostructure-substrate interface. The solution is then simply an exponential decay of  $\Delta T_{ND}$  with a characteristic time  $\tau = c_{Au}h/G$  [113]. This relation can be used to estimate the value of  $G$  in the time-resolved experiments through

$$G = \frac{c_{Au}h}{\tau}. \quad (3.2)$$

Using the previous  $\tau_1 \approx 0.4$  ns value, the estimated value for the interface conductance  $G$  is of the order of  $60 \text{ MW m}^{-2} \text{ K}^{-1}$ .

### 3.4.2 Comparison with numerical simulations

In order to have a more precise determination of the interface conductance  $G$ , the time-domain FEM thermal model described in Chapter 2 Section 2.3.2.1 is used to simulate the thermal dynamics in this system. As a reminder, this model takes into account a single gold nanodisk excited and heated by a unique pump pulse, the Kapitza thermal resistance linked to the nanodisk-substrate interface as well as Fourier's law to describe heat diffusion in the two

objects. The value used for the thermal conductivity of the sapphire substrate was the bulk one (see value in 3.1) : however, this hypothesis is questionable because heat conduction in sapphire at the vicinity of the nanodisk may be affected by hydrodynamic/ballistic effects. Nevertheless, it has a small impact on the computed thermal dynamics, which are weakly sensitive to substrate conductivity value for an interface-limited cooling. Finally, the only parameter left free in the model was the interface conductance  $G$ .

The model was able to reproduce the observed time constant  $\tau_1 \approx 0.4$  ns using  $G \approx (65 \pm 10)$  MW m<sup>-2</sup> K<sup>-1</sup> (see Figure 3.10), close to the value obtained previously with the simple analytic model (Equation 3.1). The obtained value for  $G$  is also close to the ones deduced for two samples of lithographed nanodisks,  $G \approx (60 \pm 10)$  and  $\approx (75 \pm 10)$  MW m<sup>-2</sup> K<sup>-1</sup> studied in previous work done in the FemtoNanoOptics team [25]. The deduction of similar interface conductance values in this work and the previous one, done in the context of Romain Rouxel's PhD thesis was by no means granted, as the different nanodisk synthesis could have resulted in gold-sapphire interfaces with different contact and thermal properties.

As a side note, including the repeated character of the excitation with the frequency-domain thermal model described in Chapter 2 Section 2.3.2.2 had almost no influence on the  $\Delta T'_{ND}(t)$  dynamics computed for a thick sapphire substrate (as expected from the full cooling of nanodisks after  $T_{rep}$ ), the monoexponential decay of the experimental signals after  $>0.2$  ns delays being still well reproduced using  $G = 65$  MW m<sup>-2</sup> K<sup>-1</sup> in the simulations.

## 3.5 Thermal behavior of single gold nanodisks deposited on thin amorphous membranes

### 3.5.1 Experimental results

Pump-probe experiments were also done on thinner substrates: a 40 nm thick SiO<sub>2</sub> membrane and a 50 nm thick Si<sub>3</sub>N<sub>4</sub> membrane. 4 gold nanodisks deposited on the SiO<sub>2</sub> membrane and 5 on the Si<sub>3</sub>N<sub>4</sub> membrane were studied using time-resolved experiments. The normalized temporal dynamics of the  $\Delta T_{ND}(t)$  temperature rises extracted from the measured signals as well as the  $\Delta T'_{ND}(t)$  quantity for the two thin membranes and also sapphire substrate are shown in Figures 3.12 and 3.13. For measurements on thin membranes, the  $\Delta T_{ND}(t)$  values preceding the pump excitation, at negative time delays, are around 0.1-0.2 and larger than what was observed in the case of nanodisks deposited on thick sapphire (Figure 3.9). Note that the main difference between the  $\Delta T_{ND}(t)$  signals for the 40 nm thick SiO<sub>2</sub> membrane and the 50 nm thick Si<sub>3</sub>N<sub>4</sub> membrane lies in their values at negative time delays, the former exhibiting  $\sim 0.15$  values while  $\sim 0.08$  values are observed for the latter. However, the  $\Delta T'_{ND}(t)$  normalized curves are almost identical for nanodisks deposited on silica and silicon nitride membranes, showing that they present similar cooling dynamics, which is not surprising in view of their similar thicknesses and thermal properties (Table 3.1).

The comparison of the time-resolved signals  $\Delta T_{ND}(t)$  and  $\Delta T'_{ND}(t)$  between all the three aforementioned substrates leads to several observations. First, on each substrate the  $\Delta T'_{ND}(t)$  curves overlap, meaning that there is a great repeatability of the dynamics between different gold nanodisks. Secondly, the cooling dynamics differ greatly between, on one part, the nanodisks deposited on sapphire, and, on the other part, the nanodisks deposited on thin membranes. The

$\Delta T'_{ND}(t)$  dynamics in the case of membranes are much slower than the ones observed in the sapphire case. As an example,  $\Delta T'_{ND}(t)$  is reduced to 10% of its maximum value after 0.7-0.8 ns in experiments done in the sapphire substrate case whereas for the studied membranes the time needed almost exceeds 2 ns, a 3 times larger value. Moreover, contrary to what was observed in the sapphire substrate case, the  $\Delta T'_{ND}(t)$  signals exhibit nonexponential dynamics for nanodisks on the two membranes (as observable from their non-linear variations in the semilog plot shown in Figure 3.13).

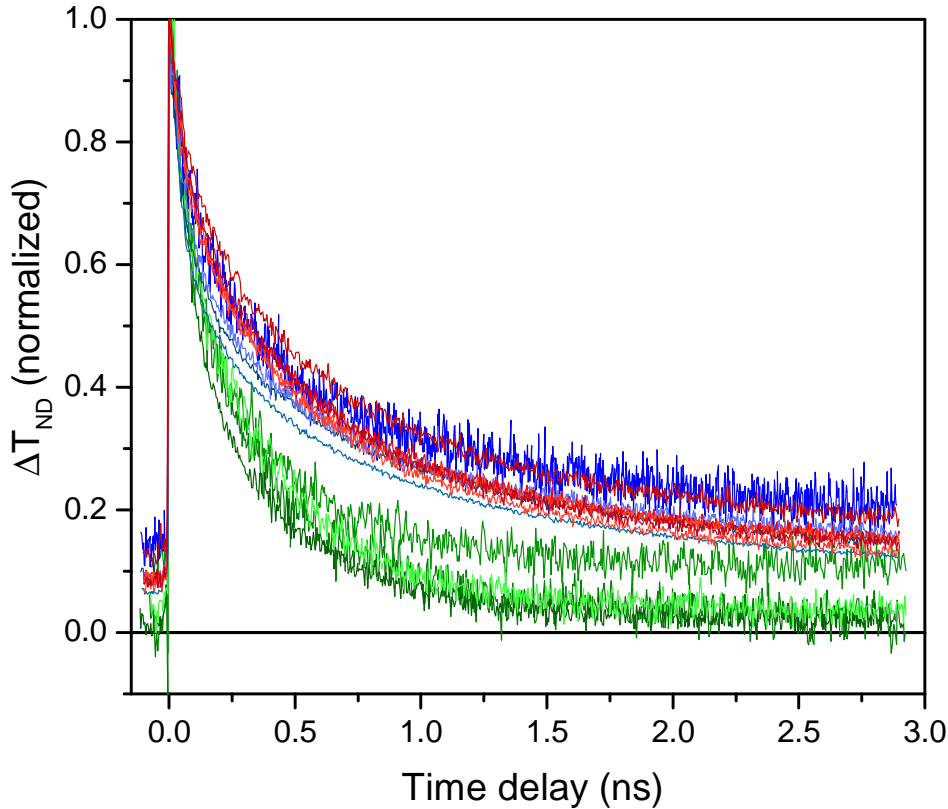


**Figure 3.12** – Comparison of the normalized  $\Delta T'_{ND}(t)$  temperature rises for single gold nanodisks deposited on thick sapphire (green), 40 nm thick  $\text{SiO}_2$  membrane (blue) and 50 nm thick  $\text{Si}_3\text{N}_4$  membrane (red) respectively.

The observation of the nonexponential decay of  $\Delta T'_{ND}(t)$  for nanodisks supported on thin membranes is a clear indicator that, in contrast with the thick sapphire case, the cooling dynamics are not solely ruled by interfacial heat transfer and also that heat propagation inside the membranes is slow enough to have a strong effect on the measured dynamics. Two reasons explain the reduction of the efficiency of heat transfer in thin membranes:

- A composition effect: indeed, the thermal conductivities of silica and silicon nitride are almost 10 times lower than the one of sapphire, as shown in Table 3.1.
- A thickness effect: heat diffusion in membranes away from a nanoheater becomes a two-dimensional process at time scales exceeding those required for heat to propagate over the membrane thickness (see below). This greatly reduces the efficiency of heat spreading

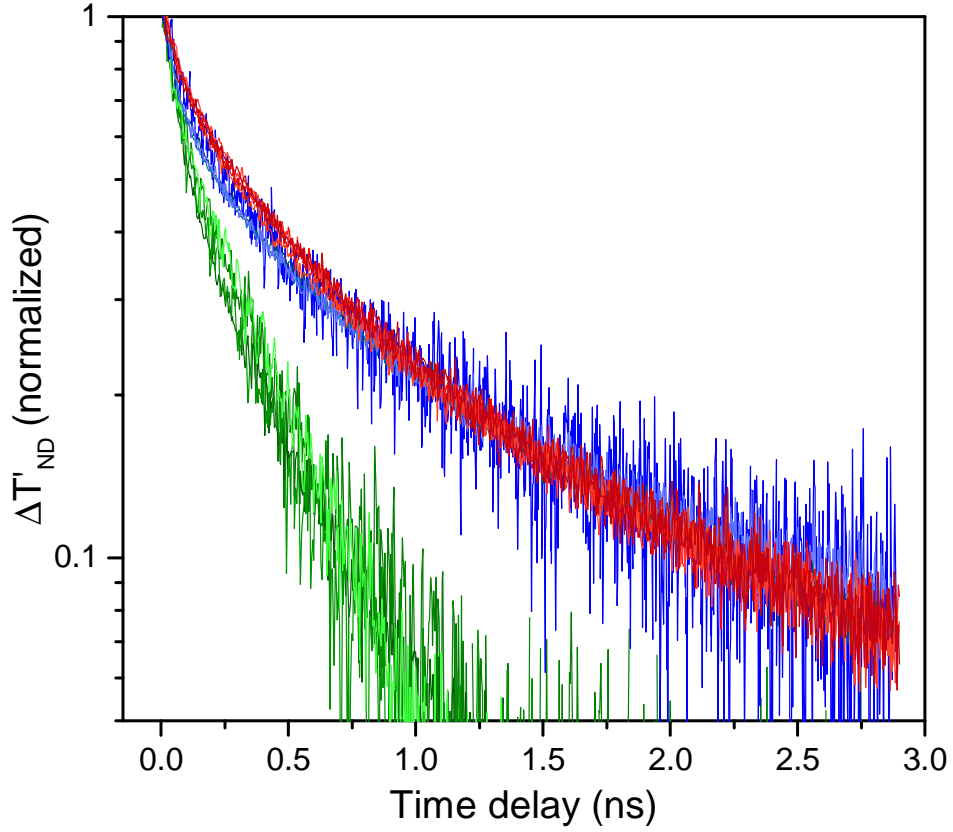


**Figure 3.13** – Comparison of the quantity  $\Delta T'_{ND}(t)$  for single gold nanodisks deposited on thick sapphire (green), 40 nm thick  $\text{SiO}_2$  membrane (blue) and 50 nm thick  $\text{Si}_3\text{N}_4$  membrane (red) respectively.

around the nanodisk as compared to the case of thick substrates, where diffusion remains three-dimensional at all experimentally relevant time scales.

Finally, the non-vanishing normalized  $\Delta T_{ND}(t)$  values at negative time delays indicate that, conversely to the thick sapphire case, the time separating two successive pump pulses,  $T_{rep} = 12.5$  ns, is not sufficient for complete cooling of the nanodisks. This accumulation effect is illustrated via arbitrary time-resolved signals in Figure 3.14. This makes therefore the comparison of the nanodisks cooling dynamics with time-domain simulations involving a single pump pulse less relevant than in the bulk substrate case and underlines the need of a more complete model taking into account the periodic excitation by pump pulses.

### 3.5.2 Modeling the accumulation effects

A different thermal modeling approach allowing to compute the thermal dynamics of the nanodisk-membrane system for any time-dependent heating process was thus performed by Aurélien Crut. The core concept of this model (already used in the literature for modeling different systems [3, 81, 82]) is the calculation of the complex frequency domain impulse response  $\tilde{h}(f)$  of the system which is then used to compute the frequency domain thermal dynamics  $\Delta\tilde{T}(f)$  through Equation 2.43 for a periodic train of delta pulses (see Chapter 2 Section 2.3.2.2) corre-

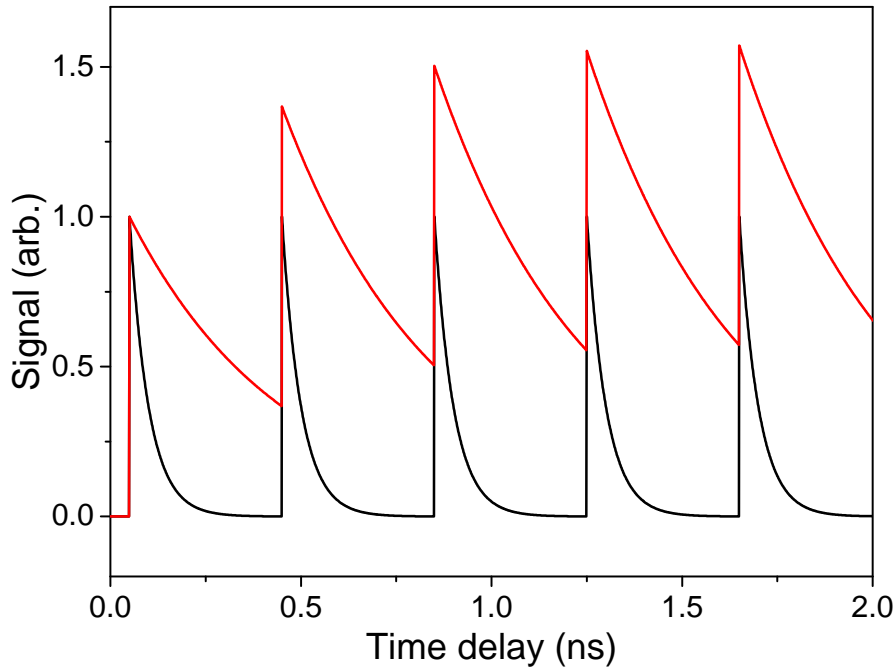


**Figure 3.14 – Schematic illustration of accumulation effects in the context of time-resolved pump-probe experiments.** Full black line corresponds to a case where the signal reaches its base value after a delay  $> T_{rep}$  while the red line illustrates an accumulation effect, for systems presenting characteristic relaxation times of the order of or large than  $T_{rep}$ .

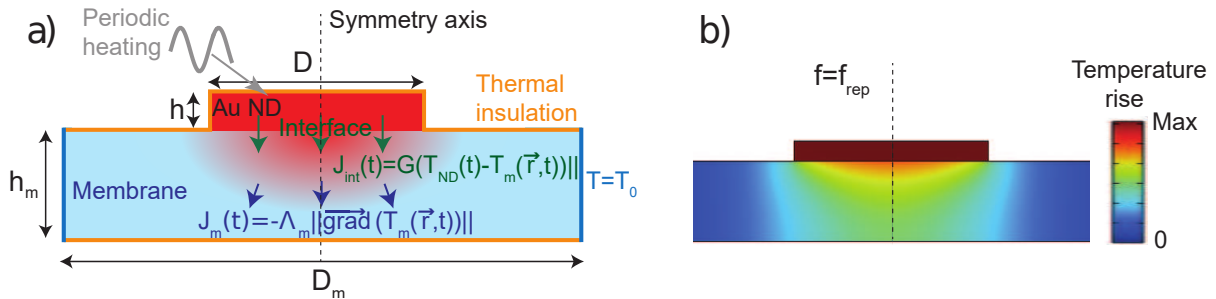


**Figure 3.15 – a) Schematic description of the FEM model used for computing the spatio-temporal temperature variations induced by a sinusoidal excitation of a gold nanodisk supported on a thin membrane. b) Temperature rise (modulus) in and near the gold nanodisk computed for excitation at the frequency  $f = f_{rep} = 80$  MHz.**

sponding to the periodic excitation of the nanodisk-membrane system by pump pulses. The final step consists in the calculation of the temporal dynamics  $\Delta T_{ND}(t)$  from the frequency domain dynamics  $\Delta \tilde{T}(f)$  by reverse Fourier transform.

It should be noted that the system considered in the simulations differs from the actual experimental configuration. Contrary to the simulation case, where a nanodisk at the center of a homogeneous, 2  $\mu\text{m}$  diameter cylindrical membrane is considered, in our experiments,

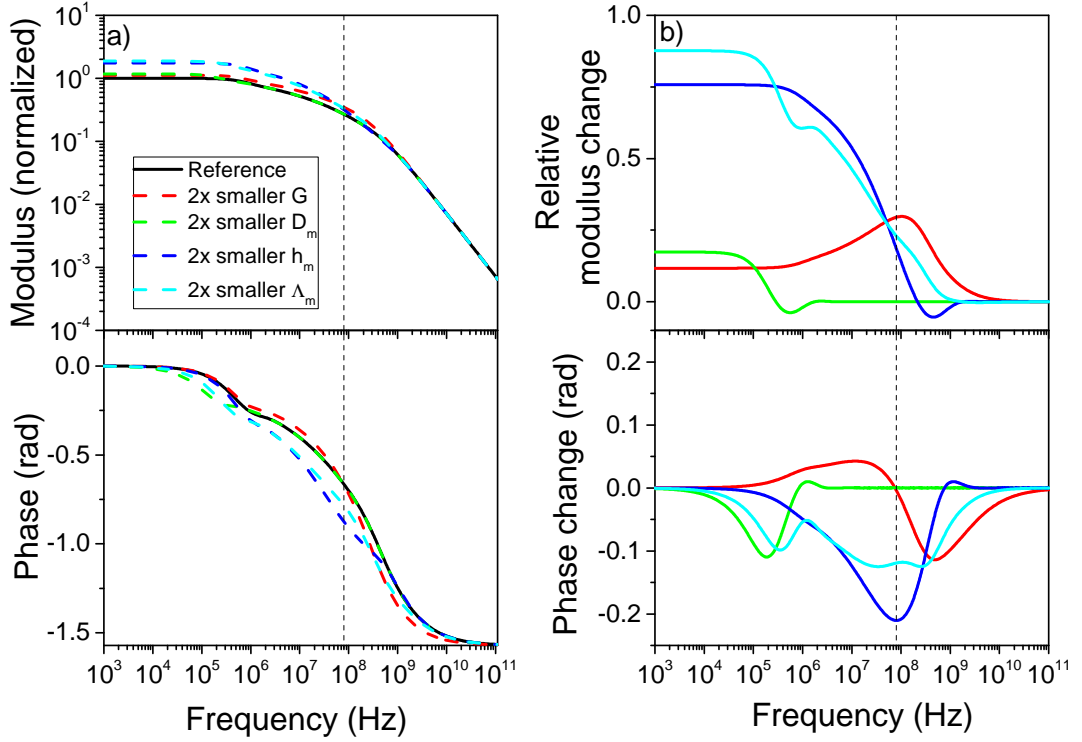


**Figure 3.16 – Numerical modeling of the effect of the modification of  $h_m$ ,  $D_m$ ,  $\Lambda_m$ , and  $G$  on the frequency domain response  $\tilde{h}(f)$  of a gold nanodisk supported by a thin membrane.** a) Frequency-dependent nanodisk temperature rise induced by a sinusoidal nanodisk excitation (modulus and phase of the frequency-domain response  $\tilde{h}(f)$ ). The case of a  $D = 100$  nm,  $h = 10$  nm gold nanodisk supported on a  $h_m = 40$  nm,  $D_m = 2$   $\mu\text{m}$  silica membrane with a  $G = 100$   $\text{MW m}^{-2} \text{K}^{-1}$  thermal conductance at their interface was first considered (plain black line). Simulations were then reproduced with  $h_m$ ,  $D_m$ ,  $\Lambda_m$  and  $G$  values reduced one by one by a factor 2 as compared to the reference situation (dashed colored lines, see legend). The vertical dashed line indicates the 80 MHz repetition frequency in our experiments. b) Sensitivity of nanodisk heating to  $h_m$ ,  $D_m$ ,  $\Lambda_m$  and  $G$  values, deduced from the computations shown in a) by calculating the associated relative modulus change and absolute phase change of nanodisk heating (same color code as in a)).

nanodisks are located at various positions on large square membrane windows (50 and 100  $\mu\text{m}$  side length for silica and silicon nitride membranes, respectively). Moreover, this model does not take into account heat dissipation to the surrounding air, as discussed in Chapter 2 Section 2.3.2. Nevertheless, these differences between the systems considered in experiments and simulations are not relevant here because, as discussed below, they only affect the nanodisk temperature rise preceding each pulse (Figure 3.12), which presents large variations from one nanodisk to another and that we did not attempt to quantitatively model, but not the  $\Delta T'_{ND}(t)$  cooling dynamics obtained after subtraction of this offset value (Figure 3.13).

The results of frequency-domain FEM simulations performed for the reference case of a  $D = 100$  nm,  $h = 10$  nm gold nanodisk located on a thin silica membrane with  $D_m = 2$   $\mu\text{m}$  diameter and  $h_m = 40$  nm thickness are shown in Figure 3.16a. The values used for the thermal conductivities of Au and SiO<sub>2</sub> were the bulk ones (see Table 3.1 in Section 3.2). The computed response globally evokes that of a low-pass filter, with the amplitude of the response being constant at low frequencies and decaying at high ones, and the phase shift between the excitation and the response going from 0 at low frequencies to  $-\pi/2$  values at high ones.

In order to clarify the influence of the key parameters of our thermal model on this frequency response, FEM calculations were reproduced with modified values of the interface conductance ( $G$ ) and of some of the membrane characteristics ( $\Lambda_m$ ,  $D_m$ , and  $h_m$ ) (Figure 3.16b). The induced changes of the response function are also shown in Figure 3.16b. As can be seen in this figure (and as previously noticed in the context of thermorefectance investigations on thin films [82, 114]), the sensitivities to interface and membrane characteristics have a different frequency dependence, which is essential to allow their independent determination. For a membrane-supported nanodisk, the low-frequency part of the response function mostly depends on membrane geometrical and thermal characteristics, while its high-frequency component is essentially sensitive to the  $G$  value. This can be ascribed to the fact that temperature oscillations in the membrane occur on a smaller volume as frequency increases, giving more importance to interfacial effects. The effect of  $G$ , which takes place over a broad frequency range, can be better understood by considering the simplified case of isothermal nanodisk and membrane (obtained in the limit of very high membrane conductivities and thus strongly differing from the situation addressed in Figure 3.16).

The nanodisk temperature evolution  $\Delta T_{ND}(t)$  for a sinusoidal heating  $A\exp(i\omega t)$  (with  $\omega = 2\pi f$ ) is then described by the differential equation

$$c_{Au}V \frac{d\Delta T_{ND}}{dt} + GS\Delta T_{ND} = A\exp(i\omega t) \quad (3.3)$$

with  $c_{Au}$ ,  $V$ , and  $S$  the nanodisk volumetric heat capacity, volume, and surface in contact with the substrate (with  $V/S = h$ ). The response function is in this case a low-pass filter one,

$$\tilde{h}(f) \propto \frac{1}{G} \frac{1}{1 + i2\pi\tau f}, \quad (3.4)$$

with  $\tau = hc_{Au}/G$  ( $=0.25$  ns in the reference case considered in Figure 3.16), whose low-frequency limit and cutoff frequency  $f_c = 1/(2\pi\tau)$  are both affected by  $G$ , which thus impacts the response function over a broad frequency range (frequencies of the order of and above  $f_c$ ).

It can also be observed in Figure 3.16 that membrane characteristics ( $\Lambda_m$ ,  $h_m$ , and  $D_m$ ) affect the response function a different way, the effects of a reduction of  $h_m$  and  $D_m$  by a factor of 2 as compared to the reference case being in particular limited to the  $<1$  GHz and  $<5$  MHz frequency ranges, respectively. The existence of such frequency thresholds for the effects of  $h_m$  and  $D_m$  can be understood by considering the frequency-dependent thermal penetration length in a material

$$L_p = \sqrt{\frac{\alpha_m}{\pi f}}, \quad (3.5)$$

with  $\alpha_m = \Lambda_m/c_m$  the membrane diffusivity ( $\alpha_m = 9 \times 10^{-7}$  m<sup>2</sup> s<sup>-1</sup> for silica) [115]. The finite thickness of the membrane thus has an influence at frequencies low enough for  $h_m$  to be smaller than  $L_p$ , i.e. for  $f < \alpha/(\pi h_m^2)$  (about 200 and 800 MHz for the 40 and 20 nm

thicknesses considered in Figure 3.16), respectively). This simple analysis thus explains why the  $2\times$  reduction of  $h_m$  investigated in Figure 3.16) is without effect at  $>1$  GHz frequencies. It also predicts a non-negligible effect of  $h_m$  on the nanodisk temperature dynamics in our experiments, which involve a periodic excitation with 80 MHz frequency. A similar analysis shows that the lateral size of the membrane impacts the response function only at frequencies lower than about 4 MHz for  $D_m = 1 \mu\text{m}$ , making a decrease of  $D_m$  from 2 to 1  $\mu\text{m}$  without effect for frequencies exceeding a few MHz (Figure 3.16)).

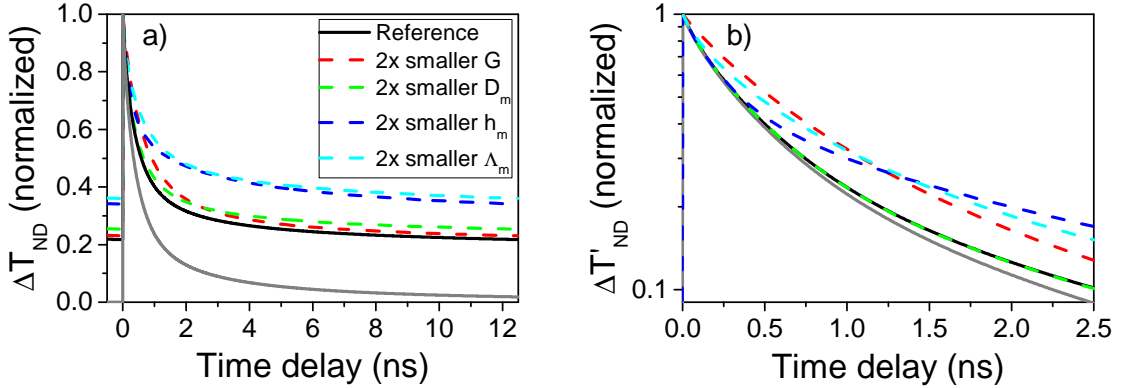


**Figure 3.17 – Numerical modeling of the effect of the modification of  $h_m$ ,  $D_m$ ,  $\Lambda_m$ , and  $G$  on the computed cooling dynamics  $\Delta T_{ND}(t)$  and  $\Delta T'_{ND}(t)$ .** a) Normalized  $\Delta T_{ND}(t)$  cooling dynamics deduced from the frequency calculations shown in 3.16a for nanodisk excitation by a periodic Dirac pulse train. b) Normalized  $\Delta T'_{ND}(t)$  cooling dynamics deduced from a). Note that modification of  $D_m$  (dashed green line) does not modify the  $\Delta T'_{ND}(t)$  dynamics as compared to the reference case (plain black line). The computed cooling dynamics following nanodisk excitation by a single pump pulse are also shown for comparison in panels a) and b) (plain gray line).

The temporal evolution of nanodisk temperature rise following each pump pulse, in the reference case of Figure 3.15a, and for modified values of  $G$ ,  $\Lambda_m$ ,  $h_m$ , and  $D_m$ , is presented in Figure 3.17a.  $\Delta T'_{ND}(t)$  signals obtained after subtraction of the value at  $t = 0^-$  (i.e., the same treatment as in the case of experimental signals, to go from Figure 3.15a) to Figure 3.15b) are shown in Figure 3.17b. Results obtained by time-domain simulations with a single pump pulse are also shown for comparison.

While the main effect of a periodical nanodisk excitation is a nonvanishing  $\Delta T_{ND}(0^-)$  value, the  $\Delta T'_{ND}(t)$  signals obtained for excitation by single (gray line in Figure 3.17b) and multiple pump pulses (black line in Figure 3.17b) also differ at time scales exceeding 1 ns, justifying the use of the complete model presented here to analyze our experimental results (note that the discrepancy between the two signals would be greater for membranes thinner than those considered in this work, as in the next section of this chapter).  $G$ ,  $\Lambda_m$ , and  $h_m$  are shown to impact the normalized signals both before and after offset subtraction, while  $D_m$  only affects the offset value. This can be easily understood from the frequency-domain investigations discussed above, as  $D_m$  has an impact only at frequencies much smaller than  $f_{rep}$ , while excitation is performed with frequencies multiple of  $f_{rep}$  (see  $\tilde{q}(f)$  expression above). Therefore,  $D_m$  only affects the

zero-frequency component of the dynamics, i.e. the average nanodisk heating. Conversely,  $G$ ,  $\Lambda_m$ , and  $h_m$  affect not only the average temperature rise but also (and in different ways) the  $\Delta T'_{ND}(t)$  cooling dynamics as they impact the response function at many frequencies multiple of  $f_{rep}$ .

The average nanodisk temperature rise is thus sensitive to the far environment of the nanodisks, while conversely, the normalized cooling dynamics  $\Delta T'_{ND}(t)$  after offset subtraction is affected only by the characteristics of the close environment of the nanodisk, i.e. in the small region around the nanodisk where thermal energy penetrates at  $f_{rep}$  frequency (Figure 3.15b). Therefore, the  $\Delta T'_{ND}(t)$  dynamics can be quantitatively analyzed even without precise knowledge of the membrane geometry and thermal properties over large scales.

### 3.5.3 Comparison between experiments and frequency-domain thermal model

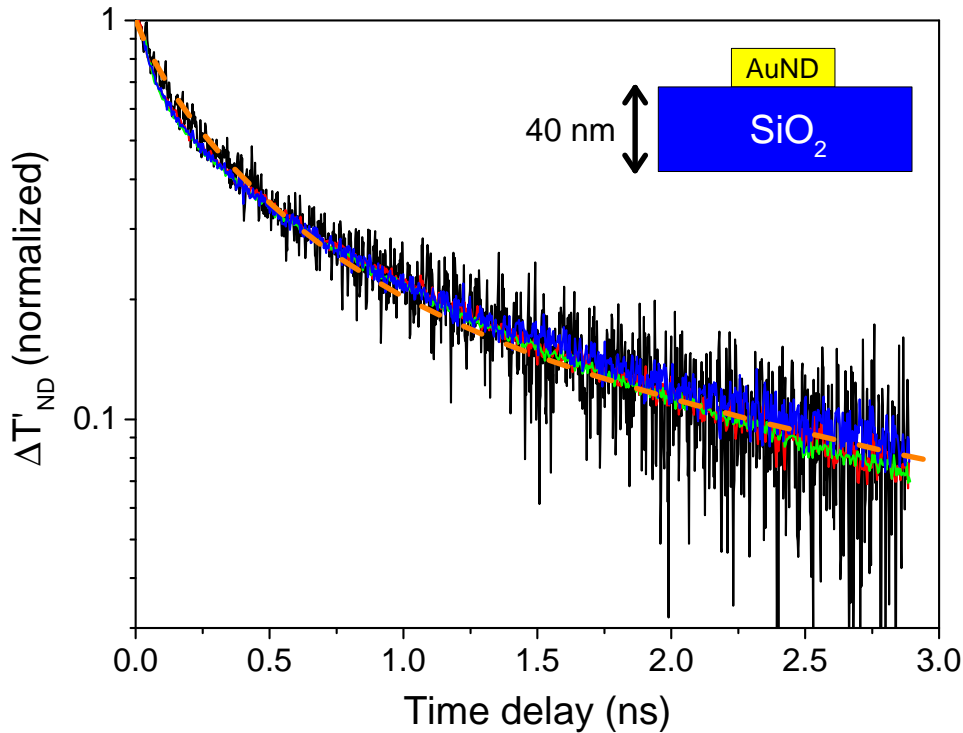


**Figure 3.18** – Comparison between measured and modeled cooling dynamics of gold nanodisks supported on a 40 nm thick  $\text{SiO}_2$  membrane. The measured signals (plain lines) correspond to those of Figure 3.13. The results of simulations based on the frequency-domain thermal model described in Chapter 2 Section 2.3.2.2 are shown as dashed orange lines. They were performed for  $D = 100$  nm,  $h = 10$  nm gold nanodisk, using  $G = 120$  MW m<sup>-2</sup> K<sup>-1</sup> and  $\Lambda_{\text{SiO}_2} = 1.4$  W m<sup>-1</sup> K<sup>-1</sup> for  $\text{SiO}_2$  thermal conductivity.

Direct comparisons between measured and modeled  $\Delta T'_{ND}(t)$  dynamics are shown in Figure 3.18 and 3.19 for the two membranes considered in this work. As the signals measured on each membrane for different nanodisks were very similar, they were collectively compared to

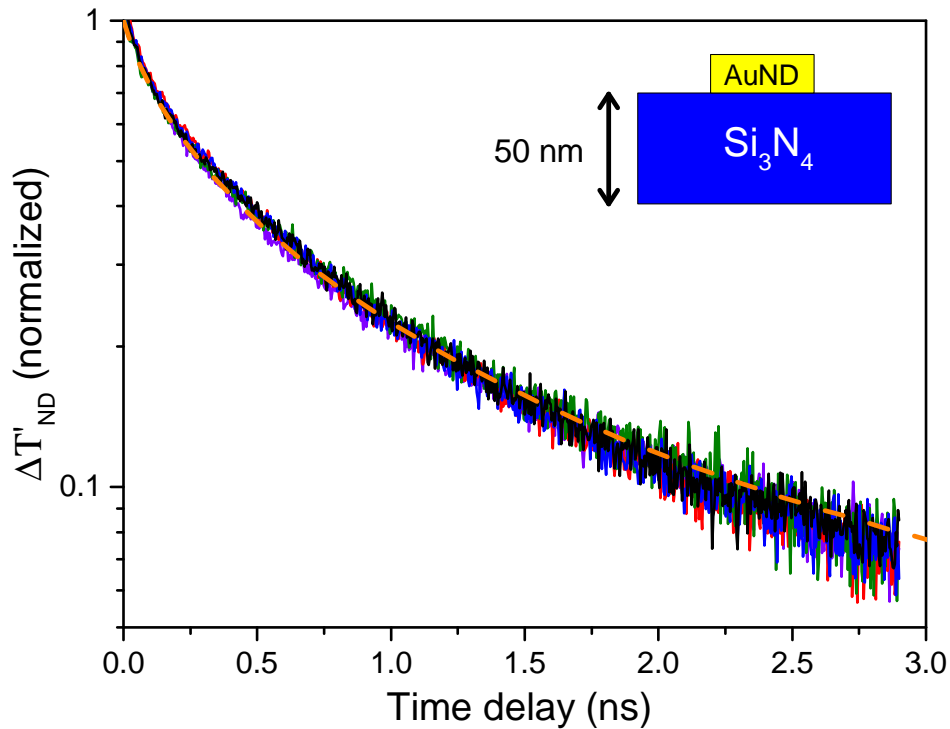


**Figure 3.19** – Comparison between measured and modeled cooling dynamics of gold nanodisks supported on a 50 nm thick  $\text{Si}_3\text{N}_4$  membrane. The measured signals (plain lines) correspond to those of Figure 3.13. The results of simulations based on the frequency-domain thermal model described in Chapter 2 Section 2.3.2.2 are shown as dashed orange lines. They were performed for  $D = 100$  nm,  $h = 10$  nm gold nanodisk, using  $G = 150$   $\text{MW m}^{-2} \text{K}^{-1}$  and  $\Lambda_m = 1$   $\text{W m}^{-1} \text{K}^{-1}$  for  $\text{Si}_3\text{N}_4$  thermal conductivity.

simulations performed for a  $D = 100$  nm,  $h = 10$  nm nanodisk, i.e.  $D$  and  $h$  values close to the average ones determined using SEM imaging and/or FEM modeling of extinction spectra (see Section 3.3.1 in this chapter and Section 2.1 in Chapter 2). The cooling dynamics of nanodisks deposited on a 40 nm thick silica membrane were well reproduced using  $G = 120$   $\text{MW m}^{-2} \text{K}^{-1}$  together with the  $\Lambda_m$  value of bulk silica (Figure 3.18). This  $G$  value stands at the upper end of the 40-140  $\text{MW m}^{-2} \text{K}^{-1}$  range of  $G$  values obtained for gold-silica interfaces in previous measurements and atomistic simulations [30–32, 116], which have also shown a large dependence of  $G$  on silica growth procedure and crystalline or amorphous character. The determined  $G$  value is also close to the  $G = 105$   $\text{MW m}^{-2} \text{K}^{-1}$  one previously obtained in the FemtoNanoOptics group in the context of thermal measurements on ensembles of gold nanospheres embedded in a glass with a large silica content [92]. The cooling dynamics of nanodisks deposited on a 50 nm thick silicon nitride membrane were also well reproduced by our simulations using slightly different parameters as in the silica case, namely  $G = 150$   $\text{MW m}^{-2} \text{K}^{-1}$  and  $\Lambda_m = 1$   $\text{W m}^{-1} \text{K}^{-1}$  (Figure 3.19). Here too, the deduced values of  $G$  and  $\Lambda_m$  are compatible with previous reports. Indeed, the deduced  $G$  value is close to the only (to our knowledge) value reported in the literature for Au/  $\text{Si}_3\text{N}_4$  interfaces,  $G = 120$   $\text{MW m}^{-2} \text{K}^{-1}$  [117], while the  $\Lambda_m$  value used for fitting our data falls within the broad 0.3-10  $\text{W m}^{-1} \text{K}^{-1}$  range of previous measurements on silicon nitride membranes with different stoichiometries and thicknesses [103–108]. The proximity of

the  $G$  and  $\Lambda_m$  values that we used for reproducing the  $\Delta T'_{ND}(t)$  dynamics on silica and silicon nitride membranes reflects the similarity of the experimental signals measured on these two membranes, whose thicknesses are also close. Not taking into account the periodical character of the excitation, which affects the  $\Delta T'_{ND}(t)$  dynamics (Figure 3.17b)), would have translated into slightly different (by about 15%) optimal values of the fitting parameters  $G$  and  $\Lambda_m$ .

### 3.6 Thermal behavior of single gold nanodisks deposited on an ultrathin amorphous membrane

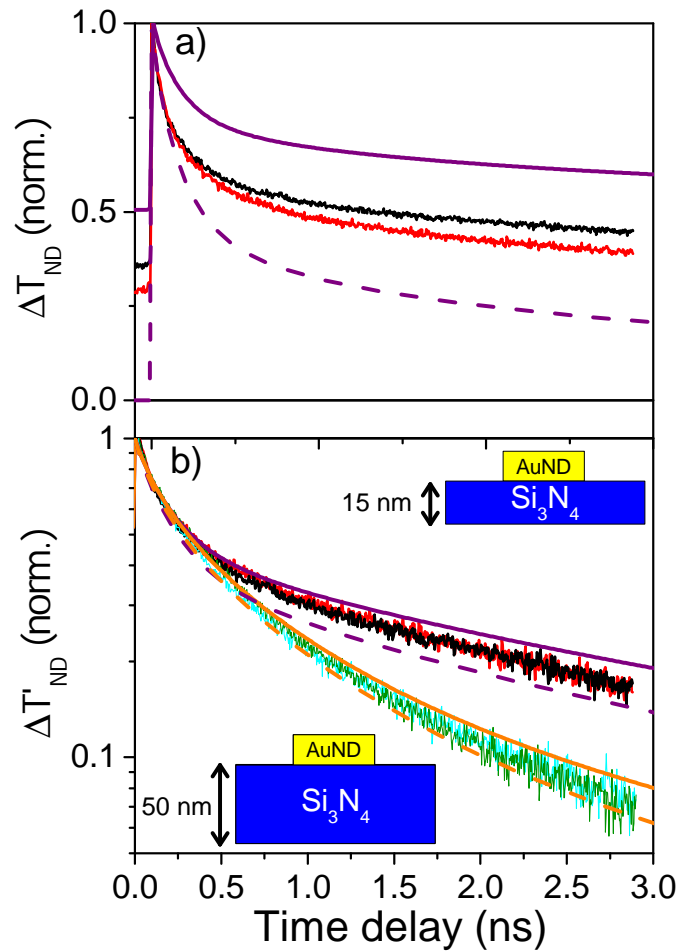


**Figure 3.20 – Thermal dynamics of single Au nanodisks on ultrathin Si<sub>3</sub>N<sub>4</sub> membranes.** (a) Normalized  $\Delta T_{ND}(t)$  temperature rise dynamics measured on two distinct gold nanodisks supported by a 15 nm thick Si<sub>3</sub>N<sub>4</sub> membrane (black and red traces) and  $\Delta T_{ND}(t)$  dynamics simulated with (solid purple line) and without (dashed line) inclusion of repetition effects in the modeling. (b)  $\Delta T'_{ND}(t)$  quantity presented with a logarithmic scale (same color code). The signals previously measured for two different nanodisks (blue and green traces) and modeled (solid and dashed orange lines) for a 50 nm thick membrane are also shown for comparison.

### 3.6. Thermal behavior of single gold nanodisks deposited on an ultrathin amorphous membrane

To more precisely analyze the membrane thickness effect on nanodisk cooling dynamics, additional time-resolved measurements were conducted on single gold nanodisks deposited on a 15 nm thick  $\text{Si}_3\text{N}_4$  membrane using a probe wavelength close to their Surface Plasmon Resonance. The normalized thermal components of the signals measured on two distinct nanodisks in these specific conditions are shown in Figure 3.20a. The normalized  $\Delta T_{ND}(t)$  dynamics of the two nanodisks exhibit slightly different average values at negative times (0.3 and 0.35). These values significantly exceed the  $\approx 0.1$  ones measured on nanodisks stemming from the same colloidal solution but deposited on a thicker (50 nm thick)  $\text{Si}_3\text{N}_4$  membrane (see Section 3.5.1 and Figure 3.12). This considerable increase of the normalized value of  $\Delta T_{ND}(0^-)$ , i.e., the temperature rise at the end of the interval separating two successive pump pulses, constitutes a first indication of the slowing down of nanodisk cooling dynamics with decreasing membrane thickness, discussed in more detail below.

The nanodisk cooling dynamics shown in Figure 3.20a become very similar if temperature rises are defined relatively to the nanodisk temperature before each pump excitation, rather than to that in the absence of any excitation. This is shown in Fig. 3.20b, where the normalized  $\Delta T'_{ND}(t)$  dynamics are plotted alongside previous measurements on nanodisks supported on a 50 nm thick  $\text{Si}_3\text{N}_4$  membrane, highlighting  $\Delta T'_{ND}(t)$  strong dependence on membrane thickness. The  $\Delta T'_{ND}(t)$  dynamics measured for nanodisks deposited on 15 nm thick  $\text{Si}_3\text{N}_4$  membranes exhibit a non-exponential behavior, indicating that they are not solely ruled by heat transfer at the nanodisk-membrane interface [92]. While they resemble those previously recorded on 50 nm thick membrane at  $<0.5$  ns delays, they become much slower at larger delays (Figure 3.20b), presenting for example  $3\times$  higher normalized  $\Delta T'_{ND}(t)$  values after 2.7 ns, the largest pump-probe delays achievable in our experiments.

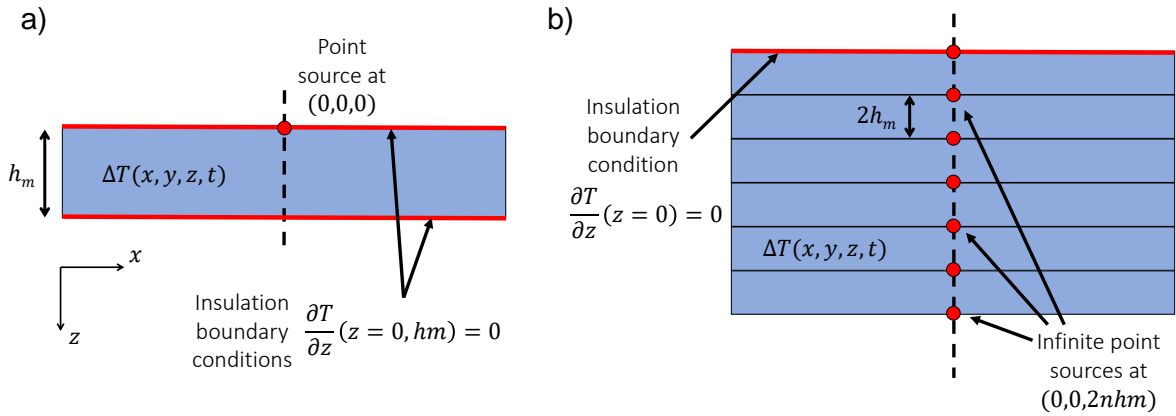


**Figure 3.21 – Schematic of a) a membrane of thickness  $h_m$  and infinite lateral extension heated by a point source located at  $(0, 0, 0)$  on its surface and b) a 3D semi-infinite medium heated by an infinite number of virtual point sources at locations  $(0, 0, 2nh_m)$ .** In both cases, there is an insulation boundary condition at the top surface of the two medium with  $\frac{\partial T}{\partial z}(z=0) = 0$  while there is an additional one at the bottom surface of the membrane with  $\frac{\partial T}{\partial z}(h_m) = 0$ .

The observed membrane thickness effect on  $\Delta T'_{ND}(t)$  dynamics can be qualitatively understood by considering the solutions of the Fourier heat equation (see Equation 1.61 in Chapter 1 Section 1.3.2.1) for a point source located at  $(0, 0, 0)$  on the surface of a membrane of thickness

$h_m$  ( $0 < z < h_m$ ) and of infinite lateral extension, initially at a uniform temperature, with insulation boundary conditions on the membrane surfaces ( $\frac{\partial T}{\partial z}(z=0) = \frac{\partial T}{\partial z}(z=h_m) = 0$ ) (see Figure 3.21). The time- and position-dependent temperature rise  $\Delta T$  in the membrane can be deduced from the solution of the heat equation in a 3D semi-infinite medium

$$\Delta T(x, y, z, t) \propto t^{-\frac{3}{2}} \exp\left(\frac{-(x^2 + y^2 + z^2)}{4\alpha_m t}\right) \quad (3.6)$$

by adding the effect of an infinity of virtual sources at positions  $(0,0,2nh_m)$ , with  $n$  an integer [118, 119] (Figure 3.21), and writes

$$\Delta T(x, y, z, t) \propto t^{-\frac{3}{2}} \exp\left(\frac{-(x^2 + y^2)}{4\alpha_m t}\right) \sum_{n=-\infty}^{\infty} \exp\left(\frac{-(z - 2nh_m)^2}{4\alpha_m t}\right). \quad (3.7)$$

The temperature rise  $\Delta T$  is thus obtained by multiplying the solution for a point source at the surface of an infinite 2D medium (Gaussian distribution with a width increasing as  $t^{1/2}$ ) by the solution for a point source on a 1D finite slab (Jacobi theta function). At short time scales ( $\alpha_m t \ll h_m^2$ ), the sum is dominated by its  $n = 0$  term, and  $\Delta T$  approximately coincides with the solution for a 3D semi-infinite substrate, with a  $t^{-3/2}$  dependence at the source position. Conversely, at long time scales ( $\alpha_m t \gg h_m^2$ , so that the sum can be approximated by an integral),  $\Delta T \propto \frac{1}{th_m} \exp\left(\frac{-(x^2+y^2)}{4\alpha_m t}\right)$ , which corresponds to a uniform temperature along the membrane thickness and a lateral 2D diffusion of heat. The transition between the two regimes occurs for  $\alpha_m t \approx h_m^2$ , i.e., for a  $\text{Si}_3\text{N}_4$  membrane ( $\alpha_m = 5 \times 10^{-7} \text{ m}^2 \text{ s}^{-1}$ , assuming a  $\Lambda_m = 1 \text{ W m}^{-1} \text{ K}^{-1}$  thermal conductivity) at times of the order of 0.5 ns and 5 ns for  $h_m = 15 \text{ nm}$  and  $h_m = 50 \text{ nm}$ , respectively. Although based on a simplified analysis, the 0.5 ns transition time for a  $h_m = 15 \text{ nm}$  membrane corresponds well with that at which experimental signals measured on the two membranes start to significantly deviate (Figure 3.20b).

The  $\Delta T'_{ND}(t)$  dynamics of nanodisks deposited on 15 nm thick membranes can be accurately reproduced using the same values of  $G$  and  $\Lambda_m$  as in the case of 50 nm thick membranes, namely  $G = 150 \text{ MW m}^{-2} \text{ K}^{-1}$  and  $\Lambda_m = 1 \text{ W m}^{-1} \text{ K}^{-1}$ . This is illustrated in Figure 3.20b, which shows the  $\Delta T'_{ND}(t)$  dynamics computed for nanodisks supported on  $\text{Si}_3\text{N}_4$  membranes using these  $G$  and  $\Lambda_m$  values (solid purple and orange lines). The excellent reproduction of experimental signals at  $< 0.5 \text{ ns}$  delays (at which  $\Delta T'_{ND}$  dynamics are mostly controlled by  $G$  and  $\Lambda_m$ ) using  $G = 150 \text{ MW m}^{-2} \text{ K}^{-1}$  and  $\Lambda_m = 1 \text{ W m}^{-1} \text{ K}^{-1}$  indicates that these values constitute accurate estimations of  $G$  and  $\Lambda_m$  (with uncertainties of the order of 10%) for both 50 and 15 nm thick membranes. The slight shift between the measured and modeled  $\Delta T'_{ND}(t)$  dynamics at  $> 1 \text{ ns}$  delays could have several causes, including a slight difference between the nominal and actual values of the membrane thickness.

Regarding the  $\Delta T_{ND}(t)$  dynamics (Figure 3.20a), one can observe that the  $\Delta T_{ND}(0^-)$  temperature rises predicted by the model are higher by about 50% than the measured ones, similarly to previous observations for  $\approx 50 \text{ nm}$  thick membranes. This difference, which would increase with the use in the modeling of larger  $D_m$  values, closer to the actual membrane size, suggests that the thermal coupling of the membrane with ambient air taking place at the top and bottom planar surfaces of the membrane (not included in the modeling where dissipation only occurs at the membrane lateral ends) plays a significant role in large-scale membrane cooling. The deduction of similar  $\Lambda_m$  values from the analysis of the  $\Delta T'_{ND}(t)$  dynamics measured on 50 nm and 15 nm thick membranes stands in stark contrast to findings on silicon membranes of similar

thickness, whose thermal conductivity was seen to be strongly thickness-dependent and up to  $\approx 5$  times smaller than the bulk silicon one [120]. This disparity in the thickness-dependence of the thermal properties of  $\text{Si}_3\text{N}_4$  and Si membranes can be attributed to the large difference between the heat conductivity and phonon mean free paths of these two materials in the bulk form. Indeed, amorphous media such as silica and silicon nitride have a  $\approx 1$  nm room temperature phonon mean free path, while in crystalline silicon a large fraction of phonons have  $>100\times$  longer mean free paths [27, 81, 91]. Experimental observations are thus consistent with the fact that membrane thickness reduction in the tens of nm range should significantly diminish the mean free path of phonons in Si, but not in  $\text{Si}_3\text{N}_4$ .

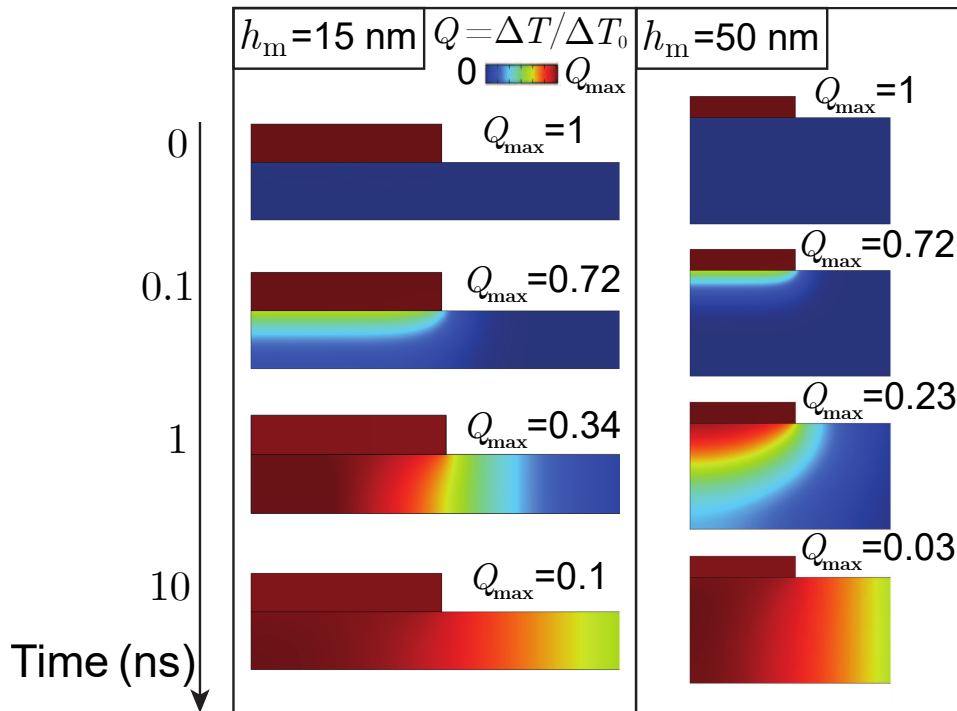


**Figure 3.22** – Temperature profiles computed using FEM at time delays of 0, 0.1, 1 and 10 ns after the sudden optical excitation of a nanodisk located on a 15 nm (left) or 50 nm (right) thick  $\text{Si}_3\text{N}_4$  membrane. The  $Q = \Delta T/\Delta T_0$  ratios are plotted using a color scale ranging from 0 to  $Q_{max}$ , which corresponds to the  $Q$  value inside the nanodisk at each considered time (indicated).

The  $\Delta T_{ND}(t)$  dynamics were also computed in the case of nanodisk excitation by a single pump pulse, which corresponds to discarding accumulation effects (dashed lines in Figure 3.20). These complementary calculations allow to appreciate the respectively strong and relatively weak influences of a repeated nanodisk excitation on the  $\Delta T_{ND}(t)$  and  $\Delta T'_{ND}(t)$  dynamics. They also enable a clear visualization of the transition from a 3D to a 2D heat diffusion in a membrane heated by a source located at its surface, discussed above based on analytical expressions. This transition is illustrated in Figure 3.22, which presents snapshots of the temperature profiles computed for single pulse excitation of a nanodisk positioned on a 15 nm or 50 nm thick membrane. At  $t = 0.1$  ns heat diffusion presents a distinct 3D character, with only regions less than 10 nm away from the nanodisk being significantly heated. Conversely, at  $t = 1$  ns the temperature

profile has become independent of depth for a 15 nm thick membrane (but not for a 50 nm thick one). At  $t = 10$  ns (a delay exceeding the experimentally accessible ones) diffusion has evolved into a 2D process in both cases, resulting in depth-independent temperature distributions.

## 3.7 Conclusion

In this chapter time-resolved experiments conducted on single gold nanodisks deposited on different substrates have shown, firstly, that on a given substrate the cooling dynamics from one nanodisk to another were reproducible. However, the observed dynamics highly depended on the substrate and especially on its thickness. The measurements were also well reproduced with FEM models with a unique excitation (sapphire substrate) or periodic excitation (thin and ultrathin membranes) using bulk values for the thermal conductivities of sapphire and  $\text{SiO}_2$  leading to reasonable interface conductance  $G$  deduced values for the gold-substrates interfaces (and thermal conductivity value for  $\text{Si}_3\text{N}_4$ ).

Experiments have also shown that, even for the ultrathin membrane, there were no clear signatures of non-diffusive heat propagation in the studied substrates. Indeed, FEM models were successful at reproducing the experimental data without having to introduce a thickness-dependent conductivity. This could be explained, in the case of the sapphire substrate, by the interface-limited dynamics, which are weakly sensitive to the way heat propagates in the substrate. Note that previous studies have shown that the effective value of the conductivity of the sapphire substrate could be modified near nanoheaters with lateral sizes around 100 nm by ballistic effects [39] [101]. Moreover, the absence of signature for thin membranes could result from the fact that their thicknesses were still much larger than their average phonon mean free paths.

The results presented in this chapter have been described in papers entitled "Cooling Dynamics of Individual Gold Nanodisks Deposited on Thick Substrates and Nanometric Membranes" and "Impact of supporting nanometric membranes on the thermo-optical dynamics of individual plasmonic nanodisks" published in *Journal of Physical Chemistry Letters* in 2023 and in *Nanoscale* in 2024, respectively [121, 122].

Future work could aim to reproduce these experiments on other thin membranes like silicon for example, for which non diffusive effects have been demonstrated [91, 97].

# Chapter 4

## Optical detection of the cooling dynamics of single plasmonic nanoparticles

### 4.1 General context

In optical time-resolved spectroscopy, the ultrafast phenomena following the sudden excitation of a nanosystem, such as its thermal cooling or acoustic vibrations, are indirectly detected from the changes of the optical response they induce. The pump-probe technique used in our FemtoNanoOptics group gives in particular access to the temporal variations of the extinction cross-section of a single nanoparticle following its initial excitation by a femtosecond pump pulse (see Chapter 1 Section 2.2.3). In the previous chapter, probing of the thermal dynamics of single nanodisks was performed using a specific probe wavelength coinciding with the central position of the nanodisk Surface Plasmon Resonance, ensuring a proportionality between the measured time-resolved signals and the transient nanodisk temperature rise.

In this chapter a more complete characterization of the transient optical response of single gold nanodisks, based on the reproduction of time-resolved experiments with multiple probe wavelengths, will be presented. This work aims at a better understanding of the link between the signals measured in the context of optical time-resolved measurements on metal nanoparticles and the thermal dynamics in these nano-objects and at their vicinity. It also aims at determining the optimal working conditions to probe the thermal dynamics in nanosystems and at their vicinity with maximal sensitivity.

#### 4.1.1 Link between optical measurements and heating of the nanoparticle and its environment

The situation considered throughout this chapter will be that of a single metallic nanodisk supported on a solid substrate, specifically a thin transparent membrane as represented in Figure 4.1. As a starting point, the case of uniform temperatures in both the nanodisk and the membrane will be considered with their temperatures being noted  $T_{ND}$  and  $T_m$ , respectively. However, a more advanced model able to account for non-uniform temperature distributions

will be presented later in this chapter (see thermo-optical model in Section 4.2.7). The complex dielectric function of the metal composing the nanodisk is denoted as  $\epsilon = \epsilon_1 + i\epsilon_2$  and  $\epsilon_m$  the real one of the transparent membrane.

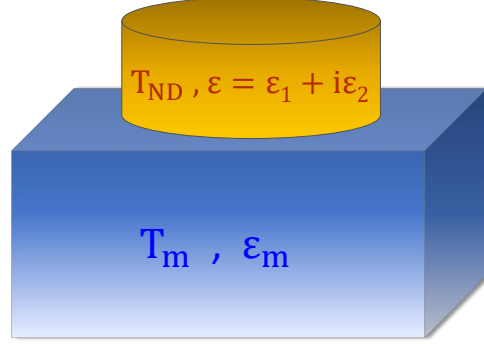


**Figure 4.1 – Schematic of the metallic nanodisk-thin membrane system considered in this chapter.** The nanodisk is characterized by its temperature  $T_{ND}$  and complex dielectric function  $\epsilon = \epsilon_1 + i\epsilon_2$  while the thin transparent membrane is described by its temperature  $T_m$  and real dielectric function  $\epsilon_m$ .

The interaction of a nanodisk with light can be described by the nanodisk extinction cross-section  $\sigma_{ext}$ , that depends on the wavelength and on the dielectric functions of the nanodisk and the membrane, as previously explained in Chapter 1 Section 1.2. If the two components of this system see their temperatures vary by quantities  $\Delta T_{ND}$  and  $\Delta T_m$ , as compared to a reference temperature (e.g. ambient temperature around 300 K) then their dielectric functions will change accordingly. Indeed, the dielectric functions generally depend on the temperature of the material. The result of these changes will then be a variation of the extinction cross-section of the nanodisk, from  $\sigma_{ext}$  to  $\sigma_{ext} + \Delta\sigma_{ext}$ .

In the case of small temperature variations, the transient extinction changes can be linearly linked to the variations of temperature of both the nanodisk and the membrane via

$$\Delta\sigma_{ext}(\lambda, t) = A_{ND}(\lambda)\Delta T_{ND}(t) + A_m(\lambda)\Delta T_m(t) \quad (4.1)$$

with

$$A_{ND}(\lambda) = \frac{\partial\sigma_{ext}}{\partial\epsilon_1}(\lambda)\frac{\partial\epsilon_1}{\partial T_{ND}}(\lambda) + \frac{\partial\sigma_{ext}}{\partial\epsilon_2}(\lambda)\frac{\partial\epsilon_2}{\partial T_{ND}}(\lambda) \quad (4.2)$$

$$A_m(\lambda) = \frac{\partial\sigma_{ext}}{\partial\epsilon_m}(\lambda)\frac{\partial\epsilon_m}{\partial T_m}(\lambda). \quad (4.3)$$

The  $A_{ND}$  and  $A_m$  quantities represent the sensitivities of the nanodisk optical response (more precisely, of its extinction cross-section) to heating in the nanodisk and in its local environment, respectively. They involve products between two types of terms:

- First, the sensitivity of the extinction cross-section of the nanodisk to the dielectric functions of the nanodisk and its environment ( $\frac{\partial\sigma_{ext}}{\partial\epsilon_{1,2}}(\lambda)$  and  $\frac{\partial\sigma_{ext}}{\partial\epsilon_m}(\lambda)$  terms, which will be referred to in the following as *plasmonic derivatives*). This sensitivity depends on the composition, morphology and environment of the considered nano-object (see Chapter 1 Section 1.2).

- Secondly, the sensitivities of the nanodisk and environment dielectric functions to temperature changes ( $\frac{\partial \epsilon_{1,2}}{\partial T_{ND}}(\lambda)$  and  $\frac{\partial \epsilon_m}{\partial T_m}(\lambda)$  terms). These terms only depend on the compositions of the nano-objects and of their environment (respectively gold and silicon nitride in the experimental work described in this chapter).

Equation 4.1 shows that, in general, the optical signal measured in the context of time-resolved measurements, in our case the temporal variations of the extinction cross-section of the nanodisk  $\Delta\sigma_{ext}(\lambda_{pr}, t)$ , is the sum of two distinct contributions: one coming from the heating of the nanodisk and another one originating from the heating of the membrane.

The environment heating contribution ( $A_m(\lambda)\Delta T_m(t)$  term in Equation 4.1) is often weak, and the assumption of a proportionality between the measured pump-probe signals and the temperature rise of the investigated nanosystems has often been implicitly performed in the literature. It is generally justified for metal nanoparticles as  $\left|\frac{\partial \epsilon_{1,2}}{\partial T}\right|$  is of the order of  $10^{-3} \text{ K}^{-1}$  (see refs. [19, 123] for gold) while  $\left|\frac{\partial \epsilon_m}{\partial T}\right|$  is of the order of  $10^{-5} \text{ K}^{-1}$  to  $10^{-4} \text{ K}^{-1}$  in the case of a solid dielectric (e.g.  $\text{Si}_3\text{N}_4$  or  $\text{SiO}_2$ , see Table 4.1). However, some transparent materials are known to possess a stronger sensitivity of their dielectric function to temperature, like ethanol for example where  $\left|\frac{\partial \epsilon_m}{\partial T}\right|$  is of the order of  $10^{-3} \text{ K}^{-1}$  [124], i.e. of the same order as the  $\left|\frac{\partial \epsilon_{1,2}}{\partial T}\right|$  value in gold (see Table 4.1).

	$\epsilon_m$	$\left \frac{\partial \epsilon_m}{\partial T}\right $ ( $\text{K}^{-1}$ )
$\text{SiO}_2$	2.1	$0.96 \cdot 10^{-5}$
$\text{Si}_3\text{N}_4$	4.1	$2.51 \cdot 10^{-5}$
Sapphire $\text{Al}_2\text{O}_3$	1.77	$5 \cdot 10^{-5}$
Water	1.77	$2.4 \cdot 10^{-4}$
Ethanol	1.86	$1.1 \cdot 10^{-3}$

**Table 4.1 – Dielectric constants and sensitivities of the dielectric function to temperature for several solids and liquids [124–127].**

### 4.1.2 Previous study: ensembles of Au nanospheres in ethanol

Work done previously in the FemtoNanoOptics group, in the framework of Tatjana Stoll’s PhD work, demonstrated a strong contribution of environment heating to the time-resolved signals measured on gold nanospheres immersed in ethanol [29, 128]. The gold nanospheres investigated in this study had a diameter  $D$  close to 20 nm and displayed a Surface Plasmon Resonance centered at 525 nm in ethanol (see Figure 4.2a)

The time-resolved signals measured using different probe wavelengths displayed very different temporal dynamics, an observation inconsistent with a probing in all cases of the nanospheres heating (by pump pulses) and cooling (by heat dissipation in ethanol). A thermo-optical model more advanced than the one described in section 4.1.1 was developed to clarify the contributions of gold and ethanol heating to the measured time-resolved signals. The modelization took into account the thermal processes (nanosphere and ethanol cooling dynamics with interface heat transfer and thermal diffusion mechanisms) and optics (temporal probe transmission changes induced by the thermal processes) involved. In particular the formalism described in equation 4.1

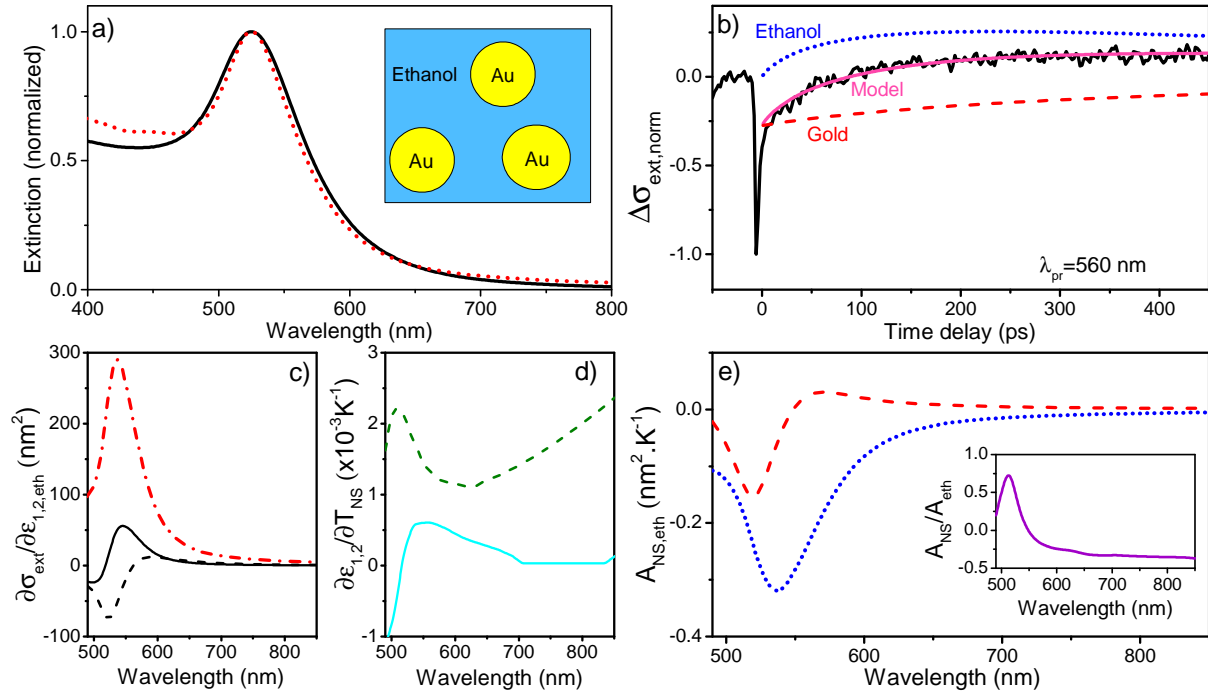


**Figure 4.2 – Time-resolved investigations and modeling of the thermo-optical dynamics of ensembles of gold nanospheres in ethanol. Figure adapted from previous work done in the FemtoNanoOptics group [29, 128].** a) Normalized extinction spectrum of gold nanospheres in ethanol (with a diameter  $D = (18.5 \pm 3.0)$  nm) and fit with Mie theory in dipolar approximation (respectively full black line and dashed red line) b) Normalized transient variations of the extinction cross-section  $\Delta\sigma_{ext}$  for an ensemble of gold nanospheres in ethanol with a probe wavelength  $\lambda_{pr} = 560$  nm (black). The colored lines correspond to the results of a semi-analytical thermo-optical model. The solid pink line corresponds to the total extinction change computed using this model, while the dashed red and dotted blue lines correspond to the contributions of gold and ethanol heating to these extinction changes, respectively. c) Plasmonic derivatives  $\frac{\partial\sigma_{ext}}{\partial\epsilon_1}$  (full black line),  $\frac{\partial\sigma_{ext}}{\partial\epsilon_2}$  (dashed black line) and  $\frac{\partial\sigma_{ext}}{\partial\epsilon_{eth}}$  (dash-dotted red line) obtained via Mie theory for a single Au nanosphere in ethanol with  $D = 18.5$  nm. d) Dielectric function temperature dependences for gold with  $\frac{\partial\epsilon_1}{\partial T_{NS}}$  as the cyan line and  $\frac{\partial\epsilon_2}{\partial T_{NS}}$  as the dashed green line (data from [19]). e) Sensitivities of the Au nanospheres optical response to nanospheres heating  $A_{NS}$  and to ethanol heating  $A_{eth}$  (dashed red line and dotted blue line, respectively) deduced from 4.2 and 4.3. The inset represents the  $A_{NS}/A_{eth}$  ratio (full purple line).

was extended through the decomposition of the nanosphere's environment into  $N$  concentric thin shells with different temperatures, allowing to take into account the inhomogeneous temperature in the surrounding ethanol. The equation describing the transient extinction changes becomes

$$\Delta\sigma_{ext}(\lambda, t) = A_{NS}(\lambda)\Delta T_{NS}(t) + \sum_{k=1}^N A_{eth}^{(k)}(\lambda)\Delta T_{eth}^{(k)}(t) \quad (4.4)$$

with

$$A_{eth}^{(k)}(\lambda) = \frac{\partial \sigma_{ext}}{\partial \epsilon_{eth}^{(k)}}(\lambda) \frac{\partial \epsilon_{eth}}{\partial T_{eth}} \quad (4.5)$$

where  $\Delta T_{eth}^{(k)}$  is the variation of temperature in the  $k^{th}$  shell,  $A_{eth}^{(k)}$  the associated optical sensitivity and  $\epsilon_{eth}^{(k)}$  the local dielectric function. The measured pump-probe signal with a probe at  $\lambda = \lambda_{pr} = 560$  nm as well as the deduced contributions from the gold nanospheres and the ethanol ( $A_{NS}(\lambda)\Delta T_{NS}(t)$  and  $\sum_{k=1}^N A_{eth}^{(k)}(\lambda)\Delta T_{eth}^{(k)}(t)$  terms in Equation 4.4) are shown in Figure 4.2b.

As shown by this figure, the heating of the ethanol leads to a significant contribution to the time-resolved measurements at the probe wavelength  $\lambda_{pr} = 560$  nm. The weights of the contribution from the heating of the gold nanospheres and from the ethanol highly depend on the probe wavelength: indeed, the plasmonic derivatives ( $\frac{\partial \sigma_{ext}}{\partial \epsilon_{1,2}}(\lambda)$  and  $\frac{\partial \sigma_{ext}}{\partial \epsilon_m}(\lambda)$ , shown in Figure 4.2c) as well as the sensitivity of the dielectric function of gold to temperature ( $\frac{\partial \epsilon_{1,2}}{\partial T_{NS}}(\lambda)$ , see Figure 4.2d) both exhibit a clear dependence on the probe wavelength. In terms of absolute values, the sensitivity of the dielectric functions of gold to temperature is of the same order ( $10^{-3} \text{ K}^{-1}$ ) as the sensitivity of the dielectric function of ethanol to temperature (with  $\frac{\partial \epsilon_m}{\partial T_m} = -1.1 \cdot 10^{-3} \text{ K}^{-1}$ ), while the maximal absolute value of  $\frac{\partial \sigma_{ext}}{\partial \epsilon_m}(\lambda)$  is 6 times larger than the maximal absolute values of  $\frac{\partial \sigma_{ext}}{\partial \epsilon_{1,2}}(\lambda)$ . Finally, the optical sensitivities to gold heating  $A_{NS}$  and to ethanol heating  $A_{eth}$ , which are represented in Figure 4.2e (with an inset showing the  $A_{NS}/A_{eth}$  ratio), were deduced from the previous quantities through Equations 4.2 and 4.3. The optical sensitivity to ethanol heating  $A_{eth}$  was found to be always larger (in absolute value) than the optical sensitivity to gold spheres heating  $A_{NS}$ . A sufficient heating of the ethanol was thus able to produce a contribution of the ethanol to the optical signal that could not be neglected compared to the contribution of the gold nanospheres, as it is the case at  $\lambda_{pr} = 560$  nm in Figure 4.2b for example. Figure 4.2e also shows that  $A_{eth}$  is always negative while  $A_{NS}$  can be either positive or negative depending on the probe wavelength and especially crosses 0 around  $\lambda_{pr} = 550$  nm: the contribution of the nanospheres heating to the optical signal can thus vanish.

### 4.1.3 Previous study: single gold nanodisk lithographed on a thick sapphire substrate

Another work performed in the FemtoNanoOptics group, in the framework of Romain Rouxel's PhD work, illustrated the other extreme case of a negligible contribution of environment heating to time-resolved signals, with in this case a proportionality between the measured optical signals and the temperature rise of the studied system (see equation 4.1), in that case a single gold nanodisk produced by electron beam lithography on a thick sapphire substrate [25, 112]. In this work, time-resolved experiments with tunable probe wavelength were performed on a single gold nanodisk exhibiting a Surface Plasmon Resonance near 700 nm wavelength. The raw signals obtained via these experiments using a large probe wavelength window, normalized by the initial temperature rise of the nanodisk induced by each pump pulse  $\Delta T_0$ , are represented in Figure 4.3. These signals exhibit a clear and high dependence on the probe wavelength linked to the wavelength dependence of the  $A_{ND}$  term in Equation 4.1. As described in Chapter 1 Section 1.2.3, the time-resolved signals display features associated to three distinct physical phenomena: an electronic excitation and internal thermalization, damped acoustic vibrations, and thermal cooling. The component associated to the first process was not considered while the acoustic

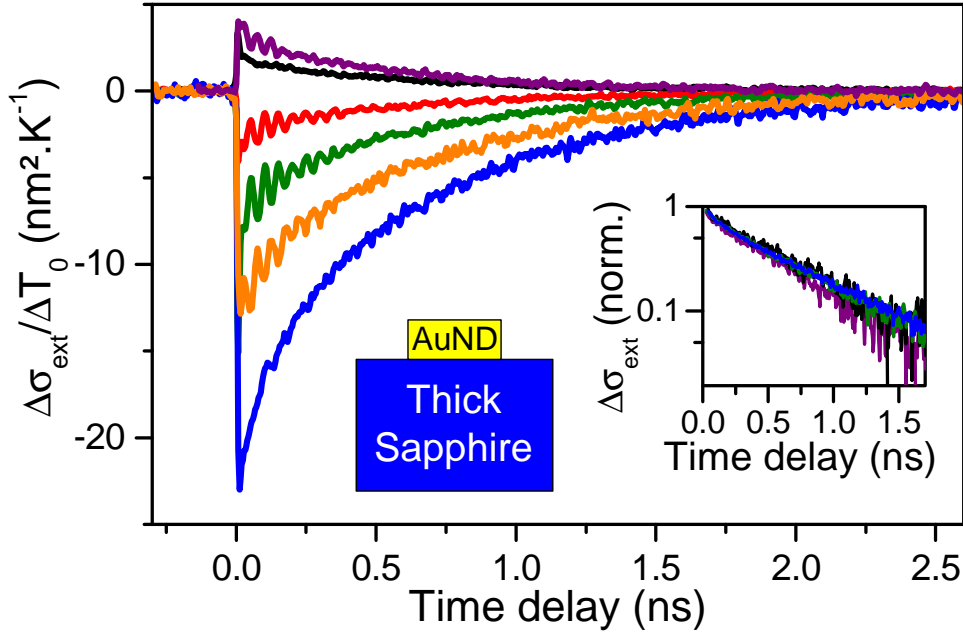


Figure 4.3 – Transient variations of the extinction cross-section normalized by the initial heating of the nanodisk and normalized thermal components (inset, in semi-logscale) for a single gold nanodisk deposited on thick sapphire with  $D = 101$  nm and  $h = 21$  nm. Figure adapted from previous work done in the FemtoNanoOptics group [25]. Measurements were done using  $\lambda_{pr} - \lambda_{SPR} = -180$  nm (black),  $-40$  nm (red),  $-25$  nm (green),  $+18$  nm (blue),  $+30$  nm (orange),  $+90$  nm (purple).

one was subtracted from the raw time-resolved signals in order to get the normalized thermal parts of the signals which are plotted in the inset of Figure 4.3 (see data treatment steps in Chapter 3 section 3.3.4).

Figure 4.3 shows that all the normalized components overlap and present a monotonic decay, which is consistent with probing of the nanodisk temperature only with a probe wavelength-dependent sensitivity, i.e.:

$$\Delta\sigma_{\text{ext}}(\lambda_{pr}, t) \propto \Delta T_{ND}(t). \quad (4.6)$$

## 4.2 Optical investigations on single Au nanodisks deposited on a thin silicon nitride membrane

### 4.2.1 Relevance of the studied system

As discussed above, the case of gold nanoparticles in ethanol is very favorable for observing the environment heating contribution to time-resolved optical signals because of the large temperature-dependence of the ethanol dielectric constant. This temperature dependence is much lower in most solid media (see Table 4.1). As far as we know, no demonstration of environment heating contribution to time-resolved signals had been reported yet in this case.

In order to be able to detect the contribution of the solid medium in experiments this substrate has to present several characteristics: first, a refraction index largely dependent on temperature and, secondly, a significant temperature rise during time-resolved experiments. In this regard, one of the solid substrates investigated in the previous chapter is especially promising: the 15 nm thick  $\text{Si}_3\text{N}_4$  membrane. Indeed this substrate exhibits a relatively high dependence of its dielectric function to temperature with  $\frac{\partial \epsilon_m}{\partial T_m} = 10^{-4} \text{ K}^{-1}$ , compared to other transparent materials. Additionally, the previous chapter has shown that time-resolved experiments conducted on single gold nanodisks supported by a thin amorphous membrane and specifically a 15 nm thick  $\text{Si}_3\text{N}_4$  membrane lead to slower cooling dynamics than for the other substrates, meaning that the most significant temperature increase was found for experiments done on single nanodisks supported by this ultrathin membrane. The last specificity of the experiments that were done here is the choice of single-particle measurements as opposed to the measurements done in ensembles for the gold nanospheres in ethanol. The absence of heterogeneous broadening effects in such experiments can effectively help to observe the contribution of membrane heating which, as discussed below, manifests only in a narrow spectral range.

## 4.2.2 Optical measurements and time-resolved signals

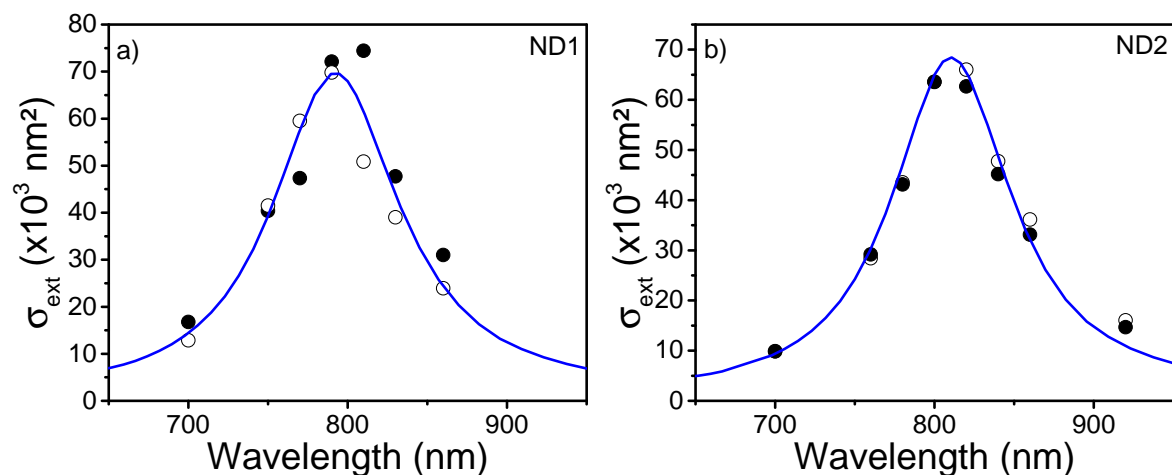


**Figure 4.4 – Extinction spectra of the gold nanodisks a) ND1 and b) ND2.** The full and empty markers in the data points correspond to the two orthogonal polarizations of the two nanodisk. The solid blue lines are the FEM simulations with  $D = 96.2 \text{ nm}$  and  $h = 10.8 \text{ nm}$  for ND1 and  $D = 93 \text{ nm}$  and  $h = 9.5 \text{ nm}$  for ND2.

In this work, we performed time-resolved measurements with tunable probe wavelength on two distinct individual nanodisks (referred to in the following as ND1 and ND2). The extinction spectra obtained by Spatial Modulation Spectroscopy (see Chapter 2 Section 2.2.2) of the gold nanodisks ND1 and ND2 are shown in Figure 4.4. These measurements were performed with two orthogonal polarizations of the incident light. The spectra, which are quasi-Lorentzian as a function of energy, present Surface Plasmon Resonances located around 800 nm for ND1 and 810 nm for ND2. There is also a slight shift of the central wavelength of the resonance ( $\approx 10 \text{ nm}$ ) between the two orthogonal polarizations for ND1, an observation consistent with quasi-circular

sections for the two investigated nanodisks [63]. As described in chapter 3, optical FEM was used to simulate the nanodisk extinction spectra and determine, for each nanodisk, the dimensions leading to a good reproduction of the experimental extinction spectra. The dimensions obtained via this method are  $D \approx 96.2$  nm and  $h \approx 10.8$  nm for ND1 and  $D \approx 93$  nm and  $h \approx 9.5$  nm for ND2. These values are close to the average diameter of the synthesized nanodisks with  $D \approx 100$  nm which was measured thanks to electron microscopy (as described in Chapter 2 Section 2.1). The deduced thicknesses are also of the same order than what was deduced from SEM images of nanodisks contacting the substrate via their lateral surface, i.e.  $h \approx 10$  nm.

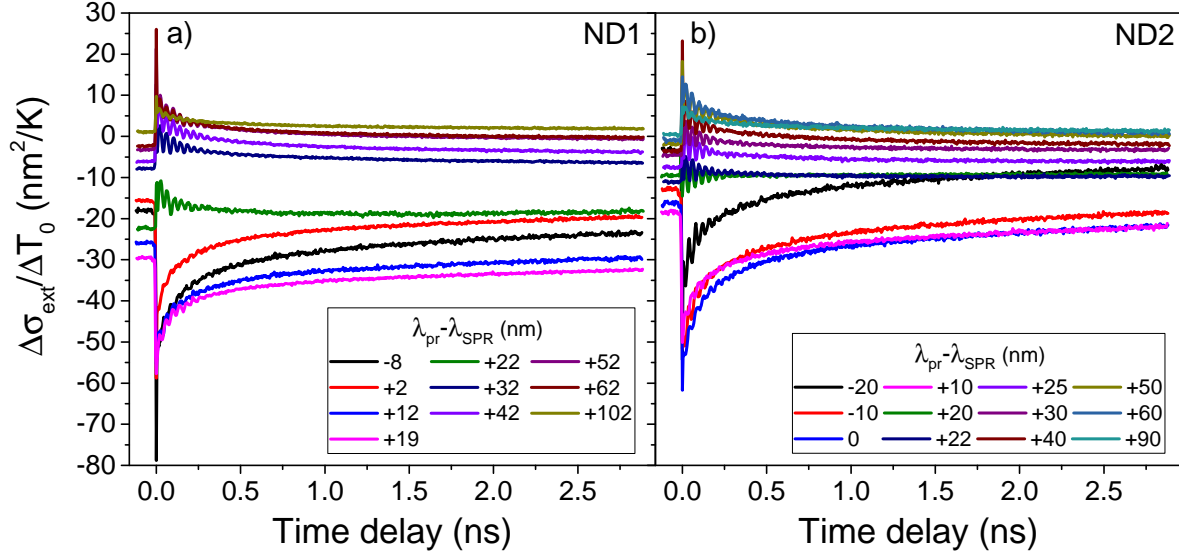


**Figure 4.5 – Time-resolved changes of the extinction cross-section normalized by initial heating for a) ND1 and b) ND2.** Each color corresponds to a different probe wavelength, indicated relatively to the Surface Plasmon Resonance of the nanodisk. All measurements were done using the same polarization for the probe beam, corresponding to full black circles symbols for both nanodisks in Figure 4.4.

Time-resolved experiments were conducted on the two selected gold nanodisks, ND1 and ND2 (see pump-probe technique in Chapter 2 Section 2.2.3), with a probe beam provided by a Ti:Sapphire pulsed laser (MaiTai) while the pump beam was generated from the same source using second harmonic generation by a frequency-doubling BBO crystal. The probe wavelength was in the 790-900 nm range, corresponding to  $\lambda_{pr} - \lambda_{SPR} \approx -10/+100$  nm and  $-20/+90$  nm for ND1 and ND2, respectively, with  $\lambda_{SPR}$ , the central position of the Surface Plasmon Resonance of the investigated nanodisks ( $\lambda_{SPR} = 800$  nm for ND1 and  $\lambda_{SPR} = 810$  nm for ND2). Additionally, the initial heating  $\Delta T_0$  of the nanodisk was evaluated (its value being of the order of 10 K, see Chapter 2 Section 2.2.3.5 for its determination) and used to normalize the time-resolved signals in order to be able to compare them despite the fact that pump beam features were not constant throughout the measurements.

The temporal variations of the extinction cross-section normalized by the initial heating of the nanoparticle are plotted for ND1 and ND2 in Figures 4.5a and 4.5b. These graphs show that the time-resolved signals, even normalized by the initial heating of the nanodisk, highly depend on the probe wavelength used in the experiments. As discussed in Chapter 1 Section 1.2.3, the

optical signals are composed of a thermal component, linked to the cooling of the nano-object, and of a vibrational component coming from acoustic vibrations. Noticeably, the amplitudes of both these components exhibit a high dependence on the probe wavelength, with cases where the thermal part is dominant and vibrations have small amplitudes (e.g. at  $\lambda_{pr} - \lambda_{SPR} = +2$  nm in Figure 4.5a) while in other cases acoustic vibrations are largely dominant as compared to the thermal part (e.g. at  $\lambda_{pr} - \lambda_{SPR} = +22$  nm in Figure 4.5a).

### 4.2.3 Experimental determination of the optical sensitivity to nanodisk heating

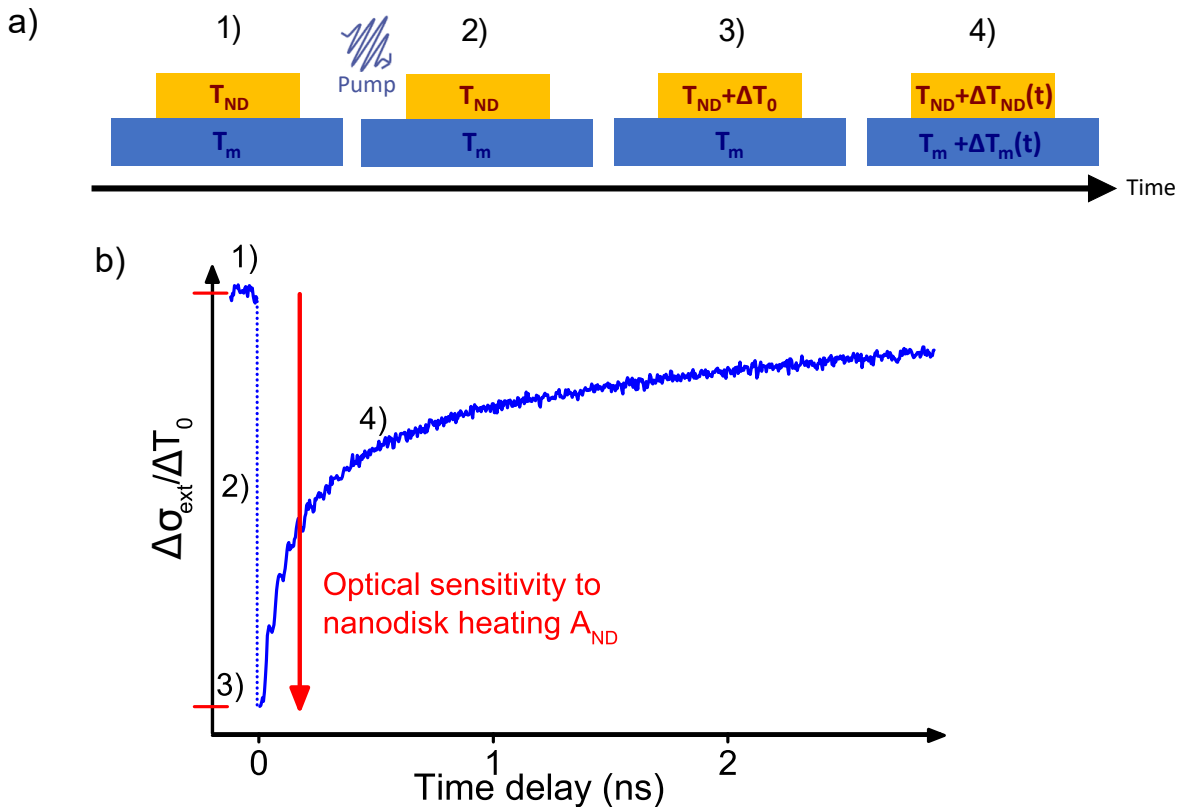


**Figure 4.6** – a) Schematic illustrating the successive physical phenomena occurring during time-resolved measurements for a single gold nanodisk and b) associated time-resolved signal with deduced optical sensitivity to nanodisk heating. 1) Initial situation (prior to excitation) 2) Arrival of the pump pulse 3) Situation after a delay of a few picoseconds allowing internal thermalization of the nanodisk but much shorter than the characteristic times of nanodisk-membrane heat exchanges 4) At longer time time delays heat exchanges between the nanodisk and the supporting membrane as well as heat evacuation far away from the nanodisk occur. The dotted blue line aims to help the visualization of the initial rise of the optical signal but does not correspond to any meaningful data.

As described in Chapter 1 Section 1.2.3 the measured time-resolved signal is the sum of three contributions associated to distinct physical phenomena: excitation and internal thermalization

of the nanodisks, acoustic vibrations and thermal relaxation. The initial peak associated to nanoparticle excitation and internal thermalization by electron-electron and electron-phonon interactions has not been analyzed and the associated data points affected by this phenomenon (over 5-10 ps typically) won't be plotted in the following. The data points at negative time-delays were kept in order to extract an average value used as a reference. The acoustic component was fitted and extracted from the time-resolved signals (see signal processing in Chapter 2 Section 2.2.3.4). The signals resulting from this processing thus purely reflect the thermal dynamics of the nanodisks.

Figures 4.6a and 4.6b illustrate the physical state of the nanodisk-membrane system associated to each temporal portion of the optical signal linked to the excitation by the pump pulse. What happens over time is the following (see the different timescales involved in Figure 2.16 in Chapter 2):

1. At negative time delay (i.e. about 12.5 ns after the last excitation by a pump pulse) most signals present a non-vanishing value. This is because the cooling dynamics of the nanodisk are not finished after such a 12.5 ns delay, as thoroughly discussed in the previous chapter.
2. The pump pulse encounters the gold nanodisk and excites it
3. The electronic excitation and internal thermalization of the nanodisk occur within a few picoseconds, a duration much shorter than the time required to significantly change the temperature of the supporting membrane through heat diffusion from the nanodisk
4. Nanodisk-membrane heat exchanges and heat evacuation far away from the nanodisk take place at subsequent delays (see section 3.6 in previous chapter).

As each pump pulse deposits energy in the nanodisk only, the extinction modification immediately following nanodisk excitation and internal thermalization is solely due to an increase of nanodisk temperature. This enables experimental extraction of the wavelength-dependent  $A_{ND}$  coefficient appearing in Equation 4.1, by evaluating the variation of the thermal components of  $\Delta\sigma_{ext}/\Delta T_0$  (see Figure 4.6b) following nanodisk excitation by the pump pulse. Figures 4.7a and 4.7b present the optical sensitivity to nanodisk heating  $A_{ND}$  for ND1 and ND2 determined by the aforementioned method.

The values obtained for ND1 and ND2 present similar values and evolutions: both reach their maximal absolute value at  $\lambda_{pr} = \lambda_{SPR}$  (around 40 nm<sup>2</sup> K<sup>-1</sup>) and change their sign on the red flank of the nanodisk Surface Plasmon Resonance.

#### 4.2.4 Modelization of the optical sensitivity to nanodisk heating and membrane heating

The  $A_{ND}$  values deduced from the experiments were compared with simulated ones based on Equation 4.2.

First, the plasmonic derivatives  $\frac{\partial\sigma_{ext}}{\partial\epsilon_{1,2,m}}(\lambda_{pr})$ , meaning the sensitivity of the extinction cross-section of the gold nanodisk to the dielectric functions of gold ( $\epsilon_1, \epsilon_2$ ) and of the membrane ( $\epsilon_m$ ), were estimated using FEM modeling and are shown in Figure 4.8. To do so, optical FEM simulations were performed using  $D = 100$  nm,  $h = 10$  nm, and  $\hbar\gamma = 100$  meV in order to

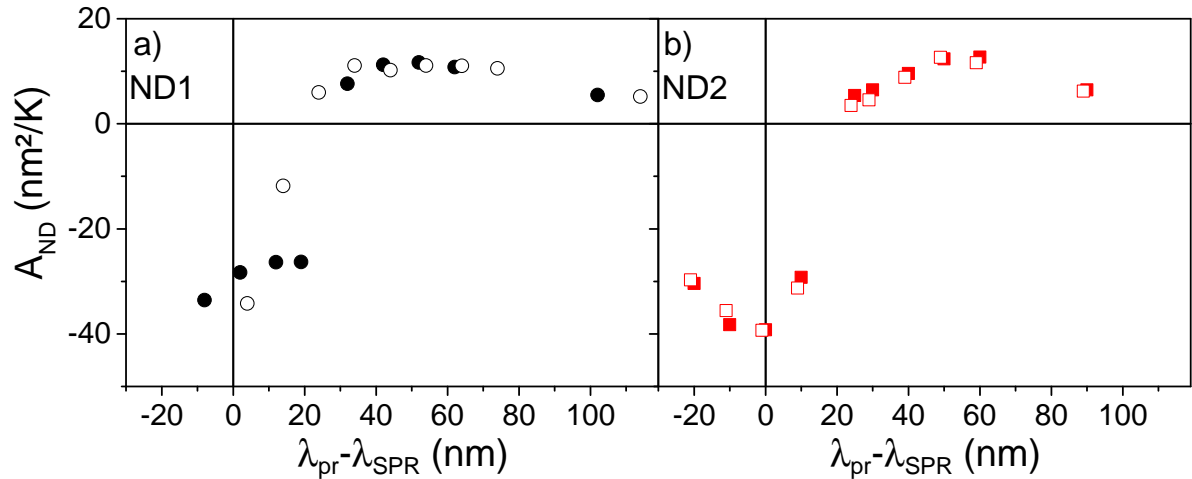


Figure 4.7 – Experimental values of the optical sensitivity to nanodisk heating  $A_{ND}$  for the investigated nanodisks a) ND1 (black markers) and b) ND2 (red markers). Similarly to Figure 4.4, full and empty markers correspond to measurements performed using two different orthogonal polarizations of the probe beam.

calculate the extinction cross-section  $\sigma_{ext}$ . This quantity was then computed for slightly different values of  $\epsilon_1$ ,  $\epsilon_2$ , and  $\epsilon_m$ . The plasmonic derivatives were then deduced by discrete derivation. The distinct profiles for  $\epsilon_1$  and  $\epsilon_2$  are a clear indicator that their effect on the surface plasmon resonance is quite different ;  $\epsilon_1$  mainly affects the position of the Surface Plasmon Resonance while  $\epsilon_2$  mainly impacts the width of the resonance.

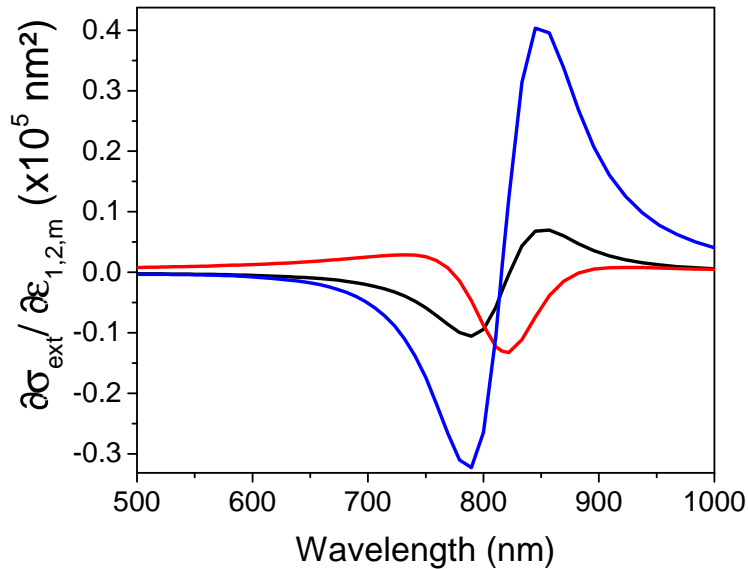


Figure 4.8 – Plasmonic derivatives  $\frac{\partial \sigma_{ext}}{\partial \epsilon_1}$  (full black line),  $\frac{\partial \sigma_{ext}}{\partial \epsilon_2}$  (full red line) and  $\frac{\partial \sigma_{ext}}{\partial \epsilon_m}$  (full blue line) of a Au nanodisk supported by a 15nm thick  $\text{Si}_3\text{N}_4$  membrane.

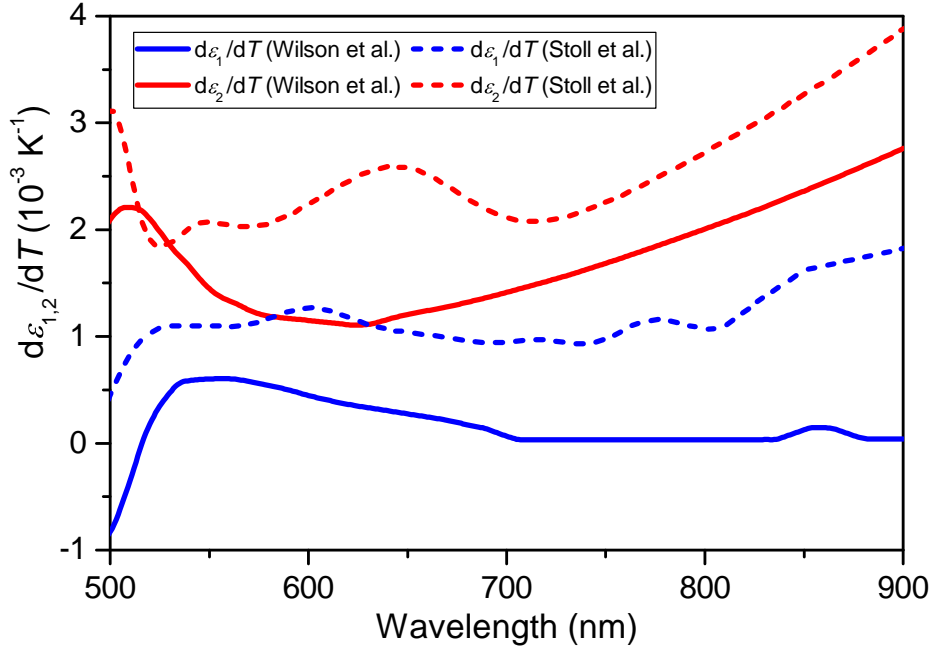


Figure 4.9 – Dielectric function temperature dependences  $\frac{\partial \epsilon_1}{\partial T}$  (in blue) and  $\frac{\partial \epsilon_2}{\partial T}$  (in red) of gold respectively from ref. [123] (solid lines) and ref. [19] (dashed lines).

Secondly, the sensitivity of the dielectric functions of gold to temperature  $\frac{\partial \epsilon_{1,2}}{\partial T_{ND}}(\lambda_{pr})$ , can be found in the literature. Several tables based on either experimental measurements or theoretical modeling have been reported for these derivatives. Two of them are presented in Figure 4.9: one coming from ellipsometry experiments performed at different temperatures in the Cahill group [123], and one stemming from theoretical modeling by the FemtoNanoOptics group [19]. These two tables, and more generally those reported in the literature, present some variability, which results, in the experiments, from the dispersion in synthesis means, morphology, and crystallinity of the samples used and, in simulations, from the assumptions of the models.

The simulated  $A_{ND}$  sensitivities (and the extent of their match with experimental values of this quantity) thus depend on the table choice. In this work the  $\frac{\partial \epsilon_{1,2}}{\partial T}$  values reported in [19] were used. Due to the variability between the tables, a perfect match between experiments and simulations was not expected. Nevertheless, the next section will show that a quite good agreement has been achieved.

The sensitivity of the nanodisk extinction cross-section to the heating of the  $\text{Si}_3\text{N}_4$  membrane  $A_m$  (see Equation 4.3) was estimated similarly to  $A_{ND}$ . The first term,  $\frac{\partial \sigma_{ext}}{\partial \epsilon_m}$ , was deduced from the same FEM computation as  $\frac{\partial \sigma_{ext}}{\partial \epsilon_{1,2}}$  and is represented in Figure 4.8. A fixed value was used for the second term, the sensitivity of the dielectric function of  $\text{Si}_3\text{N}_4$  to temperature, with  $\frac{\partial \epsilon_m}{\partial T} = 10^{-4} \text{ K}^{-1}$ , coherently with previous measurements by Elshaari et al. [125].

#### 4.2.5 Comparison between measured and modeled sensitivities

Figure 4.10 presents both the experimental values and the simulated ones obtained for the optical sensitivity to nanodisk heating  $A_{ND}$ .

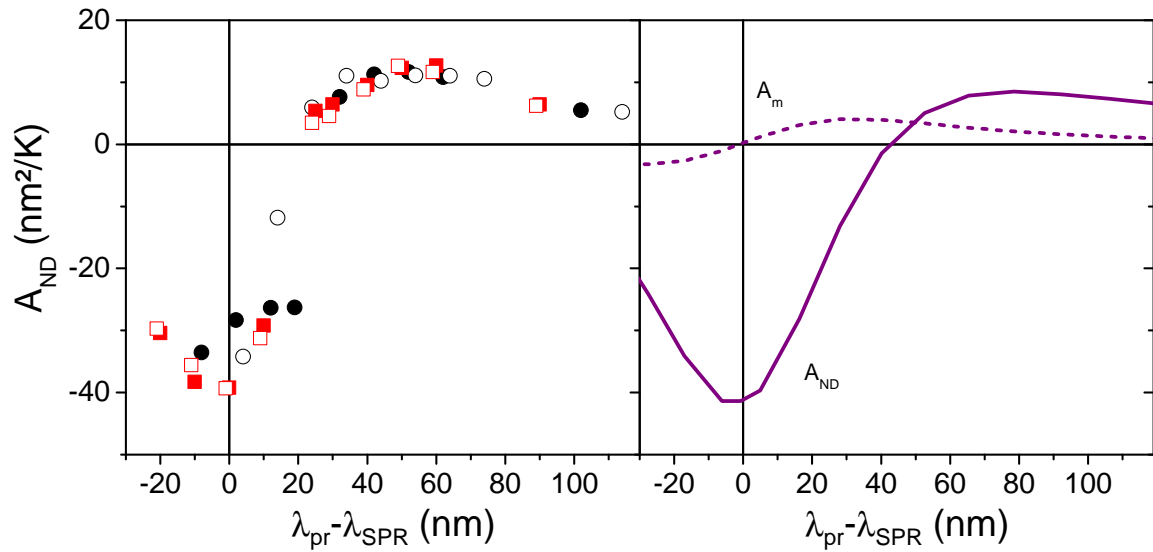


Figure 4.10 – a) Experimental values of the optical sensitivity to nanodisk heating  $A_{ND}$  for the nanodisks studied ND1 (black markers) and ND2 (red markers) b) Simulated values of  $A_{ND}$  and  $A_m$  (respectively solid and dashed lines). a) Similarly to Figure 4.4, full and empty markers correspond to measurements performed using two different orthogonal polarizations of the probe beam.

A quite good agreement is achieved between experiments and simulations for the optical sensitivity to nanodisk heating  $A_{ND}$ : similar variations and absolute values are observed in both cases. In particular:

- $|A_{ND}|$  is maximal around the Surface Plasmon Resonance of the nanodisk and close values are found in experiments and simulations.
- The variations follow a similar pattern: a decline, followed by growth, then another decline as wavelengths increase from short to long.
- At higher probe wavelengths there is a change of sign leading to a vanishing of  $A_{ND}$ .

The single discrepancy between the measured and modeled values of  $A_{ND}$  regards the wavelength on the blue flank of the Surface Plasmon Resonance at which they vanish, exceeding the central Surface Plasmon Resonance position by 20-30 nm for experiments and 40 nm in simulations. This difference may result, at least in part, from the uncertainties affecting the  $\frac{\partial \epsilon_{1,2}}{\partial T_{ND}}(\lambda_{pr})$  tables already discussed above. The computed sensitivity to membrane heating  $A_m$  spectrum is also shown in Figure 4.10b. Its spectral shape largely differs from the  $A_{ND}$  one (originating from the spectral dependence of  $\epsilon_2$ ), which is due to the fact that membrane heating mostly affects Surface Plasmon Resonance position (similarly to  $\epsilon_1$ ).  $|A_m|$  is usually much smaller than  $|A_{ND}|$  (Figure 4.10b). However, this is not the case in the  $\approx 20$  nm broad spectral range around the wavelength where  $A_{ND}$  vanishes, suggesting that measurements with  $\lambda_{pr}$  in this spectral range should be very significantly affected by membrane heating.

## 4.2.6 Analyzing the temporal profiles of the time-resolved measurements

A contribution of membrane heating to time-resolved signals is expected to modify their temporal dynamics, as the thermal dynamics of the nanodisk and of its supporting membrane are very different (see Equation 4.1 and previous chapter).

To more easily compare the temporal variations of the thermal components of the measured time-resolved signals, they were normalized to present the same initial value. The normalized thermal components for ND1 and ND2, extracted from the raw signals shown in Figure 4.5a and 4.5b, are plotted in semi-logscale in Figures 4.11a and 4.11b (for clarity only a few signals are shown for each nanodisk).

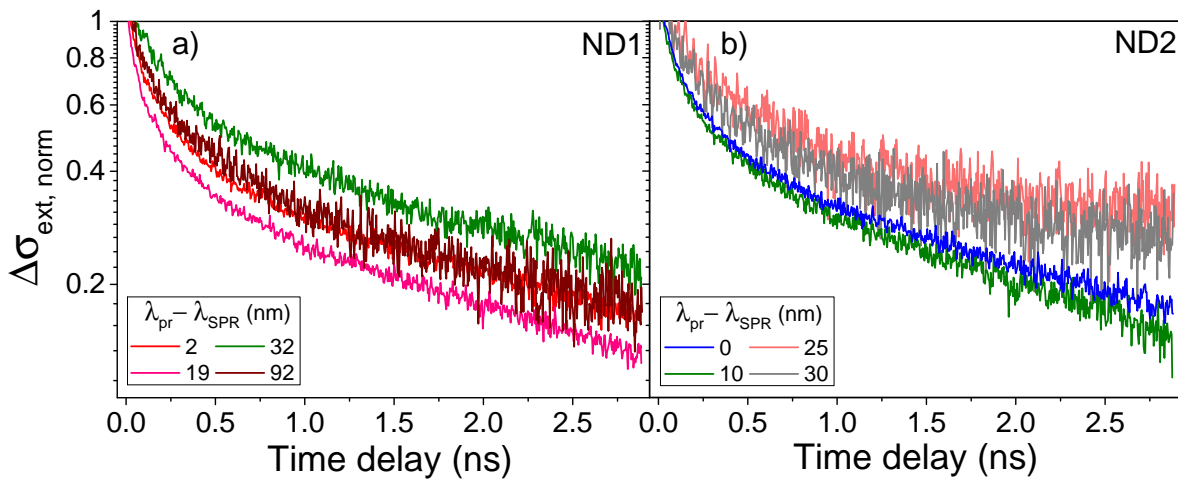


**Figure 4.11** – Normalized thermal components extracted from time-resolved measurements for a) ND1 and b) ND2. As before, each color corresponds to a different probe wavelength indicated relatively to the surface plasmon resonance of each gold nanodisk. Measurements were performed using the same probe polarization than the one corresponding to full markers in Figure 4.4.

A quick analysis of the Figure 4.11 shows that there is a clear dependence of the normalized thermal components on the probe wavelength for ND1 and ND2, demonstrating the existence of a significant contribution of the heating of the 15 nm thick  $\text{Si}_3\text{N}_4$  membrane to the optical signals for both nanodisks. This is coherent with what was shown in Chapter 3 Section 3.6, where relatively slow cooling dynamics, associated to relatively high temperature elevations were observed in this thin  $\text{Si}_3\text{N}_4$  membrane compared to the other investigated substrates: with higher  $\Delta T_m$  the contribution of the membrane becomes easier to detect. Thus, the non-overlapping of normalized curves in Figure 4.11 demonstrates the presence of a non-negligible contribution from the membrane heating affecting the optical signals. An additional visualization of the different dynamics has been done: for each probe wavelength the average value of the optical signal at maximum pump-probe delay (i.e. about 3 ns time delay) is plotted for both nanodisks in Figures 4.12a and 4.12b. These graphs confirm the high dependence of the normalized thermal components on the probe wavelength that was observed in Figure 4.11.

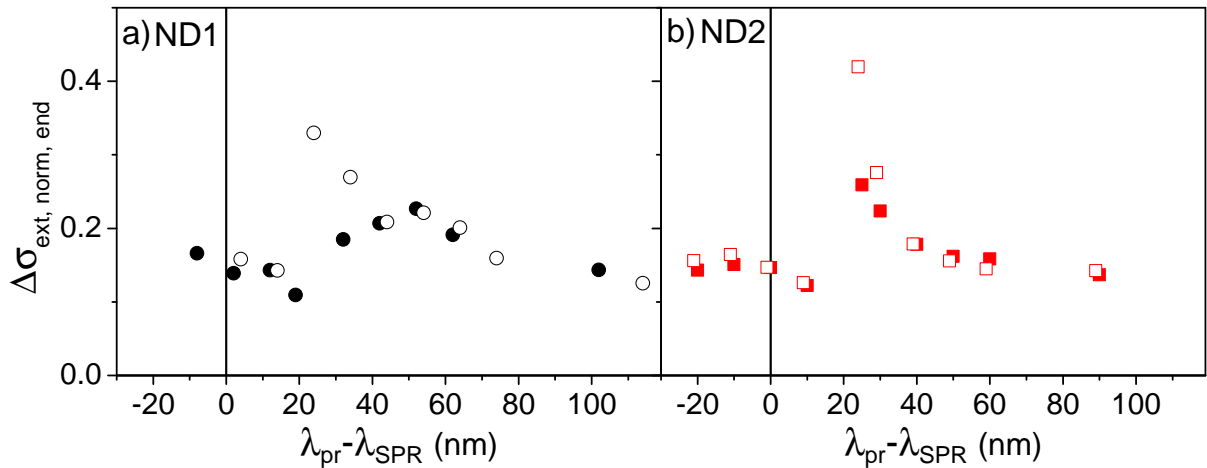


Figure 4.12 – Average value of the normalized thermal component at maximum pump-probe delay ( $\approx 2.7$  ns) a) for ND1 and b) for ND2. Similarly to Figure 4.4, full and empty markers correspond to measurements performed using two different orthogonal polarizations of the probe beam.

#### 4.2.7 Thermo-optical modeling of the transient optical response of a single supported gold nanodisk

This part aims to describe the numerical model, adapted from previous work done in the FemtoNanoOptics group [110], used to simulate the temporal dynamics observed for  $\Delta\sigma_{ext}(\lambda_{pr}, t)$  in the Figure 4.11. It is described as a "thermo-optical" model as it combines simulations of the thermal dynamics and transient optical response of a nano-object to determine the  $\Delta\sigma_{ext}(\lambda_{pr}, t)$  profiles.

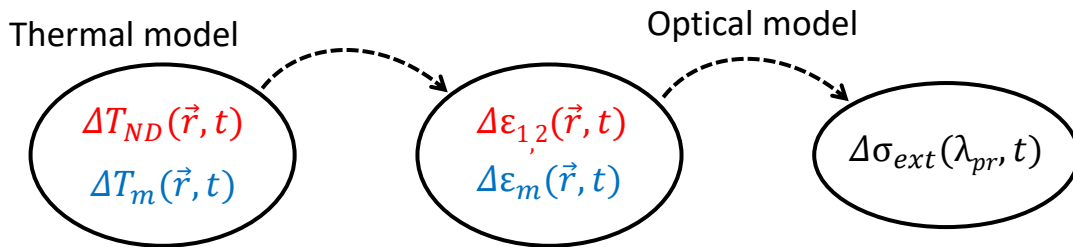


Figure 4.13 – Schematic of the computation steps involved in the thermo-optical model. The variations of temperature of the nanodisk and the membrane, computed by the thermal model, are used to define variations of the dielectric functions of both objects. These quantities are finally injected in the optical model to compute the out-of-equilibrium variations of extinction cross-section of the nanodisk  $\Delta\sigma_{ext}(\lambda_{pr}, t)$ .

The articulation between the different modelizations is presented in the Figure 4.13. First, the temperature profiles in the gold nanodisk  $T_{ND}(\vec{r}, t)$  and in the 15 nm thick  $\text{Si}_3\text{N}_4$  membrane  $T_m(\vec{r}, t)$  were computed using the frequency domain thermal model described in Chapter 2

Section 2.3.2.2. Time-dependent and locally modified (compared to room-temperature) dielectric functions were defined to take into account these temperature profiles in the nanodisk and the membrane :

$$\Delta\epsilon_{1,2}(\vec{r}, t) = \frac{\partial\epsilon_{1,2}}{\partial T_{ND}}\Delta T_{ND}(\vec{r}, t), \quad (4.7)$$

$$\Delta\epsilon_m(\vec{r}, t) = \frac{\partial\epsilon_m}{\partial T_m}\Delta T_m(\vec{r}, t). \quad (4.8)$$

In a final step, the optical model described in Chapter 2 Section 2.3.1 was used to compute the out-of-equilibrium variations of extinction cross-section  $\Delta\sigma_{ext}(\lambda_{pr}, t)$  of the gold nanodisk associated to the previously defined, spatially inhomogeneous, dielectric functions.

Thanks to this thermo-optical model it was possible to compute the simulated temporal profiles of the extinction cross-section changes  $\Delta\sigma_{ext}(\lambda_{pr}, t)$  in the nanodisk-membrane system as well as the average values of the optical signal at maximal time delay.

## 4.2.8 Normalized temporal profiles: comparison between experiments and simulations

In Figure 4.14 are represented the normalized thermal components as well as average values of the optical signals at maximal time delay coming from experiments and simulations, respectively.

The comparison between experimental data and simulations yields a good agreement overall with similar trends observed. In both experiments and modelization significantly slowed down dynamics were found at wavelengths larger than the surface plasmon resonance of the nanodisk, coherently with the location of the vanishing of the optical sensitivity to nanodisk heating  $A_{ND}$  previously discussed. The experimental curves at  $\lambda_{pr} - \lambda_{SPR} = 25$  and 30 nm as well as the simulated ones at  $\lambda_{pr} - \lambda_{SPR} = 47$  nm especially illustrates this phenomenon in the Figures 4.14a and 4.14b. This can also be seen in Figures 4.14c and 4.14d at  $\lambda_{pr} - \lambda_{SPR} \approx 20$ -30 nm and  $\lambda_{pr} - \lambda_{SPR} \approx 40$ -50 nm respectively. The wavelength dependence of the average value of the optical signal at maximal time delay observed in the experiments (Figure 4.14c) is also well reproduced in simulations (Figure 4.14d). In particular, this quantity doesn't change much around the Surface Plasmon Resonance central wavelength of the nanodisk, for  $\lambda_{pr} - \lambda_{SPR} = 0$  nm, and far from it, for  $\lambda_{pr} - \lambda_{SPR} > 60$  nm. Around the wavelength where  $A_{ND}$  vanishes the average value of the optical signal at maximal time delay is drastically reduced and then highly increased at wavelengths increasingly far from the Surface Plasmon Resonance. Indeed, slower dynamics lead to higher values at maximal time delay while faster dynamics lead to the opposite effect.

Finally, the simulations predicted faster dynamics, located around  $\lambda_{pr} - \lambda_{SPR} \approx 40$  nm in simulations in Figure 4.14d, but these could not be experimentally observed (see next section for details about the associated measurements).

The discrepancies about the vanishing wavelength for  $A_{ND}$  previously discussed are once again present here: the wavelengths where slower and faster dynamics occur are not the same between experiments (around  $\lambda_{pr} - \lambda_{SPR} = 20$ -30 nm) and simulations ( $\lambda_{pr} - \lambda_{SPR} \approx 40$ -50 nm). This gap is attributed to the same origin as before: the variability existing in the literature among the tables for the dielectric function temperature dependences for gold  $\frac{\partial\epsilon_{1,2}}{\partial T}$ .

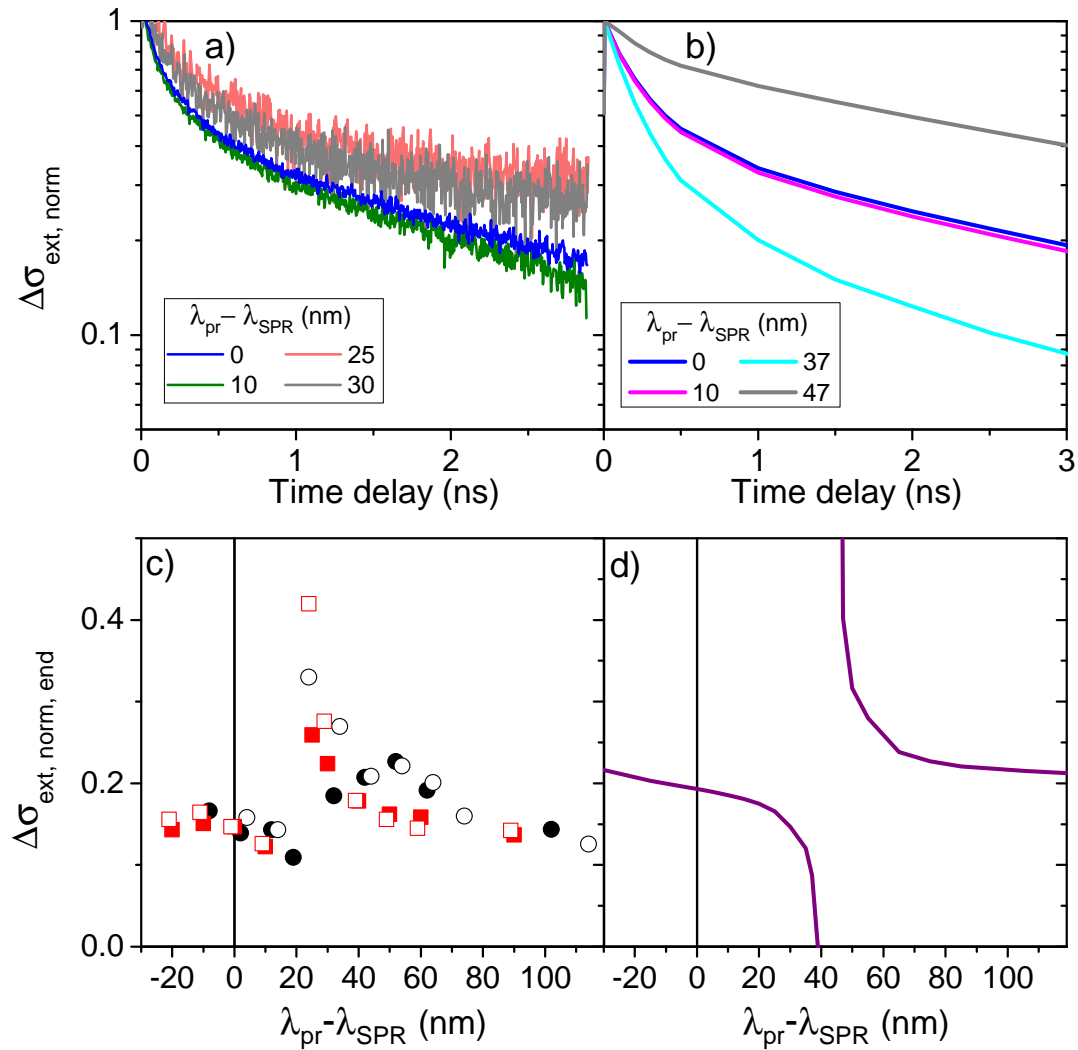


**Figure 4.14 – Temporal variations of the normalized thermal components a) for ND2 and b) for the thermo-optical model, complemented with the average values of the normalized thermal components at maximum pump-probe delay c) in experiments and d) in simulations.** In all subfigures the probe wavelength  $\lambda_{pr}$  is indicated relatively to the Surface Plasmon Resonance central wavelength  $\lambda_{SPR}$ . In a) and b) 4 probe wavelengths are selected, illustrating that slower and faster cooling dynamics can be observed in both cases. a) Measurements were performed with a probe beam polarization associated to full markers in Figure 4.4. c) Same color code as in Figure 4.10. For c) and d) plots the maximal pump-probe delay was around 2.7 ns.

#### 4.2.9 Signals measured in the spectral range of weak sensitivity to nanodisk heating

Signals measured at probe wavelengths close to the spectral range where the optical sensitivity to nanodisk heating  $A_{ND}$  vanishes are potentially very interesting as they could provide selective access to the dynamics of membrane heating. This would correspond to using nanodisks as

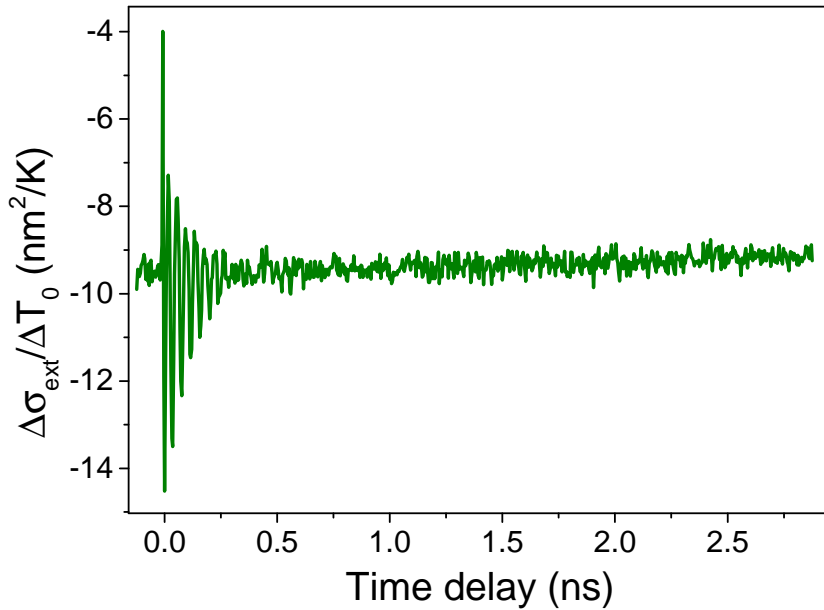


**Figure 4.15 – Time-resolved changes of the extinction cross-section normalized by initial heating for ND2 with a probe wavelength such that  $\lambda_{pr} - \lambda_{SPR} = 20$  nm. This optical signal corresponds to the green curve in Figure 4.5b.**

thermometers measuring the temperature of their local environment instead of their own.

However, the experimental signals measured in these conditions simultaneously present a thermal component of low amplitude and signal to noise ratio (as expected from the small values of  $A_{ND}$  and  $A_m$  in this spectral range) and an oscillatory component of large amplitude, reflecting sensitive probing of the nanodisk vibrations. An example of such signal for ND2 is represented in Figure 4.15.

These effects make extraction of the thermal component challenging, and despite several attempts (e.g. based on filtering in the frequency domain) we could not succeed in extracting a signal with a signal to noise ratio sufficient for further analysis.

### 4.3 Conclusion

In this chapter the study of single gold nanodisks supported by a thin glass membrane, a 15 nm thick  $\text{Si}_3\text{N}_4$  membrane, through ultrafast time-resolved experiments with a probe wavelength varied across their Surface Plasmon Resonance, allowed to perform experimental measurements of the optical sensitivity to nanodisk heating  $A_{ND}$ . The maximum absolute value of this quantity is located around the Surface Plasmon Resonance of the nanodisk and exhibits a clear dependence on the probe wavelength with a characteristic vanishing 20-30 nm on the red flank of the resonance, all features being well reproduced by simulations obtained via a thermo-optical model.

This work also demonstrated the large dependence of the nanodisks transient optical responses on probe wavelength in terms of amplitude and temporal dynamics. These transient responses exhibited significant variations and in particular slower decays of the thermal com-

ponent of the optical signals have been observed. These observations were found in a narrow wavelength range surrounding that at which the contribution of nanodisk heating to extinction changes vanishes, in which the membrane heating contribution becomes of the same order of (or even larger than) the other one. As far as we know, these results represent the first experimental demonstration of a detection of environment heating in the context of time-resolved experiments performed on nano-objects located in a solid environment. The results presented in this chapter have been described in a paper entitled "Impact of supporting nanometric membranes on the thermo-optical dynamics of individual plasmonic nanodisks" and published in *Nanoscale* in 2024 [122].

Finally, the applicative interest of these results can be found in the use of metallic nanoparticles as local probes for measuring temperature or the thermal properties of thin membranes.



## Chapter 5

# Vibrations of single gold nanodisks deposited on thin membranes

Understanding the vibrational properties of nano-objects is essential for many applications, such as, for example, mass sensing. Among the different experimental approaches available to address the vibrational properties of nanostructures, optical techniques (e.g. ultrafast time-resolved spectroscopy) allow to detect vibrational modes via the modification of optical response that they induce, providing access to their frequencies ( $f = 1/T$ ,  $T$  being the corresponding period), damping times ( $\tau$ ), and quality factors ( $Q = \pi \frac{\tau}{T}$ ). The influence of the nanoparticle size, composition, shape, and environment on the vibrational periods has been extensively studied and is now quite well understood [129]. In particular, it has been demonstrated that these periods can be accurately reproduced using the laws of continuum mechanics and the bulk elastic constants of materials even for ultrasmall nanoparticles with sizes of the order of 1 nm [130,131].

In contrast, the mechanisms involved in the damping of acoustic vibrations of nanoparticles are currently less well understood, notably due to the fact that the lifetime of vibrational modes can be radically altered by small modifications of the nanoparticle structure, morphology and environment. Moreover, damping times not only depend on the intrinsic properties of the nanoparticle (e.g. composition, morphology, and crystallinity) but are also greatly affected by the properties of the nanoparticle-environment interface, which determines the efficiency of the transmission of acoustic energy between the two media. Finally, the dispersion in size and shape of the nanoparticles leads to inhomogeneous effects making evaluation of vibrational damping times challenging in the context of ensemble experiments. Fully quantitative analyses of vibrational damping can thus be done only using a single-particle approach. The first attempt at time-resolved measurements of the vibrations of a single nano-object was performed successfully in 2005 on single gold nanospheres using time-resolved interferometry by M. Orrit et al. [133]. Several research teams then studied the vibrational properties of a number of single nanosystems (nanospheres, nanoplates, nanorods, nanoprisms, etc) [129,134–137]. Single-particle experiments using Raman spectroscopy have also been demonstrated more recently in the case of single isolated and dimerized gold nanoparticles [138]. Figure 5.1 illustrates the sharp differences that can be observed between signals obtained via ensembles and single-particle experiments for silver nanocubes deposited on glass [132], the former presenting a much faster damping originating from the progressive dephasing of the vibrations of the different nanoparticles of the probed ensemble.

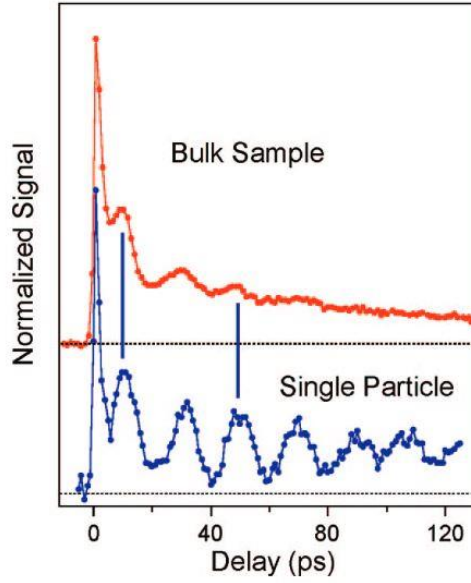


Figure 5.1 – Time-resolved signal measured in the case of silver nanocubes deposited on glass for an ensemble of nano-objects (red) and a single nanoparticle (blue). Figure taken from ref. [132].

In the work presented in this chapter the main objective was the study of the vibrational properties of single gold nanodisks and, in particular, their vibrational quality factors. Previous measurements performed in the group in the context of F. Medeghini’s PhD work [21] demonstrated the large impact of nanodisk morphology (diameter over thickness ratio) on their vibrational quality factors. Here two aspects of the previous work were modified in these new studies: first, the nanodisks were produced using colloidal chemistry (see Chapter 2) rather than electron beam lithography, a synthesis procedure expected to induce less crystalline defects. Second, the supporting substrate was here a thin membrane rather than a bulk substrate. In addition, we performed a systematic study of the optical detection of acoustic vibrations (similarly to that of the thermal dynamics reported in the previous chapter).

## 5.1 Vibrational properties of nano-objects: Navier equation, eigenmodes and quality factors

### 5.1.1 Navier equation

The mechanical deformation of an elastically isotropic solid material is described by the Navier equation, which reads:

$$\rho \frac{\partial^2 \vec{u}}{\partial t^2} = (\lambda + 2\mu) \vec{\nabla} (\vec{\nabla} \cdot \vec{u}) - \mu \vec{\nabla} \times (\vec{\nabla} \times \vec{u}), \quad (5.1)$$

with  $\vec{u}$  the displacement field,  $\rho$  the density of the material, and  $\lambda$  and  $\mu$  its Lamé constants. These constants are related to the Young modulus  $E$  and Poisson’s ratio  $\nu$  via

$$E = \mu \frac{3\lambda + 2\mu}{\lambda + \mu} \quad \text{and} \quad \nu = \frac{\lambda}{2(\lambda + \mu)}, \quad (5.2)$$

and to the longitudinal speed of sound  $c_L$  and transversal speed of sound  $c_T$  via

$$c_L = \sqrt{\frac{\lambda + 2\mu}{\rho}} \quad \text{and} \quad c_T = \sqrt{\frac{\mu}{\rho}}. \quad (5.3)$$

### 5.1.2 Eigenmodes and quality factors

The vibrational eigenmodes of a nano-object correspond to the harmonic solutions of Equation 5.1, which can be written as:

$$\vec{u}(\vec{r}, t) = \vec{u}_0(\vec{r}) \exp(i2\pi\tilde{f}t) + c.c. \quad (5.4)$$

with  $\tilde{f}$  the frequency of the vibrational mode [129]. Two main configurations can be considered. The first one consists of a nano-object in vacuum, which is characterized by a vanishing stress condition on the surface of the nano-object and leading to undamped vibrations modes with real frequencies  $\tilde{f}$ . The second one involves a nano-object in contact with an infinite environment (e.g. matrix, substrate). In this context the displacement field  $\vec{u}$  must be the solution of the Navier equation in both the nano-object and its surrounding medium, with boundary conditions being the continuity of the displacement and stress fields at the nanoparticle-matrix interface. This leads to damped vibrational modes, characterized by complex frequencies  $\tilde{f}$ , whose damping originates from the emission of acoustic waves in the matrix. For a given mode, denoted as the  $n$ th, its complex frequency  $\tilde{f}_n$  is expressed as:

$$\tilde{f}_n = f_n + i\frac{\alpha_n}{2\pi} \quad (5.5)$$

with the real frequency  $f_n = 1/T_n$  associated to the oscillation period  $T_n$ , and  $\alpha_n = 1/\tau_n$  with  $\tau_n$  the lifetime of the vibration mode. The vibration mode can be fully described using its complex frequency  $\tilde{f}_n = f_n + i\frac{\alpha_n}{2\pi}$ , and the normalized displacement field  $\vec{u}_{0,n}(\vec{r})$ :

$$\vec{u}_n(\vec{r}, t) = \vec{u}_{0,n}(\vec{r}) \cos(2\pi f_n t) \exp(-\alpha_n t). \quad (5.6)$$

The damping of a vibration mode is usually characterized by its dimensionless quality factor  $Q_n$ , which is defined as:

$$Q_n = \pi \frac{f_n}{\alpha_n} = \pi \frac{\tau_n}{T_n}. \quad (5.7)$$

Alternatively,  $\frac{\alpha_n}{\pi}$  corresponds to the bandwidth  $\Delta f_n$  of the vibration mode in the spectral domain, allowing to also write the quality factor as:

$$Q_n = \frac{f_n}{\Delta f_n}. \quad (5.8)$$

Apart from the extrinsic origin of damping discussed above (emission of acoustic waves in the environment), vibrational modes can also be damped by intrinsic processes (e.g. thermoelastic attenuation, scattering of acoustic waves by randomly oriented grains in polycrystalline materials [139]). A general expression of the quality factor of an acoustic mode, accounting for these two independent damping sources, is thus:

$$\frac{1}{Q} = \frac{1}{Q_{intrinsic}} + \frac{1}{Q_{extrinsic}}, \quad (5.9)$$

with  $Q_{intrinsic}$  and  $Q_{extrinsic}$  are the quality factors associated to intrinsic and extrinsic damping mechanisms, respectively.

## 5.2 Vibrational dynamics of single colloidal gold nanodisks deposited on membranes

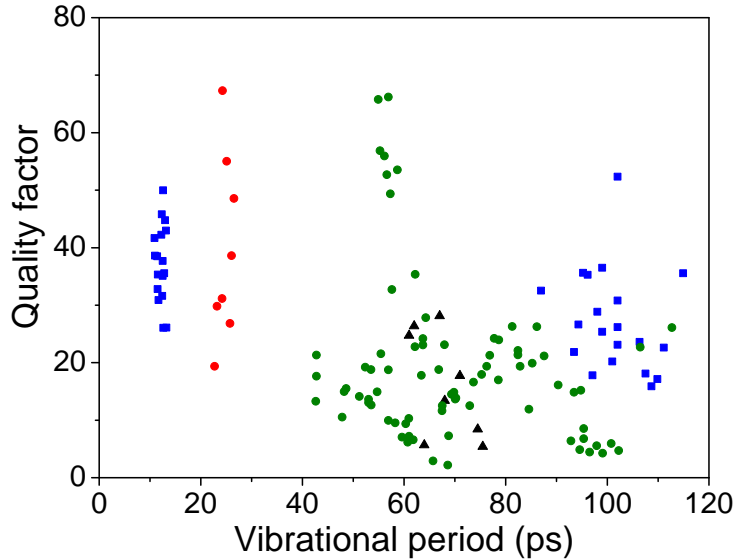


**Figure 5.2 – Vibrational periods and quality factors measured using single-particle time-resolved spectroscopy on supported gold nano-objects with different morphologies and synthesis methods. Figure adapted from ULTRA-SINGLE project.** Experimental data were obtained for nanospheres (red circles), nanoprisms (black triangles), nanorods (blue squares), and nanodisks (green circles), 2 modes being detected for the two latter types of nano-objects [62, 136, 140, 141].

A number of experiments aimed to study the vibrational quality factors of single nano-objects. Among them, experiments conducted on nano-objects obtained by chemical synthesis deposited on substrates lead to measured quality factors  $Q$  in the 5-50 range for the detected acoustic modes, mainly limited by the acoustic coupling between the nano-object and its environment [129, 132, 142]. For lithographed nano-objects smaller quality factors, explained by lower values of the intrinsic quality factor  $Q_{intrinsic}$  for such objects, have been reported [141, 143–145]. Figure 5.2 presents some examples of vibrational periods and quality factors obtained experimentally for a variety of single gold nano-objects.

However, previous work conducted in the FemtoNanoOptics group in the framework of Fabio Medeghini’s PhD work demonstrated that the quality factors of single gold nanodisks, lithographed on a thick sapphire substrate, exhibited a strong dependence on the nanodisk aspect ratio  $\eta$  (diameter  $D$  over height  $h$  ratio with  $\eta = D/h$ ) [21, 62]. In particular, a maximal quality factor of  $Q \approx 70$  was observed near  $\eta \approx 2.5$ , a value higher than what had been previously observed for nanoparticles deposited on substrates (see Figure 5.3). This observation was later ascribed to radiative coupling effects between two acoustic modes of the nanodisk presenting close frequencies in a narrow  $\eta$  range [146].

In this section we present experiments whose goal was to further extend this work by studying the influence of the deposition on a thin membrane and of a colloidal synthesis on the previous result, i.e. the dependence of the vibrational properties of single gold nanodisks on their aspect

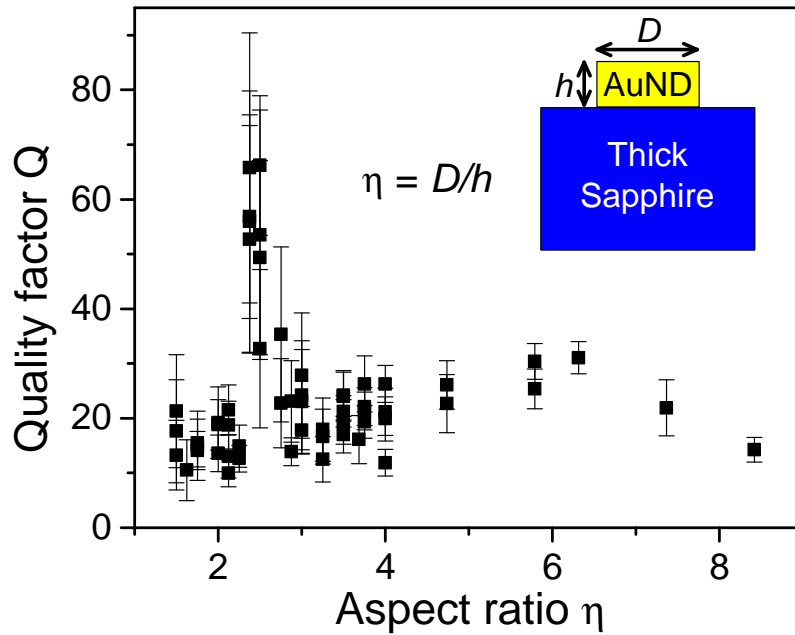


**Figure 5.3** – Quality factors of the experimentally detected acoustic modes as a function of the aspect ratio of the single gold nanodisks. Figure reproduced from previous work done in the FemtoNanoOptics group [21, 62]. Each dot corresponds to a single nanodisk measurement.

ratio.

### 5.2.1 Experimental strategy

The gold nanodisks required for this study were synthesized by Sylvie Marguet (CEA Saclay) via colloidal chemistry, similarly to the ones described in Chapter 2 Section 2.1. Several nanodisks solutions characterized by different average nanodisk aspect ratios (in the 2-5 range) were specially synthesized for this study. 3 of them were used in our experiments:

- $\eta = 2.3$ , corresponding to average dimensions  $D \approx 49$  nm and  $h \approx 21$  nm.
- $\eta = 3.5$ , corresponding to average dimensions  $D \approx 73$  nm and  $h \approx 21$  nm.
- $\eta = 4.5$ , corresponding to average dimensions  $D \approx 95$  nm and  $h \approx 21$  nm.

Figure 5.4 presents the normalized extinction spectra of each previous solution (5.4d) as well as some scanning electron microscopy images of gold nanodisks from each solution deposited on a 40 nm thick SiO<sub>2</sub> membrane (5.4a, b and c).

These nanoparticles were then deposited on 40 nm thick SiO<sub>2</sub> membranes using the protocol described in Chapter 3 (see Section 3.3.1). Additionally, gold nanodisks with  $D \approx 100$  nm and  $h \approx 10$  nm (corresponding to large aspect ratios, in the 9-14 range), coming from the solution used for the thermal studies of Chapters 3 and 4 (see synthesis in Chapter 2 Section 2.1), were deposited on the same substrate and studied.

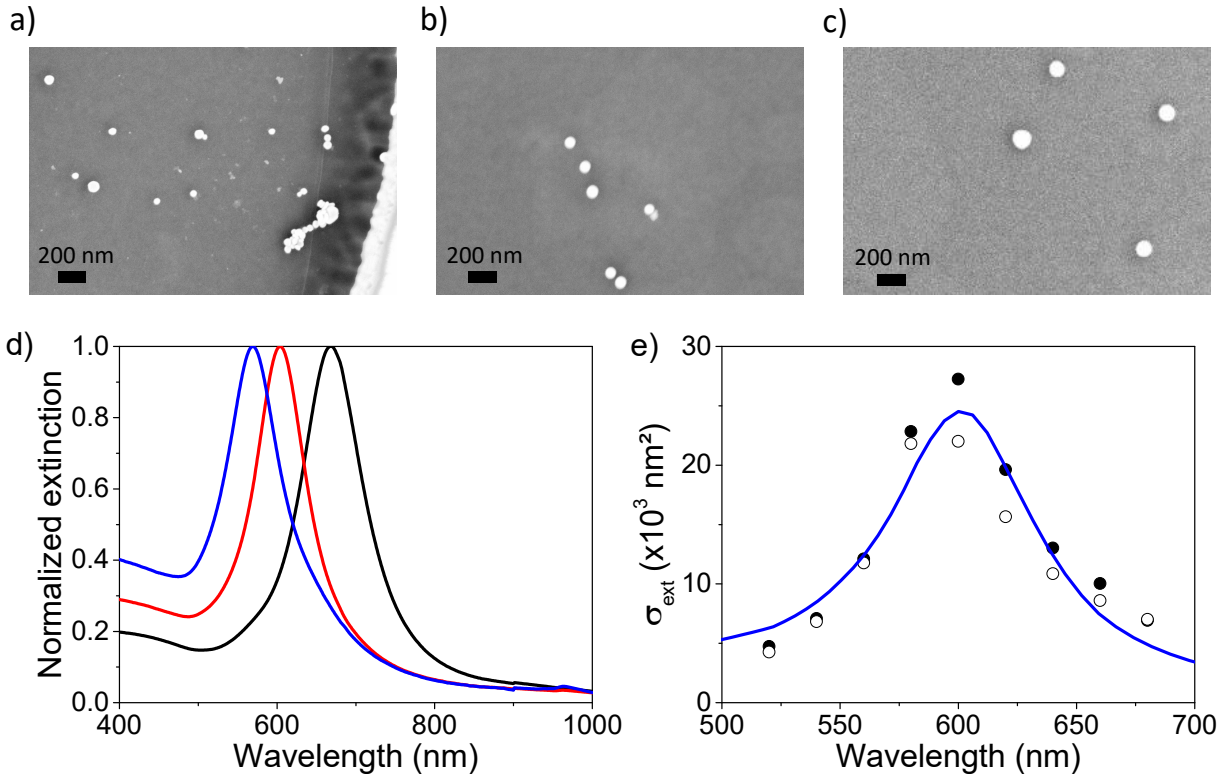
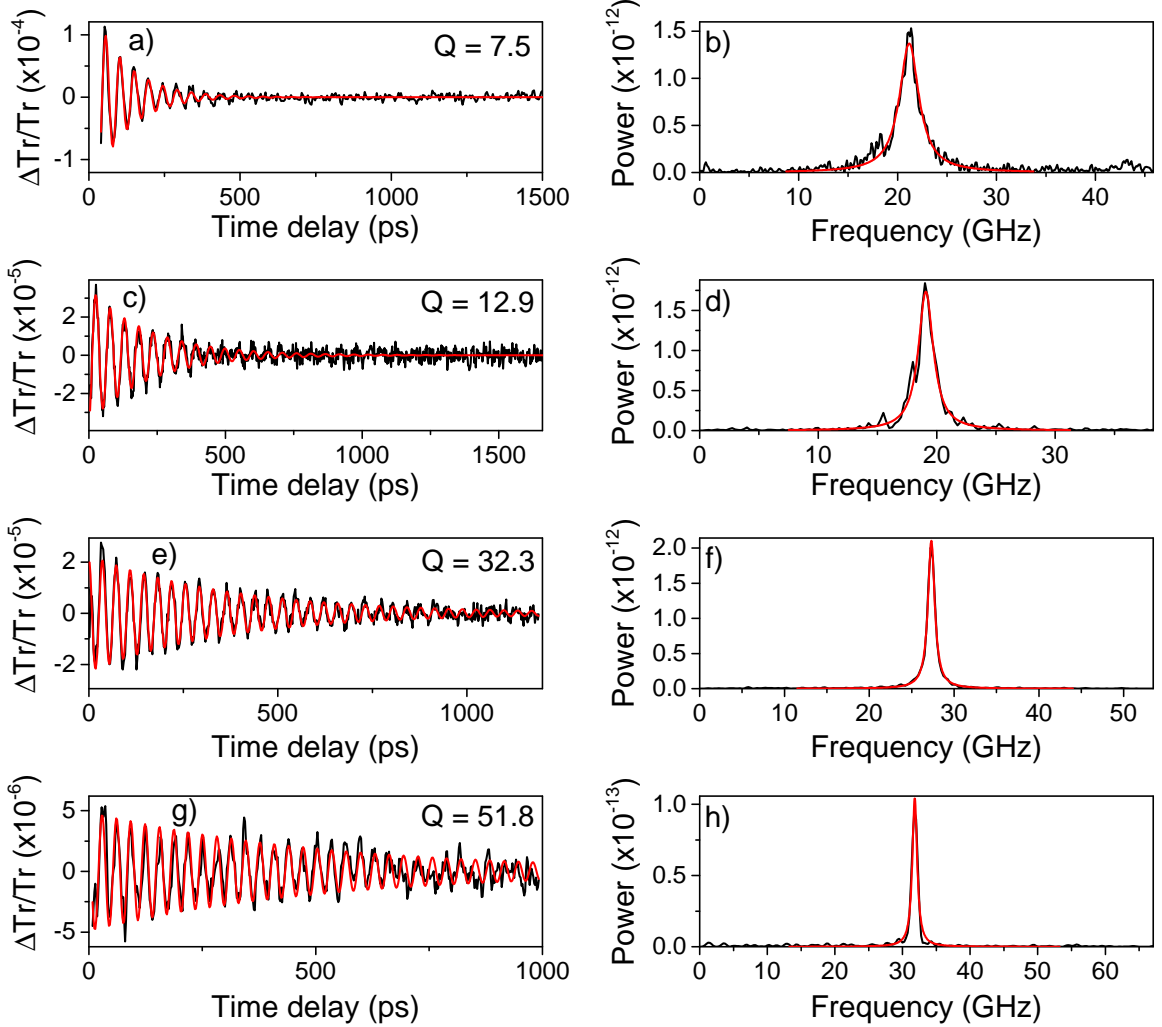


Figure 5.4 – a), b) and c) scanning electron microscopy images of gold nanodisks deposited on a 40 nm thick  $\text{SiO}_2$  membrane from solutions with  $h \approx 20$  nm and  $\eta = 2.3$ ,  $\eta = 3.5$ , and  $\eta = 4.5$  average aspect ratios, respectively. d) Normalized extinction spectra of the three solutions of gold nanodisks in water. e) Measured extinction spectrum of a single gold nanodisk from solution with average aspect ratio  $\eta = 3.5$ . Gold nanodisks in a), b), and c) come from the solutions with average aspect ratios  $\eta = 2.3$  (blue line), 3.5 (red line), and 4.5 (black line), respectively. In e), the full and empty markers in the data points correspond to two orthogonal polarizations of incident light beam. The solid blue line is the result of an optical FEM simulation with  $D = 77.8$  nm and  $h = 23.1$  nm.

Extinction spectra of single nanodisks were acquired thanks to the SMS technique and compared with optical FEM modeling for perfect cylindrical shape in order to estimate their diameter  $D$  and height  $h$  as well as the corresponding aspect ratio  $\eta$  (whose increase leads to a red shift of the nanodisk Surface Plasmon Resonance). The experimental extinction spectra of a single gold nanodisk, originating from the colloidal solutions with average aspect ratio  $\eta = 3.5$ , as well as optical FEM simulation reproducing this spectra, are represented in Figure 5.4e.

Single-particle time-resolved measurements were conducted on 5-7 gold nanodisks of each solution. The extinction spectrum of each of these nanodisks was measured prior to time-resolved measurements, allowing estimation of its diameter and thickness as in the example provided above (Figure 5.4e). In this section, probe wavelengths  $\lambda_{pr}$  on the side of the Surface Plasmon Resonances of the single gold nanodisks were chosen, i.e.  $\lambda_{pr} \pm 10\text{-}40$  nm, for each investigated nanodisk. This choice was based on previous experimental studies that have empirically shown that such configuration leads to higher amplitudes of the oscillatory components of the time-

resolved signals [21,112] (see Section 5.3 for more detailed investigations of the probe wavelength-dependence of the oscillatory amplitudes of time-resolved signals).



**Figure 5.5 – Examples of oscillatory components (black lines) extracted from raw time-resolved measurements and fit (red lines) on 4 single nanodisks with different aspect ratios.** The estimated aspect ratios for the 4 nanodisks are a)  $\eta = 12.6$ , b)  $\eta = 4.7$ , c)  $\eta = 3.3$ , and d)  $\eta = 2.2$ . The quality factors determined by time-domain fitting of the measured signals are indicated in each panel. The nanodisk corresponding to panel a) originates from the synthesis described in Chapter 2 Section 2.1 (thickness of about 10 nm) while the three other nanodisks come from the synthesis described in this chapter (Section 5.2.1, thickness of about 20 nm), all of them being supported by a 40 nm thick  $\text{SiO}_2$  membrane.

### 5.2.2 Experimental signals

Subsequently to time-resolved experiments, extraction of their oscillatory components was performed using the protocol detailed in Chapter 2 Section 2.2.3.4 (only one mode was detected in each case). A variety of acoustic components, with diverse amplitudes, frequencies, damping rates and quality factors were obtained. Figure 5.5 present a few examples of the measured oscillations (left side) as well as the corresponding Fourier transforms (right side), the quality factor values being evaluated from the optimal fits through Equation 5.7.

### 5.2.3 Experimental frequencies and quality factors

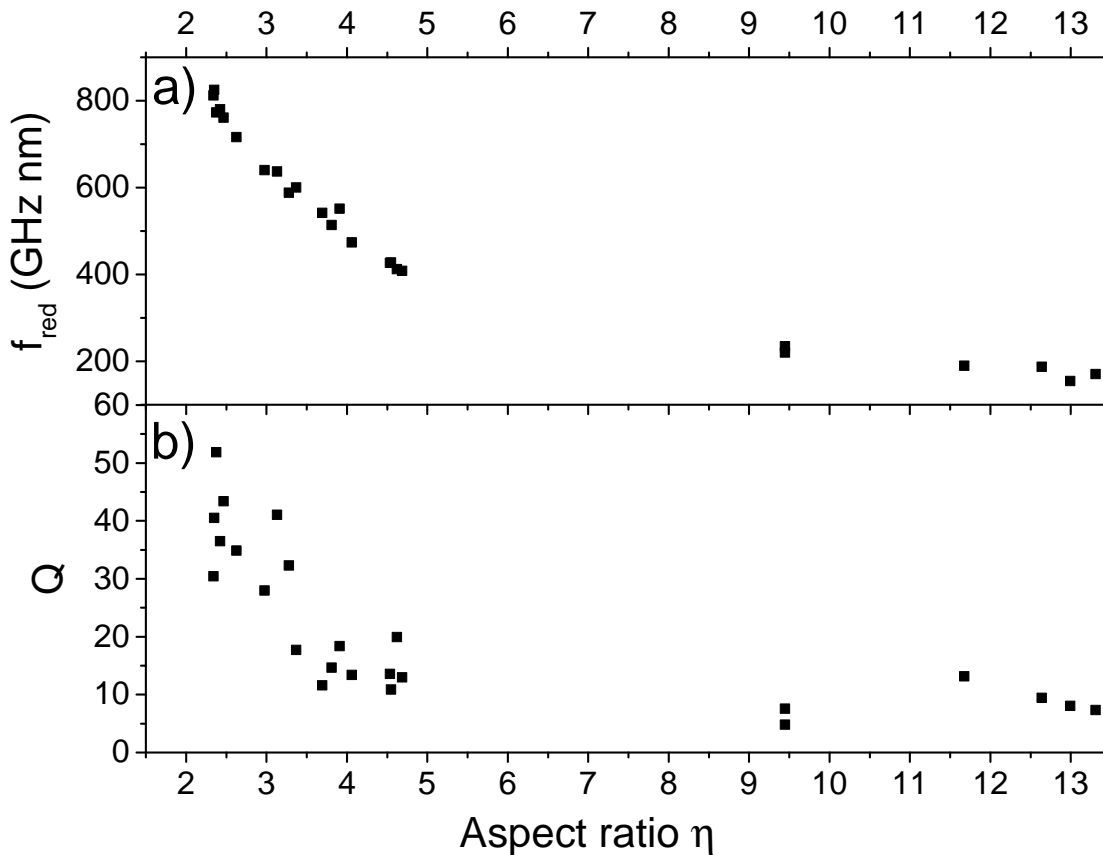


Figure 5.6 – a) Reduced frequencies  $f_{red} = fh$  and b) quality factors  $Q$ , extracted from experimentally detected vibrational components, as a function of the aspect ratio  $\eta$  of the corresponding single gold nanodisks. Thicknesses  $h$  of the nanodisks came from the previous optical FEM characterization.

As the investigated nanodisks had different thicknesses, reduced frequencies  $f_{red}$  defined as  $f_{red} = fh$  (expected to be relatively independent of nanodisk thickness) were considered for comparing all measurements. Figure 5.6 presents the reduced frequencies  $f_{red}$  and quality factors  $Q$  deduced from the fit of the oscillatory components obtained via time-resolved experiments performed on single gold nanodisks coming from the synthesis procedure described in Chapter

2 Section 2.1 ( $\eta$  in 9-15 range) as well as the one presented in Section 5.2.1 ( $\eta = 2-5$ ). The uncertainty on the experimental quality factor values is estimated to be of the order of 20 %.

The extracted reduced frequencies present a quasi monotonic evolution in the  $\eta = 2-5$  range (Figure 5.6a). Deduced quality factors values are in the 5-15 range for nanodisks with  $\eta = 9-15$ , corresponding to a low number of oscillations observed in time-resolved experiments. In contrast, the quality factors obtained for aspect ratios in the 2-5 range present increasing values for smaller  $\eta$  values and reach significantly higher values, with a maximum  $Q \approx 50$ . Figure 5.6b thus demonstrates a clear dependence of the quality factors of the detected vibrational modes on the aspect ratio  $\eta$  of single gold nanodisks supported on a 40 nm thick SiO<sub>2</sub> membrane, similarly to what was previously observed for a substrate made of sapphire [62]. However, a large dispersion of the quality factors is observed for nanodisks with close aspect ratio values, possibly linked to the morphological differences (e.g. more or less important deviations from a perfectly cylindrical shape) between gold nanodisks as well as the dispersion in the quality of the mechanical contacts between gold nanodisks and their supporting substrate.

#### 5.2.4 Numerical modeling via FEM

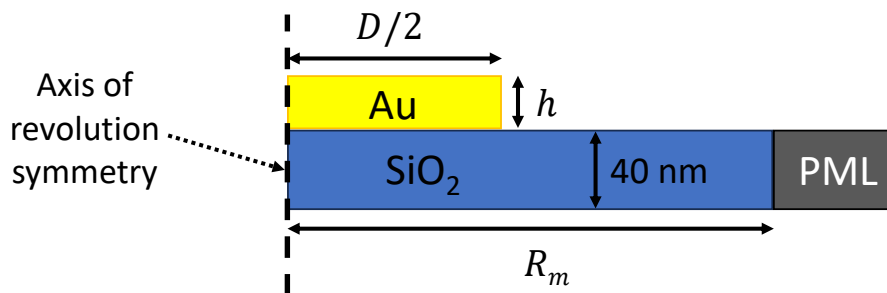


**Figure 5.7 – 2D geometry used in the vibrational FEM calculations taking advantage of the revolution symmetry of the problem.** A single gold nanodisk with a diameter  $D$  and thickness  $h$  supported on a 40 nm thick SiO<sub>2</sub> membrane of radius  $R_m$  is considered. A perfectly-matched layer is placed at the border of the simulation domain.

Finite-element modeling, based on 2D axisymmetric eigenmode numerical resolution of the Navier equation (see Equation 5.1), was performed to numerically obtain the vibrational modes of a single gold nanodisk supported by a 40 nm thick SiO<sub>2</sub> membrane and the associated frequencies and quality factors via the Structural Mechanics module of the COMSOL software. The considered FEM configuration is presented in Figure 5.7. A Perfectly Matched Layer (PML) was defined at its border in order to avoid the associated reflections and to simulate an open domain. The radius of the PML was chosen to be 10 times larger than the nanodisk thickness while the size of the mesh was about 10 times smaller. At the nanodisk-membrane interface a perfect mechanical contact, corresponding to a continuity of displacement and stress, was assumed. As for the damping of the vibrational modes, only radiative damping, linked to  $Q_{extrinsic}$  quality factor in Equation 5.9 and originating from the damping of the emission of acoustic waves in the

environment, was considered. The performed calculation not only yields nanodisk vibrational modes, but also modes associated to the substrate and the PML (whose properties depend on the simulation parameters). The latter typically display much lower quality factor allowing a simple selection of the nanodisk modes (at the exception of those displaying very low quality factors) [146].

These simulations are preliminary and will be completed in future work with the computation of excitation spectra as well as the use of different modelizations of the intrinsic damping contributions ( $Q_{intrinsic}$  in Equation 5.9).

### 5.2.5 Comparison between experimental results and FEM modelization

Due to the dispersion of the thicknesses of the investigated nanodisks with low aspect ratios, in the 20-25 nm range, FEM calculations of reduced frequencies and quality factors were performed both for  $h = 20$  nm and  $h = 25$  nm, as shown in Figure 5.8 (simulations were also performed for  $h = 10$  nm and lead to similar results in the large aspect ratio  $\eta$  range). Moreover, only the two relevant vibrational modes, corresponding to those detected in Fabio Medeghini's work [62] were represented. Further work will be needed to determine their relative excitation amplitudes in the context of our experiments.

Figure 5.8a shows that experimental reduced frequencies are qualitatively reproduced by FEM simulations with little difference between  $h = 20$  nm and  $h = 25$  nm computations. In particular, the monotonic behavior, i.e. increasing reduced frequencies for decreasing aspect ratios, is observed both experimentally and numerically (for the two computed modes, displaying similar frequency evolutions). The difference between experimental and modeled frequencies, of the order of 20 – 30%, may result from the non-perfectly cylindrical nanodisk shape or from uncertainties associated to the optical determination of nanodisks dimensions. Further work, about the modelization of the optical detection of vibrations as well as the frequency content linked to the excitation by the pump pulse, is needed to determine if the detected acoustic vibrations correspond to a single vibrational mode or to a combination of both modes.

However, as shown in Figures 5.8b and 5.8c, FEM computations of quality factors differ from experimental data for both computed modes. Despite a relatively good agreement at large  $\eta$  values for the mode represented with a full line in Figure 5.9b, significantly different behaviors are found in the 2-5 aspect ratio range, with numerical quality factors reaching up to 200 and 300 values while experimental ones are limited to a 10-50 range.

The vibrational FEM model used for these computations estimates  $Q_{extrinsic}$  and does not take into account any form of intrinsic damping : the differences observed between numerical calculations and experimental data are thus not surprising especially in the aspect ratio range where acoustic emission in the membrane is predicted to be inefficient. A simple empirical way to add an intrinsic damping to the computed quality factors is to use Equation 5.9 with a constant  $Q_{intrinsic}$  (neglecting the possible frequency dependence of this quantity). These new FEM quality factors are represented in Figure 5.9 with pale orange ( $h = 20$  nm) and light blue curves ( $h = 25$  nm). In the 2-5 aspect ratio range the mode represented with a dashed line presents a relatively good agreement with the experimental quality factors, with similar maximum value (35-45 range). This observation suggests that the quality factors of single colloidal gold nanodisks supported on a 40 nm thick SiO<sub>2</sub> membrane can be successfully

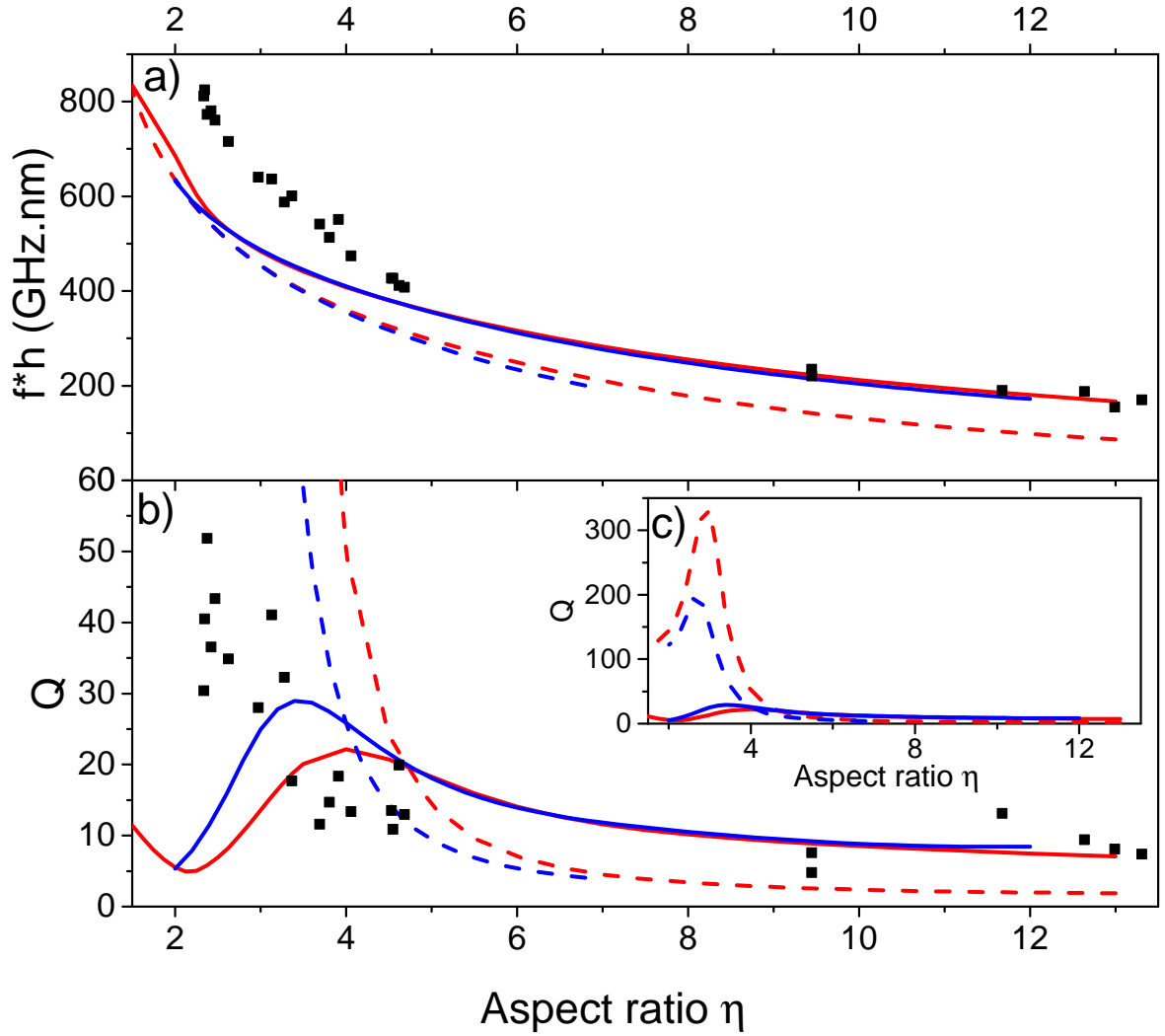


**Figure 5.8** – a) Reduced frequencies  $f_{red} = fh$  and b) quality factors  $Q$  from experimental measurements and FEM simulations as a function of the aspect ratio  $\eta$  of the corresponding single gold nanodisks. c) FEM simulations from b) are shown on a larger  $Q$  scale. FEM simulations were performed for single gold nanodisks with variable diameters  $D$  and thicknesses  $h = 20$  nm (red lines) or 25 nm (blue lines), always supported on a 40 nm thick  $\text{SiO}_2$  membrane. The two main vibrational modes playing a role in time-resolved experiments [62] are shown as solid and dashed lines, respectively.

explained by a radiative damping, computed by the FEM model and linked to the emission of acoustic waves in the membrane, as well as intrinsic damping with  $Q_{intrinsic} \approx 50$ , a value of the same order than what was observed for lithographed gold nanodisks deposited on sapphire [62]. Further studies will be needed to confirm this  $Q_{intrinsic}$  value and investigate its possible size and/or frequency dependence. Importantly, compared to what was observed for single gold nanodisks supported on bulk sapphire, for which quality factors  $Q > 50$  were observed in a narrow 2.3-2.5 aspect ratio range [62], the present work demonstrates quality factors  $Q > 30$  in

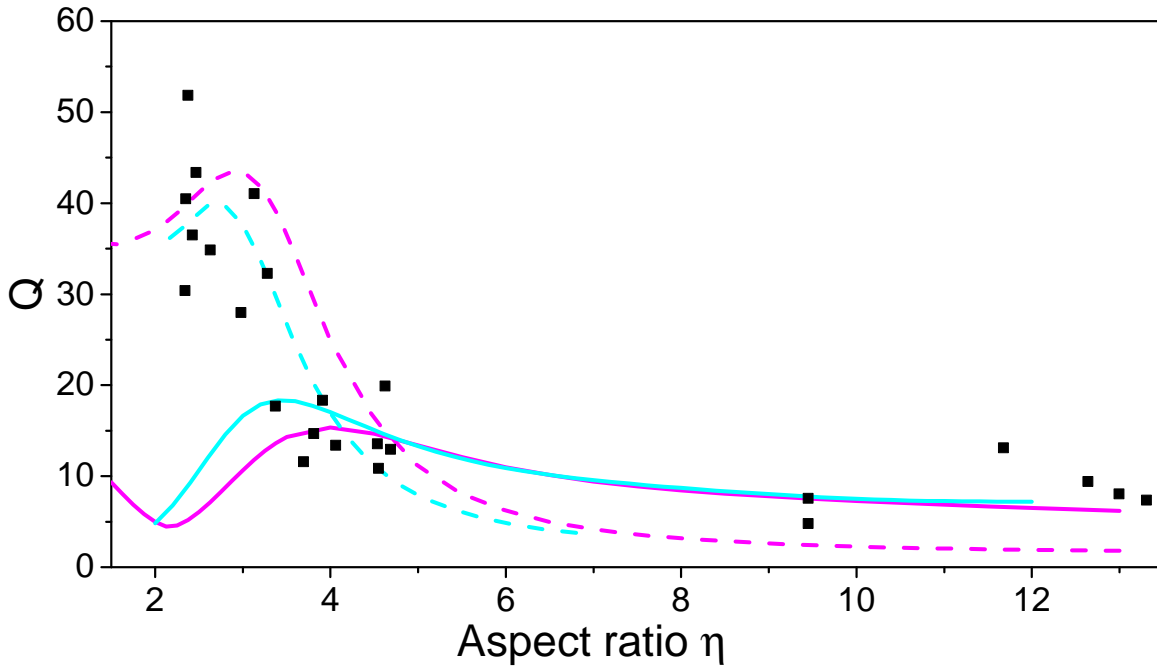


**Figure 5.9** – Quality factors  $Q$  from experimental measurements and FEM simulations including intrinsic damping, as a function of the aspect ratio  $\eta$  of the corresponding single gold nanodisks. Vibrational FEM simulations with a constant intrinsic damping ( $Q_{intrinsic} = 50$ , taken into account via Equation 5.9) were performed for single gold nanodisks supported on a 40 nm thick  $\text{SiO}_2$  membrane with variable nanodisks diameters  $D$  and thicknesses  $h = 20$  nm (pink lines) or 25 nm (light blue lines). The two corresponding vibrations modes are represented in solid and dashed lines, respectively.

a 2.3-3.3 aspect ratio range for single gold nanodisks supported on a 40 nm thick  $\text{SiO}_2$  membrane, i.e. lower quality factors but on a wider  $\eta$  range. This could be partially explained by the larger acoustic mismatch between the gold nanodisk and its substrate in the case of the  $\text{SiO}_2$  substrate than in the sapphire one ( $Z_{\text{SiO}_2}/Z_{\text{Au}} \approx 0.2 < Z_{\text{Al}_2\text{O}_3}/Z_{\text{Au}} \approx 0.7$ ), as previous modeling work has shown that it could lead to an enhancement of  $Q$  factors in a reduced aspect ratio range [146]. However these results were demonstrated in the case of bulk substrates (which is valid for the sapphire substrate but not for the silica one): therefore, further investigations will be performed to understand the impact of the thickness of the substrate on the vibrational dynamics of single supported gold nanodisks.

### 5.3 Optical detection of the acoustic vibrations of single gold nanodisks

Similarly to work presented in Chapter 4, i.e. the characterization of the transient optical response of single gold nanodisks linked to the cooling dynamics of such objects, a relevant research axis here is to study the optical aspects in the detection of the acoustic vibrations of single

nano-objects. Indeed, understanding how the characteristics of the time-resolved experiments, the probe wavelength notably, influence the detection of vibrations modes can help determine optimal working conditions for studying such acoustic modes. In this section such work on the same gold nanodisks than the ones presented in Chapter 4 will be presented.

### 5.3.1 Experimental strategy and acoustic signals

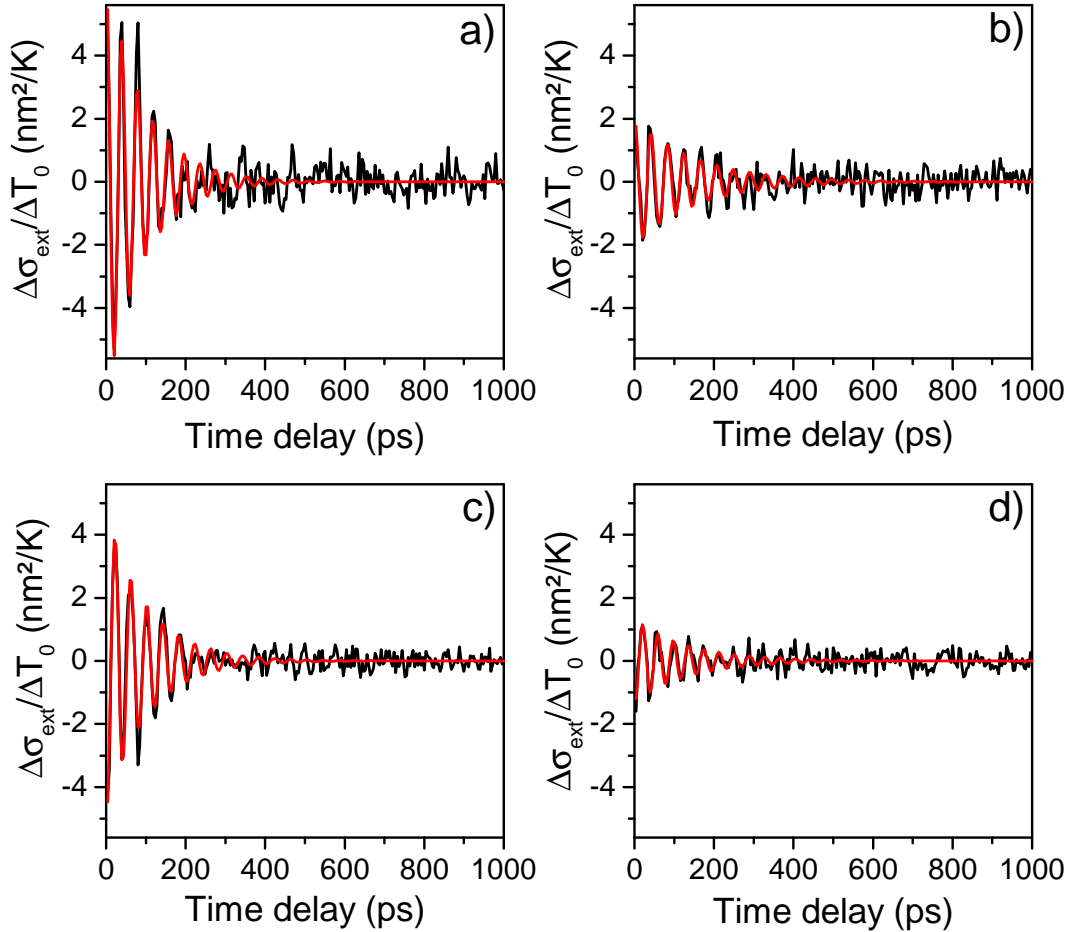


**Figure 5.10** – Examples of oscillatory components (black lines) extracted from raw time-resolved measurements and fit (red lines) performed on a single gold nanodisk (ND1) using 4 different  $\lambda_{pr}$  values. Raw acoustic components were converted into variations of extinction cross-section normalized by the initial heating of the nanodisk  $\Delta T_0$  (of the order of 10-20 K). Experimental signals correspond to  $\lambda_{pr} - \lambda_{SPR} =$  a) -20 nm, b) 0 nm, c) 40 nm, and d) 90 nm, respectively.

Single-particle time-resolved measurements were conducted on the 2 gold nanodisks ND1 and ND2 described in Chapter 4, with diameters  $D = 96.2$  nm and 93 nm and thicknesses  $h = 10.8$  nm and 9.5 nm, respectively. In this section, experiments were performed with a probe wavelength  $\lambda_{pr}$  that was varied across the Surface Plasmon Resonances of the nano-objects, similarly to the strategy used in the previous chapter. In practice, the probe wavelength was in

the same range, i.e. in the 790-900 nm range, corresponding to  $\lambda_{pr} - \lambda_{SPR} \approx -10/+100$  nm and  $-20/+90$  nm for ND1 and ND2, respectively. Performing experiments with a probe wavelength below 790 nm is quite difficult with our experimental setup as it leads to a pump beam with a wavelength in the UV-blue range, where optical aberrations and light transmission through the microscope objectives significantly alter and attenuate the light beam. Acoustic components were extracted from raw time-resolved signals using the method described in Chapter 2 Section 2.12.

Figure 5.10 presents some of the acoustic signals obtained from time-resolved experiments at different probe wavelengths for the gold nanodisk ND1. These few examples show that the amplitudes of the measured acoustic components present significantly different values depending on the probe wavelength  $\lambda_{pr}$ , with in particular different signs at their origin, the signals in Figures 5.10a and 5.10b starting with positive values, while the ones in Figures 5.10c and 5.10d begin with negative values. In contrast, the frequencies and quality factors of the modes detected in experimental measurements (which are intrinsic properties of the vibrational modes of the nanodisk) don't exhibit any dependence on the probe wavelength.

### 5.3.2 Experimental results

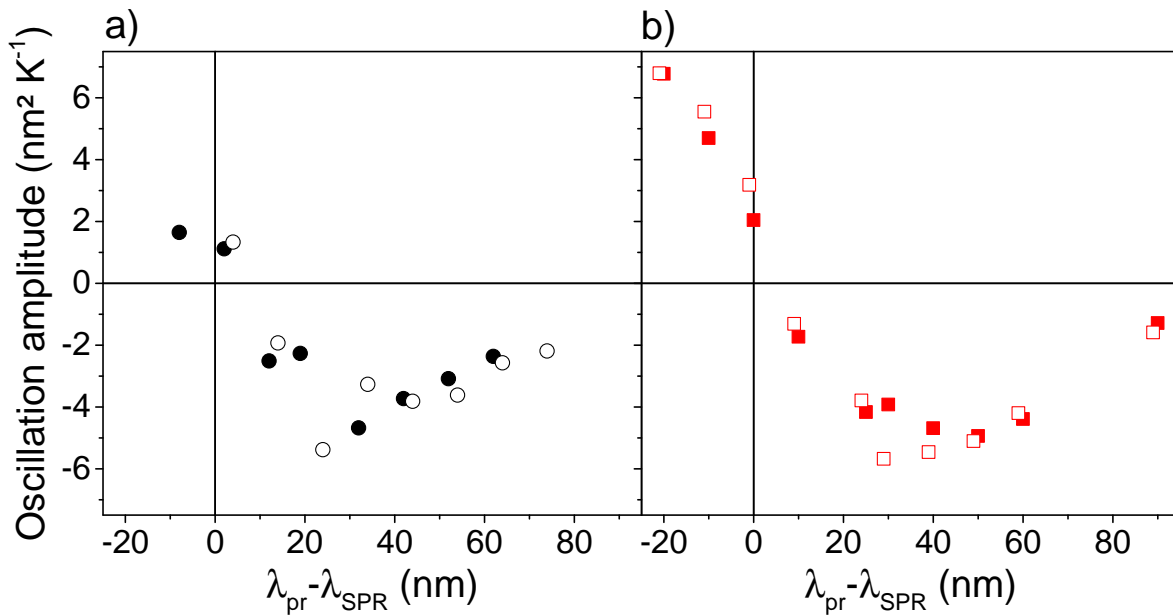


Figure 5.11 – Experimental values of the amplitudes of measured acoustic components as a function of  $\lambda_{pr} - \lambda_{SPR}$  for the investigated gold nanodisks a) ND1 (black markers) and b) ND2 (red markers). Similarly to Figure 4.4 in Chapter 4, full and empty markers correspond to measurements performed using two different orthogonal polarizations of the probe beam.

The amplitudes of the acoustic components experimentally measured for the two gold nanodisks ND1 and ND2 are represented in Figure 5.11a and 5.11b as a function of  $\lambda_{pr} - \lambda_{SPR}$ , respectively.

Figure 5.11 demonstrates a clear dependence of the amplitude of the detected acoustic vibrations on the probe wavelength. In particular, the optical sensitivity to vibrations is minimal close to the Surface Plasmon Resonance of the gold nanodisks, in opposition to what was observed for optical sensitivity to nanodisk heating. In contrast, maximal sensitivity to acoustic vibrations is observed on the flank of the Surface Plasmon Resonance at  $\lambda_{pr} - \lambda_{SPR} \approx 20\text{-}40$  nm for ND1 and  $\lambda_{pr} - \lambda_{SPR} \approx 20\text{-}50$  nm for ND2.

The spectral shape of Figure 5.11 is characteristic of the detection of a process predominantly affecting Surface Plasmon Resonance position. It strongly contrasts with that obtained in the context of the study of the optical detection of nano-object heating, which is mostly detected through the Surface Plasmon Resonance broadening that it induces (see Chapter 4, Section 4.2.5, Figure 4.10). Two reasons can be invoked to qualitatively explain this difference:

1. Conversely to nanoparticle heating, vibrational modes generally modify the shape of a nano-object, which has a strong influence on Surface Plasmon Resonance position (see for instance Chapter 1, Section 1.2.2, Equation 1.48).
2. Even if they both induce density changes, vibrations and heating differently modify the real and imaginary parts of the gold dielectric function, which respectively influence Surface Plasmon Resonance spectral position and width (see Chapter 1, Section 1.2.2). Gold heating leads to dominant modifications of  $\epsilon_2$  over  $\epsilon_1$  ones, in the investigated spectral range (see Figure 4.8 of Chapter 4). Conversely, strain induces larger variations of  $\epsilon_1$  in most of the visible spectrum [147].

These results thus constitute a new illustration of the possibility to selectively probe distinct dynamics in the context of time-resolved measurements, by an accurate choice of probe wavelength. They will be further investigated in future research.

## 5.4 Conclusion

In this chapter the study of the vibrations of single gold nanodisks was performed. First, the experimental measurement of the reduced frequencies and quality factors of acoustic vibrations detected for single colloidal gold nanodisks with different aspect ratios supported on a 15 nm thick  $\text{Si}_3\text{N}_4$  membrane was done and maximum  $Q$  values around 50 were observed for  $\eta$  in the 2-5 range, largely exceeding the typical  $Q \approx 10$  values obtained for nanodisks with  $\eta \approx 10$ . These results confirm the morphology dependence of  $Q$  factors of nano-objects already observed for bulk substrates [62]. They suggest that  $Q$  enhancement can be obtained on a broader aspect ratio range in the case of thin membranes as compared to thick substrates. Comparison with FEM simulations lead to a relatively good agreement for the reduced frequencies. Experimental quality factors could be approximately reproduced by the inclusion of intrinsic damping with  $Q_{intrinsic}$  of the order of 50. This value does not exceed that measured for lithographed nanodisks, suggesting that either our nanodisks did not present much less crystalline defects than lithographed ones, or that these defects do not constitute the dominant contribution to intrinsic damping.

Measurements with a broad probe wavelength range were also performed in order to characterize the link between the amplitude of the detected acoustic vibrations and the optical detection. The optical sensitivity to vibrations was found to be significantly dependent on the

probe wavelength and exhibited, for the two investigated gold nanodisks, ND1 and ND2, minima around the Surface Plasmon Resonance and maxima on its flank, in stark contrast with the probing of thermal dynamics. Thus, the optimal conditions for probing the heating and vibrations of nano-object strongly differ from each other, which result from the different dominant dielectric changes induced by these two phenomena and from the additional transient shape changes induced by acoustic vibrations.

Further investigations of the vibrational properties of single gold nanodisks will include numerical modelization of the amplitudes of the detected acoustic modes (in progress), of the optical response of a vibrating nanoparticle (already started in other groups [148, 149]) as well as time-resolved experiments with a probe wavelength covering the whole spectral range around the resonance of the gold nanodisk. As for the study of the dependence of quality factors on the aspect ratio of the gold nanodisks, it would be interesting to perform additional experiments on single colloidal gold nanodisks deposited on thick sapphire in order to compare them to the results obtained for lithographed gold nanodisks supported on the same substrate thus allowing to more directly address the impact of the nanodisk synthesis procedure (see ref. [62]).

# Conclusion and Perspectives

In this thesis, the thermal and vibrational dynamics of single gold nanodisks supported on different transparent substrates, as well as the induced transient optical response that they induce, were studied using the combination of spatial modulation spectroscopy and ultrafast time-resolved spectroscopy.

Time-resolved experiments performed on single gold nanodisks deposited on substrates differing via their compositions and thicknesses illustrated that the observed cooling dynamics largely depended on the characteristics of the substrate, while showing good reproducibility between different individual nanodisks on a given substrate. These findings have been interpreted and well reproduced via FEM thermal modelization (taking into account interfacial heat transfer at the nanodisk-substrate interface and heat diffusion in the substrate) with bulk substrate thermal conductivity values, a periodic excitation model being required for thin and ultrathin membranes. The observed cooling dynamics could be quantitatively reproduced using a simple diffusive model of heat conduction in the nanodisk environment. The absence of a clear signature of non-diffusive heat propagation can be explained, in the bulk sapphire case, by the interface-limited dynamics, and, for nanometric membranes, by an average phonon mean free path being much smaller than the thicknesses of the membranes. While the temporal dynamics of nanodisk cooling could be quantitatively reproduced by simulations, the measured average heating of the nanodisks was only qualitatively explained. To achieve a fully quantitative description of time-resolved signals, the work described in this manuscript could be complemented by experimental measurements aiming at clarifying the heat exchanges occurring at the interface of the membranes with air and at their ends. This could be attempted through experiments involving longer time scales, or by investigating the possible dependence of the cooling dynamics of nanodisks on the distance separating them from the membrane edge. In the future, these experiments could be reproduced on thin membranes with different composition, silicon for example, in order to observe non-diffusive heat propagation, as such effects have been demonstrated in the case of networks or metal nanowires on bulk silicon [97].

Vibrational properties of single gold nanodisks deposited on thin membranes have been investigated both from experimental and modeling points of view. First, the frequencies and quality factors of the detected acoustic vibrations of colloidal single gold nanodisks with different aspect ratios were measured experimentally, with quality factors reaching up to 50 in a specific aspect ratio range. Observations confirm the morphology dependence of quality factors of nanoparticles demonstrated in previous work of the FemtoNanoOptics group, while suggesting that an enhancement of quality factors can be obtained in a broader aspect ratio range for thin supporting membranes, as compared to thick sapphire. Experimental frequencies were relatively well reproduced by vibrational FEM simulations, whereas a qualitative agreement for the quality factors of single colloidal gold nanodisks could be achieved by including an intrinsic

damping contribution, associated with a quality factor of the same order as that previously obtained for lithographed nanodisks. The similarity of these two values, despite the large difference between the used synthesis procedures, suggests that either crystalline defects are similar for the two samples or they do not constitute the dominant source of intrinsic damping. Additional characterizations of nanodisk crystallinity would thus be interesting to refine the interpretation of our experimental results. The understanding of the dependence of quality factors on the aspect ratio of the gold nanodisks could benefit from experiments on single colloidal gold nanodisks supported on thick sapphire, allowing to compare them with previous results obtained for lithographed nanodisks supported on the same substrate and to further understand the effect of the nanodisk synthesis procedure on the quality factors. As a result, experiments and simulations allowed to further understand the thermal and vibrational dynamics of single supported gold nanodisks by underlining in particular the influence of the characteristics of the supporting substrate.

Another essential part of this work was the study of the optical detection of the thermal and vibrational dynamics. First, we focused on the study of the optical detection of the cooling dynamics of membrane-supported single gold nanodisks. To achieve this, time-resolved experiments were conducted with a probe wavelength varied across the Surface Plasmon Resonance of the single nanodisks and gave access to an experimental measurement of the optical sensitivity to nanodisk heating. This quantity was shown to present a maximum value around the resonance of the nano-object, as well as a significant spectral dependence, complemented with a vanishing on the red flank of the resonance. A thermo-optical model allowed to well reproduce the experimental data and its characteristic features. Moreover, the amplitudes and temporal dynamics of the transient variations of the extinction cross-section of the single nanodisks were shown to largely depend on the probe wavelength. Slower decays, as well as noticeable variations, of the transient optical responses were observed experimentally in a narrow spectral range enclosing the one where the contribution of nanodisk heating to extinction vanishes, the membrane heating contribution becoming of the same order of (or larger than) the latter. To our knowledge, these results constitute the first experimental demonstration, in the context of ultrafast time-resolved spectroscopy measurements, of a detection of the heating of the environment for nanoparticles supported on a solid environment. Such results could contribute to the development of some applications using metallic nano-objects as local probes of temperature. In parallel, the optical detection of acoustic vibrations of single gold nanodisks deposited on thin membranes was also investigated. Time-resolved measurements were performed using a broad wavelength range and demonstrated a large dependence of the optical sensitivity to vibrations on the probe wavelength with the observation of minimum around the Surface Plasmon Resonance and maximum on its flank, a spectral shape largely different from the one of the thermal dynamics. Future work about the vibrational properties of single gold nanodisks could aim to perform numerical modelization of the amplitudes of the detected acoustic modes as well as ultrafast time-resolved experiments with a probe wavelength covering the whole spectral range around the resonance of the gold nanodisk. Thus, the conditions for optimal probing of the heating and the acoustic vibrations of a nanoparticle present strong differences, a fact that could be explained by the dissimilar dielectric changes induced by these two phenomena and also from the shape modifications linked to acoustic vibrations. Further investigations will be required for a more quantitative understanding of the transient optical response induced by vibrations.

# Bibliography

- [1] U. Kreibig and M. Vollmer, *Optical properties of metal clusters*, vol. 25. Springer Science & Business Media, 2013.
- [2] D. G. Cahill, W. K. Ford, K. E. Goodson, G. D. Mahan, A. Majumdar, H. J. Maris, R. Merlin, and S. R. Phillpot, “Nanoscale thermal transport,” *Journal of applied physics*, vol. 93, no. 2, pp. 793–818, 2003.
- [3] D. G. Cahill, “Analysis of heat flow in layered structures for time-domain thermoreflectance,” *Review of scientific instruments*, vol. 75, no. 12, pp. 5119–5122, 2004.
- [4] K. A. Willets and R. P. Van Duyne, “Localized surface plasmon resonance spectroscopy and sensing,” *Annu. Rev. Phys. Chem.*, vol. 58, no. 1, pp. 267–297, 2007.
- [5] G. J. Snyder and E. S. Toberer, “Complex thermoelectric materials,” *Nature materials*, vol. 7, no. 2, pp. 105–114, 2008.
- [6] G. Baffou, F. Cichos, and R. Quidant, “Applications and challenges of thermoplasmonics,” *Nature Materials*, vol. 19, no. 9, pp. 946–958, 2020.
- [7] A. Crut, P. Maioli, N. Del Fatti, and F. Vallée, “Optical absorption and scattering spectroscopies of single nano-objects,” *Chemical Society Reviews*, vol. 43, no. 11, pp. 3921–3956, 2014.
- [8] A. Arbouet, D. Christofilos, N. Del Fatti, F. Vallée, J. Huntzinger, L. Arnaud, P. Billaud, and M. Broyer, “Direct measurement of the single-metal-cluster optical absorption,” *Physical review letters*, vol. 93, no. 12, p. 127401, 2004.
- [9] H. Baida, D. Mongin, D. Christofilos, G. Bachelier, A. Crut, P. Maioli, N. Del Fatti, and F. Vallée, “Ultrafast nonlinear optical response of a single gold nanorod near its surface plasmon resonance,” *Physical review letters*, vol. 107, no. 5, p. 057402, 2011.
- [10] O. L. Muskens, N. Del Fatti, and F. Vallée, “Femtosecond response of a single metal nanoparticle,” *Nano letters*, vol. 6, no. 3, pp. 552–556, 2006.
- [11] “Simple periodic table chart-blocks,” 2021. Author is User:Double sharp, based on File:Simple Periodic Table Chart-en.svg by User:Offnfopt. Available at [https://en.m.wikipedia.org/wiki/File:Simple\\_Periodic\\_Table\\_Chart-blocks.svg#globalusage](https://en.m.wikipedia.org/wiki/File:Simple_Periodic_Table_Chart-blocks.svg#globalusage).
- [12] R. Wyckoff, *Crystal Structures*, vol. 1. R.E. Krieger Pub. Co., 1982. p. 467.

- [13] N. Ashcroft and N. Mermin, *Solid State Physics*. HRW International Editions, 1976.
- [14] P. Debye, “Zur theorie der spezifischen wärmen,” *Annalen der Physik*, vol. 344, pp. 789 – 839, 03 1912.
- [15] B. Diu, C. Guthmann, D. Lederer, and B. Roulet, *Éléments de physique statistique*. Collection Enseignement des sciences, Hermann, 1989.
- [16] J. Arblaster, “Thermodynamic properties of gold,” *Journal of Phase Equilibria and Diffusion*, vol. 37, no. 2, pp. 229–245, 2016.
- [17] P. B. Johnson and R.-W. Christy, “Optical constants of the noble metals,” *Physical review B*, vol. 6, no. 12, p. 4370, 1972.
- [18] J. Lindhard, “On the properties of a gas of charged particles,” *Kgl. Danske Videnskab. Selskab Mat.-Fys. Medd.*, vol. 28, 1954.
- [19] T. Stoll, P. Maioli, A. Crut, N. Del Fatti, and F. Vallée, “Advances in femto-nano-optics: ultrafast nonlinearity of metal nanoparticles,” *The European Physical Journal B*, vol. 87, pp. 1–19, 2014.
- [20] C. F. Bohren and D. R. Huffman, *Absorption and scattering of light by small particles*. Wiley-VCH Verlag GmbH, 1983. pp. 82-129.
- [21] F. Medeghini, *Optics and acoustics with a single nano-object : environment effects*. Phd thesis, University of Claude Bernard Lyon 1, Lyon, February 2018. Available at <https://theses.hal.science/tel-01804173>.
- [22] C.-K. Sun, F. Vallée, L. Acioli, E. Ippen, and J. Fujimoto, “Femtosecond investigation of electron thermalization in gold,” *Physical Review B*, vol. 48, no. 16, p. 12365, 1993.
- [23] P. L. Kapitza, “Heat transfer and superfluidity of helium II,” *Phys. Rev.*, vol. 60, pp. 354–355, Aug 1941.
- [24] E. T. Swartz and R. O. Pohl, “Thermal boundary resistance,” *Reviews of modern physics*, vol. 61, no. 3, p. 605, 1989.
- [25] R. Rouxel, M. Diego, F. Medeghini, P. Maioli, F. Rossella, F. Vallée, F. Banfi, A. Crut, and N. Del Fatti, “Ultrafast thermo-optical dynamics of a single metal nano-object,” *The Journal of Physical Chemistry C*, vol. 124, no. 28, pp. 15625–15633, 2020.
- [26] O. M. Wilson, X. Hu, D. G. Cahill, and P. V. Braun, “Colloidal metal particles as probes of nanoscale thermal transport in fluids,” *Physical Review B*, vol. 66, no. 22, p. 224301, 2002.
- [27] R. M. Costescu, M. A. Wall, and D. G. Cahill, “Thermal conductance of epitaxial interfaces,” *Physical Review B*, vol. 67, no. 5, p. 054302, 2003.
- [28] H.-K. Lyeo and D. G. Cahill, “Thermal conductance of interfaces between highly dissimilar materials,” *Physical Review B—Condensed Matter and Materials Physics*, vol. 73, no. 14, p. 144301, 2006.

- 
- [29] T. Stoll, P. Maioli, A. Crut, S. Rodal-Cedeira, I. Pastoriza-Santos, F. Vallée, and N. Del Fatti, “Time-resolved investigations of the cooling dynamics of metal nanoparticles: impact of environment,” *The Journal of Physical Chemistry C*, vol. 119, no. 22, pp. 12757–12764, 2015.
- [30] A. N. Smith, J. L. Hostetler, and P. M. Norris, “Thermal boundary resistance measurements using a transient thermoreflectance technique,” *Microscale Thermophysical Engineering*, vol. 4, no. 1, pp. 51–60, 2000.
- [31] M. G. Burzo, P. L. Komarov, and P. E. Raad, “Thermal transport properties of gold-covered thin-film silicon dioxide,” *IEEE Transactions on Components and Packaging Technologies*, vol. 26, no. 1, pp. 80–88, 2003.
- [32] D. B. Brown, T. L. Bougher, B. A. Cola, and S. Kumar, “Oxidation limited thermal boundary conductance at metal-graphene interface,” *Carbon*, vol. 139, pp. 913–921, 2018.
- [33] D. G. Cahill, P. V. Braun, G. Chen, D. R. Clarke, S. Fan, K. E. Goodson, P. Keblinski, W. P. King, G. D. Mahan, A. Majumdar, *et al.*, “Nanoscale thermal transport. II. 2003–2012,” *Applied physics reviews*, vol. 1, no. 1, 2014.
- [34] E. M. Greitzer, Z. S. Spakovszky, I. A. Waitz, and D. Quattrochi, “Radiation heat transfer between planar surfaces.” in: *Unified: Thermodynamics and Propulsion*, 2007. Available at <https://web.mit.edu/16.unified/www/FALL/thermodynamics/notes/node136.html>.
- [35] J.-B.-J. Fourier, *Théorie analytique de la chaleur*. F. Didot père et fils (Paris), 1822.
- [36] G. Chen, “Non-fourier phonon heat conduction at the microscale and nanoscale,” *Nature Reviews Physics*, vol. 3, no. 8, pp. 555–569, 2021.
- [37] Y. Guo and M. Wang, “Phonon hydrodynamics and its applications in nanoscale heat transport,” *Physics Reports*, vol. 595, pp. 1–44, 2015.
- [38] M. V. Fischetti, D. J. DiMaria, L. Dori, J. Batey, E. Tierney, and J. Stasiak, “Ballistic electron transport in thin silicon dioxide films,” *Physical Review B*, vol. 35, no. 9, p. 4404, 1987.
- [39] M. E. Siemens, Q. Li, R. Yang, K. A. Nelson, E. H. Anderson, M. M. Murnane, and H. C. Kapteyn, “Quasi-ballistic thermal transport from nanoscale interfaces observed using ultrafast coherent soft X-ray beams,” *Nature materials*, vol. 9, no. 1, pp. 26–30, 2010.
- [40] P. Torres, A. Ziabari, A. Torelló, J. Bafaluy, J. Camacho, X. Cartoixà, A. Shakouri, and F. Alvarez, “Emergence of hydrodynamic heat transport in semiconductors at the nanoscale,” *Physical Review Materials*, vol. 2, no. 7, p. 076001, 2018.
- [41] R. Stoner and H. Maris, “Kapitza conductance and heat flow between solids at temperatures from 50 to 300 K,” *Physical Review B*, vol. 48, no. 22, p. 16373, 1993.
- [42] Y. Xu, H. Wang, Y. Tanaka, M. Shimono, and M. Yamazaki, “Measurement of interfacial thermal resistance by periodic heating and a thermo-reflectance technique,” *Materials transactions*, vol. 48, no. 2, pp. 148–150, 2007.

- [43] J. P. Freedman, X. Yu, R. F. Davis, A. J. Gellman, and J. A. Malen, “Thermal interface conductance across metal alloy–dielectric interfaces,” *Physical Review B*, vol. 93, no. 3, p. 035309, 2016.
- [44] M. Blank and L. Weber, “Influence of the thickness of a nanometric copper interlayer on Au/dielectric thermal boundary conductance,” *Journal of Applied Physics*, vol. 124, no. 10, 2018.
- [45] M. Blank and L. Weber, “Towards a coherent database of thermal boundary conductance at metal/dielectric interfaces,” *Journal of Applied Physics*, vol. 125, no. 9, 2019.
- [46] S. Link and M. A. El-Sayed, “Size and temperature dependence of the plasmon absorption of colloidal gold nanoparticles,” *The Journal of Physical Chemistry B*, vol. 103, no. 21, pp. 4212–4217, 1999.
- [47] C. Voisin, N. Del Fatti, D. Christofilos, and F. Vallée, “Ultrafast electron dynamics and optical nonlinearities in metal nanoparticles,” 2001.
- [48] G. V. Hartland, “Measurements of the material properties of metal nanoparticles by time-resolved spectroscopy,” *Physical Chemistry Chemical Physics*, vol. 6, no. 23, pp. 5263–5274, 2004.
- [49] M. Memesa, S. Lenz, S. G. Emmerling, S. Nett, J. Perlich, P. Müller-Buschbaum, and J. S. Gutmann, “Morphology and photoluminescence study of titania nanoparticles,” *Colloid and polymer science*, vol. 289, pp. 943–953, 2011.
- [50] S. Sohila, M. Rajalakshmi, C. Ghosh, A. Arora, and C. Muthamizhchelvan, “Optical and Raman scattering studies on SnS nanoparticles,” *Journal of Alloys and Compounds*, vol. 509, no. 19, pp. 5843–5847, 2011.
- [51] A. Ponce, J. A. Aguilar, J. Tate, and M. J. Yacamán, “Advances in the electron diffraction characterization of atomic clusters and nanoparticles,” *Nanoscale Advances*, vol. 3, no. 2, pp. 311–325, 2021.
- [52] Y. Fujiyoshi, T. Nemoto, and H. Kurata, “Studying substrate effects on localized surface plasmons in an individual silver nanoparticle using electron energy-loss spectroscopy,” *Ultramicroscopy*, vol. 175, pp. 116–120, 2017.
- [53] D.-W. Oh, A. Jain, J. K. Eaton, K. E. Goodson, and J. S. Lee, “Thermal conductivity measurement of aluminum oxide nanofluids using the 3-omega method,” in *ASME International Mechanical Engineering Congress and Exposition*, vol. 47861, pp. 343–349, 2006.
- [54] G. Pyrgiotakis, C. O. Blattmann, S. Pratsinis, and P. Demokritou, “Nanoparticle–nanoparticle interactions in biological media by atomic force microscopy,” *Langmuir*, vol. 29, no. 36, pp. 11385–11395, 2013.
- [55] S. Kano, T. Tada, and Y. Majima, “Nanoparticle characterization based on STM and STS,” *Chemical Society Reviews*, vol. 44, no. 4, pp. 970–987, 2015.

- 
- [56] M. Faraday, "The Bakerian lecture: Experimental relations of gold (and other metals) to light," *Philos. Trans. R. Soc. London*, vol. 147, pp. 145–181, 1857.
- [57] W. E. Moerner and L. Kador, "Optical detection and spectroscopy of single molecules in a solid," *Physical review letters*, vol. 62, no. 21, p. 2535, 1989.
- [58] M. Orrit and J. Bernard, "Single pentacene molecules detected by fluorescence excitation in a *p*-terphenyl crystal," *Physical review letters*, vol. 65, no. 21, p. 2716, 1990.
- [59] J. Macklin, J. Trautman, T. Harris, and L. Brus, "Imaging and time-resolved spectroscopy of single molecules at an interface," *Science*, vol. 272, no. 5259, pp. 255–258, 1996.
- [60] C. R. Carey, T. LeBel, D. Crisostomo, J. Giblin, M. Kuno, and G. V. Hartland, "Imaging and absolute extinction cross-section measurements of nanorods and nanowires through polarization modulation microscopy," *The Journal of Physical Chemistry C*, vol. 114, no. 38, pp. 16029–16036, 2010.
- [61] D. Christofilos, J.-C. Blancon, J. Arvanitidis, A. S. Miguel, A. Ayari, N. Del Fatti, and F. Vallée, "Optical imaging and absolute absorption cross section measurement of individual nano-objects on opaque substrates: single-wall carbon nanotubes on silicon," *The Journal of Physical Chemistry Letters*, vol. 3, no. 9, pp. 1176–1181, 2012.
- [62] F. Medeghini, A. Crut, M. Gandolfi, F. Rossella, P. Maioli, F. Vallée, F. Banfi, and N. Del Fatti, "Controlling the quality factor of a single acoustic nanoresonator by tuning its morphology," *Nano letters*, vol. 18, no. 8, pp. 5159–5166, 2018.
- [63] F. Medeghini, R. Rouxel, A. Crut, P. Maioli, F. Rossella, F. Banfi, F. Vallée, and N. Del Fatti, "Signatures of small morphological anisotropies in the plasmonic and vibrational responses of individual nano-objects," *The Journal of Physical Chemistry Letters*, vol. 10, no. 18, pp. 5372–5380, 2019.
- [64] R. Rouxel, M. Diego, P. Maioli, N. Lascoux, F. Violla, F. Rossella, F. Banfi, F. Vallée, N. Del Fatti, and A. Crut, "Electron and lattice heating contributions to the transient optical response of a single plasmonic nano-object," *The Journal of Physical Chemistry C*, vol. 125, no. 42, pp. 23275–23286, 2021.
- [65] S. Mitiche, S. Marguet, F. Charra, and L. Douillard, "Plasmonics of regular shape particles, a simple group theory approach," *Nano Research*, vol. 13, pp. 1597–1603, 2020.
- [66] K. L. Young, M. R. Jones, J. Zhang, R. J. Macfarlane, R. Esquivel-Sirvent, R. J. Nap, J. Wu, G. C. Schatz, B. Lee, and C. A. Mirkin, "Assembly of reconfigurable one-dimensional colloidal superlattices due to a synergy of fundamental nanoscale forces," *Proceedings of the National Academy of Sciences*, vol. 109, no. 7, pp. 2240–2245, 2012.
- [67] J. Rodríguez-Fernández, J. Pérez-Juste, P. Mulvaney, and L. M. Liz-Marzán, "Spatially-directed oxidation of gold nanoparticles by Au (III)-CTAB complexes," *The Journal of Physical Chemistry B*, vol. 109, no. 30, pp. 14257–14261, 2005.
- [68] M. N. O'Brien, M. R. Jones, K. L. Kohlstedt, G. C. Schatz, and C. A. Mirkin, "Uniform circular disks with synthetically tailorable diameters: two-dimensional nanoparticles for plasmonics," *Nano letters*, vol. 15, no. 2, pp. 1012–1017, 2015.

- [69] M. Husnik, S. Linden, R. Diehl, J. Niegemann, K. Busch, and M. Wegener, “Quantitative experimental determination of scattering and absorption cross-section spectra of individual optical metallic nanoantennas,” *Physical review letters*, vol. 109, no. 23, p. 233902, 2012.
- [70] M. Born and E. Wolf, “Principles of optics,” *Pergamon Press, New York*, 1965.
- [71] R. A. Askey and A. B. Olde Daalhuis, “Generalized hypergeometric functions and Meijer  $G$ -function.” in: *NIST Handbook of Mathematical Functions*, Cambridge University Press, 2010. Available at <https://dlmf.nist.gov/16>.
- [72] H. Hövel, S. Fritz, A. Hilger, U. Kreibig, and M. Vollmer, “Width of cluster plasmon resonances: Bulk dielectric functions and chemical interface damping,” *Physical Review B*, vol. 48, no. 24, p. 18178, 1993.
- [73] H. Baida, P. Billaud, S. Marhaba, D. Christofilos, E. Cottancin, A. Crut, J. Lerme, P. Maioli, M. Pellarin, M. Broyer, *et al.*, “Quantitative determination of the size dependence of surface plasmon resonance damping in single Ag@SiO<sub>2</sub> nanoparticles,” *Nano letters*, vol. 9, no. 10, pp. 3463–3469, 2009.
- [74] V. Juvé, M. F. Cardinal, A. Lombardi, A. Crut, P. Maioli, J. Pérez-Juste, L. M. Liz-Marzán, N. Del Fatti, and F. Vallée, “Size-dependent surface plasmon resonance broadening in nonspherical nanoparticles: single gold nanorods,” *Nano letters*, vol. 13, no. 5, pp. 2234–2240, 2013.
- [75] P. Zijlstra, P. M. Paulo, K. Yu, Q.-H. Xu, and M. Orrit, “Chemical interface damping in single gold nanorods and its near elimination by tip-specific functionalization,” *Angewandte Chemie-International Edition*, vol. 51, no. 33, p. 8352, 2012.
- [76] B. Foerster, V. A. Spata, E. A. Carter, C. Sönnichsen, and S. Link, “Plasmon damping depends on the chemical nature of the nanoparticle interface,” *Science advances*, vol. 5, no. 3, p. eaav0704, 2019.
- [77] M. Alam, A. Raghu, M. A. Haque, C. Muratore, and A. A. Voevodin, “Structural size and temperature dependence of solid to air heat transfer,” *International journal of thermal sciences*, vol. 73, pp. 1–7, 2013.
- [78] C. Cheng, W. Fan, J. Cao, S.-G. Ryu, J. Ji, C. P. Grigoropoulos, and J. Wu, “Heat transfer across the interface between nanoscale solids and gas,” *ACS nano*, vol. 5, no. 12, pp. 10102–10107, 2011.
- [79] S. Chen, A. L. Moore, W. Cai, J. W. Suk, J. An, C. Mishra, C. Amos, C. W. Magnuson, J. Kang, L. Shi, *et al.*, “Raman measurements of thermal transport in suspended monolayer graphene of variable sizes in vacuum and gaseous environments,” *ACS nano*, vol. 5, no. 1, pp. 321–328, 2011.
- [80] B. Graczykowski, A. El Sachat, J. S. Reparaz, M. Sledzinska, M. R. Wagner, E. Chavez-Angel, Y. Wu, S. Volz, Y. Wu, F. Alzina, *et al.*, “Thermal conductivity and air-mediated losses in periodic porous silicon membranes at high temperatures,” *Nature communications*, vol. 8, no. 1, p. 415, 2017.

- 
- [81] S. Dilhaire, G. Pernot, G. Calbris, J.-M. Rampnoux, and S. Grauby, “Heterodyne picosecond thermoreflectance applied to nanoscale thermal metrology,” *Journal of Applied Physics*, vol. 110, no. 11, 2011.
- [82] K. C. Collins, A. A. Maznev, J. Cuffe, K. A. Nelson, and G. Chen, “Examining thermal transport through a frequency-domain representation of time-domain thermoreflectance data,” *Review of Scientific Instruments*, vol. 85, no. 12, 2014.
- [83] N. Feste, “Technologie cryogénique pour mémoire basse consommation destinées aux centres de données,” 2024. Available at <https://www.elektormagazine.fr/news/technologie-cryogenique-pour-memoire-basse-consommation-destinees-aux-centres-de-don>
- [84] K. Moore Tibbetts, “Size of nanoparticles from laser ablation: Lessons from wet-chemical synthesis,” 2019. Available at <https://www.openaccessgovernment.org/size-of-nanoparticles/74582/>.
- [85] E. Pop, S. Sinha, and K. E. Goodson, “Heat generation and transport in nanometer-scale transistors,” *Proceedings of the IEEE*, vol. 94, no. 8, pp. 1587–1601, 2006.
- [86] G. CHEN, “Nonlocal and nonequilibrium heat conduction in the vicinity of nanoparticles,” *Journal of heat transfer*, vol. 118, no. 3, pp. 539–545, 1996.
- [87] A. J. Schmidt, R. Cheaito, and M. Chiesa, “A frequency-domain thermoreflectance method for the characterization of thermal properties,” *Review of scientific instruments*, vol. 80, no. 9, 2009.
- [88] K. T. Regner, D. P. Sellan, Z. Su, C. H. Amon, A. J. McGaughey, and J. A. Malen, “Broadband phonon mean free path contributions to thermal conductivity measured using frequency domain thermoreflectance,” *Nature communications*, vol. 4, no. 1, p. 1640, 2013.
- [89] R. Wilson and D. G. Cahill, “Anisotropic failure of Fourier theory in time-domain thermoreflectance experiments,” *Nature communications*, vol. 5, no. 1, p. 5075, 2014.
- [90] A. J. Minnich, J. A. Johnson, A. J. Schmidt, K. Esfarjani, M. S. Dresselhaus, K. A. Nelson, and G. Chen, “Thermal conductivity spectroscopy technique to measure phonon mean free paths,” *Physical review letters*, vol. 107, no. 9, p. 095901, 2011.
- [91] J. A. Johnson, A. A. Maznev, J. Cuffe, J. K. Eliason, A. J. Minnich, T. Kehoe, C. M. S. Torres, G. Chen, and K. A. Nelson, “Direct measurement of room-temperature nondiffusive thermal transport over micron distances in a silicon membrane,” *Phys. Rev. Lett.*, vol. 110, p. 025901, Jan 2013.
- [92] V. Juvé, M. Scardamaglia, P. Maioli, A. Crut, S. Merabia, L. Joly, N. Del Fatti, and F. Vallée, “Cooling dynamics and thermal interface resistance of glass-embedded metal nanoparticles,” *Physical Review B*, vol. 80, no. 19, p. 195406, 2009.
- [93] M. Hu and G. V. Hartland, “Heat dissipation for Au particles in aqueous solution: relaxation time versus size,” *The Journal of Physical Chemistry B*, vol. 106, no. 28, pp. 7029–7033, 2002.

- [94] F. Banfi, V. Juvé, D. Nardi, S. Dal Conte, C. Giannetti, G. Ferrini, N. Del Fatti, and F. Vallée, “Temperature dependence of the thermal boundary resistivity of glass-embedded metal nanoparticles,” *Applied Physics Letters*, vol. 100, no. 1, 2012.
- [95] J. Park and D. G. Cahill, “Plasmonic sensing of heat transport at solid–liquid interfaces,” *The Journal of Physical Chemistry C*, vol. 120, no. 5, pp. 2814–2821, 2016.
- [96] A. Von Reppert, R. Sarhan, F. Stete, J. Pudell, N. Del Fatti, A. Crut, J. Koetz, F. Liebig, C. Prietzel, and M. Bargheer, “Watching the vibration and cooling of ultrathin gold nanotriangles by ultrafast X-ray diffraction,” *The Journal of Physical Chemistry C*, vol. 120, no. 50, pp. 28894–28899, 2016.
- [97] K. M. Hoogeboom-Pot, J. N. Hernandez-Charpak, X. Gu, T. D. Frazer, E. H. Anderson, W. Chao, R. W. Falcone, R. Yang, M. M. Murnane, H. C. Kapteyn, *et al.*, “A new regime of nanoscale thermal transport: Collective diffusion increases dissipation efficiency,” *Proceedings of the National Academy of Sciences*, vol. 112, no. 16, pp. 4846–4851, 2015.
- [98] T. D. Frazer, J. L. Knobloch, K. M. Hoogeboom-Pot, D. Nardi, W. Chao, R. W. Falcone, M. M. Murnane, H. C. Kapteyn, and J. N. Hernandez-Charpak, “Engineering nanoscale thermal transport: Size- and spacing-dependent cooling of nanostructures,” *Physical Review Applied*, vol. 11, no. 2, p. 024042, 2019.
- [99] Y. Hu, L. Zeng, A. J. Minnich, M. S. Dresselhaus, and G. Chen, “Spectral mapping of thermal conductivity through nanoscale ballistic transport,” *Nature nanotechnology*, vol. 10, no. 8, pp. 701–706, 2015.
- [100] H. Zhang, C. Hua, D. Ding, and A. J. Minnich, “Length dependent thermal conductivity measurements yield phonon mean free path spectra in nanostructures,” *Scientific Reports*, vol. 5, no. 1, p. 9121, 2015.
- [101] T. Oyake, M. Sakata, and J. Shiomi, “Nanoscale thermal conductivity spectroscopy by using gold nano-islands heat absorbers,” *Applied Physics Letters*, vol. 106, no. 7, 2015.
- [102] A. Beardo, J. L. Knobloch, L. Sendra, J. Bafaluy, T. D. Frazer, W. Chao, J. N. Hernandez-Charpak, H. C. Kapteyn, B. Abad, M. M. Murnane, *et al.*, “A general and predictive understanding of thermal transport from 1D- and 2D-confined nanostructures: Theory and experiment,” *ACS nano*, vol. 15, no. 8, pp. 13019–13030, 2021.
- [103] X. Zhang and C. P. Grigoropoulos, “Thermal conductivity and diffusivity of free-standing silicon nitride thin films,” *Review of scientific instruments*, vol. 66, no. 2, pp. 1115–1120, 1995.
- [104] S.-M. Lee and D. G. Cahill, “Heat transport in thin dielectric films,” *Journal of applied physics*, vol. 81, no. 6, pp. 2590–2595, 1997.
- [105] L. La Spina, A. W. van Herwaarden, H. Schellevis, W. H. Wien, N. Nenadovic, and L. K. Nanver, “Bulk-micromachined test structure for fast and reliable determination of the lateral thermal conductivity of thin films,” *IEEE/ASME Journal of Microelectromechanical Systems*, vol. 16, no. 3, pp. 675–683, 2007.

- 
- [106] M. Alam, M. P. Manoharan, M. A. Haque, C. Muratore, and A. Voevodin, “Influence of strain on thermal conductivity of silicon nitride thin films,” *Journal of Micromechanics and Microengineering*, vol. 22, no. 4, p. 045001, 2012.
- [107] M. Bogner, A. Hofer, G. Benstetter, H. Gruber, and R. Y. Fu, “Differential  $3\omega$  method for measuring thermal conductivity of AlN and Si<sub>3</sub>N<sub>4</sub> thin films,” *Thin Solid Films*, vol. 591, pp. 267–270, 2015.
- [108] H. Ftouni, C. Blanc, D. Tainoff, A. D. Fefferman, M. Defoort, K. J. Lulla, J. Richard, E. Collin, and O. Bourgeois, “Thermal conductivity of silicon nitride membranes is not sensitive to stress,” *Physical Review B*, vol. 92, no. 12, p. 125439, 2015.
- [109] A. Movsesyan, S. Marguet, A. Muravitskaya, J. Béal, P.-M. Adam, and A.-L. Baudrion, “Influence of the CTAB surfactant layer on optical properties of single metallic nanospheres,” *JOSA A*, vol. 36, no. 11, pp. C78–C84, 2019.
- [110] M. Gandolfi, A. Crut, F. Medeghini, T. Stoll, P. Maioli, F. Vallee, F. Banfi, and N. Del Fatti, “Ultrafast thermo-optical dynamics of plasmonic nanoparticles,” *The Journal of Physical Chemistry C*, vol. 122, no. 15, pp. 8655–8666, 2018.
- [111] M. Ferrera, G. Della Valle, M. Sygletou, M. Magnozzi, D. Catone, P. O’Keeffe, A. Paladini, F. Toschi, L. Mattera, M. Canepa, *et al.*, “Thermometric calibration of the ultrafast relaxation dynamics in plasmonic Au nanoparticles,” *ACS Photonics*, vol. 7, no. 4, pp. 959–966, 2020.
- [112] R. Rouxel, *Ultrafast thermo-optical dynamics of single plasmonic nanoparticles*. Phd thesis, University of Claude Bernard Lyon 1, Lyon, December 2020. Available at <https://theses.hal.science/tel-03186398>.
- [113] C. Caddeo, C. Melis, A. Ronchi, C. Giannetti, G. Ferrini, R. Rurali, L. Colombo, and F. Banfi, “Thermal boundary resistance from transient nanocalorimetry: a multiscale modeling approach,” *Physical Review B*, vol. 95, no. 8, p. 085306, 2017.
- [114] A. J. Schmidt, R. Cheaito, and M. Chiesa, “Characterization of thin metal films via frequency-domain thermoreflectance,” *Journal of Applied Physics*, vol. 107, no. 2, 2010.
- [115] Y. K. Koh and D. G. Cahill, “Frequency dependence of the thermal conductivity of semiconductor alloys,” *Physical Review B*, vol. 76, no. 7, p. 075207, 2007.
- [116] S. M. Hatam-Lee, F. Jabbari, and A. Rajabpour, “Interfacial thermal conductance between gold and SiO<sub>2</sub>: A molecular dynamics study,” *Nanoscale and Microscale Thermophysical Engineering*, vol. 26, no. 1, pp. 40–51, 2022.
- [117] T. Jeong, J.-G. Zhu, S. Chung, and M. R. Gibbons, “Thermal boundary resistance for gold and CoFe alloy on silicon nitride films,” *Journal of Applied Physics*, vol. 111, no. 8, 2012.
- [118] H. S. Carslaw and J. C. Jaeger, *Conduction of Heat in Solids*. Oxford, 1959.

- [119] A. Tadeu and N. Simões, “Three-dimensional fundamental solutions for transient heat transfer by conduction in an unbounded medium, half-space, slab and layered media,” *Engineering Analysis with Boundary Elements*, vol. 30, no. 5, pp. 338–349, 2006.
- [120] J. Cuffe, J. K. Eliason, A. A. Maznev, K. C. Collins, J. A. Johnson, A. Shchepetov, M. Prunnila, J. Ahopelto, C. M. S. Torres, G. Chen, *et al.*, “Reconstructing phonon mean-free-path contributions to thermal conductivity using nanoscale membranes,” *Physical Review B*, vol. 91, no. 24, p. 245423, 2015.
- [121] C. Panais, R. Rouxel, N. Lascoux, S. Marguet, P. Maioli, F. Banfi, F. Vallée, N. Del Fatti, and A. Crut, “Cooling dynamics of individual gold nanodisks deposited on thick substrates and nanometric membranes,” *The Journal of Physical Chemistry Letters*, vol. 14, no. 23, pp. 5343–5352, 2023.
- [122] C. Panais, N. Lascoux, S. Marguet, P. Maioli, F. Banfi, F. Vallée, N. Del Fatti, and A. Crut, “Impact of supporting nanometric membranes on the thermo-optical dynamics of individual plasmonic nanodisks,” *Nanoscale*, 2024.
- [123] R. Wilson, B. A. Apgar, L. W. Martin, and D. G. Cahill, “Thermoreflectance of metal transducers for optical pump-probe studies of thermal properties,” *Optics express*, vol. 20, no. 27, pp. 28829–28838, 2012.
- [124] R. Jiménez Riobóo, M. Philipp, M. Ramos, and J.-K. Krüger, “Concentration and temperature dependence of the refractive index of ethanol-water mixtures: Influence of intermolecular interactions,” *The European Physical Journal E*, vol. 30, pp. 19–26, 2009.
- [125] A. W. Elshaari, I. E. Zadeh, K. D. Jöns, and V. Zwiller, “Thermo-optic characterization of silicon nitride resonators for cryogenic photonic circuits,” *IEEE Photonics Journal*, vol. 8, no. 3, pp. 1–9, 2016.
- [126] M. E. Thomas, S. K. Andersson, R. M. Sova, and R. I. Joseph, “Frequency and temperature dependence of the refractive index of sapphire,” *Infrared physics & technology*, vol. 39, no. 4, pp. 235–249, 1998.
- [127] M. Daimon and A. Masumura, “Measurement of the refractive index of distilled water from the near-infrared region to the ultraviolet region,” *Applied optics*, vol. 46, no. 18, pp. 3811–3820, 2007.
- [128] T. Stoll, *Ultrafast electronic, acoustic and thermal properties of metal nanoparticles and clusters*. Phd thesis, University of Claude Bernard Lyon 1, Lyon, December 2014. Available at <https://theses.hal.science/tel-01128276>.
- [129] A. Crut, P. Maioli, N. Del Fatti, and F. Vallée, “Acoustic vibrations of metal nano-objects: time-domain investigations,” *Physics Reports*, vol. 549, pp. 1–43, 2015.
- [130] V. Juvé, A. Crut, P. Maioli, M. Pellarin, M. Broyer, N. Del Fatti, and F. Vallée, “Probing elasticity at the nanoscale: terahertz acoustic vibration of small metal nanoparticles,” *Nano letters*, vol. 10, no. 5, pp. 1853–1858, 2010.

- 
- [131] H. E. Saucedo, D. Mongin, P. Maioli, A. Crut, M. Pellarin, N. Del Fatti, F. Vallée, and I. L. Garzón, “Vibrational properties of metal nanoparticles: Atomistic simulation and comparison with time-resolved investigation,” *The Journal of Physical Chemistry C*, vol. 116, no. 47, pp. 25147–25156, 2012.
- [132] H. Staleva and G. V. Hartland, “Transient absorption studies of single silver nanocubes,” *The Journal of Physical Chemistry C*, vol. 112, no. 20, pp. 7535–7539, 2008.
- [133] M. A. van Dijk, M. Lippitz, and M. Orrit, “Detection of acoustic oscillations of single gold nanospheres by time-resolved interferometry,” *Physical review letters*, vol. 95, no. 26, p. 267406, 2005.
- [134] K. Yu, J. E. Sader, P. Zijlstra, M. Hong, Q.-H. Xu, and M. Orrit, “Probing silver deposition on single gold nanorods by their acoustic vibrations,” *Nano letters*, vol. 14, no. 2, pp. 915–922, 2014.
- [135] G. V. Hartland, “Ultrafast studies of single semiconductor and metal nanostructures through transient absorption microscopy,” *Chemical science*, vol. 1, no. 3, pp. 303–309, 2010.
- [136] J. Burgin, P. Langot, N. Del Fatti, F. Vallée, W. Huang, and M. El-Sayed, “Time-resolved investigation of the acoustic vibration of a single gold nanoprism pair,” *The Journal of Physical Chemistry C*, vol. 112, no. 30, pp. 11231–11235, 2008.
- [137] T. A. Major, M. S. Devadas, S. S. Lo, and G. V. Hartland, “Optical and dynamical properties of chemically synthesized gold nanoplates,” *The Journal of Physical Chemistry C*, vol. 117, no. 3, pp. 1447–1452, 2013.
- [138] A. Girard, H. Gehan, A. Mermet, C. Bonnet, J. Lermé, A. Berthelot, E. Cottancin, A. Crut, and J. Margueritat, “Acoustic mode hybridization in a single dimer of gold nanoparticles,” *Nano Letters*, vol. 18, no. 6, pp. 3800–3806, 2018.
- [139] B. Auld, *Acoustic Fields and Waves in Solids*, vol. 1. John Wiley & Sons, 1973. pp. 1-167.
- [140] P. V. Ruijgrok, P. Zijlstra, A. L. Tchebotareva, and M. Orrit, “Damping of acoustic vibrations of single gold nanoparticles optically trapped in water,” *Nano letters*, vol. 12, no. 2, pp. 1063–1069, 2012.
- [141] W.-S. Chang, F. Wen, D. Chakraborty, M.-N. Su, Y. Zhang, B. Shuang, P. Nordlander, J. E. Sader, N. J. Halas, and S. Link, “Tuning the acoustic frequency of a gold nanodisk through its adhesion layer,” *Nature communications*, vol. 6, no. 1, p. 7022, 2015.
- [142] P. Zijlstra, A. L. Tchebotareva, J. W. Chon, M. Gu, and M. Orrit, “Acoustic oscillations and elastic moduli of single gold nanorods,” *Nano letters*, vol. 8, no. 10, pp. 3493–3497, 2008.
- [143] R. Marty, A. Arbouet, C. Girard, A. Mlayah, V. Paillard, V. K. Lin, S. L. Teo, and S. Tripathy, “Damping of the acoustic vibrations of individual gold nanoparticles,” *Nano letters*, vol. 11, no. 8, pp. 3301–3306, 2011.

- [144] M.-N. Su, P. D. Dongare, D. Chakraborty, Y. Zhang, C. Yi, F. Wen, W.-S. Chang, P. Nordlander, J. E. Sader, N. J. Halas, *et al.*, “Optomechanics of single aluminum nanodisks,” *Nano letters*, vol. 17, no. 4, pp. 2575–2583, 2017.
- [145] C. Yi, M.-N. Su, P. D. Dongare, D. Chakraborty, Y.-Y. Cai, D. M. Marolf, R. N. Kress, B. Ostovar, L. J. Tauzin, F. Wen, *et al.*, “Polycrystallinity of lithographically fabricated plasmonic nanostructures dominates their acoustic vibrational damping,” *Nano letters*, vol. 18, no. 6, pp. 3494–3501, 2018.
- [146] A. Crut, “Substrate-supported nano-objects with high vibrational quality factors,” *Journal of Applied Physics*, vol. 131, no. 24, 2022.
- [147] M. Garfinkel, J. Tiemann, and W. Engeler, “Piezorefectivity of the noble metals,” *Physical Review*, vol. 148, no. 2, p. 695, 1966.
- [148] O. Saison-Francioso, G. Lévêque, and A. Akjouj, “Numerical modeling of acousto-plasmonic coupling in metallic nanoparticles,” *The Journal of Physical Chemistry C*, vol. 124, no. 22, pp. 12120–12133, 2020.
- [149] A. Ahmed, M. Pelton, and J. R. Guest, “Understanding how acoustic vibrations modulate the optical response of plasmonic metal nanoparticles,” *ACS nano*, vol. 11, no. 9, pp. 9360–9369, 2017.



## **Abstract:**

This thesis work focuses on the optical study of the thermal and vibrational properties of metallic nano-objects. Two optical techniques operating at the scale of a single nano-object (spatial modulation spectroscopy and time-resolved pump-probe spectroscopy) were used to localize single gold nanodisks randomly deposited on a solid substrate, characterize their optical properties, and study their ultrafast dynamics.

The first part of this work describes the optical study of the cooling of colloidal gold nanodisks deposited on substrates of different compositions and thicknesses, complemented by numerical simulations. Experiments and simulations demonstrated that the thermal dynamics, governed by thermal transfer at the nanodisk-substrate interface and heat diffusion in the substrate, strongly depend on the characteristics of the substrate, with a significant slowdown in the case of nanometric membranes.

The second part of this work allowed to characterize the transient optical response of a single gold nanodisk induced by its thermal dynamics. A strong dependence of the sensitivity of the optical measurements to nanodisk heating on the wavelength of the light beam used to probe this heating was demonstrated and quantified. A dependence of the temporal dynamics of the measured optical signals on the probe wavelength was also observed in the spectral range where the contribution of the heating of the membrane is not negligible compared to that associated with nanodisk heating, and was quantitatively reproduced by a thermo-optical model.

The final section of this thesis focuses on the study of the vibrational properties of single gold nanodisks. The experiments carried out allowed to confirm the strong dependence of the vibrational quality factors of deposited nano-objects on their morphology, demonstrated in previous work. In particular, improved quality factors were observed for nanodisks with a diameter/thickness ratios between 2 and 5. The sensitivity of measured optical signals to the vibrations of a nanodisk was also measured. It strongly depends on the probe wavelength, while presenting a very different spectral shape from that of optical sensitivity to nanodisk heating.

This research work has thus led to a better understanding of the cooling and vibrational dynamics of single gold nanodisks deposited on nanometer-thick membranes, and has allowed to precisely quantify the sensitivity of signals measured by optical pump-probe spectroscopy to these dynamics. Future work could focus on studying nanoparticles deposited on membranes of different compositions that are more favorable for demonstrating non-diffusive modes of heat transfer, or investigate the nature of internal vibrational damping phenomena, which determine the vibrational quality factors of nano-objects in the absence of coupling with the environment.

## **Keywords:**

Single metallic nanoparticles, Nanothermics, Pump-probe spectroscopy, Thermoplasmonics, Spatial modulation spectroscopy, Vibrational eigenmodes

**Résumé :**

Ce travail de thèse porte sur l'étude optique des propriétés thermiques et vibrationnelles de nano-objets métalliques. Deux techniques optiques opérant à l'échelle du nano-objet unique (la spectroscopie par modulation spatiale et la spectroscopie pompe-sonde résolue en temps) ont été utilisées pour localiser des nanodisques d'or individuels déposés aléatoirement sur un substrat solide, caractériser leurs propriétés optiques et étudier leur dynamique ultrarapide.

La première partie de ce travail décrit l'étude optique du refroidissement de nanodisques d'or colloïdaux déposés sur des substrats de différentes compositions et épaisseurs, complétée par des simulations numériques. Les expériences et simulations réalisées ont démontré que la dynamique thermique, régie par le transfert thermique à l'interface nanodisque-substrat et la diffusion de la chaleur dans le substrat, dépend fortement des caractéristiques du substrat, avec notamment un ralentissement marqué dans le cas de membranes nanométriques.

La deuxième partie de ce travail a permis de caractériser la réponse optique transitoire d'un nanodisque d'or unique induite par sa dynamique thermique. Une forte dépendance de la sensibilité des mesures optiques à l'échauffement du nanodisque vis-à-vis de la longueur d'onde du faisceau lumineux utilisé pour sonder cet échauffement a pu être démontrée et quantifiée. Une dépendance de la dynamique temporelle des signaux optiques mesurés en fonction de la longueur d'onde de sonde a également été observée dans la gamme spectrale où la contribution de l'échauffement de la membrane n'est pas négligeable devant celle associée à l'échauffement du nanodisque, et a pu être reproduite quantitativement par un modèle thermo-optique.

La dernière section de cette thèse se concentre sur l'étude des propriétés vibrationnelles de nanodisques d'or uniques. Les expériences menées ont permis de confirmer la dépendance marquée des facteurs de qualité vibrationnels de nano-objets déposés vis-à-vis de leur morphologie, démontrée dans des travaux antérieurs. En particulier, des facteurs de qualité améliorés ont été observés pour des nanodisques avec des rapports diamètre/épaisseur compris entre 2 et 5. La sensibilité des signaux optiques mesurés aux vibrations d'un nanodisque a également été mesurée. Elle dépend fortement de la longueur d'onde de la sonde, tout en présentant une forme spectrale très différente de celle de la sensibilité optique à l'échauffement du nanodisque.

Ce travail de recherche a ainsi permis de mieux comprendre les dynamiques de refroidissement et vibrationnelle de nanodisques d'or individuels déposés sur des membranes d'épaisseur nanométrique, et de quantifier précisément la sensibilité des signaux mesurés par spectroscopie optique pompe-sonde à ces dynamiques. Des travaux ultérieurs pourraient se focaliser sur l'étude de nanoparticules déposées sur des membranes de composition différente et plus favorable à la mise en évidence de modalités non-diffusives de transfert thermique, ou encore chercher à préciser la nature des phénomènes internes d'amortissement vibrationnels, qui déterminent les facteurs de qualité vibrationnels des nano-objets en l'absence de couplage avec l'environnement.

**Mots-clés :**

Nanoparticules métalliques individuelles, Nanothermique, Spectroscopie pompe-sonde, Thermo-plasmonique, Spectroscopie par modulation spatiale, Modes propres de vibration